Technische Universität München

TUM School of Life Sciences

Schädigung des optischen Apparats von *Mus musculus* nach Exposition gegenüber ionisierender Strahlung moderater Dosis: *In-vivo-* und *post-mortem*-Analyse der Linse, Retina und Cornea

Daniel Pawliczek

Vollständiger Abdruck der von der Fakultät TUM School of Life Sciences der Technischen Universität München zur Erlangung des akademischen Grades eines

Doktors der Naturwissenschaften (Dr. rer. nat.)

genehmigten Dissertation.

Vorsitzende:	Prof. Angelika Schnieke, Ph. D.
Prüfende der Dissertation:	1. Priv.-Doz. Dr. Sabine Hölter-Koch 2. Prof. Dr. Gabriele Multhoff 3. Priv.-Doz. Dr. Anna Friedl

Die Dissertation wurde am 17.02.2021 bei der Technischen Universität München eingereicht und durch die Fakultät TUM School of Life Sciences am 27.08.2021 angenommen.

Abstract

Ionising radiation (IR) is a physical trigger for cataractogenesis to which a considerable portion of the population is exposed by medical applications. To assess the risks for vision impairment posed by a certain dose of IR, more experimental data on model organism and detailed observations on the principal radiation-related cataract, the posterior subcapsular cataract, are required to understand the underlying mechanism. It is also uncertain how strongly possible lenticular or even corneal/retinal alterations may affect vision. The here presented thesis endeavoured to an answer and to define radiation sensitivity of the eye as a whole.

Mice of hybrid C57BL6/JG and C3H background (with\without heterozygous *Ercc2* point mutation) were whole body-irradiated with low linear energy transfer (LET) radiation (γ- and X-rays) at postnatal days 2 (P2) and 70 (P70). State-of-the-art *in-vivo* lens investigation methods, Scheimpflug imaging and optical coherence tomography (OCT) were used to assess lenticular, retinal and corneal damages *post* irradiation. Visual acuity was determined and correlated with individual ocular impairments. Histological and immunohistochemical analyses were conducted to assess and understand observed phenotypes.

In course of this work, a new OCT-based subcapsular cataract classification was introduced that built upon pure light-scattering properties of the lesions. It was shown that 0.5 Gy increased significantly the fraction of more scattering lesion types in irradiated P70 mice. Within the murine first half of life, only 2 Gy proved to increase the number of posterior subcapsular cataracts in histology. Visual acuity of P70 mice was reduced by 12 %/Gy. The high importance of age at irradiation in combination with the genetic background was revealed and inner cortical cataracts specified for irradiated P2 mice for the first time. Retinal damage was observed only in P2 mice within 10 weeks after irradiation and corneal damage with a high latency only in P70 mice. Summarised ocular impairment was larger and more momentous for vision in neonatal than in adult irradiated mice.

Clear vision is a crucial part of life quality. Therefore, guidelines for radiation protection are under constant review. The here presented data could not support a high impact of moderate doses on the vision of young adult mice, exemplary determined by the visual acuity. Nonetheless, the effects are important because high acuity vision is of utmost importance for humans and reductions of roughly one tenth per Gy could subjectively be very vision-impairing. Furthermore, this thesis underlines the necessity to protect unborn human life from moderate doses of IR.

Key words: cataracts, cornea, ionising radiation, lens, OCT, retina, Scheimpflug imaging

Zusammenfassung

Die Kataraktbildung kann durch das physikalische Agens ionisierende Strahlung (IS) ausgelöst werden, dem ein umfangreicher Teil der Bevölkerung z. B. über medizinische Untersuchungen ausgesetzt ist. Um die Gefahr zu bewerten, die von einer gewissen Dosis IS ausgeht, sind mehr experimentelle Daten nötig. Detaillierte Beobachtungen der strahlenassozierten subkapsulären Katarakte sind erforderlich, um zugrundeliegende Mechanismen zu verstehen. Es ist ebenso offen wie Schädigungen der Cornea oder Retina das Sehvermögen beeinträchtigen. Die vorliegende Arbeit versucht diese Fragen zu beantworten und die Strahlenempfindlichkeit des Auges als Ganzes neu zu bewerten.

F1-Hybriden aus einer C57BL6/JGxC3H-Kreuzung (mit\ohne heterozygoter *Ercc2*-Mutation) wurden an Tag 2 (P2) und 70 (P70) postnatal mit niedriger linearer Energietransferstrahlung (γ- und Röntgenstrahlen) ganzkörperbestrahlt. Scheimpflug-Bildgebung und optische Kohärenztomographie (OCT) wurden genutzt, um entweder Linsen-, Retina- oder Corneaschäden *in vivo* zu bewerten. Die Sehschärfe wurde ermittelt und mit individuellen Schädigungen korreliert. Aufgetretene strahlenassoziierte Schäden wurden mit Hilfe histologischer und immunhistologischer Untersuchungen bewertet.

In dieser Arbeit wurde eine neue OCT-basierte Klassifikation subkapsulärer Katarakte eingeführt, die sich an Lichtstreueigenschaften orientiert. Es konnte gezeigt werden, dass bereits 0,5 Gy einen signifikanten Anstieg lichtstreuender Läsionen in bestrahlten P70 Mäusen verursachen, aber nur 2 Gy in der Lage waren innerhalb der murinen Lebenshalbzeit die Zahl posteriorer subkapsularer Katarakte in Histologien signifikant zu erhöhen. Die Sehschärfe von P70-Mäusen wurde um 12 %/Gy reduziert. Weiterhin konnte der Einfluss der Kombination [Alter bei Bestrahlung*genetischer Hintergrund] aufgedeckt und Katarakte in bestrahlten P2-Mäusen erstmals als innere kortikale Läsionen spezifiziert werden. Retinaschäden konnten nur in P2-Mäusen 10 Wochen nach Bestrahlung nachgewiesen werden und Corneaschäden mit einer hohen Latenz nur in P70-Mäusen. Insgesamt waren okuläre Schäden größer und folgenreicher für die Sehfähigkeit in Mäusen bestrahlt zu P2 als P70.

Auf Grund der hohen Stellung ungetrübter Sicht für die Lebensqualität werden Strahlenschutzrichtlinien unentwegt überarbeitet. Die hier vorgelegten Daten können jedoch keinen erheblichen Einfluss moderater Dosen auf die Sehschärfe von P70-Mäusen belegen. Dennoch könnten die Effekte im Menschen abträglich sein. Schlussendlich belegt diese Arbeit die Wichtigkeit ungeborenes Leben vor moderaten Dosen von IS zu schützen.

Schlagwörter: Cornea, ionisierende Strahlung, Katarakte, Linse, OCT, Retina, Scheimpflug-Bildgebung

Vorwort

Eine kurze Apologetik des reinen Wissenschaftsverständnisses im Licht der Spätphilosophie Martin Heideggers

Der deutsche Forschungsdiskurs scheint von einem wiederkehrenden Motiv bestimmt zu sein. Er fokussiert sich auf die Existenzberechtigung der *Grundlagenforschung*, wobei der Konkurrent bzw. Wettbewerber bei der Verteilung von unternehmerischer und staatlicher Finanzierung in der *Angewandten Forschung* zu sehen ist [1]. Die *Grundlagenforschung* war phasenweise schwer in der Defensive und musste der agilen, zeitgemäßeren, d.h. verwertbaren *Angewandten Forschung* das Feld überlassen oder aber als solche auf Umwegen erkennbar sein, indem sie eines unbestimmten Tages einen entscheidenden Beitrag bei der Entwicklung von Techniken und Produkten liefert.

Letztere Darstellung fällt Verteidigern der *Grundlagenforschung* nicht allzu schwer, da doch, dank intakter quervernetzter Berichterstattung von Tages- und Wochenpresse, mittlerweile jedes Kind weiß, dass bspw. Penicillin - der Fackelträger im erfolgreichen Kampf gegen bakterielle Infektionskrankheiten - einem reinen Laborzufall zu verdanken war. Unzählige andere Entdeckungen waren ebenfalls Ergebnisse wissenschaftlicher Koinzidenz, Früchte reiner Spielerei, deren Motivation in erster Linie Wissensliebe und nicht die antizipierte Verwendung war. Diese Tatsachen sind, bar jeder Übertreibung, Allgemeinplätze geworden. Wortführer der Grundlagenforschung wussten also eine faktische Gleichsetzung mit praktisch orientierter Forschung zu erreichen, wobei das Hauptunterscheidungsmerkmal beim gesellschaftlichen Nutzen auf eine zeitliche Verzögerung zusammenschmolz.

Es ist wichtig zu verstehen, dass diese Argumentation bei der Finanzierung von *Grundlagenforschung* immer eingepreist wird und nicht auf taube Ohren stößt. Tatsächlich lässt sich z.B. am Wachstum der Budgets der Deutschen Forschungsgemeinschaft (DFG) von fast 25 % zwischen 2010 und 2020 (von 2,64 Mrd. EUR auf 3,3 Mrd. EUR) erkennen, dass Forschungsförderung im Allgemeinen - und Grundlagenforschung im Besonderen - keine Depression erfährt, mithin also die Akzeptanz bei den Entscheidungsträgern schlechter sein könnte (wobei das BIP-Wachstum im gleichen Zeitraum stärker war).

Die Bewertung der Bedeutung grundlagenorientierter Forschung sollte sich jedoch nicht darin erschöpfen, ob sie den praktischen Erfordernissen einer innovationsgetriebenen Volkswirtschaft Rechnung tragen kann. Es ist aus ersichtlichen Gründen nicht einmal möglich diese Frage für eine beliebig gewählte wissenschaftliche Behandlung elementarer Zusammenhänge zu beantworten. Gleichwohl kann sich die *Grundlagenforschung* auch nicht entkoppeln und sich einer gesellschaftlichen Rolle verschließen. Diese Gefahr besteht auch nicht, wie Prof. Dr. Ulrich Nierste treffend analysierte, indem er die wissenschaftliche Vorgehensweise als Treiber der Aufklärung hervorhob [1]. So wirkt sie noch heute, insofern Sie das methodische Rüstzeug liefert den Gegnern des Faktischen zu begegnen.

Obwohl durch die aufklärerische Beimessung ein versöhnlicher Aspekt zugesprochen werden muss, der die latent utilitaristische Handhabung der Grundlagenforschung ausbalanciert, kann gezeigt werden, dass beide Ansätze nicht zwingend erforderlich sind, um Grundlagenorientierung zu rechtfertigen. Zum Verständnis dieser Behauptung soll der Blick auf ontologische Denkfrüchte des letzten Jahrhunderts gelenkt werden.

Es war der schäferlyrische Geist aus Meßkirch, der Verstand eines politisch vollkommen entgleisten Martin Heideggers, der, über den Umweg des Verständnisses vom Wesen der Technik, einen unschätzbaren Beitrag zum Verständnis der Forschung geliefert hat.
„Im folgenden [sic] *fragen* wir nach der Technik", beginnt Heidegger seinen für die Nachwelt festgehaltenen Vortrag [2] und kommt zum Schluss, dass Technik nicht bloß ein Mittel zum Zweck ist. Vielmehr stellt er fest: „Die Technik ist eine Weise des Entbergens". Diese *Entbergen* ist ein äußerst interessanter Begriff und beschreibt, gemäß Heidegger, das Kommen des *Verborgenen* ins *Unverborgene*. Dieses Kommen muss nicht, wenn man Heidegger nur wenige Zeilen vorher praktisch fasst, passiv geschehen. Es kann auch aktiv sein und ist dann ein *Her-vor-brigen*. Dieses *Her-vor-brigen* hat eine für unsere Ohren sehr vertraute altgriechische Bezeichnung: ποίεσις .
Neben dieser Verhaltensweise gegen über der Natur, wie sie bspw. durch Künstler an den Tag gelegt wird, gibt es nach Heidegger noch das andere Entbergen in Form einer *gestellten* Herausforderung. Am eindringlichsten beschreibt Heidegger das Beispiel des Wasserkraftwerkes, dass in den Rhein *gestellt* ist. In diesem Kraftwerk wird das Wasser auf sein Wasserdruck hin *gestellt*.

Alle Komponenten des Kraftwerks und die sich daran anschließenden Strukturen sind darauf *gestellt* aus einem mechanischen Strom einen elektrischen Strom zu formen, zu transformieren und zu verteilen. Das einfach dahinfließende Wasser wird mit dem Wissen seiner physikalischen Beschaffenheit aufgeschlossen und einem Zweck überführt. Mit Heidegger gesprochen, in den *Bestand bestellt*.

In der modernen Welt sich expansiv ausweitender Anwendungen bleibt keine Erkenntnis über die Funktionalität natürlicher Phänomene ungenutzt. Alles wird früher oder später genötigt *zuhanden* zu sein. Es fällt nicht schwer jüngere Beispiele zu finden, die sich von dem Technikverständnis Heideggers der Fünfziger Jahre des letzten Jahrhunderts abheben. In den Lebenswissenschaften wimmelte es von natürlichen Phänomenen, die in den *Bestand* bestellt wurden.
Denken wir nur an die unmittelbar erdachten Anwendungen, die auf die Entdeckung der kurzen palindromischen Wiederholungssequenzen, die in Kombination mit dem Enzymen der Cas-Familie eine Revolution in der Genomeditierung auslösten. CRISP/Cas9 wurde entdeckt und gnadenlos in den *Bestand* gestellt.

Ohne Zweifel fällt es jedem Menschen der zeitgenössischen Zivilisation schwer eine Problematik in der beschriebenen Vorgehensweise translationalen Forschung zu sehen (hochpräzise Genscheren sind zentral für gentherapeutische Anwendungen). Warum sollte ein Wissen nicht in den Dienst am Menschen gestellt werden? Es ist beinah unmöglich zu vermitteln, dass diese Geisteshaltung keine zwangsläufig natürliche Position ist. Dinge ihrer selbst Willen zu verfolgen, ist geradezu ein abwegiger Gedanke geworden. Aber es ist gerade die autotelische Haltung des *la science pour la science*, die viel nobler erscheint, da sie die grundlegende Neugier des Wissenschaftlers an der Sache mit der Ehrfurcht vor einem nicht leichtfertig verwerfbaren Schöpfungsakt kombiniert.
Eine Utopie der Wissenschaft, wie sie niemals vom Meister des Fachs Ernst Bloch ersonnen wurde, aber unbedingt in das Standardwerk *Das Prinzip Hoffnung* hätte aufgenommen werden müssen [3], könnte mit diesem Aufschlag kräftezehrender Rückorientierung auf das reine *Entbergen* begonnen haben.

Ulm, den 20. Mai 2019

CONTENTS

LIST OF FIGURES

LIST OF TABLES

Part I.

Introduction

1

ELEMENTS OF THE MURINE VISUAL SYSTEM

1.1 THE LENS

General characterisation

The lens development starts in *Mus musculus* at the day 9.5 of murine embryogenesis (E9.5) via forming of the lens pit out of the lens placodes [4][5]. Two days later (E11.5), the pit develops to the lens vesicle, and at E13 first primary fibre cells populate it, initiating a life-long growing process. Within one year, the lens grows to a equatorial diameter of about 2.4 mm with 600 cell layers in total [6]. Murine lenses have one of the lowest equatorial/sagittal indices of all investigated animals [7].
Once in a functional state, the crystalline lens (old Greek: πηακός) and the cornea form the dioptric apparatus of the murine eye [8]. Both components are crucial for converging light, but only the lens possesses the ability to accommodate within its constraints. Given a healthy cornea, a normally developed lens provides the refraction properties for emmetropia (normal vision conditions [9]), the unimpaired convergence of light on the photoreceptor layer of the retina in distance of the focal length of the lens [10]. In order to achieve this function, the lens in general and the murine lens in particular excel with some peculiarities in composition.

1.1.1 *Anatomy and characteristics of lenticular cells*

Lens embedding & anatomy

The murine crystalline lens is a transparent tissue in the centre of the eye (Fig. 1, A, black arrow). It is embedded in the vitreous body and attached by zonular fibre to the ciliary body (Fig. 1, F, violet arrow). The lens is surrounded by the humour of the anterior chamber (Fig. 1, A, plus) and of the vitreous body (Fig. 1, A, star), which supply the lens.
The crystalline lens is composed of two populations of cells: cuboidal epithelial cells, which cover the anterior surface of the lens in a monolayer (Fig. 1, B, blue arrow), and a bulk of fibre cells that form the body of the lens. Both types of cells are fine-structured. The epithelium is subdivided into a central zone directly at the most anterior lens part (Fig. 1, B), a germinative zone with mitotically active cells (Fig. 1,

C) and a transitional zone where epithelial cells get incorporated into to equator of the transparent lens body (Fig. 1, D). This structure of tightly packed and regularly composed fibre cells is usually structured into a lens nucleus, comprised of old fibre cells, and a younger cortex coating the former. The posterior lens is not covered by epithelial cells and the capsule is thinnest at this section (Fig. 1, B, green arrow)

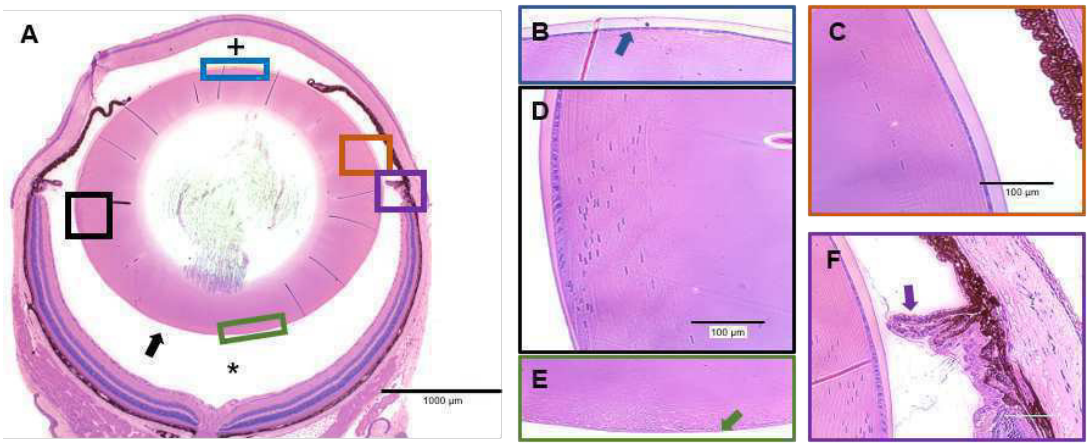

Figure 1.: Lenticular anatomy and relation to other eye tissues in histology (male B6RCF1, 6.5 months old). Whole eye section with the lens (black arrow), the anterior chamber (plus) and the vitreous (star), 4x **(A)**. Anterior part of the lens with the epithelium (blue arrow), 40x **(B)**. Fibre cells in final denuclarisation process, 40x **(C)**. Lens bow with transitional (left) and organelle-free zone (right), 40x **(D)**. Posterior part of the lens with the thin capsule (green arrow), 40x **(E)**. Ciliary body with zonular fibres (violet arrow), 40x **(F)**.

The epithelium is covered by the capsule (also called basement membrane [11]) whose molecules are secreted by the epithelial cells. 90 % of the capsule consists of type IV collagen [12], glycoproteins (e.g. laminin) and proteoglycans. Most prominent amino acid is glycine [13]. The capsule is thickest at the equator and thinnest at the posterior pole.

Fibre cell differentiation

The fibre cells are completely void of common cellular organelles like cell nucleus, endoplasmatic reticulum or mitochondria. They derive from epithelial cells after FGF-induced differentiation [14] in the transitional zone (Fig. 1, D) in a process similar to autophagy and mitophagy [15]. Primary fibre cells in the early lens nucleus lose their organelles between E15 and E18 [16], long before the opening of the eye around P12-P14 [17]. This process of reducing scattering centre is crucial for the transparency of the crystalline lens [18] and is induced by members of the fibroblast growth factor (FGF) family with low concentrations of FGF at the anterior

epithelium inducing proliferation and migration, while high concentrations at the equator induce differentiation [19]. Differentiating fibre cells elongate until their apical and basal end contact elongating fibre cells from the opposite equator. Those contact zones are assigned anterior (Fig. 1, B) and posterior (Fig. 1, E) sutures. Degrading cell nuclei of differentiating fibre cells are discernible as stretched methylene blue-positive components (Fig. 1, C).
Within the onion-like structure, fibre cells get more compressed the deeper they lay in the lens. The fibre cell packing is a highly coordinated process to avoid light scattering textures of the lens. Compaction of fibre cells is also necessary for establishing the gradient index (GRIN) of the lens [6].

Cytosceleton of lenticular cells

Epithelial cells of adult mammalians contain the intermediate filament (IF) vimentin and GFAP(Glial fibrillary acidic protein), Synemin and K8/K18/K19, whereas fibre cells contain only vimentin, synemin and the beaded filament structural proteins 1 and 2 (BFSP1 and 2, also filensin and CP49) [20]. Vimentin, BFSP1 and BFSP2 are most abundant in the fibre cells and interact with IF-binding proteins of the spectraplakin family in the cell membrane (plakoglobin, plectin, periplakin and desmoyokin) [21] [22] [23]. Epithelial cell and fibre cell membranes stay in interaction with an actin subplasma membrane network [24], which is hypothesised being connected with the intermediate filaments by plectin [25]. The microtubule network disappears completely with fibre cell differentiation [26].

Cell-cell interactions

Intercellular spaces are reduced by tight connections mediated by cortex adherence mosaics [20]. On the short side of the hexagonal fibre cells, a N-cadherin-based complex is represented and on the long side a EPPD complex (Ezrin, Periplakin, Periaxin, Desmoyokin) [22]. Aquaporin 0 (AQP0 aka mayor intrinsic protein) channel fulfils a function as stable junction molecule between fibre cells too [27] [28] and interacts with BFSP1 [29]. Also the integral membrane lens intrinsic protein 2 (Lim2) is present in mature fibre cells and is posited to serve in two functions: tight junction and communication/transport [30]. Gap junctions as Connexin 46 and 50 (Cx46, Cx50) are typically present at the broad face of fibre cell membranes [31]. Zona ocludens-1 (ZO-1) interacts with all junction complexes, the adherens, the tight and the gap junctions [32][33].

Special macrobiomolecules

Human eyes have a cytoplasmic protein concentration of 0.32 g/ml [34]. It is highly lens-specific that most of theses enriched proteins are of the crystallin protein

family, in detail αA and αB-crystallin [35], β-crystallins and γ-crystallins. αA-crystallins are enriched in the lens cortex, whilst the γ-crystallins are concentrated in the nucleus [36]. Crystallins do not act as independent scattering centre, which would cause massive scattering of incident light, but are short-range-ordered like glass or a liquid [37]. Their function is not restricted to the crucial task of preserving lens transparency. Crystallins are also important in protecting the lens against externally detrimental influences (see section 2.3).

1.1.2 *Lenticular physiology and metabolism*

Circulation & and transport

Fluid currents of the lens follow a quadrupole pattern. That means, streams are intruding at the sutures and leaving the lens at the equators [38]. Water flows passively (osmosis) through the abundant, but low-permeable AQP0 [27] and the connexins, driven by a Na^+/K^+ gradient, which is established by Na^+/K^+-ATPases located in the equatorial epithelium [39][40]. Gap junctions can sluice only small molecules inside the lens. An additional pathway was discovered that works ventricular to the radial concentric-orientated gap junctions: the large molecule diffusion pathway (LMDP) which renders the entire lens nucleus a syncytium [41] and starts to evolve in *Mus musculus* at E15 [42]. Lim2 is necessary for the LMDP [43].

Hydrostatic & oncotic pressure

It is proposed that the hydrostatic pressure gradient (reverse to the Na^+-concentration), resulting from the resistance of gap junctions to the pouring water (350 mmHg in the nucleus vs. 0 mmHg beneath the lens surface), might cause the refraction-relevant GRIN (gradient refractive index) [44] [45] [46].
The oncotic pressure (mediated by colloids), on the other hand, seems to have an enormous effect on the compaction process. The hypothesis says that uneven distribution of crystallins (α-crystallins in the cortex and γ-crystallins in the nucleus) causes a high oncotic pressure in the cortex and a low pressure in the nucleus, explaining the loss of water volume in the inner mature fibre cells [6] [47].

Energy supply

Aerobic energy production is restricted to the epithelial cells since the fibre cells are depleted of mitochondria. Fibre cells have access to glucose, which is provided by the circulatory system. Glucose transport was sufficiently investigated in rats: the transporter GLUT1 can only be found in epithelial cells, whereas the GLUT3 transporter and the sodium-dependent transporter SGLT2 can be detected

in differentiating fibre cells [48] [49]. This enables mature fibre cells to produce ATP by glycolysis. Reducing equivalents will be provided by the pentose phosphate pathway in the cortex [50].

1.1.3 *Optics of the murine lens*

Refraction

The emmetropic human eye lens possesses a refraction power of +19 D [51]. Lenticular refraction of C57BL/6J mice at P70 on the other hand (measurable with infrared photoretinoscopy [52]) reaches +7.0 $\pm$ 2.5 D [53]. This value is reached after a short period of myopia after birth and a hyperopic peak at P47 [54]. A GRIN is suggested for mice as well, but no data is published to support this. Instead, an equivalent homogeneous refractive index was calculated by several teams in the paraxial region of the murine lens with numerically high results of $n < 1.55$ [55] and 1.659 [56]. In the end, refractive errors may have no critical impact on mice's vision [53].

Accommodation

Actually, little is known about the murine lens accommodation ability. Baradia et al. [57] postulated that mice do not accommodate at all due to 'diminutive ciliary muscle', but supplied evidence for age-dependent increase of lenticular stiffness in C57BL/6J mice. If elasticity of the lens is age-dependent, accommodation according to Helmholtz's theory [58] might be biomechanically affected. Ott [8] claimed also that nocturnal-active animals and such animals with little eyes do not need to accommodate. Walls [59] numbered the accommodation capability with 0 D.

1.2 THE RETINA

Anatomy-function relation

The retina covers the posterior segment of the eye and acts as a interface between the sensual information of the outer world and the neuronal processing. The entire tissue evolved as light-streaming set-up for a loss-free transformation of optical information into electrical signals [60]. This requires a clear functional and spatial organisation (Fig. 2, left). Of central importance are the outer nuclear layer with the inner and outer segments (Fig. 2, F, G, H) which comprise the photoreceptor cells in a columnar order. The outer segments carry the actual visual pigment rhodopsin (opsin + 11-cis retinal). In contrast to humans, mice do not have a macula and a fovea (spot of highest cone density without any rods) respectively, and therefore no retinal spot enabling them to high visual acuity [61]. However, the retina of

the C57BL/6 mouse is mainly densely populated with rods and therefore suited for scotopic vision [62]. The RPE has an important function in the retinal restore cycle (all-trans to 11-cis retinal isomerisation) and removal of older inner and outer segments by phagocytosis (Fig. 2, I) [63].

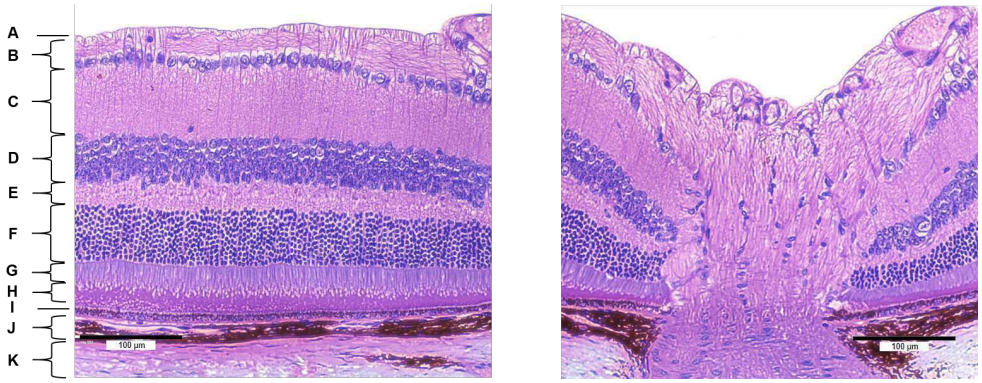

Figure 2.: Retinal layer organisation of an adult B6C3F1 mouse. Left side: Inner limiting membrane (ILM) **(A)**. Ganglion cell layer (GCL) with axons **(B)**. Inner plexiform layer (IPL) **(C)**. Inner nuclear layer (INL) **(D)**. Outer plexiform layer (OPL) **(E)**. Outer nuclear layer (ONL) **(F)**. Inner segments (IS) **(G)**. Outer segments (OS) **(H)**. Retinal pigment epithelium (RPE) **(I)**. Choroidea **(J)**. Sclera **(K)**. Right side: Optic cup and nerve. Labelling according Kolb et al. [60].

The inner and outer plexiform layers are basically composed of axons and dendrites of the ganglion cells (Fig. 2, C+E), the amacrine, Müller and bipolar cells. In fact, 3.1 % of the inner nuclear layer cells are horizontal cells, 41 % bipolars, 16 % Müller and 39 % amacrine cells [62]. Other studies come to similar proportions [64]. While bipolar cells simply relay the input of the cones to the ganglion cells, horizontal and amacrine cells (highest variety with 29 cell types) modify those signals in a more or less understood way. In the end, axons of the ganglion cells confluence at the optic cup and bundle to the optic nerve which carries the signals to the visual cortex of the brain (Fig. 2, right).

Retinal glia

Like the brain, the retina as neuronal tissue is interspersed with glial cells, namely, the Müller cells and astrocytes [65]. In first postnatal week, astrocytes 'spread in a concentric wave, with a high density from the optic nerve toward the periphery' [66]. They are supposed to be tightly coupled to the vascularisation of the retina and remain located in the innermost layer. Müller cells are the latest developing cell type in the retina and represent 90 % of the retinal glia [67]. Müller cells are crucial for physiological balance in the retina [65] [68], they act with their

bundled intermediate filaments as light fibre [69], and they help to stabilise the shape of photoreceptor cells by forming adherence junctions [70]. Injuries of the retina always prompt reactive Müller cells to molecular and cytological answers [65]. This process, called Müller gliosis, includes protective release of antioxidants or the structural regeneration by forming of progenitor cells [71]. They could also become dysfunction after a retinal injury and form detrimental glial scars by hypertrophy [65]. However, one interesting predicate of the reactive Müller cell is the overexpression of the IF GFAP [72] and the expression of the vascular epithelial growth factor (VEGF) during gliosis with possible neurodegenerative effects [73].

Neonatal retina

In context of this thesis it is very intriguing to realise the structure of the neonatal B6C3F1 retina at postnatal day 2. The only layer fairly recognisable is the ganglion cell layer, but not yet in the monolayer appearance as known from the adult retinae of the same strain (Fig. 3, A). Similar to the C57/BL [sic] mice investigated by Politi et al. [74], the inner and outer nuclear layer is not yet differentiated (Fig. 3, C). Photoreceptor cells are not yet discernible, and some cell bodies close to the RPE appear to be mitotic (by comparison with [74]).

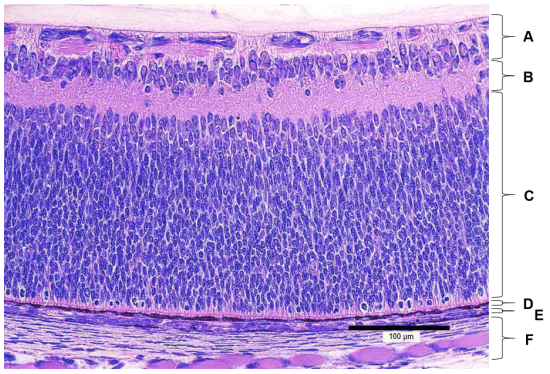

Figure 3: Retinal anatomy of the B6C3F1 mouse at postnatal day 2. Labelling according [74].
(A) Early ganglion cell layer.
(B) Early inner plexiform layer.
(C) Undifferentiated nuclear layer.
(D) Retinal pigment epithelium.
(E) Choroidea.
(F) Sclera.

1.3 THE CORNEA

Anatomy & function

Cornea is a transparent tissue of and together with the lens part of the visual refraction apparatus [51]. Corneal thickness is static around 137 ± 14 µm (C57BL/6 mice, [75]). The cornea shares not the ability of the lens to accommodate. Murine corneae are comprised by an anterior limiting lamina (ALL)/ Bowman's layer (Fig. 4, B) covered by columnar basal epithelial cells, polyhedral epithelial wing cells and a final layer of squamous epithelial cells (Fig. 4, A). The ALL functions as a basal

lamina for the epithelial cells and is an acellular layer of collagen I, laminin, nidogen and perlecan coming from the stroma which is itself mainly built up by collagen fibre (Fig. 4, C) [76]. The cornea is completed by a posterior limiting lamina (PLL)/ Descement's layer (Fig. 4, D), and the endothelium (Fig. 4, F) [75] [77]. As a matter of fact, the thickening of the PLL is age-dependent [78]. The existence of the ALL in mice remains disputed though [79].

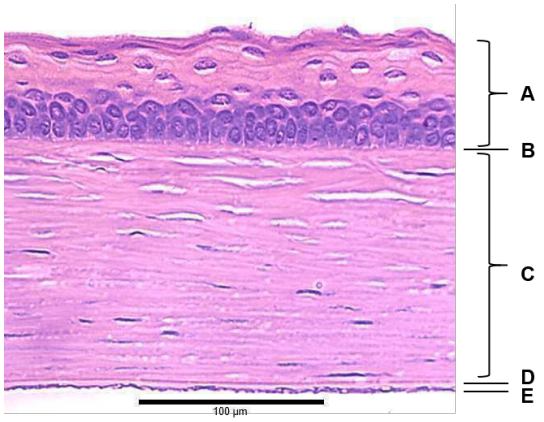

Figure 4: Corneal anatomy of a adult B6C3F1 mouse.
(A) Epithelium.
(B) Anterior limiting lamina.
(C) Stroma.
(D) Posterior limiting lamina.
(E) Endothelium.

The epithelium acts as first barrier as in other mesenchymial tissues. Injuries to the epithelium results in disturbance of the water content regulation following edematous swelling of the stroma, and, hence, clouding of the cornea [80]. A stem cell population at the limbus, the transition zone between cornea and sclera, replenishes epithelial cell loss after injury [81].
The extracellular matrix of the stroma is synthesized by keratocytes (fibroblasts) which are recognisable as flat black inlays (Fig. 4) in a magnitude of 8-12 layers [82]. The anterior part of the stroma is pervaded by intercellular spaces and appears to be more regular ordered than close to the PLL. This parallel orientation of lamellae differs murine corneal stromae from humans ones [75] [83].

Refraction

The murine cornea has a lower refraction index over the entire spectrum of optic light than the lens, while the dioptric power of the anterior cornea with the epithelial cells is higher than the posterior cornea that has even a negative (divergent) contribution for the entire eye [56]. This fact contrasts with the dioptric power of human corneae, which is remarkable higher than that of the lens [51]. It was determined by the selfsame team of authors that the anterior cornea has an refractive index which exceeds the index of the anterior lens at wavelengths higher than ~ 590 nm.

2

IONISING RADIATION AND MOLECULAR INTERACTIONS

General information

Ionising radiation (IR) is a general term for all sorts of radiation that induce ionisations in the interacting matter. This applies for dens particle radiation as α-radiation (helium cores), or lose radiation forms as β-radiation (electrons), γ- or Röntgen radiation (photons) [84] [85]. For focus sake, we will deal hereinafter solely with γ- and Röntgen rays. The later radiation types deposit energy linearly per length track in the medium with a maximum deposition rate of 3.5 keV/μm. Therefore, they count as low linear energy transfer (LET) radiation types [86].
All γ-radiation comes from the decay of radionuclides. These could have primordial (produced in stars [87]), secondary (after decay of primordials) or cosmogenic (atmospheric nuclear interaction [88]) origin, while Röntgen rays (aka x-rays) can also be produced artificially, e.g. with linear accelerators [89]. To understand the topic, we introduce all the relevant physical quantities:

a. Activity [Bq] = Decays/time[s]
b. Absorbed dose [Gy] Activity * specific nuclide factor
c. Equivalent dose [Sv] = Absorbed dose * radiation weighting factor
d. Effective dose [Sv] = Equivalent dose * tissue weighting factor

Avarage exposure

Exposure to γ- and Röntgen radiation can be of natural origin (cosmic, terrestrial) or derive from artificial medical applications (computer tomography and Röntgen imaging). Natural background γ-radiation contribute with 0.817 mSv to the annual dose in Germany (range: 0.5-1.5 mSv/a) [90]. Terrestrial sources comprise mainly the γ-radiators ^{40}K, ^{238}U and ^{232}Th. More important is the exposure to medical applications summing up to 1.7 mSv/a with rising tendencies [91] [92]. Diagnostic computer tomographies, simple X-ray imaging and radiotherapy were responsible for an individual increase of the effective dose for an US citizen by a factor of 5.7 to 6.2 mSv/year (2006 vs. early 1980s) as published by Dauer et al. [93].

High exposure scenarios

Individual exposure during radiotherapy (e.g. stray radiation of dozens of mSv per therapeutic dose in proton radiotherapy [94]) or interventional procedures (e.g. cerebral embolisation) could easily exceed several hundreds of mGy or mSv

[95] [96] [97]). Other occupational groups are also affected, notably interventional cardiologists/neurologists [98] and flight crews [99]. Astronauts, on the other hand, could receive far higher doses [100], but of mixed radiation quality.

2.1 DIRECT INTERACTION OF IONISING RADIATION WITH BIOLOGICAL STRUCTURES

High energy photons can hit DNA helices directly causing devastating effects: deposited energy can break the ribose backbone of both helix strands (10-20 bp apart) resulting in double-strand breaks (DSB) [101]. Clustered damage of DSB, single-strand breaks (SSB) and base lesions are rather typical for dense IR (α-radiation) than for γ-radiation [102] [103] [104] [105].
Besides immediate breaking of the strands, IR could induce ionization of DNA as electron spin experiments have proven [106]. After protonation and deprotonation reactions, neutral nucleotide radicals remain [107]. More importantly for this work, collected data indicate that γ-radiation might induce the formation of cyclobutane pyrimidine dimers normally induced by superficially ionising radiation as UV [108] or thymine dimers [109].

2.2 INDIRECT INTERACTION OF γ-RADIATION WITH BIOLOGICAL STRUCTURES

Water radiolysis

Even a mature lenticular fibre cell consists mostly of water (human lens nucleus 63.4 $\pm$ 2.9 % [110] [111]). Therefore, interaction between high energy photons and this polar molecule are a primary source for damage-inducing agents in the cell. Because damage is mediated by those agents, the interaction of γ-radiation with the biological structure is indirect. In this context, oxygen stands out as 'electron sink' [112]. Compounds with this reduced oxygen are designated as reactive (aka reduced) oxygen species (ROS).

$$H_2O \xrightarrow{\gamma\text{-rays}} H_2O^{\bullet+} + e^-, \quad H_2O^* \tag{1}$$

$$H_2O^{\bullet+} + H_2O \longrightarrow {}^{\bullet}OH + H_3O^+ \tag{2}$$

$$H_2O^* \longrightarrow H^{\bullet} + {}^{\bullet}OH, \quad H_2 + O^{\bullet} \tag{3}$$

$$e^- + nH_2O \longrightarrow e^-_{(aq)} \tag{4}$$

Normally, ROS are reactive because of the exergonic nature of their potential reactions. Mayor first reactions after initial water radiolysis producing ROS (Equ. 1) (according to [113]) follow within 10^{-12} s (Equ. 2, 3). Hydrolysis produces not only oxidants, but also reductants as $e^-_{(aq)}$ (Equ. 4, reduction potential - 2.9 V) and $H^\bullet$ (Equ. 3, reduction potential - 2.3 V) [114]. The transient radical species $H_2O^{\bullet+}$, $H^\bullet$ and $^\bullet OH$ undergo together with H_3O^+ recombination and dimerisation processes until after 10^{-7} s either H_2, O_2, the non-reactive 'ROS' H_2O_2 and H_2O is formed, or a scavenger intercepts [86]. Hydrogen peroxide and the hydroxyl radical are considered as the mayor oxidizing species in the wake of radiolysis by γ-radiation (reduction potential of $^\bullet OH$ + 2.7 V), whereas 40 % of the hydroxyl radicals contribute to the formation of H_2O_2 [115]. The approximate amount of H_2O_2 after hydrolysis with 2 Gy is around 10^{-7} M [116]. This equals the estimated normal physiological molar concentration [117] [118].

Cellular ROS damage

Radical scavengers, which interact with the transient hydrolysis species, are potentially all kind of solutes in the cell, notably DNA and biomacromolecules like proteins, lipids and polysaccharides [119]. Especially $^\bullet OH$ is able to damage DNA by tandem lesions, intra- and interstrand cross-links, DNA-protein cross-links [120] and SSB [121]. The altered nucleoside 8-hydroxy-2-deoxyguanosine (8-OHG) is also a typical DNA oxidation product [122] because of the comparable low reduction potential of guanine (+ 1.29 V vs. + 1.7 V for tyrosine) [123] [124].

Polyunsaturated fatty acids from membranes are inclined to react with ROS which yields lipoperoxyl radicals, an intermediate product to the formation of lipid hydroperoxides [125]. Break down products of this peroxide like malondialdehyde (MDA) or 4-hydroxy-2-nonenal (HNE) are reactive too [126], and can then mutate DNA [127] and aggregate/degradate proteins [128] [129]. Hence, more saturated lipids as dihydrosphingomyelin are less prone to ROS damage [130]. ROS-damaged bilayers could have altered ion permeability and thus fail to uphold ion gradients [131] [132].

It is known of lens proteins that they underlie several post-translational modifications with age of which oxidative stress might be one of the main reasons [133] [134]. Additional exposure to increased levels of ROS could exacerbate this process. Over 35 protein oxidation modifications are reported [118] of which carbonylation, cleavage of the protein backbone and amino side chains respectively or amino acid oxidation are the most prominent [135].

2.3 CELL PROTECTION AND REPAIR MECHANISM

General protection and repair

Mammalian cells have a variety of protective enzymes and repair mechanism to cope with the direct and indirect consequences of γ-irradiation: ROS homeostasis is preserved by catalase, peroxiredoxin (Prx) and glutathione peroxidase (GPx) detoxifying H_2O_2 [118]. More universal antioxidants are the oligopeptide glutathione (GSH) as well as the vitamins ascorbic acid and tocopherol, which are able to target radicals as $^{\bullet}OH$ and oxidized biomacromolecules [118] [136].
DSBs are repaired either by classical non-homologous end joining (C-NHEJ) and homologous recombination (HR), or by more error-prone/mutagenic alternative end joining (alt-EJ) and single-strand annealing (SSA) [137]. The prevalence of those mechanism depends on the status of the cell cycle and on DNA end resection [138] [139]. Single nucleotide lesions, especially photoproducts as dimers of nucleic acids are repaired by the single nucleotide excision repair (NER) mechanism [140].

Lens-specific protection

Apart from the listed natural counter-measurements, the lens has some special arrangements against ROS. The first one is of cytoarchitectural nature: mature fibre cells are depleted of organelles by autophagy. That means the radical $O_2^{\bullet+}$ is of no endangering relevance for the bulk of lens cells (since mitochondria are depleted). IR can increase the endogenous production in mitochondria though (shown in tumour and A549 cells [141] [142]), and, hence, be relevant in epithelial cells.
Glutathione seem to be a crucial line of lenticular ROS defence. Normally, GSH (reduced form of glutathione) is measured with cellular concentrations of 0.1-10 mM [143]. But in lens cortices (e.g. rabbits or guinea pigs) concentrations reach 20 mM ([144] published far lower concentrations for several animals) and are assumed to be even higher in epithelial cells [145] (five times higher in rabbit lens epithelium, though, overall in comparable lower concentrations), but lower in the nucleus. After oxidation by ROS (GSH to GSSG), lens-wide distributed glutathione reductase (GR) replenish GSH under consumption of NADPH [146].
Complementary protection is supplied by the mentioned α-crystallin proteins (αA and αB), which have properties of heat shock proteins (e.g. huge sequential coverage of αB-crystallin with Hsp27 [147]) [148], namely chaperon functions [149]. Their main benefit to the lens is the prevention of 'non-specific aggregation in the intact lens' [35]. Furthermore, αA-crystallin is necessary for lens epithelial cells to express glutathione [150] and αB-crystallin is colocalised with cytochrome C protecting it from oxidation and hence the cell of apoptosis [151].

3

PHAKOPATHOLGY

3.1 CATARACTS

General information

In contrast to basically all other parts of the eye, the lens exhibits only one pathological phenotype if age-related stiffening and subsequent presbyopia is neglected and alterations and luxation diagnoses are considered of minor relevance: the cataract [51]. A cataractous lens is characterised by an opaque appearance (therefore the waterfall analogy) [152]. Depending on location of first appearing opacification, and especially because of their different localisations, cataracts are roughly divided in nuclear (NC), cortical (CC), and posterior subcapsular (PSC), anterior subcapsular (ASC), and annular cataract (cataracta coronaria), although combined phenotypes may occur [153]. Finally, the 'total cataract' stage without non-affected lens areas completes the cataract list. Aetiology seems only a definition criteria for the 'senile cataract' (basically an NC) [154]. The 'complicated cataract' is rather a medical expression, if there are secondary complications in eye inflammations [155].

Main processes

All cataract types base on few, more or less scientifically elucidated, cellular processes that increase the scattering properties of the lens: failing epithelial cell differentiation, fibre cell swelling, disorganisation or liquefaction, intracellular aggregate formation or collapse of the ROS protection system (Fig. 5) [156] [119]. It is fallacious to understand those processes independently. For instance, aberrant fibre cells which have not lost their nuclei, migrate to one of the lenticular sutures and induce swelling of the surrounding fibre cells by expression of extracellular material that hampers the microcirculation system and causes osmotic imbalance.

Scattering theory

All the occurring membrane and protein alterations in the lens undermine the optimised lenticular purpose as transparent, light-converging optical device. Rayleigh's theory of scattering can be excluded for the lens because it seems that glare by cataracts is rather not dependent on the wavelength of the light [7][157]. Therefore, scattering centre have to be smaller than $\lambda/20$ as F. Bettelheim argues in Maisel [7] and the Mie theory of scattering applies [158].

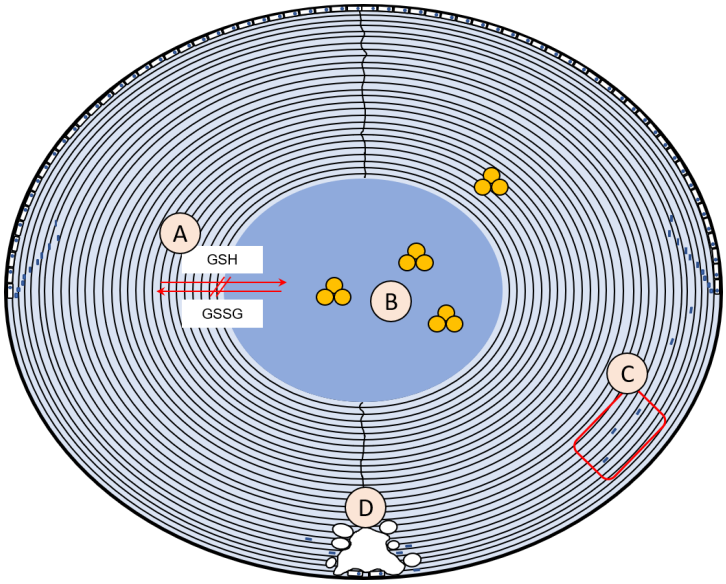

Figure 5.: Main cataractous processes in the murine lens (mid-sagittal section). Collapse of the ROS protection system in the nucleus **(A)**. Aggregate formation in the nucleus and the cortex **(B)**. Dysplasia of the lensbow and failing fibre cell differentiation **(C)**. Fibre cell swelling, disorganisation and liquefaction, e.g. at the posterior pole **(D)**.

3.2 VARIETY OF CATARACT TRIGGERS

Cataracts could evolve after all kinds of physical and chemical insults or genetic modifications. For a better mechanistic understanding of cataract formation after irradiation, it is helpful to elucidate these insults.

Natural changes

The lens undergoes natural age-related changes, which is another expression for the sum of infinitesimal physical and chemical insults of all kinds to which an average organism is exposed in its lifetime (in accordance with the concept of 'cataractogenic load' [119]). This comprises the reduction of the GSH level in the lens nucleus with age [159], and the reduced permeability for glutathione between the epithelium were it is mainly reduced and the nucleus as GSH sink [160]. Tightly connected to the loss of ROS protection in the nucleus is the oxidation and condensation of lenticular macromolecules, namely of crystallin proteins [154] [161]. Raman-spectroscopy experiments by Costello et al. [162], on the other hand, rebutted the oxidation hypothesis by protein profile analysis. The authors revealed a 7.5 fold increase of multi-lamellar bodies (MLB), low volume density accumulations with a higher refraction index than the surrounding cytoplasm, in the aged lens nucleus.

Physical insults

Cataracts could appear after local temperature loss (cold cataract), which induces a phase separation of the protein-water suspension (central turbidity) [163], but also as a result of temperature increase due to infrared light exposure or microwaves (thermal cataract) [164] [165]. Thermal cataracts are nothing else than posterior subcapsular cataracts (3 months after thermal insult) [166]. UV light has superficial ionising effects with inconclusive cataractogenic potential. UV light is reported to promote nuclear cataracts in humans (geographically correlated with high sun intensity areas) [167]. In albino mice posterior cortical cataracts were observed half a year following irradiation [168], while in several other mouse experiments anterior subcapsular cataracts were observed [169] [170] [171]. Such phenotypes were partially explained by several epithelial effects [172], although plurality of phenotypes suggests multiple mechanistic reasons. Very rare cases of an electric cataract were also published [173] [174] [175] with a very intriguing first anterior subcapsular opacification 1-12 months after injury and total cataract formation after varying time periods [176] [177]. Furthermore, traumatic cataracts (subcapsular capacities with rosette appearance) were reported [178].

Chemical insults

Cataractogenic substances from medical treatments or the unbalanced metabolism could induce cataracts. Corticosteroids (e.g. cortison, prednisone, dexamethasone) induce PSCs after daily administration (incidence of 69 % for human patients older than 4 years, averaged for all doses) [179]. In model organism corticosteroids cause very different outcomes: ASCs, PSCs and nothing at all in rabbits, supranuclear opacities progressing to nuclear cataracts in mice, chicken and rat [19]. Whether steroids cause an osmotic imbalance by inhibition of the Na^+/K^+-ATPase seems to be still uncertain. Steroid-induced cataracts could also be retracted to an increase of the intraocular pressure (IOP) why steroid-induced cataracts basically could be lesions caused by a physical insult [180].
Diabetes is another disease inducing cataracts [181]. Glucose, delivered to lens in unchallenged high concentrations, is turned into sorbitol by the enzyme aldose reductase (though not in mice [182]). Sorbitol accumulates in the lens because it can not be metabolised further and creates hyperosmotic conditions leading to an influx of water and fibre cell swelling [183]. As secondary effect, Na^+/K^+-ATPase inefficiency (discussed as effect of concurring oxidation) leads to Ca^{2+}-influx [184]. Eventually, calcium-dependent cysteine protease (calpain) is activated and cleaves lens crystallins with further cataractogenic impact [185]. Cataracta myotonica

appears to be a variant of disturbed calcium regulation cataract (SERCA impairment [186]) [187]. It is also relevant to review which molecules could prevent cataractogenesis [188].

Mutations

A lot can be learned about the importance of single factors in cataractogenesis by mutational studies and congenital diseases. Especially crystallin mutation go along with cataract formation. *Crybb2*$^{Aey2/Aey2}$ [189] and *Crygd*$^{Aey4/Aey4}$ mice [190] are characterised by nuclear cataracts, *Cryaa*$^{Aey7/Aey7}$ [191] by anterior cortical cataracts and quaint posterior vacuoles, *Crybb*$^{O377/O377}$ [192] and *Crybb2*$^{Philly/Philly}$ mice [193] fail completely to form regular shaped lenses without vacuoles in the entire structure, while *Cryba2*$^{Aca30/Aca30}$ [194] displays minor nuclear opacities and a Milky Way-like distribution of scattering centre from equator to equator [195]. Knockout of AQP0 causes the loss of the characteristic hexagonal shape of the fibre cells and leaves nucleus and cortex in disarray [196]. Lenses of the *Aquo*$^{-/-}$ mice displayed cataracts and had an increased focal length [197] [198]. Also interacting IF like the BFSP2 (CP49) have their part in preserving lens transparency. Knockout lenses were more opaque in the centre, but not yet cataractous [199]. Identified mutations in *Epha2* have been shown to cause inherited cataracts. *Epha2*$^{-/-}$ mouse models have proven that EPHA2 would be necessary for lens fibre cell 'guidance' in the growing lens because lack of it prevents correct suture formation and worse thus refraction properties of the lens [200].

Ercc2 & Trp53

In context of this thesis, 2 genes are of special interest: *Ercc2* and *Trp53*. The role of ERCC2 (XPD) in mice and the lens phenotype of a heterozygous *Ercc2*$^{+/-}$ mutant on C3HeB/FeJ background was described by Kunze et al. [201]. ERCC2 is a XP helicase acting on recognised dsDNA lesions within the nucleotide excision repair (NER) [202]. A homozygous *Ercc2*$^{S737P/S737P}$ mutation of this enzyme (single amino acid exchange) causes nuclear cataracts in the investigated mice, while a total knock out would be lethal [140]. Heterozygous mice are not differentiable from wild types (WTs) by their appearance.

The TRP53 protein is able to identify damages in DNA caused by IR and is able to stall cell cycle of the affected cells [203]. Conditional knockout of TRP53 in lens epithelial cells hampers the correct lens development and subsequently induces the formation of posterior subcapsular cataracts [204].

3.3 CATARACTS INDUCED BY IONISING RADIATION

The impressive compilation of causes for all sort of cataracts, and posterior subcapsular cataracts in particular, has demonstrated that the posterior subcapsular phenotype can not be considered to be singularly associated to ionising radiation as initial insult. Nonetheless, the PSC is the most frequently observed IR-induced cataract [205] [206].

PSC structure

PSCs have been investigated meticulously by Streeten and Eshaghian [207] in flat preparations and by Eshaghian and Streeten [208] with transmission electron microscopy on human samples. They stated the 'tendency of the migratory cells and of bladder cells to accumulate at the edge of the PSC' [208]. Bladder cells, aka Wedl cells, first described eponymously by Wedl [209], are characterised as swollen fibre cell, in all figurative descriptions partially still carrying nuclei [210], while migratory cells definitely carry a nucleus. To stay with structures visible in the light microscope, they describe the arrangement of those cells around a semi-liquefied centre that lay at the posterior suture. Additionally, degenerating fibre cells could release vesicles of proteinaceous material called Morgagnian globuli which represent the first step to a continuous liquefaction of the cortex [210]. In the comment of Eshaghian and Streeten [208], the authors draw a connection between possible stimuli at the posterior pole and the propensity of nucleated fibre cells to migrate posteriorly. In any case, metabolic active cells are, as the authors stated, able to secret extracellular material and possibly lysosomal enzymes.

Modifying conditions

Some marginal condition are pivotal to the eventual impact of IR exposure. In context of this thesis, age at irradiation and sex are two factors of considerable relevance. Early studies of Merriam Jr and Szechter [211] on rats and of Gajewski et al. [212] on mice, revealed a higher sensitivity of young murine lenses to develop cataracts with a shorter latency than in adults. De Stefano et al. [213] contributed also to those observations by investigating wild-type and $Ptch^{+/-}$ mice at postnatal day 2 (P2 mice).
Hormonal expression is sex-dependent. For instance, females express more estrogen. Dynlacht et al. [214] could show that estrogen modifies the radiation sensitivity of the female lens in rats dependent on the time of administration/release of it. Administration before irradiation enhances and administration after irradiation protects against radiation damages.

Cataract scoring

The cataract scoring proved to be a tricky venture and had to be put in place as sheer necessity. First merits were earned by the pioneers G. R. Merriam and E. F. Focht who presented a discrete grading for female White Sherman rats [215]. The human system in use dates back to 1993, when Chylack et al. published the lens opacification classification system III (LOCS III) [216]. Worgul et al. stressed the fact that LOCS III does not grade first possible transient posterior or anterior changes at all and is rather unsuitable for radiation-induced cataracts. They implemented a modified 5 stage system based on Merriam&Focht [205]. Anyway, LOCS III was used by Pei et al. [217] as basis for a Scheimpflug density/LogMAR (visual acuity) correlation for human nuclear cataracts and is therefore the only clinical system pertinent for comparisons with more contemporary ophthalmologic examinations, in contrast to the Oxford clinical cataract classification (OCCC) [218].

Age-dependent classification

Gajewski et al. [212] introduced a simple binary systematisation based on observations of inbred A strain mice irradiated at different postnatal stages. The authors differed between cataract onsets, either beginning with 'opaque strands running from the periphery of a lens' (type I) or with 'opaque dots, mostly in the lower region of the posterior cortex' (type II). The occurrence of these types was strongly dependent on age at irradiation. In young adults (P70) or older, only type II cataracts were found via slit lamp, while neonatal mice developed type I cataracts (note decreasing proportionally of cataract frequency and age following irradiation between P1 and P5).

Cataract as tissue reaction

Epidemiological data gained from the early studies of A-bomb survivors, Mayak workers [206] and Chernobyl liquidators [205], guided the International Commission on Radiological Protection (ICRP) to decide on a deterministic cataract model for humans (aka tissue reaction model for cataracts) setting a threshold of 0.5 Gy for low LET irrespective of dose rate [219] [220]. Furthermore, it was stated that 20 years after irradiation (p.i.) 1 % of the exposed individuals develop a vision-impairing cataract (VIC). It is also important to state that other councils as the US National Council on Radiation Protection and Measurements (NCRP) did not come to conclusion concerning a threshold for low LET-induced cataracts, but definitely deem cataract formation as a tissue reaction [93]. Nonetheless, it can not be completely ruled out that larger cohorts of irradiated people (especially with lower doses then 0.5 Gy) could reveal a linear dependency with dose without a threshold (stochastic model).

4

RETINAL AND CORNEAL INTERACTION WITH IONISING RADIATION

4.1 INTERACTION WITH THE RETINA

The retina is generally known for her comparably low sensitivity to ionizing radiation. For example, it was demonstrated that C57BL/6J mice have to be exposed to at least 15 Gy of IR in order to cause a significant reduction of the outer nuclear layer [221].
Very much in contrast to these results gained in an experimental earth-based setup, Overbey et al. [222] demonstrated more recently how a spaceflight on the ISS for several months could affect the retina and promote layer degeneration in C57BL/6J mice, although Mao et al. [223] argued that not low dose irradiation but microgravity might be responsible for retinal alterations. Effects of γ-radiation on the retina in C57BL/6J mice (increased apoptosis or eNOS immunoreactivity) were rebutted till 0.5 Gy [224].
Young mice are far more sensitive to ionising radiation. P4 mice of the CBA/H strain irradiated with ~ 6 Gy of X-rays displayed subsequently thinner inner and outer nuclear layer than controls, already 72 h after the exposure [225]. Offspring of pregnant Swiss mice, irradiated with ~ 4 Gy, formed retinae with lower cell density and neuron population [226].

There are two types of macroglial cells that populate the retina: astrocytes and Müller cells. The later normally do not secret glial fibric acidic protein (GFAP), yet they do in the wake of impairment [227]. Grosche et al. [228] referred to the closely intertwined metabolism of photoreceptor and Müller cells, why the loss of photoreceptor cells must affect Müller cells as well. This was shown exemplary by the irradiation of Sprague-Dawley rats with visible light [229].

Blodi [230] underlined the importance of corneal complications in course of radiotherapy in comparison to possible lenticular or retinal impairment. Accordingly, IR has the potential to induce epithelial keratinisation, vascularisation in the stroma, stroma infiltration by inflammatory cells, massive epithelial proliferation, ulceration and even perforation of the cornea. However, transient clouding and restored stem cell function was also observed in patients [231].

5

AIMS AND WORKING HYPOTHESES

Exposition

From a public health angle, it is almost embarrassing how strongly the scientific field has to operate upon pure assumptions concerning cataracts in general and radiation-induced cataracts in particular, and how little the actual mechanism of their formation is understood. The scenario of an increasing exposure to IR is a very realistic one if one considers the increase of IR-releasing imaging methods in healthcare. Apart from the low dose range, confrontation with an IR-intense environments, as in space and on thin atmosphere planets, is immanent in mankind's progression.

LDLensRad

The EU-funded LDLensRad project was initiated to address this grievance in understanding radiation-induced cataracts (https://www.researchgate.net/project/LDLensRad-the-European-CONCERT-project-starting-in-2017-Towards-a-full-mechanistic-understanding-of-low-dose-radiation-induced-cataracts). Teams from Public Health England (PHE), the Agenzia Nazionale per le Nuove Tecnologie, l'Energia e lo Sviluppo economico sostenibile (ENEA) and the Helmholtz Zentrum München - Deutsches Forschungszentrum für Gesundheit und Umwelt GmbH (HMGU) allied to elucidate the mechanism of radiation-induced cataractogenesis based on data gained from large murine cohorts exposed to lower/moderate doses (range 0.5 - 2 Gy). The project focussed also on the effects of different chosen factors like 'genetic background', 'housing facility' and 'dose rate'.

Aims

The thesis at hand presents mainly experiments conducted at the HMGU. Naturally, the primary aim of this thesis is congruent with the LDLensRad's goal to reveal details of cataractogenesis after exposure to IR that the scientific community does not possess thus far. Additionally, this thesis strives to examine the actual relevance of possible lenticular changes by gathering visual acuity data of the experimental mice. Due to the whole-body irradiation of the mice, the influence of IR on the retina and the cornea can be analysed too with great benefit for the assessment of potential visual impairments. This thesis also lays emphasis on the

possibly highly relevant factor 'age at irradiation' because only few studies were done regarding this factor, although the results indicate an enormous influence on the eventual damage on lenticular and retinal tissue.

Hypotheses

In coherence with the fundamental abductional principle to evolve falsifiable hypotheses instead of proving facts, and based on the combined current knowledge in ophthalmology as well as radiation biology/protection, we postulate sets of working hypotheses. Those will address firstly, the lens, its dose-dependent phenomenological changes and the mechanistic steps of cataractogenesis. Secondly, the impact of the factors 'age at irradiation', 'strain' and 'line'. Thirdly, the question whether there is a mouse model for radiation-induced cataracts will be raised to have an alternative for future irradiation experiments. Finally, a general consideration will be articulated about the most radiation-sensitive eye tissue, in order to put the results concerning the lens in perspective:

1. *'Linear increase of mean and maximum lens density with dose in B6C3F1 mice.'*

$\rightarrow$ Energy transfer of γ-radiation to the lenticular tissue should happen linearly. The subsequent accumulation of biomacromolecular damage (proteins and lipids) might also follow a linear or even a sub-exponential course, since linear genetic damage (dicentrics, acentrics etc.) and cell death was observed in experiments before (lymphocytes, [232]). Hence, the lens density should increase at least linearly.

2. *'Partial progression of posterior subcapsular cataracts to nuclear cataracts in B6C3F1 mice after exposure to a dose $\leqslant$ 2 Gy.'*

$\rightarrow$ Merriam Jr and Focht [215] as well as Gajewski et al. [212] introduced cataract scoring and assessment systems based on rodent experiments starting with opacities at the posterior pole that progress to nuclear cataracts (in both systems stage 3+, beginning sclerosis of the nucleus). Gajewski et al. [212] gave precise median times for progression from stage 1+ to stage 3+ cataracts: $\sim$ 100 d for P2 mice (type I+II cataract) and $\sim$ 400 days for P70 mice (type II cataract). Considering the higher dose in the paper of $\sim$ 2.8 Gy, and considering the very short latency of below 100 days for progression to stage 1+ cataracts in P2 mice and almost 200 days in P70 mice, nuclear cataracts should not necessarily occur in P70 B6C3F1 mice in the present study, but definitely in P2 B6C3F1 mice.

3. *'Linear subcapsular cataract occurrence in B6C3F1 mice after exceeding an IR threshold of 0.5 Gy with a dose-dependent latency of a few months.'*

→ For radiation protection reasons, the radiation-induced cataract is considered as tissue reaction in order to establish an awareness for radiation exposure [233]. Nonetheless, a stochastic, non-threshold model for cataracts in dependence on dose is possible. In both cases, a linear increase with dose should be visible if the maximum dose is high enough (fulfilled by 2 Gy). 0.5 Gy as a threshold is less instigated by the 118th ICRP report conclusion/advise than by unpublished data concerning B6C3F1 mice (personal communication with Dr. Claudia Dalke).

4. *'Irradiated neonatal mice (P2) develop predominantly and exclusively type I cataracts with a latency of a few months.'*

→ Gajewski et al. [212] described that type I cataracts are a unique feature of irradiated neonatal mice $\leqslant$ 5 days old (see chapter 1.3.3). Irradiated P70 mice should not display this phenotype at all.

5. *'Irradiated neonatal mice (P2) are prone to develop earlier stage 1+ posterior subcapsular cataracts (type II cataracts) than young adult mice (P70).'*

→ Gajewski et al. [212] stated clearly that 40 % of the irradiated P2 mice developed a type II cataract, meaning a phenotype beginning with alterations at the posterior pole. No other study gave such concrete details concerning the quotient of type I/type II cataracts, why nothing modifies the assumption of a general rule. Therefore, to expect the appearance of both types in P2 B6C3F1 mice is reasonable. In combination with the median times after irradiation (see hypothesis 2), P2 mice should display also earlier stage 1+ (posterior subcapsular changes) and stage 2+ (additional anterior subcapsular changes) of the type II cataract development.

6. *'Inbred C57BL/6J mice are more prone to form radiation-induced posterior lesions than B6C3F1 mice.'*

→ Several studies founded the attribution of inbred C57BL6 mice as more radiation-resistant than e.g. BALB/c mice by investigating their dose-dependent mortality [234]

[235] [236]. But Grahn [236] showed additionally that F1-F3 offspring of both strains were even less radiation-sensitive. This may be a helpful indicator with regard to F1 hybrids of (C3HeB/FeJ x C57BL/6JG). Lenses of irradiated C57BL/6J mice were not investigated before, only the lenticular alterations of B6C3F1 mice [237]. However, other investigations with respect to radiation sensitivity of the lung suggest that C3H mice might be more radiation-resistant than C57BL6 mice [238] [239]. Hence, the assumption that inbred C57BL/6J mice should be inclined to form eventually more PSCs than B6C3F1/B6RCF1 mice appears to be justified.

7. *'Possible radiation-induced posterior subcapsular cataracts cause vision impairment.'*

→ Increased forward scattering by cataracts can have vision-impairing effects [240]. Of all possible forms of vision alterations (e.g. myopic shift, astigmatism, contrast sensitivity reduction, colour shift, glare, visual acuity loss, [241]) only visual acuity will be investigated in course of this work. Glare sensitivity, for instance, is known to be also increased in human patients with PSCs [242], but can not be tested with mice. Without existing correlations between visual acuity of mice and humans via a measure lenticular measure, 'vision impairment' has to be gauged purely by statistical means without clinical judgment.

8. *'Radiation-induced alterations in murine lenses start with the simultaneous appearance of vacuoles and nuclei-containing cells at the posterior pole.'*

→ Every cited study on irradiated rodents showed that the first stage is dominated by observed vacuoles and diffuse opacities [215] [243] [212]. Logic commands to consider 'vacuoles' (slit lamp term that equates with swollen fibre cells in histology) as secondary effects of site-disturbing nuclei-containing aberrant fibre cells. Nonetheless, no study was able to clarify the question by identification of a sequence. Therefore, a concurrent occurrence was hypothesised for the present thesis.

9. *'The $Trp53^{CKO}$ mouse lens is a structural model for radiation-induced posterior cataracts.'*

→ Irradiation is a harsh treatment and should be applied scarcely in scientific experiments, in order to reduce suffering of experimental animals. Therefore, a murine mutant that forms PSCs without irradiation would be highly desirable. Based on histological H&E analyses provided by Wiley et al. [204], the $Trp53^{CKO}$ mouse is perhaps

such a promising model for the investigation of radiation-induced posterior subcapsular cataracts in terms of migrating nuclei and swollen fibre cells (without involving irradiation). As long as no fine structure is revealed, the positive hypothesis stands.

10. *'No influence of the heterozygous Ercc2 mutation on lenticular and retinal phenotypes in B6RCF1 mice within the observation time of 20 months p.i.'*

→ Maximum Scheimpflug density data from Dalke et al. [237] analysed with ANOVA did not suggest any genotype effect (comparison of pooled data from 1-4 months vs. 20-24 months p.i., $p = 0.41$). Heterozygous mutation had only an effect on retinal thickness (significant thinner in mutants beginning 20 months p.i., but only 1-2 % mean thickness reduction). Therefore, the initial hypothesis is kept conservative.

11. *'The lens is the most radiation-sensible ocular tissue in B6C3F1 mice.'*

→ Previous whole-body expositions of organism to a moderate dose, which is used in the present thesis ($\leqslant$ 2 Gy), showed that the lens is actual the only eye tissue changing (see Poppe [244], adult male white rabbits). Since irradiation experiments with focus in on the retina in postnatal animals were only performed with doses higher than 2 Gy [225], observed retinal damage can not be satisfyingly compared to the anticipated lenticular damage in neonatal and adult mice, why a conservative hypothesis was chosen.

Part II.

Materials and methods

1

MURINE MODEL ORGANISMS

1.1 EXPERIMENTAL MICE AND HOUSING

In context of this thesis, several mice were investigated for short- and long-term purposes (Tab. 1).

Table 1.: Experimental mice of LDLensRad consortium facilities of which material was taken for this thesis.

Facility	Strain	Line	Sex
HMGU	B6C3F1	WT	♂/♀
		Ercc2$^{+/-}$	♂/♀
	FVB/N	*Trp53*^{CKO}	♂/♀
PHE	C57BL/6J	WT	♀
	129S2/SvHsd	WT	♀

Mice were housed by the the Helmholtz Center Munich (HMGU) and Public Health England (PHE) until their respective endpoint.

C57BL/6JG (BL6; MGI:6198736) for breeding of *Ercc2*$^{+/-}$ and *Ercc2*$^{+/+}$ mice were obtained by in-house supply, and were C57BL/6J mice that were not refreshed after 10 generations with new mice from Jackson Laboratory (via Charles River Germany). C3HeB/FeJ carrying the *Ercc2* mutation after treatment with ENU were also of the regular breeding stock from the HMGU. *LeCre* mice for breeding of *Trp53*^{CKO} mice were obtained by Prof. Ruth Ashery-Padan (University Tel Aviv) and *Trp53*$^{fx/fx}$ mice by the Jackson Laboratory (Stock No. 008462). 129S2/SvHsd and C57BL/6J mice - housed by PHE - were purchased from Envigo (Bicester, UK).

Mice were housed under SPF condition in the German Mouse Clinic (GMC, `https://www.mouseclinic.de`) in accordance with the German Law of Animal Protection, the ARVO Statement for the Use of Animals in Ophthalmic and Vision Research, and the tenets of the Declaration of Helsinki.
Mice were housed in groups of maximum 4 animals in standard individually

ventilated cages (IVC) at day/night rhythm (light between 6 am and 6 pm) and fed *ad libitum* with standard diet pellets (Altromin, Lage, Germany). Mice housed by PHE were fed with RM3(E) (LBS Biotechnology, Hookwood, Surrey, U.K.).

1.2 BREEDING AND GENOTYPING

Ercc2 mutants

WTs and heterozygous *Ercc2* mutants were bred on hybrid BL6 x C3H background according to Dalke et al. [237]:

$$\begin{aligned} \textit{Ercc2}^{-/-}\ \male\ \text{C3HeB/FeJ} \quad &\text{x} \quad \textit{Ercc2}^{+/+}\ \female\ \text{C57BL/6JG} \\ &\rightarrow \textit{Ercc2}^{+/-}\ (\text{(C3HeB/FeJxC57BL/6JG)F1}) \quad := \quad \text{B6RCF1} \\ \textit{Ercc2}^{+/+}\ \male\ \text{C3HeB/FeJ} \quad &\text{x} \quad \textit{Ercc2}^{+/+}\ \female\ \text{C57BL/6JG} \\ &\rightarrow \textit{Ercc2}^{+/+}\ (\text{(C3HeB/FeJxC57BL/6JG)F1}) \quad := \quad \text{B6C3F1} \end{aligned}$$

Because female mice are generally sterile, only male homozygous mutants could be use as carrier of the *Ercc2* mutation. B6C3F1 are designated as WTs and B6RCF1 as mutants.

The earmark material from weaned mice was used to gain DNA templates for genotyping according the following protocol:

1. Shaking incubation of every ear sample in 500 µl lysis buffer (TRIS, NaCl, EDTA, +20 µl SDS, +25 µl protein kinase K) for 2-3 h at 55 °C.
2. Addition in 250 µl of 5 M NaCl for 15 min and subsequent laying on ice for 10 min.
3. Centrifugation of samples at 8000 rpm for 10 min at RT and transferation of 500 µl supernatant to 1 ml of $C_2H_5OH_{abs.}$.
4. 15 min centrifugation (13000 rpm) at 4 °C and removal of supernatant. Resolution in 70 % $C_2H_5OH_{abs.}$ and anew centrifugation for 7 min (13000 rpm) at 4 °C.
5. Drying of the samples for less than 15 min and resuspension of the pallet in 80 µl TE.

Purified DNA was taken as template for a PCR mix according to the scheme in Tab. 3. Primer L1 and R1 were chosen to start copy of the *Ercc2* gene locus (Tab. 2). PCR was conducted according to Tab. 4. A 490 kb band in PCR gel plot indicated the

right gene product (Fig. 6, A). Further digestion with mix of 8 µl PCR product, 1 µl MwoI (5u), 1.2 µl CutSmart and 1.5 µg H_2O at 60 °C for 1 h was conducted to differ between *Ercc2*$^{+/-}$ and *Ercc2*$^{-/-}$ mice (Fig. 6, B).

Table 2.: Primers for genotyping of *Ercc2*$^{+/-}$ mice with PCR.

Allele	Primer	Sequence (5′→3′)	Size [bp]
Ercc2	L1	ACAAGCGTGGTAAGCTGCC	490
	R1	CTCTTGTAGATCGCTCCCTGC	320

According to Table 1 in supplemental of Kunze et al. [201].

Table 3.: PCR mix for *Ercc2*$^{+/-}$ genotyping.

Input	Item
5 µl	DreamTaq™ Polymerase
1 µl	L1 primer
1 µl	R1 primer
1 µg	DNA template
2 µl	H_2O

L1 and L2 primer according Tab. 2.

Table 4.: PCR protocol for *Ercc2*$^{+/-}$ genotyping.

Cycles	Temperature	Time
1x	95°	1′
40x	95°	30″
	64°	30″
	72°	30″
1x	72°	5′

PCR of mix from Tab. 3.

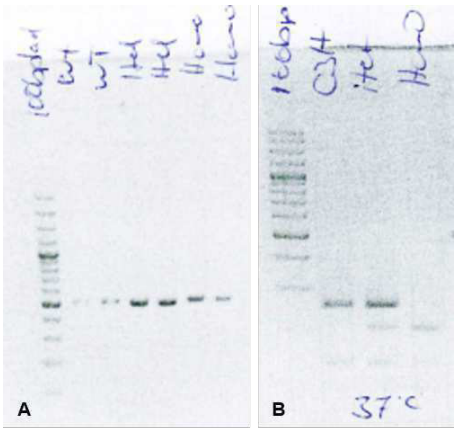

Figure 6: PCR on 1.5 % agarose gel **(A)** and digestion on 2.5 % agarose gel **(B)** in *Ercc2*$^{+/-}$ genotyping. Material from C3H mice, WT, putative heterozygous **(Het)** and putative homozygous **(Hom)**. First line in both pictures displays DNA ladder. Gene Ladder (**Ladder**) (Gene Ruler 100bp Plus (Thermo Fisher, SM0321).

Trp53^{CKO} *mice*

Mice with a conditional *Trp53* knock out in the lens were bred by mating *Trp53*$^{fx/fx}$ mice (mice with floxP site at the *Trp53* intron 1 and 10), introduced by Jonkers et al. [245], with *LeCre*$^{+/-}$ mice (mice expression Cre recombinase under the control of the

Pax6 Po promoter/enhancer), introduced by Ashery-Padan et al. [246], according the breeding schema from Wiley et al. [204]:

$$
\begin{aligned}
Trp53^{fx/fx} \quad & \text{x} \quad LeCre^{+/-} \\
& \rightarrow Trp53^{WT/fx};\ LeCre^{+/-} \\
& \rightarrow Trp53^{WT/fx}, LeCre^{-/-}
\end{aligned}
$$

$$
\begin{aligned}
Trp53^{WT/fx}; LeCre^{+/-} \quad & \text{x} \quad Trp53^{fx/fx} \\
& \rightarrow Trp53^{fx/fx};\ LeCre^{+/-} \quad := \quad Trp53^{CKO} \\
& \rightarrow Trp53^{fx/fx}, LeCre^{-/-} \\
& \rightarrow Trp53^{WT/fx}; LeCre^{+/-} \\
& \rightarrow Trp53^{WT/fx}; LeCre^{-/-}
\end{aligned}
$$

Mice of both breeding steps were genotyped with the set of primers in Tab. 5. $Trp53^{WT/fx};\ LeCre^{+/-}$ mice have been tested positive for the $Trp53^{F2\text{-}10}$ allele with the primer pair 1F/1R and 10F/10R yielding products of 288 bp and 431 bp. They were also positive for the PCR product yielded by the Cre-3/Cre-5 primer pair (408 bp). *In-vivo* analysed lenses of $Trp53^{CKO}$ and their brains were collected 4 months after

Table 5.: Primers for genotyping of $Trp53^{CKO}$ mice with PCR.

Allele	Intron	Primer	Sequence (5′→3′)
$Trp53^{F2\text{-}10}$	1	1F	CACAAAAACAGGTTAAACCCAG
	1	1R	AGCACATAGGAGGCAGAGAC
	10	10F	AAGGGGTATGAGGGACAAGG
	10	10R	GAAGACAGAAAAGGGGAGGG
$Trp53^{\Delta 2\text{-}10}$	1	1F	CACAAAAACAGGTTAAACCCAG
	10	10R	GAAGACAGAAAAGGGGAGGG
Cre	-	Cre-5	GCATTA CCGGTCGATGCAACGAGTGATGAG
	-	Cre-3	GAGTGAACGAACCTGGTCGAAATCAGTGCG
β-*Actin*	-	L	GGGTGTATTCCCCTCCATCGTGG
	-	R	ACAGAGTACTTGCGCTCAAGGAGGAGC

According to Table B in supplemental of Jonkers et al. [245]. Primers purchased from Sigma-Aldrich®.

birth for RNA purification according to following protocol:

1. Homogenisation of lenticular tissue and 600 µl Trizol (Invitrogen™, 15596026) and incubation for 5 min at RT; adding of 120 µl chloroform, tilting for 15 sec and incubation for 3 min at RT.
2. Centrifugation with 13000 rpm for 5 min at 4 °C and incubation of the supernatant with 5 µl RNaseI for 15 min at 37 °C. Adding of the same volume $C_2H_5OH_{abs.}$.
3. Proceeding with the RNeasy® Plus Mini Kit, protocol point 4 (Qiagen, No. 74134). Final dilution with 30 µl of RNase-free water.

C-DNA synthesis was done with the SensiFAST™ cDNA Synthesis Kit (Bioline, BIO-65054) and 1 µg RNA as template. PCR of cDNA of the $Trp53^{\Delta 2\text{-}10}$ yielded a clear band of 612 bp product in the lens but not in the brain (Fig. 7, $Trp53^{\Delta 2\text{-}10}$). No products of the $Trp53^{F2\text{-}10}$ allele were amplified in the lens, but in the brain. The *LeCre* transgene was in both tissues present.

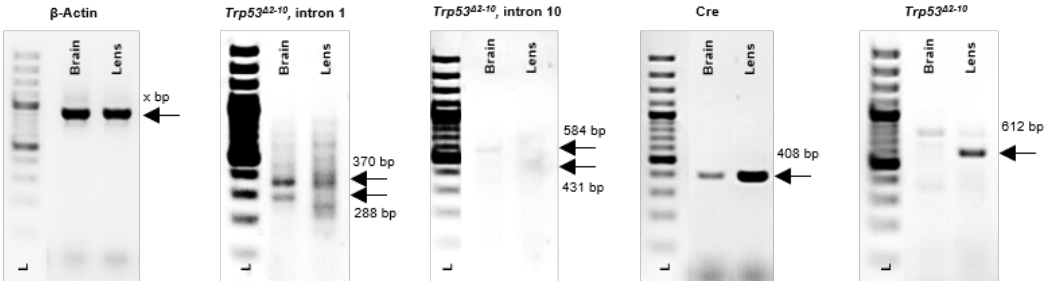

Figure 7.: PCR of cDNA purified from RNA of the brain and lens displaying the distinctive phenotype of a $Trp53^{CKO}$ mouse according to Wiley et al. [204]. Investigated alleles written above the plots. Ruler (**L**) (Gene Ruler 100 bp Plus (Thermo Fisher, SM0321).

1.3 COHORTS AND IRRADIATION

HMGU mice

To investigate the factors age at irradiation and latency of radiation-induced effects, we whole-body-irradiated mice at different postnatal stages: neonatal mice at postnatal day 2 (P2 mice) and mice as young adults 70 days after birth (P70 mice). Exposure to γ-radiation (1.33 MeV) was performed with a a ^{60}Co source (Eldorado 78 teletherapy irradiator, AECL, Canada) and exposure to X-rays (195 keV) with a cathode ray device (X-Strahl RS225 irradiator). Previous experiments with rats have proven the practical equivalence of γ- and X-rays [247].

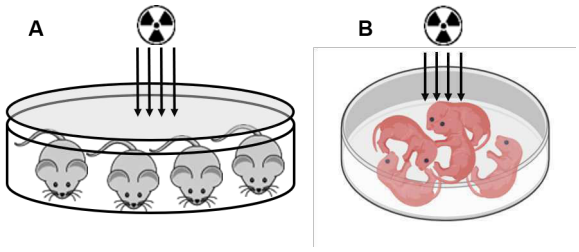

Figure 8.: Illustration of irradiation procedures with P70 **(A)** and P2 mice **(B)** (created with Biorender.com).

All HMGU mice were exposed to sources with a dose rate of 0.3 Gy/min in plastic cylinder (P70) or a Petri dish (P2) with a plastic lid to block β-rays from the ^{60}Co decay (Fig. 8). More than 20 mice of every group of HMGU mice were irradiated with γ-rays or treated as controls (Tab. 6). Six mice per group were irradiated with X-rays and 3 sham-irradiated in the same procedure. Several cohorts of P70 mice were exposed to γ-rays according to the scheme in Tab. 7. For a comprehensive study of the long-term effects, at least 20 mice of every group were sham- or γ-irradiated with the aim of an endpoint of 20 months p.i..

Table 6.: Number of sham- and IR-irradiated P2 mice of B6C3F1 background.

Dose [Gy]	Group	# each group	Endpoint p.i.
0 Gy	WT ♂/♀ + Mut ♂/♀	3	10 weeks
	WT ♂/♀ + Mut ♂/♀	20	9 months
2 Gy	WT ♂/♀ + Mut ♂/♀	6	10 weeks*
	WT ♂/♀ + Mut ♂/♀	20	9 months†

All animals sham or IR-irradiated at P2. Irradiation with γ-rays (†) and X-rays (⋆).

All HMGU mice were irradiated and examined with the permission of the Government of Upper Bavaria under ROB-55.2-2532.Vet_02-16-167.

Table 7.: Number of sham- and IR-irradiated P70 mice of B6C3F1 background.

Dose [Gy]	Groups	# each group	Endpoint p.i.
0 Gy	WT ♂	3	4 h
0.5 Gy	WT ♀	3	24 h
1 Gy	Mut ♂	4	12 months
2 Gy	Mut ♀	4	12 months
		21	20 months

All animals (80 groups) of sham or IR-irradiated at P70. Irradiation with γ-rays.

PHE mice were irradiated according McCarron et al. [248].

2

OPHTHALMOLOGIC EXPERIMENTS

2.1 SPECTRAL DOMAIN - OPTICAL COHERENCE TOMOGRAPHY (SD-OCT)

Spectralis® OCT

The SD-OCT (hereinafter only OCT) is well established as a retina investigation method and was also introduced as lens monitoring method by Pawliczek et al. [195]. All measurements were performed with the Spectralis® SD-OCT device (Heidelberg Engineering, Heidelberg, Germany). To image the lens and the retina, a near infrared LASER was applied that could penetrate the transparent tissue.

Experimental setup

Examinations of the retina and the lens were performed with modifications according to Puk et al. [249]. The main modification was the application of a 78-diopter double aspheric lens (Volk Optical, Inc., Mentor, OH, USA) put directly on the optical outlet of the Spectralis® (Fig. 9, blue arrow). Additionally, a plan-convex contact lens (Roland Consult, Brandenburg, Germany) was attached to the murine eye which had to be examined (Fig. 9, red arrow). Contact was mediated by 2 % Methocel (OmniVision, Puchheim, Germany). For the imaging of murine lenses, the handling was adjusted according Pawliczek et al. [195]. Mice were anaesthetised 10 min before examination with ketamine (100 mg/kg)/xylazine (10 mg/kg) and put without constrains on an examination platform. Since lenticular OCT was quite

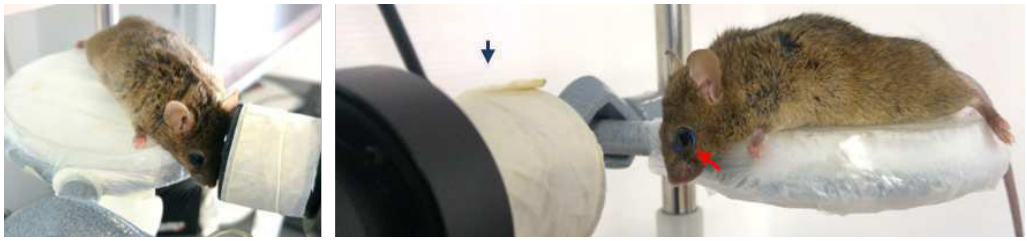

Figure 9.: Illustration of OCT measurement. Double aspheric lens at the OCT device (blue arrow). Contact lens on the eye of the anaesthetised mouse (red arrow).

late applied for this specific purpose, measurements were done 10.5, 14.5 and 18.5 months p.i. for the 2 Gy cohort, 13.5 and 17.5 months p.i. for the 1 Gy and only

17.5 months p.i. for the 0.5 Gy cohort. Retinae were investigated for all cohorts regularly 3 months p.i. and subsequently in intervals of 4 months (0.5 + 1 Gy cohort and associated controls) and only in 4 month intervals after irradiation in the 2 Gy cohort.

2.2 SCHEIMPFLUG TOMOGRAPHY

Scheimpflug's principle

The conditions for a sharp imaging of spacious objects not lying in parallel with the image plane of photographic system were discovered by Theodor Scheimpflug in 1907 [250]. Scheimpflug accomplished to avoid distortions of object image by arranging the image plane according to the angle of object plane to the lens plane (Fig. 10). This principle is implemented in the Scheimpflug camera (note intersection of plane AB and A'B' in the prolonged lens plane).

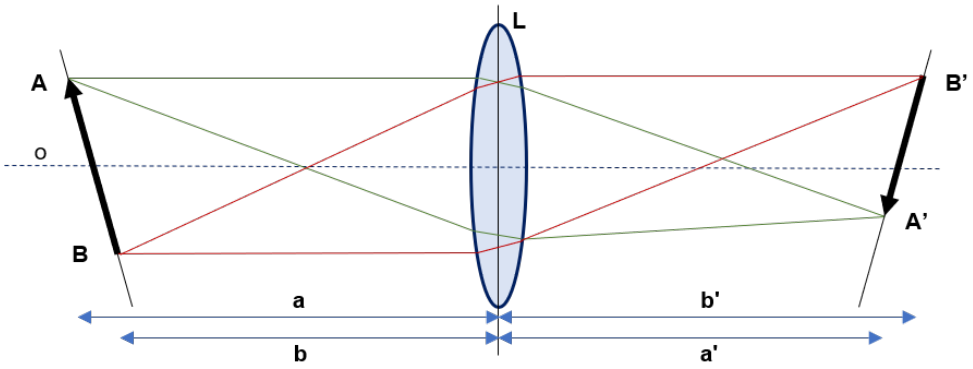

Figure 10.: Illustration of the Scheimpflug principle. Converging lens **(L)**. Optical axis **(o)**. Object in object plane **(A-B)**. Image in image plane **(A'-B')**. Object distance **(a-b)**. Image distance **(a'-b')**. According to Wegener and Laser-Junga [251].

Oculus Pentacam®

This basic rule of photogrammetry was applied by several vendors to construct a camera for the precise imaging of the eye lens. Within the scope of this work, the Oculus Pentacam® was used for long-term examinations. The Scheimpflug camera is basically a perfect solution for imaging the anterior part and nucleus of the lens in mice, but not able to detect the posterior pole (see [195]).

Experimental setup/ analysis

Practically, B6C3F1 mice were analysed every month p.i. after treatment with 0.5 % atropine to dilate the eye pupils. Examination was done relinquishing on anaesthesia. In every examination, only one picture was recorded that satisfied the

requirements for lens recording within the limits of the method. Lens density was determined preferentially of records taken as mid-frontal tomographies (Fig. 11, A) but also off-centre if a minor corneal opacification hampered the optimal analysis or the mice were not calm enough to measure in reasonable time (Fig. 11, B). Records showing pronounced corneal clouding were discarded for lenticular density analysis (Fig. 11, C). Density analysis was performed with the bar tool (in every adult irradiated mouse cohort and their controls) and with the free area tool if necessary (irradiated neonatal mice and their controls).

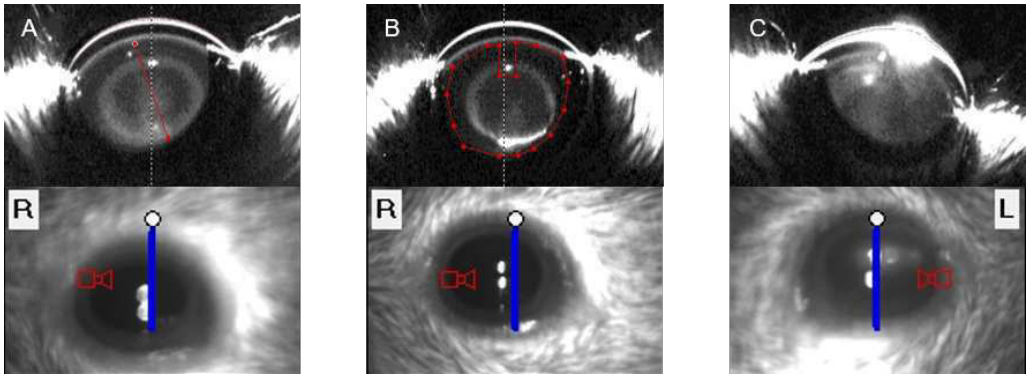

Figure 11.: Methodology of Scheimpflug measurements. Regular lens, recorded in the mid-frontal plane, measured with analysis bar **(A)**. Lens with massive localised opacification, bit off-centre recorded, measured with the free area tool **(B)**. Eye with corneal opacification, measured in mid-frontal plane, but not analysed at all **(C)**. Red closed or dotted lines indicate analysis tool route or area.

2.3 LASER INTERFERENCE BIOMETRY (LIB)

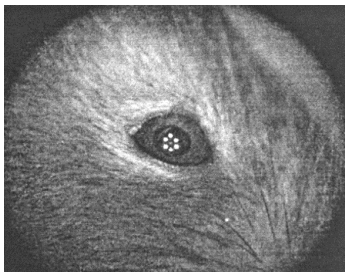

Figure 12.: Illustration of LASER interference biometry measurement. Picture taken from Puk et al. [252].

Lenticular thickness was partially determined with a LASER interference biometry (LIB) device (ACMaster, Zeiss). As in the OCT, an incident 850 nm beam (semiconductor LASER diode) was applied to the anaesthetised mouse (see OCT) that laid unconstrained and without contact lens on a platform. The measurement started when 5 bright dots appeared on the examined eye in the right position on the pupil (Fig. 12).

To determine the optokinetic reflex, mice were measured with the virtual optomotor system (Cerebral Mechanics, Lethbridge, Canada) [253], and some controls counterchecked with another automatically evaluating system (OptoDrum, Striatech GmbH, Tübingen, Germany). The manual system from Cerebral Mechanics is hereinafter designated as VD1 and the automatic system of Striatech as VD2. The mice were put on the observation platform of the drum 30 min after adaption to room conditions and were immediately measured. In the VD1 this procedure was done in the *measure/combine* mode. The measurement was conducted continuously without breaks of the displayed surrounding strip pattern. Measurements in the VD2 started with a relatively high expectation value which was corrected by testing of spatial frequencies in a staircase procedure with breaks of the displayed pattern after each positively determined intermediate value. Staircase procedure in both drums guaranteed a oscillatory approximation of the final spatial frequency the mice is capable to recognise.

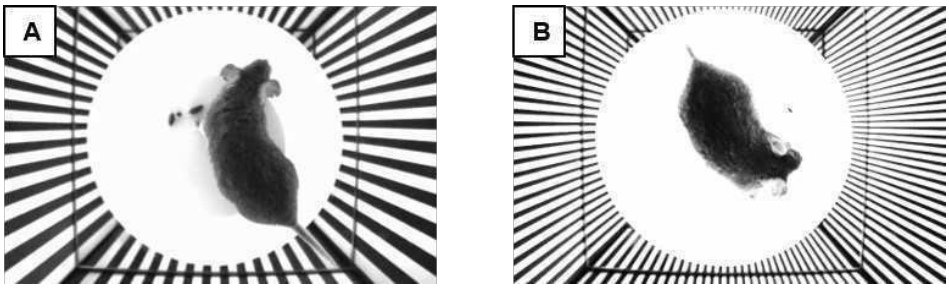

Figure 13.: Determination of spatial frequency with the virtual drum (exemplary shown for VD2). Start of the staircase procedure with a low level of spatial frequency **(A)**. Example of a mice succeeding to a higher examination level (denser stripe pattern) **(B)**.

3

ANALYSIS *POST MORTEM*

Mice were killed at the respective endpoints at 4 h, 24 h, 4 mths., 9 mths., 12 mths. and 20 mths (Tab. 7 + 6) in accordance with animal welfare by CO_2 gas. The murine eyes were than taken for *post-mortem* analysis and bodies examined by pathologists if the concerning mice were of a long-term cohort (endpoint 20 months after irradiation) and not whole-body-perfused.

3.1 IMMUNOHISTOCHEMISTRY

Immunohistochemistry (IHC) experiments were performed on eyes fixed for at least 12 h in 4 % paraformaldehyde (PFA). Those samples were after fixation kept in 70 % ethanol, gradually dehydrated (Infiltration automate TP1020, Leica) and embedded in paraffin (HistoStar™, ThermoFisher Scientific). Eye sections of 5 µm thickness were gained under cool conditions with a microtome. Immunohistochemical experiments were conducted according the following protocol:

1. De-paraffinisation of sections gained from PFA-fixed and paraffin-embedded samples starting with 2 x 15 min in Roti Histol, 2 x 4 min of pure C_2H_5OH, 1 x 4 min 95 % C_2H_5OH, 1 x 4 min 80 % C_2H_5OH, 1 x 4 min 60 % C_2H_5OH, 1 x 4 min 30 % C_2H_5OH and re-hydration with 3 x 15 min H_2O_{dest}.
2. Heating of samples in boiling citrat buffer (0.01 mM, pH = 6.4) for 25 min and slow adaption to room temperature (RT); washing of samples 2 x 10 min in PBS afterwards.
3. Blocking of samples with 5 % skimmed milk buffer for 1 h.
4. Applying of primary antibody in blocking buffer according dilution in Tab. 8 at 4 °C over night under humid conditions. Washing of samples 3 x 5 min in PBS afterwards.
5. Incubation of samples with secondary antibodies according to Tab. 9 for 90 min in a humid chamber at RT. Washing of samples 3 x 5 min in PBS.

6. Staining with DAPI (1:1000 in H_2O) for 15 min at RT and 1 min washing in PBS. Subsequent incubation of samples with 0.15 % Sudan black solution for 20 min and washing 2 x 10 min in PBS and 1 x 1 min in H_2O.

Table 8.: Primary antibodies used in experiments of IHC and immunoblotting.

Antibody	Target	Provider	Catalogue#	Dilution
αA-cry	αA-crystallin	Ales Cveki	⋆	1:500
αSMA	α smooth muscle actin	Sigma-Aldrich	A5228	1:300
Bac	β-Actin	Sigma-Aldrich	A2228	1:2000
BFSP1	Beaded filament structural protein 1	Roy Quinlan	+	1:100
γ-cry	γ-crystallin	Santa Cruz	sc-365256	1:100
CALB2	Calretinin	Swant	7699/3H	1:100
ColIV	Collagene IV	Santa Cruz	sc-70246	1:200
Cry	Crystallin (unsp.)	Roy Quinlan	+	1:50
Cx46	Connexin 46	ThermoFisher	700384	0.8 µg/ml
Cx50	Connexin 50	Fisher Scientific	89131086	1:1500
GFAP	Glial fibrillary acidic protein	Sigma-Aldrich	G9269	1:250
GPX1	Glutathione peroxidase 1	Novus Biologicals	NBP1-33620	1:100
Lim2	Lens intrinsic protein 2	GeneTex	GTX55691	1:1000
PKCα	Phosphore kinase C α	Abcam	ab-11723	1:100
Rhd	Rhodopsin	Santa Cruz	57432	1:100
SOD1	Superoxide dismutase 1	Novus Biologicals	NBP2-24915	1:7000
SOD2	Superoxide dismutase 2	Novus Biologicals	NBP2-20535	1:7000
TGFβ	Tumour growth factor β	Fisher Scientific	89131086	-

Anti-target primary antibodies with dilution indication for step 4 in IHC protocol. Relayed by Dr. Ales Cvekl (⋆), NY/USA, use according [254] and Prof. Dr. Roy Quinlan (+).

3.2 HISTOLOGY

Scores of eyes were taken for histological analysis. For this purpose, eyes were fixed in modified Davidson liquid (3 parts $ethanol_{ab.}$, 3 parts $aqua_{dest.}$, 2 parts formaldehyde, 1 parts acetic acid) for at least 3 days. Fixed eyes were embedded in Technovit® 8100 (Heraeus Kulzer, Wehrheim, Germany), and then were the hardened samples

Table 9.: Secondary antibodies used in experiments of IHC and immuno blotting.

Antibody	Provider	Catalogue#	Dilution
Cy3-anti-mouse	Jackson immuno	715-165-150	1:250
Cy3-anti-rabbit	Jackson immuno	715-165-152	1:250
Alexa 488-anti-mouse	Invitrogen	A-21202	1:250
Alexa 488-anti-rabbit	Invitrogen	A-21206	1:250

Anti-target secondary antibodies with dilution indication for step x in IHC protocol.

cut in 2 µm mid-sagittal sections with a glass knife ultramicrotome (OM U 3, C. Reichert, Austria). The collected sections were heat-fixed on superfrost slides and stained with basic fuchsin and methylene blue (3 parts methylene blue (0.13 % w/v in $aqua_{dest.}$), 4 parts basic fuchsin (0.13 % w/v in $aqua_{dest.}$), 5 parts 0.2 M PBS, 3 parts $ethanol_{ab.}$).

3.3 WESTERN BLOTTING

1. Shock-frosted lenses were dissolved in lens extraction buffer (50 µM Tris-HCL, 3 mM DDT, 0.1 mM PMSF), smashed with a pestle and spun down at 10.000 rpm for 10 min.
2. 20 µg of protein were adjusted to a concentration of 4 µg/ml and run for every sample (4 µl of protein solution + 2 µl of Roti load 1 after 5 min incubation at 95 °C) in a SDS gel embedded in running buffer (25 mM Tris, 190 mM glycine, 0.1 % SDS). Samples were run at a voltage of 100 V for 90-95 min.
3. Separated protein blot was transferred to a sandwiched membrane bathed in transfer buffer (Bio-Rad transfer buffer) whilst voltage application of 100 V over night at 4 °C.
4. Protein transfer was proved by Ponceau staining (see exemplified in 14). Blot was washed 2x in water and 1 min in Ponceau solution (0.2 % (w/v) Ponceau S, 5 % acetic acid) before taking a photo. Afterwards, blot was washed again 2x5 min with water and 3x5 min with PBS-T (1 M PBS, 0.1 % Tween).
5. Membrane was blocked with 5 % skimmed milk in PBS+T at room temperature and subsequently washed 3 times in PBS-T.
6. First antibody was applied at given dilution and incubated over night at 4 °C.

7. Blot was washed 3x in PBS-T for 5 min each. Horseradish peroxidase-conjugated antibody was applied for 1 h at RT. Blot was washed 3x5 min in PBS-T.
8. Blots were treated with chemoluminescent solution (Luminol) and imaged in a chemoilluminescene chamber (Bio-Rad gel documentation center).

In case of reprobing, membranes were stripped:

a. Antibody-treated plots were incubated for 45 min in 50 °C hot stripping buffer (20 ml of 10 % SDS, 12.5 ml 0.5 M Tris HCl, 67.5 ml $aqua_{dest.}$, 0.8 ml 2-mercaptoethanol).
b. Steps 5-8 again with different primary antibody.

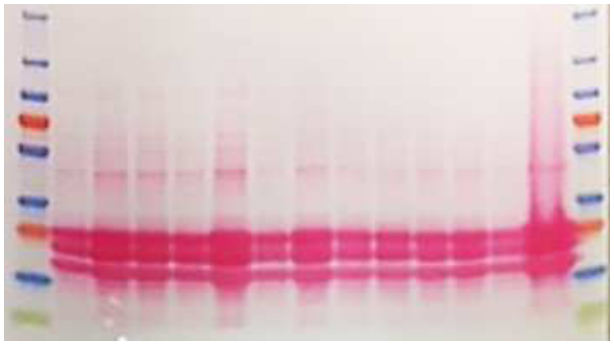

Figure 14.: Example of a Ponceau-stained protein blot after transfer to the membrane. Samples were taken from 20 months old lenses.

4

STATISTICAL ANALYSIS, DATA TRANSFORMATION AND STORAGE

4.1 STATISTICS

Mean differences

Data sets were analysed with OriginPro 2017 on distribution differences, irrespective of their quality via the non-parametric Mann-Whitney test because several observation quantities within the monitoring time deviated from a normal distribution. The Mann-Whitney test performs exactly as the Students t-test in normally distributed data sets, but could cope with distributional asymmetries if necessary. The test was generally performed both-sided why an α-level of 5 % and the asymptotic probability of the test displayed in analysis of lenticular signal-free areas, mean and maximum lens densities, retinal thickness, intra-lenticular damage distances, optic nerve lesions, spatial frequencies, cell populations in the retina and lenticular thickness. Median and 95 % confidence intervals were always accompanying drawn in graphical illustrations. Paired t-test was used for analysis of the same samples at two different time points (PSFA comparison, retinal thickness of neonatal mice).

MANOVA

To determine the influence of independent factors (e.g. sex, line and dose), multiple analysis of variances (MANOVA) was performed for lens densities and weights. Here, mean differences between populations according all 7 forms of interaction in the three-way ANOVA were investigated and *post hoc* analysed with Tukey test. Levens test was performed by default to test the data set on variance homogeneity.

Regression analyses

Regression analyses were conducted according the fundamental biological hypothesis of a linear dose-response dependency. Pearson correlation coefficient (R) was given for every determined linear regression, and the corrected square correlation coefficient (cor. R^2) was specified if it modified the scientific conclusion based on R. Linear regression was also applied to score-response dependencies, although scores could express a sketchy representation of biological endpoints.

Odds ratios

Binary information (phenotype or not) from histology and lenticular phenotypes were analysed by calculating odds ratios. These were calculated by multiplication of the quotient of exposed lenses (affected/non-affected) and the quotient of the control lenses (non-affected/ affected) according to Altman [255]. To consider the eventuality of no affected animals in the denominator, 0.5 was added to every number [256]. 95 % confidence intervals and p-values were also given in tabular summaries.

4.2 IMAGE ANALYSIS

Histological sections were scanned at given magnification with the FL Auto Imaging System, EVOS®. Images were processed by contrast adjustment and background correction with GIMP (2.8.2, 2017, The GIMP team). Pictures were colour-levelled with Microsoft PowerPoint® by adjusting contrast and brightness. Immunohistochemical experiments were assessed by the ZEISS Axiovert 200. *Ex-post* correction was also carried out with Microsoft PowerPoint®, but equally for every picture of an experimental batch.
Scheimpflug images were always displayed with the highest possible contrast adjustable by the Oculus software and were not corrected otherwise.

4.3 DATA STORAGE

All raw data sets of the optical coherence tomography measurements, Scheimpflug imaging and histological analysis were saved in the public data repository STORE^{DB} (`https://www.storedb.org/store_v3/index.jsp`). Every thesis-related data set and all lists for example descriptions can be found in the LDLensRad_HMGU folder (DOI:10.20348/STOREDB/1113). Raw Scheimpflug measurements data of C57BL/6J and 129S2/SvHsd mice that have been housed and monitored by PHE can be found in the LDLensRad_PHE folder (DOI:10.20348/STOREDB/1112). No recordable data was obtainable via the ACMaster measurements (LIB) due to technical limitations.

Part III.

Results

1

LENSES OF THE TRP53 CKO MOUSE MODEL

The $Trp53^{CKO}$ mouse model was investigated *in vivo* and in histology *post mortem* as possible model for radiation-induced cataracts (due to reported posterior lenticular alterations as a consequence of the conditional KO) (Fig. 15).

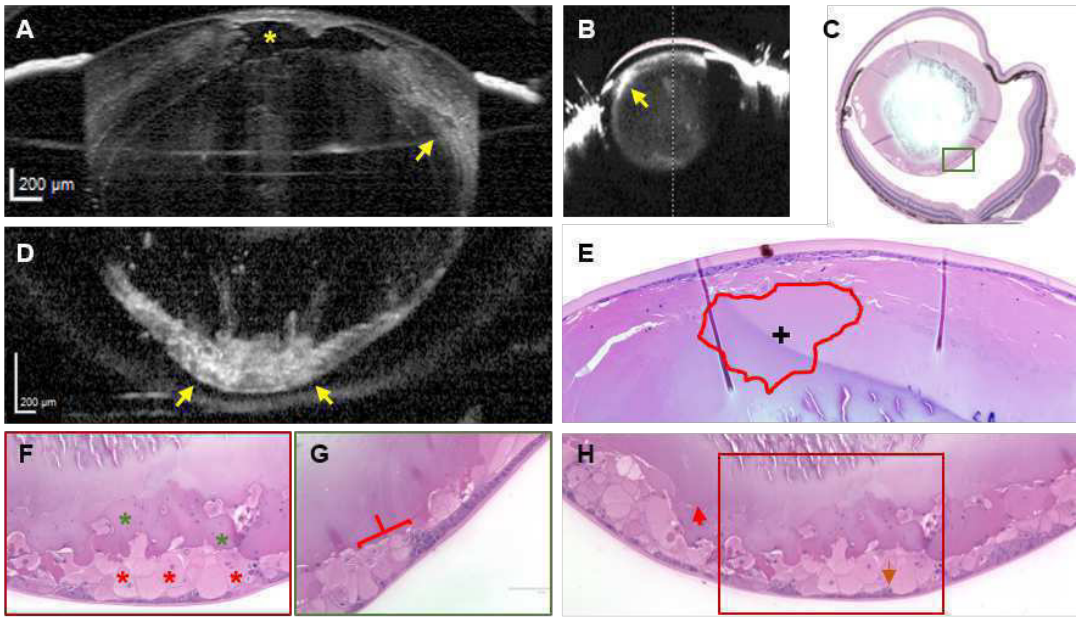

Figure 15.: *In-vivo* and *post-mortem* analysis of a $Trp53^{CKO}$ lens with published phenotype according to Wiley et al. [204] (4 months of age after birth). OCT image of the anterior lens **(A)**. Scheimpflug image **(B)**. Histological overview of the eye (4x) **(C)**. OCT image of the posterior lens **(D)**. Anterior lens in histology (20x) **(E)**. Histological detail of the posterior suture (40x) **(F)**. Histological detail of the dextrolateral posterior lens (40x) **(G)**. Posterior lens in histology (20x) **(H)**. Anterior signal-free area (yellow star; A). Scattering area in OCT and Scheimpflug imaging (yellow arrows; A, B, D). Large poorly structured area in anterior histology (red encircled area; E). Morghanian cells (red stars; F). Fibre cells with totally shrunken nuclei (green stars; F). 'Transitional zone' of aberrant fibre cell differentiation (red bracket; G). Intact fibre cells with missing basal alignment (red arrow; H). Pseudoepithelial cells (brown arrow; H).

All *in-vivo* records and the histology of the posterior lens of the $Trp53^{CKO}$ (Fig. 15, C+D+F+G+H) resembled a phenotype published by Wiley et al. [204]. This

PSCs

Table 10.: Phenotypes of ($Trp53^{WT/fx}$;$LeCre^{+/-}$ x $Trp53^{fx/fx}$) mice determined with Scheimpflug/OCT.

Sex	Phenotype	Occurrence	Frequency [%]
Males	No finding	87/156	55.7
	Published PT	14/156	8.9
	Total cataract	50/156	32.1
	Others	5/156	3.2
Females	No finding	87/135	64.4
	Published PT	7/135	5.2
	Total cataract	37/135	27.4
	Others	4/135	2.9

Phenotypes 4 months after birth. Published phenotype (PT) according to Wiley et al. [204]. Distinctive nuclear cataract or lens extrusion (Others). Frequencies rounded.

particular phenotype with posterior subcapsular plaques was seen in ~ 7.2 % of the investigated murine lenses (average of males and females), whilst males formed this phenotype a bit more frequently (Tab. 10). The anterior lens was characterised by signal-free areas (yellow star) and lateral scattering areas (yellow arrows). Those features were not explicitly mentioned by Wiley et al. [204]. Scattering in higher intensity and specific localisation was seen in the posterior lens (Fig. 6, D, yellow arrows). Minor scattering in the subcapsular and lateral area could be detected with the Scheimpflug camera (Fig. 15, B, yellow arrow). In histology, lenses appeared to be not misshaped (Fig. 15, C) because the posterior cortex seemed to be thinner and the nucleus to protrude posteriorly. The histological analysis revealed also that the signal-free area in the anterior lens was correlated to a big reservoir without inner structure (Fig. 15, E, red encircled area). The epithelial cells appeared to accumulate directly under the regular epithelial monolayer. The posterior lens was pervaded by swollen subcapsular fibre cells (Fig. 15, H). Above those irregular fibre cells, regular shaped fibre cells could not align at their basal ends with fibre cells from the opposite side and missed to form a posterior suture (red arrow). Overall, many swollen fibre cells carried still a nucleus of different degeneration stage, of which some appeared to be classically described Morghanian cells (red stars) in a later stage of nucleus degeneration within the more inner cortex (green stars). Those fibre cells came obvious from misled epithelial cells formed in a monolayer within the lateral posterior surfaces. From there, they differentiated untypically into Morghanian cells (red bracket).

Total cataracts

The excessive appearance of the described features reassembled a total cataract

(Fig. 16). Such a lens was characterised by an eccentrical shape exaggerating the posterior outgrowth as in the published phenotype (Fig. 16, C). Magnified, the lens disclosed a make-up of failed differentiating lens fibre cells (Fig. 16, D, red and green stars), pseudoepithelial cells pervading the entire lens (brown arrow), huge reservoirs of possible proteinaceous solutions (Fig. 16, F, black cross) and large obvious vacuoles. All together, this assembly led to total scattering in the Scheimpflug investigation (Fig. 16, B). Alterations were thus severe that only the anterior could be imaged in OCT (Fig. 16, A). This phenotype was seen four times more often than the published phenotype with sex-overarching frequency of 29.9 %, whereas the males displayed also a slightly higher frequency (Tab. 10).

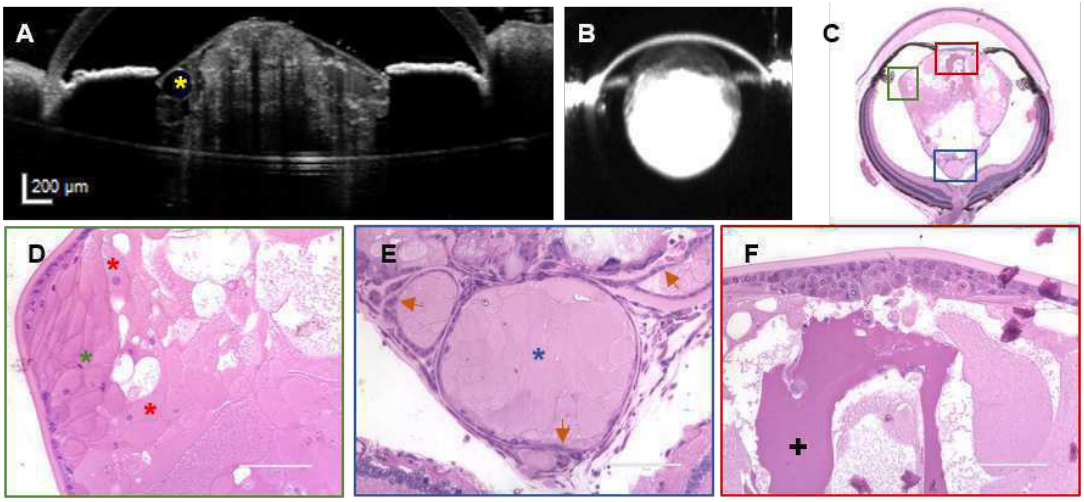

Figure 16.: *In-vivo* and *post-mortem* analysis of a $Trp53^{CKO}$ lens with a total cataract (4 months after birth). OCT image of the anterior lens **(A)**. Scheimpflug image **(B)**. Histological overview of the eye (4x) **(C)**. Lensbow in histology (40x) **(D)**. Posterior lens histology (40x) **(E)**. Anterior lens histology (40x) **(F)**. Scattering-free area in OCT (yellow star; A). Morghanian cells (red stars; D). Fibre cells with totally shrunken nuclei (green star; D). Swollen fibre cells enclosed by layer of pseudoepithelial cells (blue star; E). Reservoir of liquefied protein/ large fibre cell (black cross; F). Pseudoepithelial cells (brown arrow; F).

Rare phenotype

Very few lenses displayed very defined, pure nuclear scattering (not shown), and two lenses derived completely by forming a scattering fringe (Fig. 17, blue arrow) of which one lens developed also a possible lens extrusion characterised by material outside the lens (Fig. 17, yellow arrow), and an area of strongly increased scattering between the capsule and the fringe in the cortex (Fig. 17, red arrow). Overall, other phenotypes like the described above were seen in 3.1 % of the lenses.

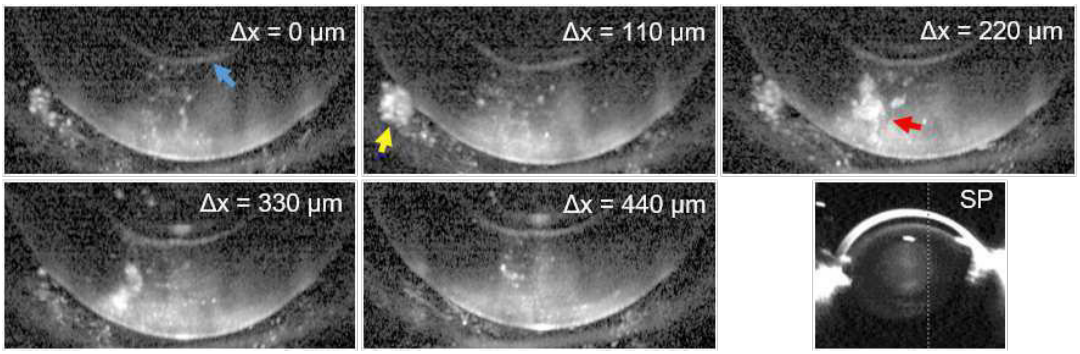

Figure 17.: OCT volume scan of an extrusion in a $Trp53^{CKO}$ lens (4 months after birth). Distance between single records Δx = 110 µm. Scattering fringe (blue arrow). Scattering material outside the lens (yellow arrow). Intense broad scattering area (red arrow). Scheimpflug image (SP).

Crystallin distribution

As mentioned in the introduction, crystallins of the lens are not homogeneously superposed. αA-crystallin (αA-cry) is higher expressed in the epithelium and in the outer cortex, while γ-crystallin (γ-cry) is not present in the lensbow, strongly expressed within the inner cortex and weak within the outer cortex. Lenses of the $Trp53^{CKO}$ mouse deviate from this natural stratification (Fig. 18, A). In the lensbow the distribution relations was more or less intact (Fig. 18, C): only αA-cry was expressed in the remnant of the epithelium, and both crystallins were colocalised in the transitional zone. The strong expression of αA-cry in the subcapsular zone was also obvious within the posterior lens (Fig. 18, D). The γ-cry signal was generally week, but differed not much within the cortex. Very different was the anterior cortex. Here, the crystallin expression was completely mixed up with strong αA-cry signals in the more inner cortex and quite strong γ-cry signals in the subcapsular region (Fig. 18, B).
As shown in histology, many fibre cells arrested differentiation and migrated with intact cell nuclei into the lens body. Interspersed DAPI-stained structures were observed in the anterior lens and subcapsularly accumulated.

Total cataracts of $Trp53^{CKO}$ mice could be very divers. A sample stained for the chosen set of crystallins was characterised by some features already introduced in the histology of this phenotype including overall polygonal lens shape and massive accumulation of migratory nuclei-containing fibre cell in the posterior lens

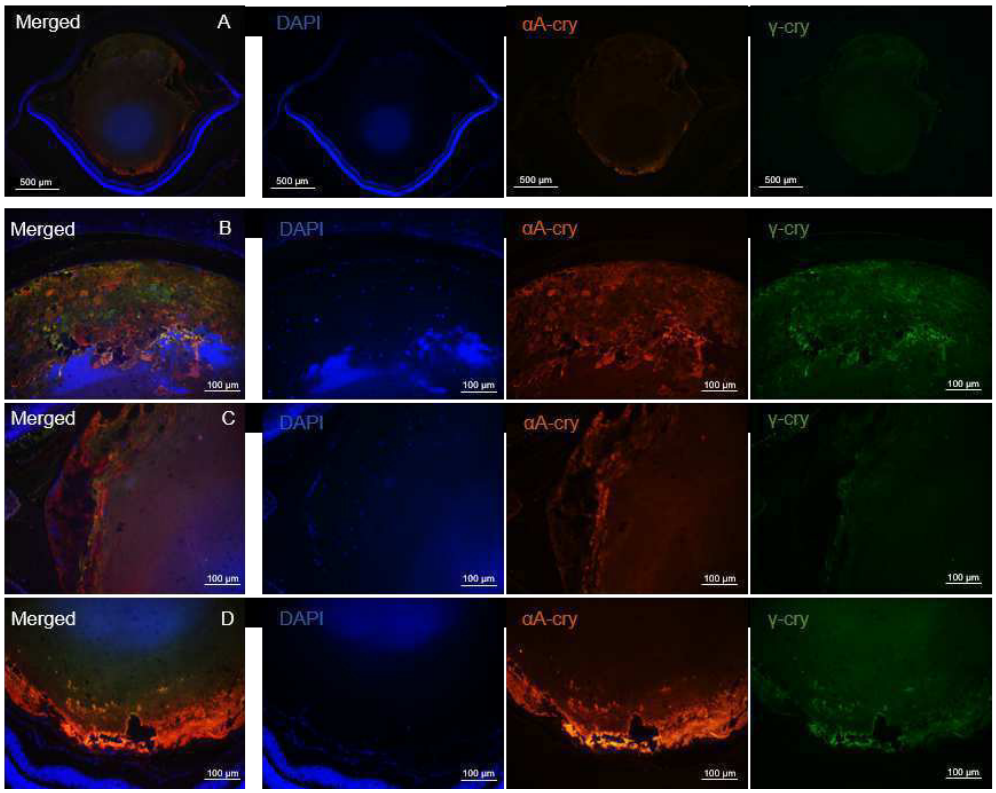

Figure 18.: IHC of *Trp53*^{CKO} lens with the published phenotype according Wiley et al. [204]. DAPI (blue), αA-crystallin (red), γ-crystallin (green). 4x-magnified entire eye **(A)**. 20x-magnified anterior lens **(B)**, 20x-magnified lensbow **(C)** and 20x-magnified posterior lens **(D)** of A.

(Fig. 19, A+B, merged). But there were also differences compared with the published phenotype. For instance, the anterior was not dominated by huge discernible fibre cells as in Fig. 18, B, merged, where several cells clearly had a predominant crystallin content. In the total cataract, such a differentiation was not recognisable and γ-cry was unusually present in the outer cortex. The posterior lens crystallin distribution was comparable with the posterior of the published phenotype (Fig. 19, B vs. 18, D). It was striking, though, that no γ-cry was detectable in the thick layer of accumulated nuclei-containing cell layers and, more importantly, that α-cry was also barely detectable.

Histology of a total cataract suggest the incursion of capsular material into the lens (Fig. 16, E). Testing on collagen IV (col IV), the main component of the lens capsule, confirmed that col IV is present inside the lens (Fig. 20, A). Beside in the clearly discernible lens capsule, col IV signal was strongly present in the chosen sample in

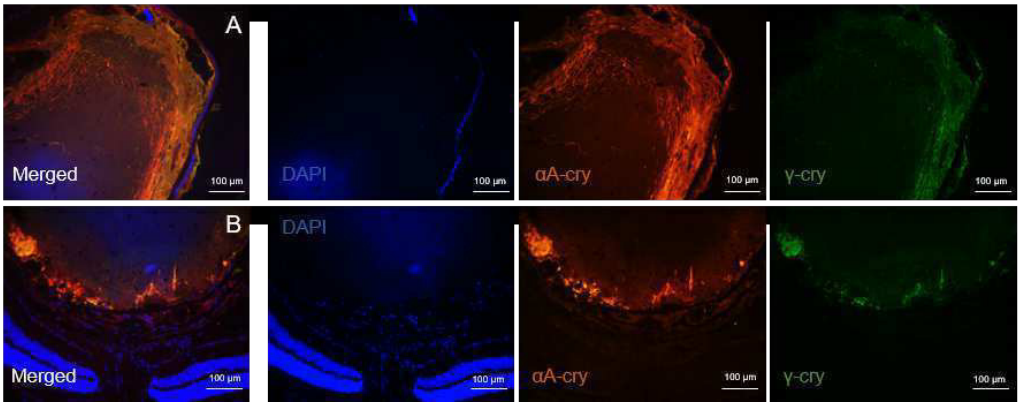

Figure 19.: Crystallin distribution in a total cataract of a $Trp53^{CKO}$ mouse lens. DAPI (blue), αA-crystallin (red), γ-crystallin (green). 20x-magnified anteriorly lensbow **(A)**. 20x-magnified posterior lens **(B)**.

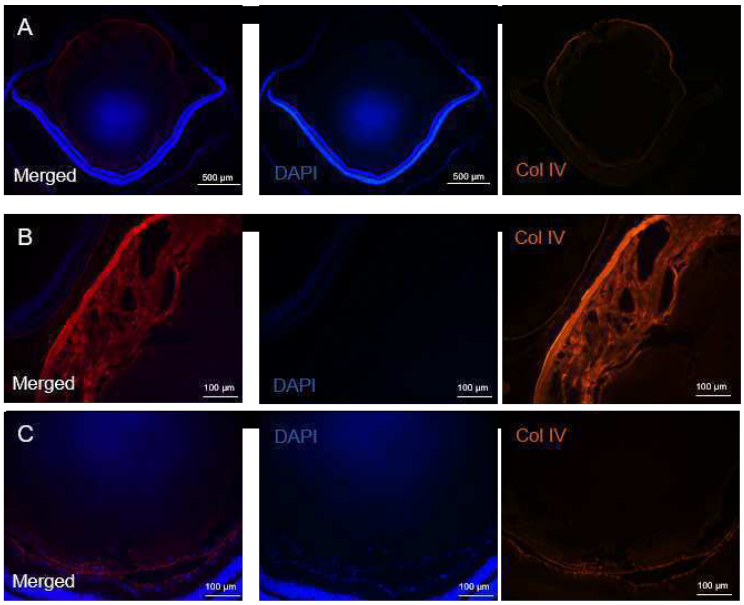

Figure 20.: Collagen IV distribution in a total cataract of a $Trp53^{CKO}$ mouse lens. DAPI (blue), collagen IV (red/orange). 4x-magnified entire eye **(A)**. 20x-magnified anterior lens **(B)** and 20x-magnified posterior lens **(C)** of A.

the more anterior cortex, but not as much as expected in the posterior lens (Fig. 20, B+C).

2

OPHTHALMOLOGIC *IN-VIVO* CHARACTERISATION OF IRRADIATED ADULT MURINE LENSES

This chapter strives to establish a purely physical categorisation of suture-associated lens alteration pattern observable via OCT in B6C3F1 mice. Accordingly, no biological conclusions will be drawn until in a later section (7.1) histological data could substantiate matching assignments.

2.1 COHORT-OVERARCHING PHENOMENOLOGICAL CATEGORISATION

Posterior alterations

The OCT monitoring of murine lenses revealed 4 distinctive phenotypes at the posterior lenticular pole, identified between 10.5 and 19.5 months following sham irradiation or exposure to low LET radiation (Fig. 21):

a. N-type (Normal)
b. S-type (Scattering)
c. SF-type (Scattering-free)
d. SF/S-type (Signal-free/ scattering)

Due to minimal changes at the clearly visible suture and only rarely appearing punctual scattering centre, the phenotype depicted in Fig. 21 A was assigned as 'N-type'. Despite being defined as normal, the lens in general is a natural scatterer and therefore never completely signal-free. That might be slightly different for a younger lens, but the basic principle is not affected. Significant alterations of the lens were identified as single or accumulated signal intensity increases. An example for such an alteration in the shape of a scattering plane coming from the subcapsular suture was given by the 'S-type' (Fig. 21, B). In clear difference, the 'SF-type' was characterised by a unique patch free of signal with almost no scattering boundary indicating the rest of the surrounding fibre cells (Fig. 21, C and see also volume scan in the supplemental data of [257]). This cavern was always found at the suture with little or evanescent distance to the capsule. Finally, the 'SF/S-type' represented a mixture of the S-type and the SF-type, combining a ragged, less round

cavern of signal depletion and structures of increased scattering within the cavern or surrounding it (Fig. 21, D).

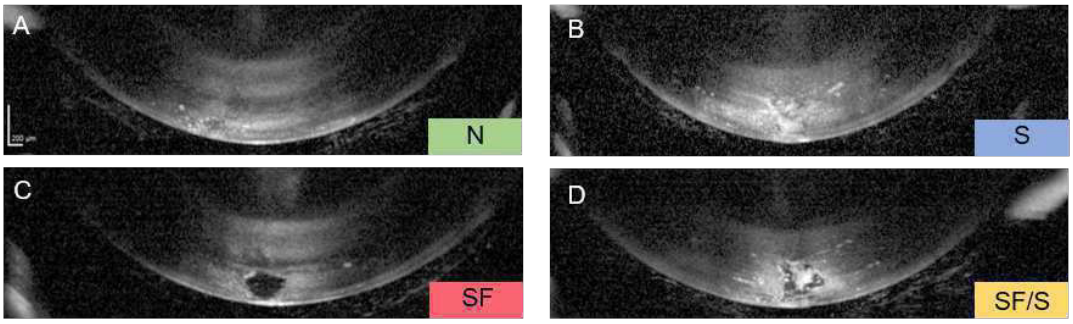

Figure 21.: Representative OCT-recorded posterior lens phenotypes in adult irradiated B6C3F1 mice. Normal phenotype (N) with no obvious alterations **(A)**. Scattering phenotype (S) with massive scattering centre occurrence **(B)**. Phenotype with signal-free (SF) area **(C)**. Combined phenotype (SF/S) with characteristics of the SF- and S-type **(D)**. Picture taken from [257].

Volume scans of the respective phenotypes facilitated further insight: The caverns of the SF-type took a space of approximately 150 µm * 400 µm * 500 µm (rostral/caudal * lateral/lateral * dorsal/ventral) and never carried an isle of signal-positive structures. On the other hand, scans of the SF/S-type proved that scattering-intense structures were apparently having little contact to the rest of the fibre cell bulk within the residual signal-free cavern (Fig. 22, between Δx = 104 µm and Δx = 416 µm).

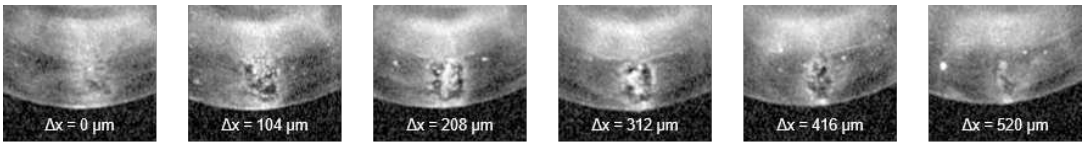

Figure 22.: Unfolded OCT volume scan of an SF/S-type lesion of a female WT irradiated with 1 Gy, beginning on the left side. Distance between the sections 104 µm. Please mind the typical dense signal isle between 208 µm and 312 µm.

Anterior alterations

Very similar to the posterior *in-vivo* types of peculiarities, alterations of the anterior outer cortex could be classified too (Fig. 23). Yet, three aberrations to the posterior phenotypes were observed (but only recorded in the 2 Gy cohort): firstly,

common scattering areas of the S-type (Fig. 23, B, red arrow) were more well defined than in the posterior cortex. While in the posterior S-type the surrounding of a scattering area was also partially scattering, the anterior S-type surrounding scattering signal was unsuspicious. The same applied for the SF/S-type (Fig. 23, D, red arrow). Secondly, alterations of the SF/S-type could appear deeper in the cortex than posterior alterations of the same type within the posterior cortex. Obviously, more or less intact lens material lied between the spot of alteration and the capsule, judged by the regular scattering level. Thirdly, in all samples examined, independent of the observed phenotype, a deep latent scattering layer in the perinuclear zone was observed; even in controls (Fig. 23, A-D, green arrows).

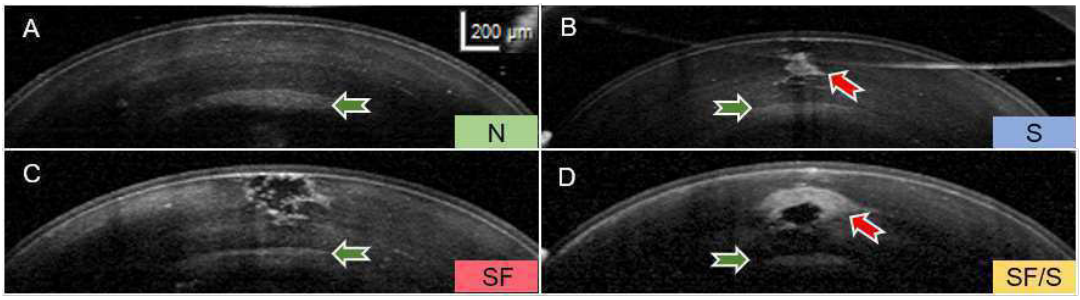

Figure 23.: Representative OCT-recorded anterior lens phenotypes in adult irradiated B6C3F1 mice. Normal phenotype (N) with no obvious alterations **(A)**. Scattering phenotype (S) with massive scattering centre occurrence **(B)**. Phenotype with signal-free (SF) area **(C)**. Combined phenotype (SF/S) with characteristics of SF- and S-type **(D)**. Signal-free area-associated scattering (red arrows). Deep cortical scattering (green arrows). Picture taken from [257].

2.2 DISTRIBUTION OF OBSERVED *in-vivo* PHENOTYPES

The large amount of surviving experimental mice allowed to summarise the very distribution of the enumerated *in-vivo* phenotypes.

Posterior distribution

A whole picture for the posterior changes was gained for all cohorts 18.5-19.5 months after irradiation (Fig. 24, A). One of the most striking difference was recognisable in comparison of controls and irradiation cohorts independent of sex or genotype: controls exhibited a lower fraction of the SF/S-type alteration (yellow bars), and exhibited across all groups a higher fraction of N-type lenses (green bars). This finding could be substantiated by calculation of the odds ratio for the SF/S-type. Indeed, those were significantly increased (Tab. 11, rows 10-12), whereas the 1 Gy cohort displayed the highest odds ratio for this type. The only other deviating odds

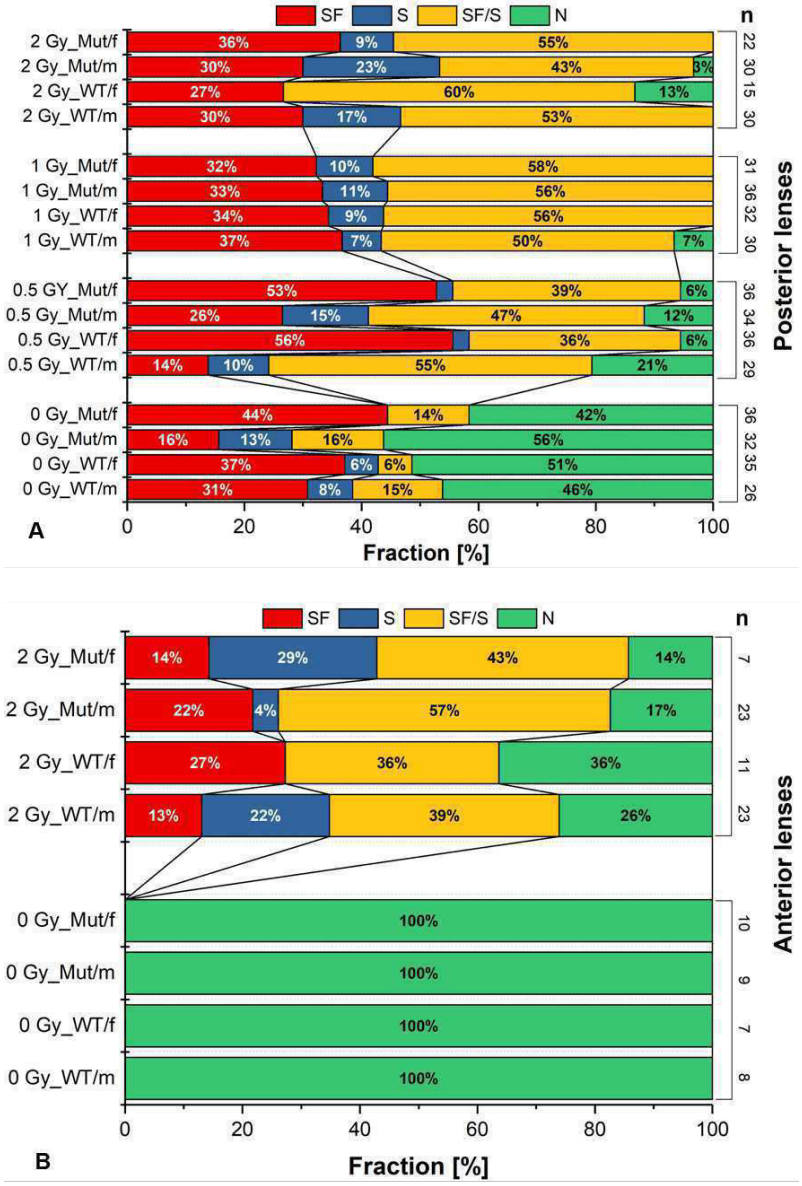

Figure 24.: Distribution of posterior *in-vivo* phenotypes in adult irradiated B6C3F1 mice. 18.5-19.5 months p.i. Fraction of the N-, SF-, S- and SF/S-phenotypes for every cohort **(A)**. Number of investigated lenses on the right side (n). Fraction numbers rounded. Distribution of anterior *in-vivo* phenotypes 18.5-19.5 months p.i. **(B)**. Fraction of the N-, SF-, S- and SF/S-phenotypes for every group of the 2 Gy cohort. Picture taken from [257].

ratio for another one of the three phenotypes standing for lens alterations, was found for the S-type in the 2 Gy cohort. Here, the odds ratio was 2.55. The fraction of N-type samples was roughly decreased by dose increase, but the difference was

highest in comparison to the sham-irradiated cohort (Tab. 11, rows 1-3).
It is noteworthy that the 1 Gy cohort displayed such a consistency of type distributions in each group, very much in contrast to the 0.5 Gy cohort which, besides the increase in the SF/S-type and the decrease of the N-type, displayed a group-specific distribution similar to the control cohort. The 2 Gy cohort derived also from the appearance of the 1 Gy cohort, but this could have been an effect of the higher mortality of the 2 Gy-irradiated mice and the subsequent shifts in lens *in-vivo* phenotype distributions. For instance, the female WT group was less than half the number than the female WT group irradiated with 1 Gy.

Table 11.: Odds ratios of posterior *in-vivo* phenotypes 18.5-19.5 months p.i.

Type	Comparison	Odds ratio	95 % CI	p-value
N	0.5 Gy vs. 0 Gy	**0.12**	0.06 - 0.22	< 0.001
	1 Gy vs. 0 Gy	**0.12**	0.003 - 0.069	< 0.001
	2 Gy vs. 0 Gy	**0.03**	0.01 - 0.11	<0.001
S	0.5 Gy vs. 0 Gy	1.2	0.46 - 3.16	0.69
	1 Gy vs. 0 Gy	1.55	0.61 - 3.93	0.35
	2 Gy vs. 0 Gy	**2.55**	1.02 - 6.35	0.04
SF	0.5 Gy vs. 0 Gy	1.29	0.78 - 2.15	0.31
	1 Gy vs. 0 Gy	1.07	0.63 - 1.79	0.79
	2 Gy vs. 0 Gy	0.92	0.52 - 1.63	0.79
SF/S	0.5 Gy vs. 0 Gy	**5.4**	2.93 - 10.23	< 0.001
	1 Gy vs. 0 Gy	**8.64**	4.61 - 16.2	< 0.001
	2 Gy vs. 0 Gy	**7.51**	3.89 - 14.5	< 0.001
Type	**Comparison**	**Frequency [%]**	**Odds ratio**	**p-value**
S+SF+SF/S	0 Gy	51.6	1	-
	0.5 Gy vs. 0 Gy	89.6	**8.25**	< 0.001
	1 Gy vs. 0 Gy	98.4	**60.6**	< 0.001
	2 Gy vs. 0 Gy	96.9	**29.9**	< 0.001

Odds ratios for every posterior OCT-based *in-vivo* phenotype of the irradiated cohorts in comparison to controls. Increased ratios in bold font. For every odds ratio the 95 % confidence interval (CI) and the level of significance was given. Modified table taken from [257].

Half of the controls had some sort of alteration at the endpoint (S-, SF- or SF/S-type). From this summarising perspective, 0.5 Gy were enough to significantly increase the odds ratio regarding the appearance of the aforementioned alterations (89.6 %, OD = 8.25).

Anterior distribution

Distribution of anterior *in-vivo* phenotypes was not congruent with the distribution of posterior phenotypes in the 2 Gy cohort 19.5 months p.i. (Fig. 24, B): every irradiated group possessed a comparable higher fraction of N-type lenses (Tab. 12). Accordingly, odds ratio were significantly small. Yet, the SF/S-type fraction formed here also the majority. Only a small number of female mutants could be investigated anteriorly, because almost every cornea was clouded which led to signal depletion in the anterior segment but not in the posterior one.

Table 12.: Odds ratios of anterior *in-vivo* phenotypes 18.5-19.5 months p.i.

Comparison	Type	Odds ratio	95 % CI	p-value
2 Gy vs. 0 Gy	N	**0.004**	0.0003 - 185.5	< 0.001
	S	10.2	0.57 - 182.3	0.11
	SF	16.442	0.94 - 286.6	0.055
	SF/S	**57.3**	33.6 - 975.7	0.005

Odds ratios for every anterior OCT-based *in-vivo* phenotype of the 2 Gy cohort (19.5 months p.i.) in comparison to controls (18.5-19.5 months p.i.). Increased ratios in bold font. For every odds ratio the 95 % confidence interval (CI) was given and the level of significance.

Due to the late start of lenticular OCT measurements, the exact onset of posterior or anterior alterations could not be determined and hence not the latency of phenotype formation. This uncertainty was suspended by histological analysis.

2.3 LESION DYNAMICS

Domagenesis

Posterior phenotypes described in Fig. 21 were not stable in nature. As juxtaposed in Fig. 25, alterations of the SF- or SF/S-type could change with age in a quite coherent way.

Starting from a signal-free area, first signs of increased scattering appeared rostral of the cavern and spread laterally, in parallel to the capsule and vertical to the suture (Fig. 25, B + F). Finally, the signal-free area disappeared or the SF-type changed at least to an SF/S-type. Because of the canonical path of formation, especially the appearance of the lateral scattering in form of a roof on top of the disappearing cavern, we designated this process δῶμαγένεσις (domagenesis). Domagenesis was not restricted to irradiated lenses and could also occur in controls (Fig. 25, D-F). Overall, 3.8 % of the controls and 5.5 % of lenses of irradiated mice displayed this dynamic process posteriorly, never anteriorly.

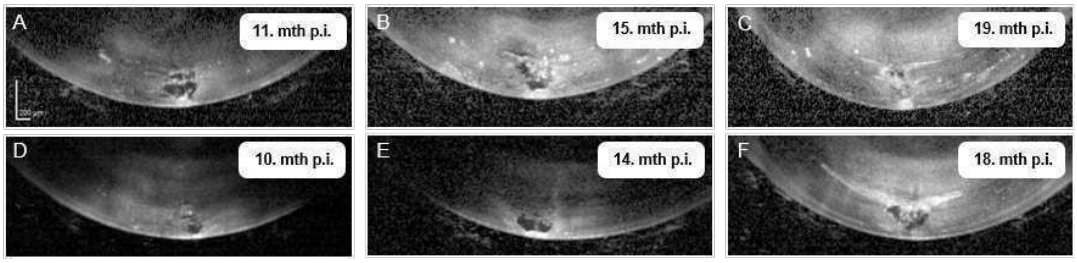

Figure 25.: Exemplified dynamic of posterior phenotypes within a period of 8 months. Male WT from the 2 Gy cohort **(A-C)**. Female mutant control **(D-F)**. Modified picture taken from [257].

PSFA

The development of the signal-free area in the posterior lens cortices was tightly connected with the process of domagenesis and the progression of SF- to SF/S-type lesions. As depicted for 17.5-18.5 months p.i., the posterior signal-free area (PSFA) was plotted for every applied dose (Fig. 26, A). All mean PSFAs (from SF- and SF/S-type) of every irradiation cohort were significantly increased in size compared to the controls. But between the radiation cohorts was no further difference discernible (as recognisable by comparison of the 95 % confidence intervals). Monitoring of the 2 Gy cohort allowed to determine whether the missing differences between the different irradiation cohorts was a lasting phenomenon (Fig. 26, B). Indeed, only 4 months earlier the PSFA of all groups of the 2 Gy cohort were significantly larger in size with the exception of the female mutants. This finding was clearly connected to the tendency for lesion fragmentation and domagenesis. Analysis of Fig. 26 A+B was conducted irrespective of association of the PSFA with an SF- or an SF/S-type alteration. If one separates PSFAs dependent on association, either with SF- or SF/S-type, the differences between controls and irradiation cohorts remains (Fig. 26, D). But it became also clear that there were no differences between the size of PSFAs in SF- or SF/S-types (notice overlapping CI).

ASFA

Only for the 2 Gy cohort a complete data set for the anterior signal-free area (ASFA) 18.5 months after irradiation could be gained (Fig. 26, C). Those ASFAs were coherently smaller than those of the posterior counterparts. In fact, average ASFA of all 4 groups was 0.011 mm^2, while the average PSFA of the 2 Gy cohort at the same time was 0.0245 mm^2 (red dotted line, $\approx$ median PSFA).

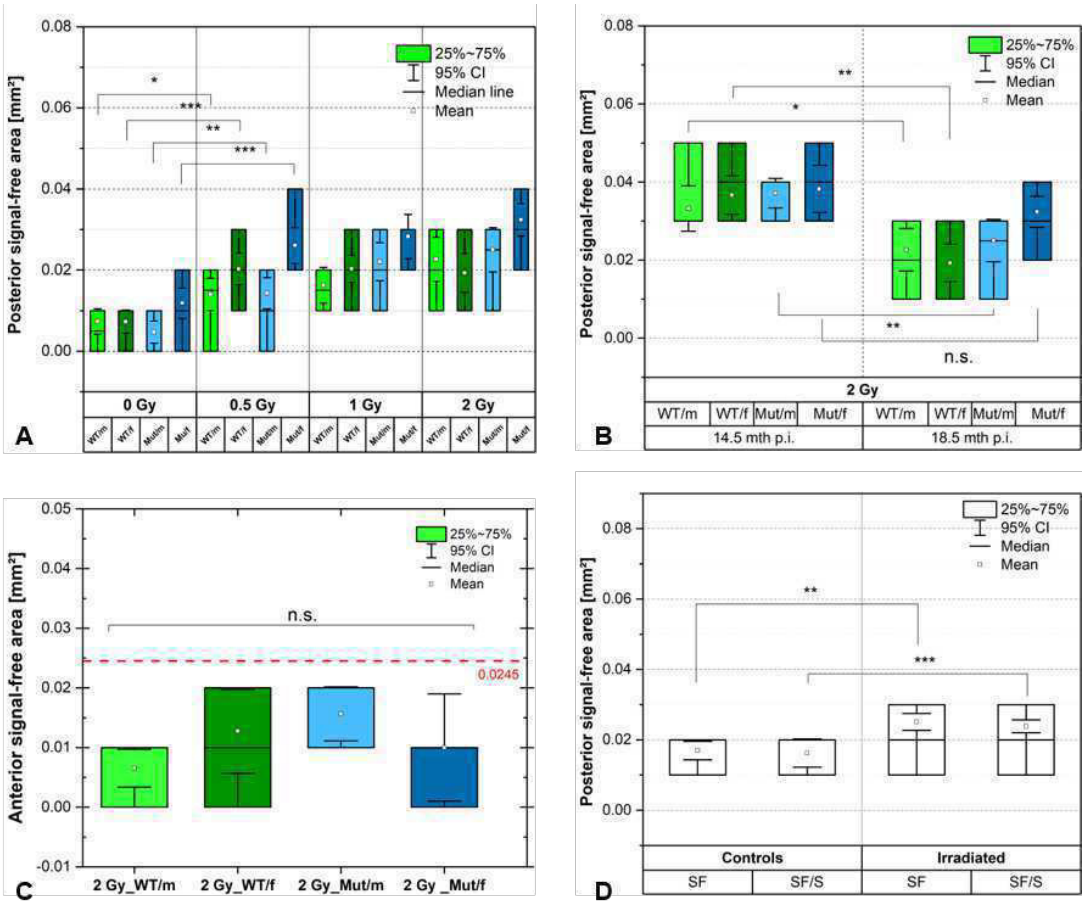

Figure 26.: Posterior signal-free area (PSFA) of all irradiation cohorts 17.5-18.5 months p.i. **(A)**. Comparison of PSFA of all groups of the 2 Gy cohort 14.5 and 18.5 months p.i. **(B)**. Anterior signal-free area (ASFA) of the 2 Gy cohort 18.5 months p.i. **(C)**. Red line indicates mean PSFA of the 2 Gy cohort 18.5 months p.i.. PSFA of all control and irradiated SF- and SF/S-type alterations **(D)**. Significances determined with Mann-Withney test (A, C, D) and paired t-test (B). Pictures A+C taken from [257].

2.4 IMPAIRMENT BILATERALITY AND SYMMETRY

C_{BLat}

Lenses of control mice were characterised by a small bi-laterality coefficient C_{BLat} (fraction of animals with an S-, SF- or SF/S-type in both lenses) below 0.4 (Fig. 27, A). Animals of the 0.5 Gy cohort lay in a range of 0.6-0.9. All groups of the 1 Gy cohort reached at least a level of 0.9. This degressive increase of laterality with dose was for 3 of 4 groups in the 2 Gy cohort enhanced or reproduced, but not for the female WT (dark green). If the degressive fit is some sort of guide, increase with

dose was strongest in females until a dose of 1 Gy.

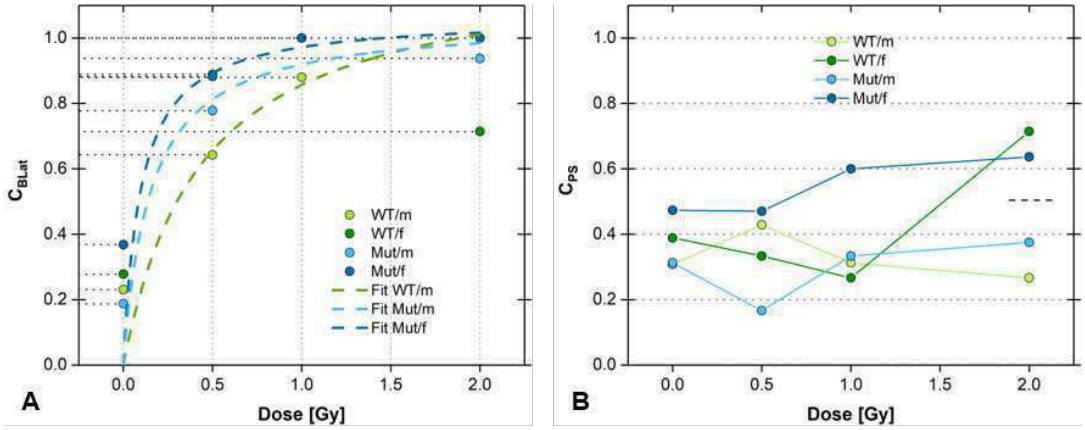

Figure 27.: Laterality and phenotype symmetry in adult mice dependent on dose and based on *in-vivo* data at the end of cohort lifetime. Laterality for all groups **(A)**. Phenotype symmetry for all groups **(B)**. Sex separation in the 2 Gy cohort (dashed black line).

If asked for the exact congruence of phenotype (e.g. SF/S-type in both lenses, but also N-type in both lenses), female mutants display until a dose of 1 Gy the highest value for the phenotype symmetry coefficient C_{PS} (Fig. 27, B). In the 2 Gy cohort female WT displayed the highest symmetry with a value around 0.7. A separation by sex in the 2 Gy cohort seemed to be existent (dashed black line).

C_{PS}

2.5 SCHEIMPFLUG MEASUREMENTS

Mean lens density of all cohorts increased within the observation time of 20 months after irradiation slightly from around 5 % to around 7 % (Fig. 28, A+B). The monthly recording of lenticular density revealed that this increase happened rather linearly with an apparent plateau-ish phase between 6 and 11 months. Fitting with linear regression, though, did not deliver a convincing regression coefficient. Polynomial fitting seemed to be the best choice, but was not substantiated by a plausible working hypothesis based on biological processes (not shown).

Lenticular density monitoring

Pooled densities of the last three months confirmed that none of the doses triggered a remarkable increase of lenticular density (Fig. 28, D). Only the mean density of the 1 Gy cohort was slightly higher than the control cohort mean (α = 5 %) and also higher than that of the 0.5 Gy cohort (α = 1 %). Maximum densities of controls and

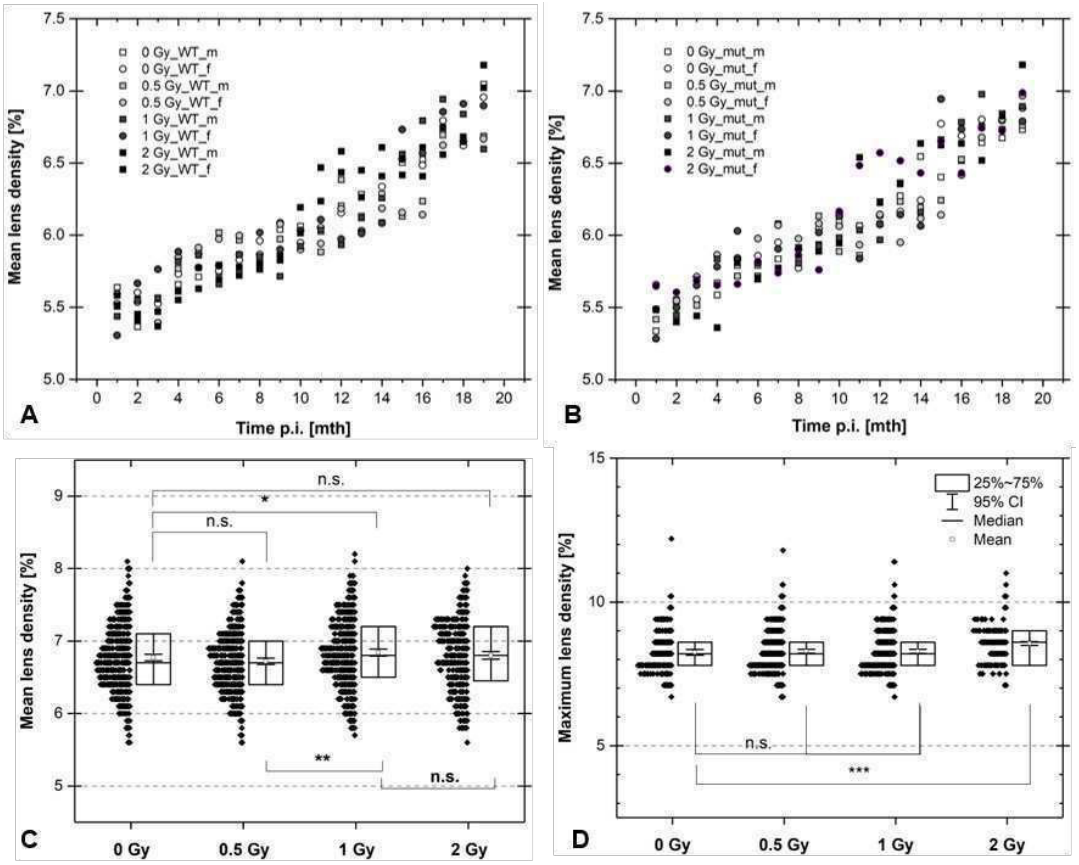

Figure 28.: Scheimpflug monitoring of mean lens density of irradiated adult mice. WTs **(A)** and mutants **(B)** separated by sex and genotype. Mean lens density of pooled cohorts 20 months p.i. **(C)**. Maximum lens density of pooled cohorts 20 months p.i. **(D)**. Significances determined with Mann-Withney test. Split dataset of D illustrated in [248].

the 0.5 and 1 Gy cohorts were almost identical (Fig. 28, D). A dose of 2 Gy triggered a highly significant increase of maximum density (with Mann-Whitney test). In contrast to the mean densities, the maximum densities followed not an acceptable normal distribution, but medians did not veer away from the mean maximum densities.

MANOVA

Applying a three-way analysis of variance (MANOVA) of the examined groups revealed that the factor dose had significant influence, but was in contrast to the Mann-Whitney test caused by a significant mean difference of the 0.5 Gy/1 Gy pair (Tab. 13). The factors genotype and sex had no influence, also not the interactions of two factors together, but the interaction of all three factors was signifiant ($p = 0.022$).

MANOVA for maximum values did not reveal a significant difference in the single factor analysis (Tab. 14). In contrast to the mean densities, also all three combined independent factor interaction had no explanatory power.

Table 13.: Main effects for murine **mean** lens densities determined by three-way ANOVA and Tukey *post-hoc* test at the end of observation time (pooled for 17.-19. month p.i.).

Factor	Level	Mean	ΔMean	p-value
Genotype	WT	6.77	-0.02	n.s.
	Mut	6.79		
Sex	Male	6.78	0	n.s.
	Female	6.78		
Dose	0 Gy	6.77	0.053 (0 vs. 0.5) -0.061 (0 vs. 1) -0.033 (0 vs. 2)	0.007
	0.5 Gy	6.71	-0.114 (**0.5 vs. 1**) -0.086 (0.5 vs. 2)	
	1 Gy	6.84	0.0027 (1 vs. 2)	
	2 Gy	6.82	-	
Genotype*Sex*Dose	-	-	-	0.022

Significant differences (Tukey test) are written in bold font. Two-way interactions not displayed. P-values refer to level-overarching significances. Model (DF = 15) p = 0.001.

Table 14.: Main effects for murine **maximum** lens densities determined by three-way ANOVA and Tukey *post-hoc* test at the end of observation time (pooled for 17.-19. month p.i.).

Factor	Level	Mean	ΔMean	p-value
Sex	Male	8.35	0.097	0.06
	Female	8.26		
Dose	0 Gy	8.29	0.005 (0 vs. 0.5) 0.006 (0 vs. 1) -0.04 (0 vs. 2)	n.s
	0.5 Gy	8.28	0.016 (0.5 vs. 1) -0.047 (0.5 vs. 2)	
	1 Gy	8.28	-0.049 (1 vs. 2)	
	2 Gy	8.39	-	
Sex*Dose	-	-	-	0.015

Three-way interaction not shown. P-values refer to level-overarching significances. Model (DF = 8) p = 0.037.

Only the two way interaction of sex and dose was significant (p = 0.015). Those results were of weak explanatory power because Levene's test proved that mean and maximum variances of the pooled samples were not equal (data set and ANOVA published in [248], notice differences in methodology and outcome, see discussion).

Clincal significance

Despite the fine differences between the cohorts, missing visible differences were quite obvious (Fig. 29, right). Nothing irregular was seen in the lenses 4 months after sham- and 2 Gy-irradiation in control and irradiated mice, apart from the reflection point (B+D) and also 16 months later nothing else besides the increased age-related nuclear opacification appeared in the lenses (C+E).

Subsequently, no cohort exceeded the nuclear opalescence threshold of a mean density of 9.7 % for controls (score $\leqslant$ 0.9) according the LOCS III system not to mention the threshold for a score 1.0 cataract at 10.5 % or a score 2.0 cataract at 14.1 % (Fig. 29, A). Low lens densities were not synonymous with defect-free lenses at all (see chapter 2.2).

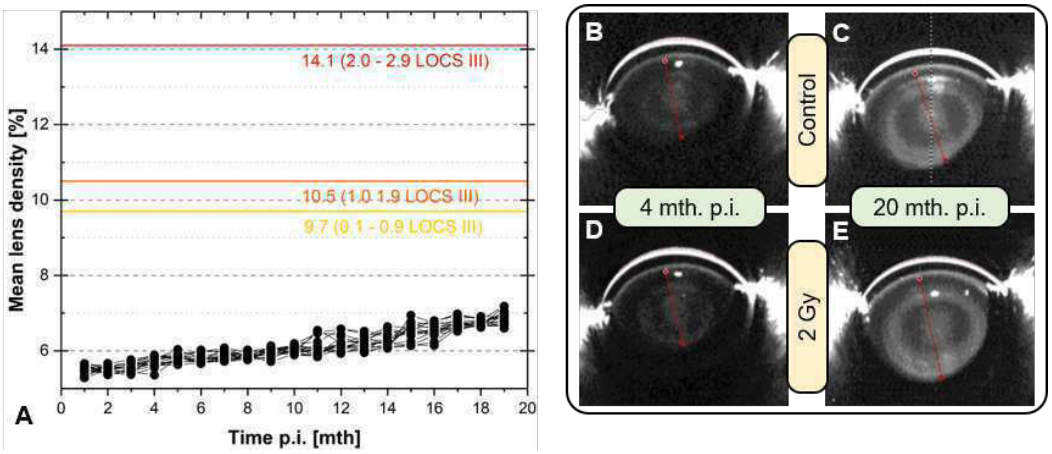

Figure 29.: Measured lenticular densities in comparison to LOCS III nuclear opalescence scores for normal human lenses, score 1.0-1.9 and score 2.0-2.9 cataracts **(A)**. Male WT examples of Scheimpflug images. Controls 4 and 20 months after sham-irradiation **(B+C)**. 2 Gy-irradiated lens 4 and 20 months p.i. **(D+E)**. Mind increased contrast of Scheimpflug images.

Fallacies

All Scheimpflug values presented in Fig. 28 and 29 were gained by measuring the lens with the bar tool. In doing so, the corneal reflection was avoided, but also every other opacification that seemed to be artificial. This was done because of a continuous missing cross evaluation method. As depicted in Fig. 30, A+B, such

suspicious opacification in Scheimpflug could be a real anterior alteration in the lens (Fig. 30, A+B, left pictures, red arrowheads). OCT served as cross-checking method (Fig. 30, A+B, right pictures), but was only used for the last measurement of the 2 Gy cohort. For consistencies sake, even those proven lesions were spared in the density analysis. The same applied for posterior transient signals in Scheimpflug imaging (Fig. 30, C+E, yellow arrowheads). Such phantom signals were recorded when the camera was not positioned exactly in the middle of the pupil but at the rim (Fig. 30, C+E, little frontal pictures on the upper right). Even if OCT (Fig 30, F) confirmed a lesion in the posterior part, the phantom signal was not included in the analysis, because we know from previous work that Scheimpflug can not detect the posterior cortices of mice (see Pawliczek et al. [195]). Picture D reflected the true conditions of the posterior inner cortex (measurement in the middle of the pupil). Therefore, all densities cited represented the processes of the bulk of the fibre cells without subcapsular alterations (which justified the comparison to the nuclear opalescence values according to LOCS III).

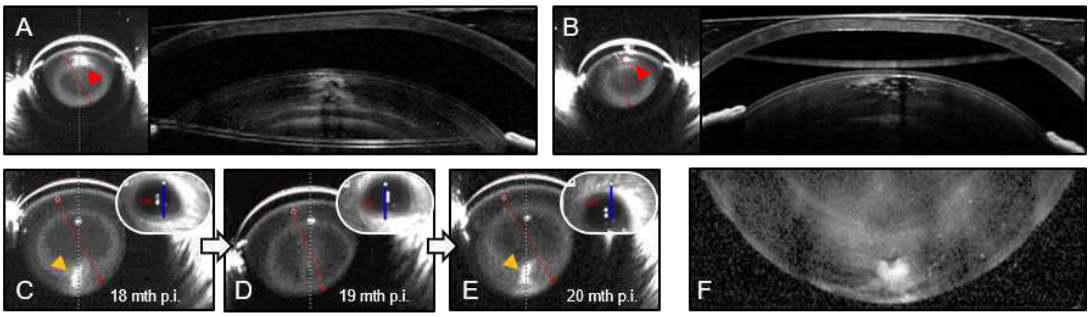

Figure 30.: Real and phantom signals in Scheimpflug imaging. Scheimpflug (left) and OCT images (right) of two eyes with real subcapsular lenticular alteration, 20 months p.i. **(A+B)**. Phantom signals **(B)**. Scheimpflug imaging of the same eye, 18 **(C)**, 19 **(D)** and 20 months p.i. **(E)**. Frontal picture of measured section in the upper right, yellow arrowheads indicate phantom signals. OCT of the same eye 20 months p.i. **(F)**.

Adjustments

Taken the information of the complementing *in-vivo* method OCT into account, an adjusted data set of lens densities could be created for the 2 Gy cohort alone. Here, analysis bars were laid through anterior opacification if they were confirmed via OCT. Such an adjusted mean density (SP/OCT) did not differ significantly from the non-adjusted (SP) though (Fig. 31, A).
Also the maximum density did not vary from the original data set (Fig. 31, B). A

huge amount of maximum densities in an excess range of absolute 30 % could not change the fact. One-way ANOVA of the mean density (factor evaluation), though, revealed a significant difference (p = 0.001). Anyway, Levene's test was positive. The same result was found for the maximum data ($p = 8*10^{-5}$).

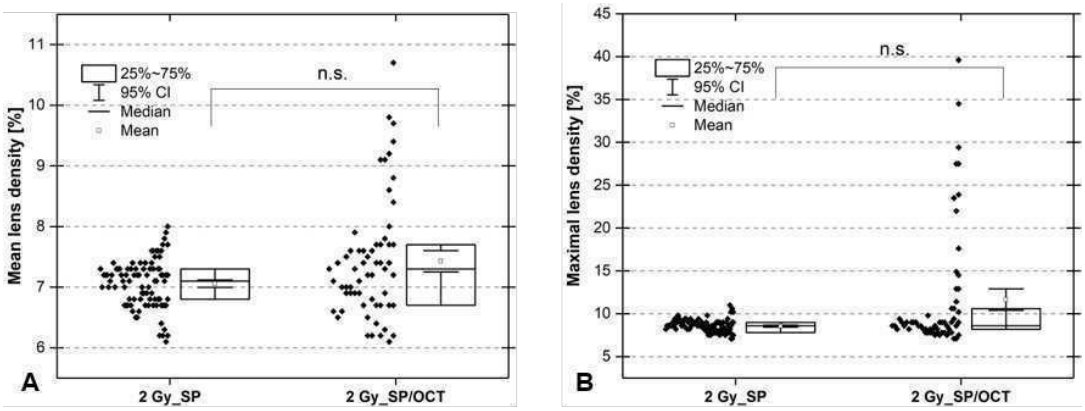

Figure 31.: Mean lens density of the pooled 2 Gy cohort, where putative phantom signals were avoided (SP) and lens density of the same cohort taking those signal in after cross-evaluation with OCT (SP/OCT) **(A)**. Maximum lens density according the same scheme **(B)**. Significances determined with Mann-Withney test.

OCT-adjusted data was of limited use to obtain a more realistic impression of mean and max lens density data because only 29,8 % (14 of 47 eyes displaying lesions in OCT) of the 2 Gy-Scheimpflug images were recorded perfectly mid-frontal to display the alterations which were proven by OCT to exist.

3

CHARACTERISATION OF IRRADIATED ADULT MURINE RETINAE AND CORNEA

3.1 RETINAL CHARACTERISATION

Retinae of adult mice irradiated with a dose of 0.5 to 2 Gy differed in appearance not a bit from control retinae of the same age. All layers in the *in-vivo* examination appeared to be regular in proportions (Fig. 32, A-D). Final data 19-20 months after sham- or γ-irradiation, edited by dose, however, displayed a small but significant difference in retinal thickness between control retinae and such irradiated with a dose whatsoever (Fig. 32, E). Hereby, mean retinal thickness was slightly increased in irradiated mice compared with controls (~ 2 µm). This difference was only significant because data was perfectly distributed according a normal distribution.

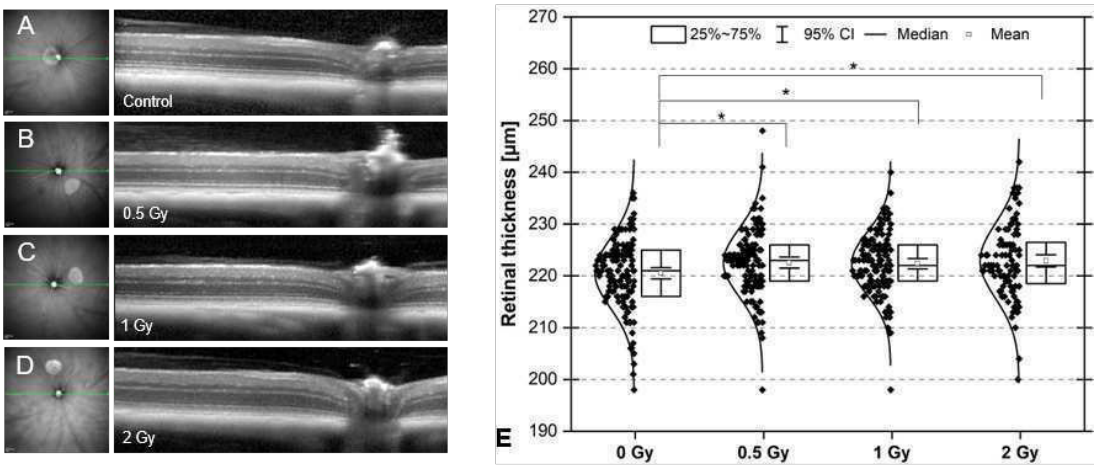

Figure 32.: OCT images of retinae taken 19-20 months p.i.; fundus picture and tomography at optic nerve level from male WTs. Control **(A)**. 0.5 Gy **(B)**. 1 Gy **(C)**. 2 Gy **(D)**. Mean retinal thickness of every cohort (pooled sexes and genotypes) at the end of the observation time 19-20 months p.i. **(E)**.

Data separation by sex and genotype did reveal hidden differentiation criteria (Fig. 33, A-D). Mean retinal thickness of every radiated group was within the

standard deviation of another irradiated or control group. The general reduction of retinal thickness from around 235 µm to around 225 µm was purely age-dependent. It was also a tendency that variations between groups disappeared and thickness became more and more equal (19-20 months).

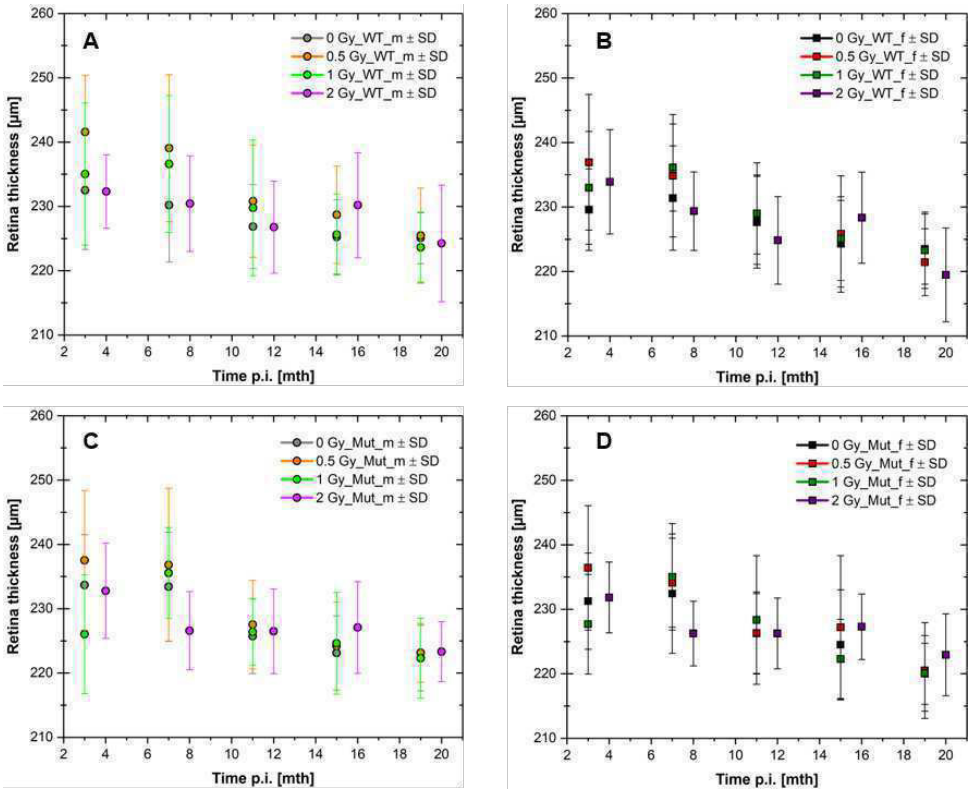

Figure 33.: Retinal thickness of adult mice monitored over up to 20 months. Male WTs **(A)**. Female WTs **(B)**. Male mutants **(C)**. Female mutants **(D)**. Whiskers represent standard deviation (SD).

3.2 CORNEAL CHARACTERISATION

Categorisation

Lenticular analysis with Scheimpflug was often hampered by corneal clouding. Corneal opacification could be classified roughly by 4 categories: normal corneae were completely clear and displayed only the typical reflection points (Fig. 34, A). Dependent on whether a possible opacification was placed at the edge of the pupil or in the centre of the pupil and, of course, dependent on their size, corneal clouding was classified. Minor opaque patches besides the optic axis were count with 1,

central opacification of minor or medium size were count with 2 and large patches in the centre with the value 3 (Fig. 34, B-D). The summed values of each eye of the mouse equalled the corneal index (CoI). A mouse with severe opacification in both eyes had a corneal index of 6.

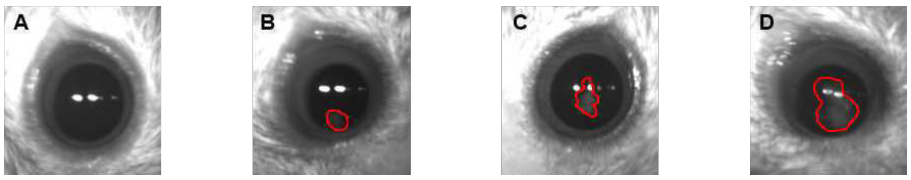

Figure 34.: Degrees of corneal clouding imaged with Scheimpflug camera. Normal cornea **(A)**. First appearance of minor opacification at the edge **(B)**. Minor or medium opacification at the centre of the cornea **(C)**. Large area of opaque cornea in the centre **(D)**. Red encircled area indicates opaque cornea.

Occurrence

General occurrence of corneal clouding was not restricted to irradiated mice. Up to a quarter of a control mouse group (e.g. female WT) could form such visible corneal alterations too (Tab. 15). By this, the fraction of mice is meant which

Table 15.: Corneal clouding occurrence in adult sham- and 0.5 to 2 Gy-irradiated mice.

Dose	Group	Frequency [%]	Mean CoI	Median CoI
0 Gy	WT ♂	8.3	0.25	0
	WT ♀	21	0.73	0
	Mut ♂	0	0	0
	Mut ♀	20	0.44	0
0.5 Gy	WT ♂	24.1	0.63	0
	WT ♀	52.7	1.86	2
	Mut ♂	27	0.76	0
	Mut ♀	61.2	2.57	2.5
1 Gy	WT ♂	21.8	0.5	0
	WT ♀	37.5	1	1
	Mut ♂	22.2	0.33	0
	Mut ♀	25	1	0.5
2 Gy	WT ♂	12	0.41	0
	WT ♀	0	0.42	0
	Mut ♂	14	0	0
	Mut ♀	95.4	4.27	5

Corneal clouding occurrence as fraction of every group eye number, mean and median corneal index (CoI) of adult mice 19-20 months p.i. (mice without corneal information in both eyes excluded). Modified table from [257].

displayed any kind of clouding in one or both eyes. The occurrence of corneal clouding and index seemed not to depend linearly on dose. In fact, frequency of corneal clouding in female WT and male mutants was lower in the 2 Gy cohort than in the other irradiation cohorts and in the female WT group even lower than in controls. Mean corneal index was also inconclusive. More robust was the median corneal index that was indeed only above 0 in groups of irradiated cohorts: Females of the 0.5 Gy cohort, female WTs in the 1 Gy cohort and especially female mutants in the 2 Gy cohort had a median index above 0. With 95.4 % of affected mice and a very high median corneal index of 5, the female mutants exposed to 2 Gy differed drastically of every other group.

Corneae of the 2 Gy cohort could also be investigated by OCT to evaluate the frontal pictures from the Scheimpflug recording. A normal cornea presented itself by a slightly scattering layer where the epithelium is supposed to be and a scattering unsuspicious stroma beneath (Fig. 35, A). As seen in form of gathered occurrence rates of corneal clouding in controls by Scheimpflug, opacification could appear as proven by OCT (Fig. 35, B, yellow arrowhead). Massive opacification was characterised by scattering layers below the epithelium in the upper part of the cornea (Fig. 35, C+D, yellow arrowheads). Cornea could severely affected with waved appearance (Fig. 35, D, blue arrowhead) and overall increased thickness. Additionally, transitional zone between pupil and sclera (limbus) was altered (Fig. 35, C, red arrowhead). This phenotype was only detected in irradiated mice. Corneal clouding had a huge importance for vision as lenticular areas depleted of signal suggested (Fig. 35, B, area between red bares).

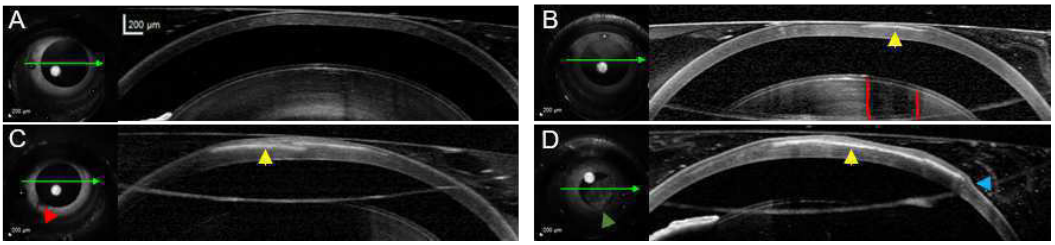

Figure 35.: Corneal clouding imaged with OCT. Control mouse cornea without any detectable clouding **(A)**. Control mouse cornea with minor opacification off-centre **(B)**. Massive opacification at the corneal centre of two irradiated mice **(C+D)**. Opacification (yellow arrowheads), waved cornea (blue arrowhead), limbus irregularity (red arrowhead), visible cornea alteration in frontal infrared picture (green arrowhead), area of signal depletion (area between red lines).

4

OPHTHALMOLOGIC *IN-VIVO* CHARACTERISATION OF IRRADIATED NEONATAL MURINE LENSES

4.1 PHENOMENOLOGICAL CATEGORISATION

Cortical alterations

In contrast to the mice irradiated at the age of 10 weeks, the mice irradiated at the age of 2 days (P2 mice) displayed almost only lenticular alterations in the inner posterior cortex. Those alterations were very different in type and magnitude. Samples with clear and regular appearance were assigned 'no finding' (Fig. 36, A). Irradiated mice displayed a crescent-shaped well-defined line of increased scattering in the inner cortex (perinuclear zone). This scattering sickle could be a fine line, barely recognisable as alteration but still obvious compared with control lenses (Fig. 36, D). This phenotype of a mild alteration was designated 'C1-type' (category 1). Increased scattering in the same area with a small central zone strong signal, apparently as a beginning double layer formation was designated 'C2-type' (Fig. 36, E).

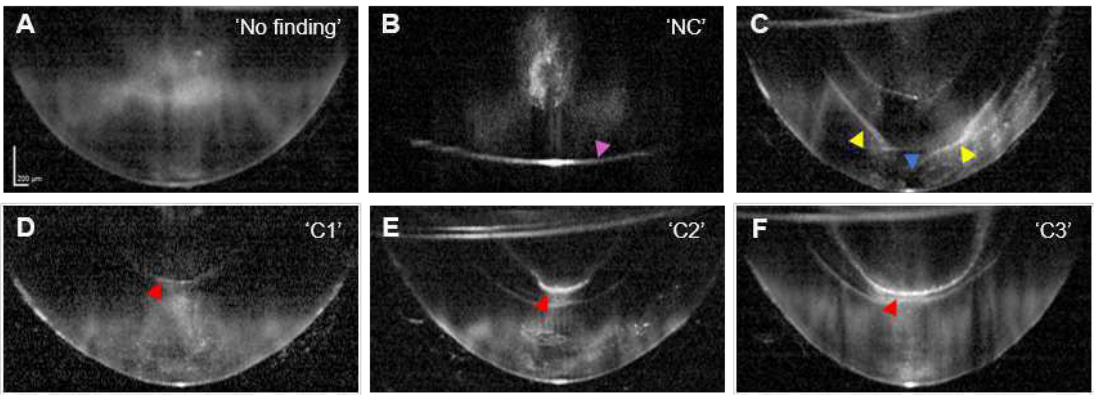

Figure 36.: Representative *in-vivo* phenotypes in lenses of neonatal irradiated mice 8.5 months p.i. Normal lens of a control **(A)**. Mild alteration **(B)**. Medium alteration **(C)**. Severe alteration **(D)**. Additional scattering structures **(E)**. Nuclear scattering **(F)**. Inner cortical alterations (red arrows), miscellaneous scattering (yellow arrows), posterior signal-free area (blue arrow). Modified picture taken from [258].

The severest form with strong signal along the entire sickle including double layers and signal stretching to both lateral perinuclear zones was designated 'C3-type' (Fig.

36, F).
In 2 of 160 cases the SF-type alteration - introduced in the adult mice section - was observed (Fig. 36, C, blue arrowhead) and miscellaneous scattering in a more or less sickle form but not within the inner cortex (Fig. 36, C, yellow arrowheads). Nuclear scattering in punctual forming was observed in 7 of 160 cases (Fig. 36, B). Some of these cases progressed to shrunken, totally scattering masses of liquefied lens material.

4.2 DISTRIBUTION OF OBSERVED CORTICAL *in-vivo* PHENOTYPES

γ-irradiated cohort

At least 87.5 % across the irradiated groups displayed cortical alterations of any type *in vivo* 8.5 months after irradiation, but none of the 154 surviving controls of any genotype or sex (Tab. 16). Clearly, the inner cortical alterations were irradiation- and not age-related. Only about 5 % of the irradiated animals displayed no cortical phenotype. Male mutants formed more often a C3-type than female WTs (Odds ratio = 2.86, p = 0.014). Overall, C1-, C2- and C3-types were observed in 94.4 % of the irradiated P2 mice (Odds ratio = 4800, $p \to 0$).

Table 16.: *In-vivo* lens phenotypes of P2 mice irradiated with 2 Gy of γ-radiation, 8.5 months p.i.

Dose	Group	No finding	C1	C2	C3
Controls	WT ♂	34	0	0	0
	WT ♀	36	0	0	0
	Mut ♂	40	0	0	0
	Mut ♀	40	0	0	0
2 Gy	WT ♂	1	14	12	11
	WT ♀	5	16	12	7
	Mut ♂	1	9	9	19
	Mut ♀	2	17	10	8

Phenotypes in OCT-based in-vivo investigation of P2 mice, 8.5 months p.i. with γ-rays. Occurrence of mild (C1), medium (C2) and severe (C3) inner cortical alterations in all lenses of every group (max 40 lenses per group). Modified table taken from [258].

X-irradiated cohort

All animals irradiated with X-rays displayed some sort of cortical alteration, but not a single lens was not affected (Tab. 17). This finding stood in contrast to the γ-irradiated mice (Tab. 16). Increased occurrence of the C3-phenotype male mutants

Table 17.: *In-vivo* lens phenotypes of P2 mice irradiated with 2 Gy of X-rays, 2.5 months p.i.

Dose	Group	No finding	C1	C2	C3
2 Gy	WT ♂	0	5	6	1
	WT ♀	0	10	2	0
	Mut ♂	0	1	5	6
	Mut ♀	0	5	5	2

Phenotypes in OCT-based *in-vivo* investigation of P2 mice, 2.5 months p.i.. with X-rays. Occurrence of mild (C1), medium (C2) and severe (C3) inner cortical alterations in all irradiated groups (max 12 lenses per group).

exposed to γ-rays was supported by the X-rayed animals of that group and was accompanied by decreased occurrence of C1-phenotype lenses.

4.3 IMPAIRMENT BILATERALITY AND SYMMETRY

Irradiated neonatal mice were characterised by high levels of damage bi-laterality (Tab. 18, left side). Whilst 95 % of the mutants formed a lesion of any type on both sides, only 85 % of the WT mice did so. These numbers matched the high coefficient of 2 Gy-irradiated P70 mice, 20 months p.i., whereas the WT mice fell out of line. C_{BLat}

Phenotype symmetry results deviated from the adult irradiated mice insofar as lenses of neonatal irradiated mice formed more lesions of the same type in both lenses (Tab. 18, right side). The symmetry coefficients of the female WTs and the male mutants were smaller, but still as high as the highest symmetric group of the irradiated P70 mice, the female WTs. It is mention-worthy that no animal of the 80 irradiated mice displayed a phenotype difference distance of more than one (e.g. C1-type in one and C3-type in the other lens). C_{PS}

Table 18.: Lesion bi-laterality and phenotype symmetry in γ-irradiated neonatal mice 8.5 months p.i.

Group	C_{BLat}	C_{PS}
WT ♂	0.85	0.9
WT ♀	0.85	0.7
Mut ♂	0.95	0.7
Mut ♀	0.95	0.85

Lesion bilaterality (C_{BLat}) and phenotype symmetry (C_{PS}) as fractions of entire groups.

In C2- and especially in C3-type lenticular alterations, fringe separation was immanent latest 5.5 months after irradiation (Fig. 37, A+B left). After 3 more months some scattering fringes split and one, two, or even three additional fringes appear beneath the original scattering sickle (Fig. 37, A+B right, red arrowheads). Those daughter fringes could overlap, creating the appearance of interfering waves. Because of the divergence of the original scattering front, we call this process hereinafter διάστασις (diastasis).

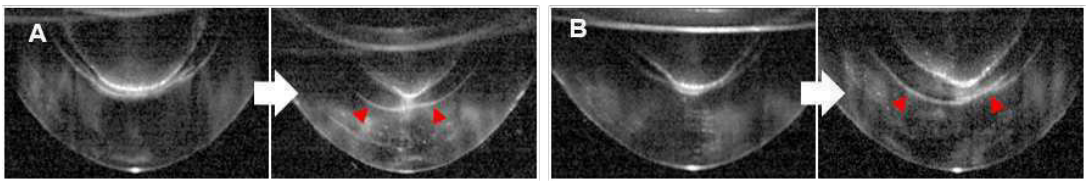

Figure 37.: OCT records of diastasis examples. White arrows symbolize a time step of 3 months from 5.5. to 8.5 months p.i. New appearing scattering fringes (red arrows). Modified picture taken from [258].

Diastasis happened at least in 37.8 % of the lenses of an irradiated group (male WT) and could happen on top in 59.4 % of the lenses (male mutants) (Tab. 19). Here, in C1-type alterations diastasis was less often observed than in C2- or C3-type alterations. Because of the high frequency of diastasis, we conclude that this process is the likely progression step of inner cortical lesions in irradiated P2 mice.

Table 19.: Fraction of samples displaying diastasis in irradiated P2 mice.

Dose	Group	C1 [%]	C2 [%]	C3 [%]	Total [%]
2 Gy	WT ♂	0	90.9	30	37.8
	WT ♀	13.3	75	100	48.5
	Mut ♂	22.2	100	57.9	59.4
	Mut ♀	29.4	90	62.5	55.3

Fraction of lenses displaying diastasis in every irradiation group. Modified table taken from [258].

4.5 EXTREME PHENOTYPES

Finally, lenses of P2 mice developed an additional severe posterior alteration (Fig. 38), a bolt-like line of increased scattering along or close to the suture connecting the inner cortical scattering fringe with the capsule (red arrows). This phenotype was detected in lenses with all three cortical alteration types and was not always perfectly recordable whole in one tomography (if not, volume scans proved the connection between the scattering fringe and the posterior pole). Increased directed scattering bolt was associated with an accumulation of scattering material outside the lens in the vitreous (Fig. 38, B, blue arrow).

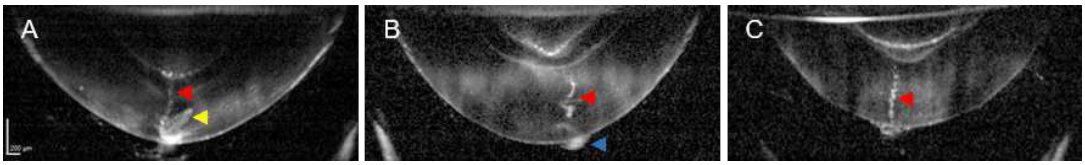

Figure 38.: Representative *in-vivo* examples of lenticular extrusion in irradiated neonatal mice, 8.5 months p.i. Scattering structure between scattering fringe and capsule (red arrowhead). Extralenticular scattering structure (blue arrowhead). Modified picture taken from the supplement of [258].

This severe phenotype was observed in every irradiated group with a frequency of at least 2.5 % (female mutants) and maximal 12.5 % (female WTs and male mutants, Tab. 20). Controls displayed never such a phenotype and only in 2 X-rayed groups similar cases were observed, but this result has to be framed by the fact of low numbers.

4.6 MEASUREMENTS *in vivo* WITH SCHEIMPFLUG IMAGING

General characterisation

Scheimpflug measurements supplied an additional *in-vivo* monitoring tool evaluation of OCT-based results of P2 mice. A regular lens of a control mouse was totally unsuspicious and nothing more was identifiable than the age-dependent contrast increase of nuclear and cortical lens zone (Fig. 39, A). Besides the few cases of nuclear scattering mentioned in section 4.1 and confirmed by Scheimpflug (Fig. 39, B), the inner cortical scattering was hardly recordable with Scheimpflug due to limited capability of the technique to image posterior cortical areas (Fig. 39, C+D). Scheimpflug imaging could reveal, though, that the inner cortical scattering was not

Table 20.: Lens extrusion frequencies in irradiated P2 mice.

Irradiation	Group	Extrusion occurrence	Frequency [%]
Controls	all	0	0
X-rays	WT ♂	1/12	8.3
	WT ♀	0/12	0
	Mut ♂	1/12	8.3
	Mut ♀	0/12	0
γ-rays	WT ♂	3/40	7.5
	WT ♀	5/40	12.5
	Mut ♂	5/40	12.5
	Mut ♀	1/40	2.5

Numbers of lenses of each radiation group displaying lens extrusion phenotypes. Modified table taken from the supplement of [258].

simply restricted to the posterior part, but could stretch to the anterior as well.

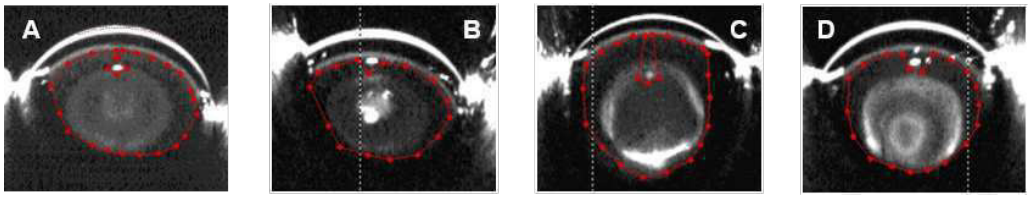

Figure 39.: *In-vivo* Scheimpflug images of phenotypes in P2 mice, 8.5 months p.i. Control lens **(A)**. Punctual nuclear scattering **(B)**. Inner cortical scattering **(C)**. Inner cortical scattering of severe type with beginning increase of nuclear scattering **(D)**. Mind increased contrast for depiction. Red encircled area was measured. Modified picture taken from [258].

Group perspective

Despite obvious alterations in the irradiated lenses, mean lens density of female and male WTs 8.5 months after irradiation was not differentiable from controls (Fig. 40, A). In both groups mean density remained below 6 %. The mean density value for female mutants was significantly increased but changes were marginal (relative increase of 4.6 %). Only the mean density of male mutants was strongly increased, but the group contained some drastic outliers (nuclear/total scattering).

For the maximum lens densities the picture changed (Fig. 40, B). All maximum densities of every irradiated group were significantly increased with the exception of the female WT. In all irradiated groups the median derived strongly from the mean. Lens alteration information gathered by OCT confirmed that only ~ 50 % of the Scheimpflug images covered the alteration actually there.

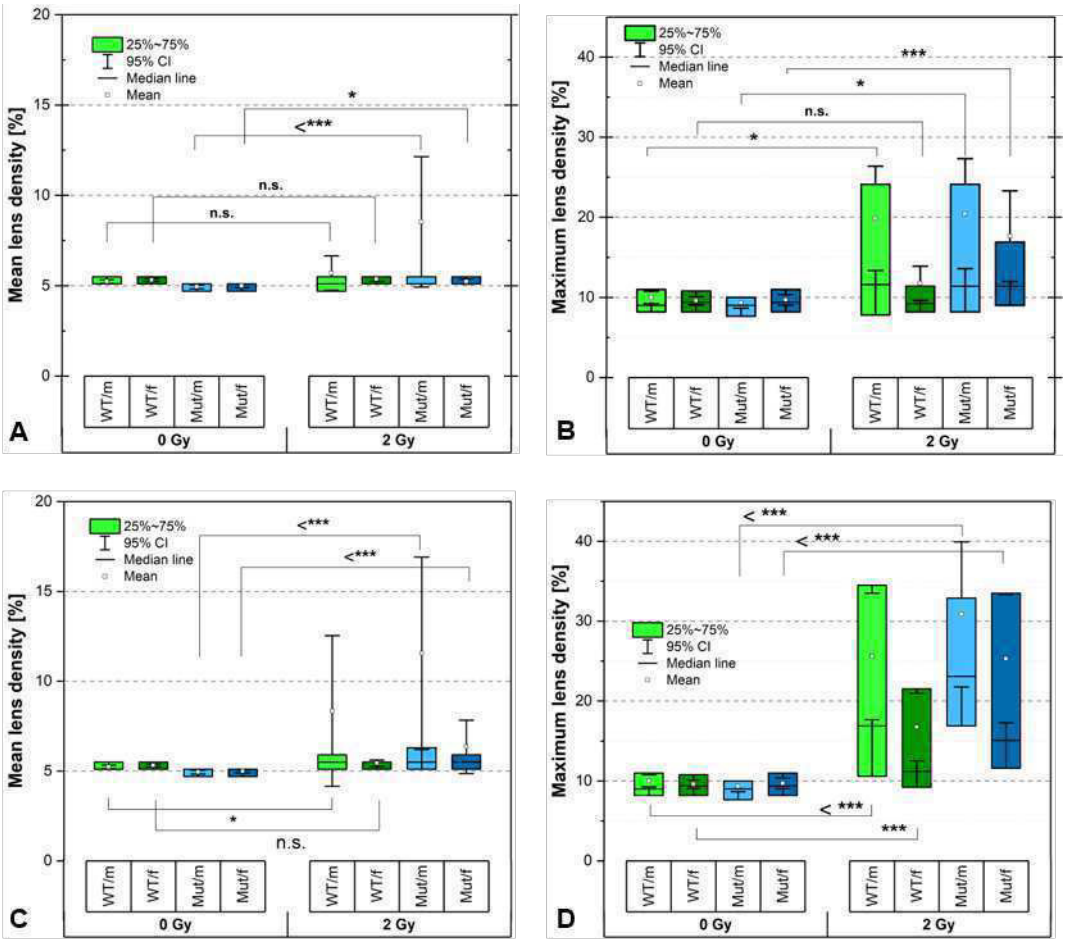

Figure 40.: *In-vivo* mean and maximal lens density determined with Scheimpflug in P2 mice 8.5 months p.i.. All values **(A+B)** and only with values were OCT-confirmed lesion were visible **(C+D)**. Mean lens density of all groups, 8.5 months p.i. **(A)**. Maximum lens density of all groups, 8.5 months p.i. **(B)**. Corrected mean lens density **(C)**. Corrected maximum lens density **(D)**. Significances determined with Mann-Withney test. Modified pictures A+B taken from [258].

Therefore, also those Scheimpflug values were analysed which actually displayed the lesion present or not as OCT-measurements insinuated. In contrast to the unselected data, only the mean lenticular density of the female WTs was not increased (Fig. 40, C). The controls and irradiated male WTs differed in this analysis significantly. In the analysis of corrected maximum lenticular density, all irradiated groups differed significantly, including the female WTs (Fig. 40, D).

Table 21.: Main effects for corrected **mean** lens densities of P2 mice (Fig. 40, C) determined by three-way ANOVA and Tukey *post-hoc* test at the end of observation time 8.5 month p.i.

Factor	Level	Mean [%]	ΔMean	p-value
Sex	Male	6.88	1.89	0.02
	Female	5.4		
Dose	0 Gy	5.11	-2.73	$8*10^{-4}$
	2 Gy	7.99		
Sex*Dose	-	-	-	0.014

Three-way interaction not displayed. P-values refer to level-overarching significances. Model (DF = 4) p = $2.8*10^{-4}$.

Table 22.: Main effects for corrected **maximum** lens densities of P2 mice (Fig. 40, D) determined by three-way ANOVA and Tukey *post-hoc* test at the end of observation time 8.5 month p.i.

Factor	Level	Mean [%]	ΔMean	p-value
Line	WT	14.38	-3.24	0.059
	Mut	15.82		
Sex	Male	16.71	3.65	0.034
	Female	13.43		
Dose	0 Gy	9.64	-15.01	$4.4*10^{-16}$
	2 Gy	24.76		
Line*Dose	-	-	-	0.035
Sex*Dose	-	-	-	0.033

Three-way interaction not displayed. P-values refer to level-overarching significances. Model (DF = 5) p = $3.3*10^{-15}$.

MANOVA

MANOVA of the corrected data revealed clear differences of the cohorts separated by the factors sex and dose. For the mean (p = 0.02) as well as for the maximum data (p = 0.034), density differences on a statistical level just below α = 5 % could be stated for the factor sex (Tab. 21 + 22). Far more drastic were the mean differences along the independent factor dose. The mean difference of the mean lenticular density between the controls (5.11 %) and the 2 Gy-irradiated mice (7.99 %) was highly significant (p = $8*10^{-4}$). The mean difference of the maximum lenticular density between controls (9.64 %) and 2 Gy-irradiated mice (24.76 %) was beyond consideration of a sample overlap (p = $4.4*10^{-16}$). In both ANOVAs

also the interaction of sex and dose was significant; for the maximum data also the interaction of line and dose.

4.7 LESION POSITION AND MIGRATION

Focus-dependent position

Since the first examinations of γ-irradiated neonatal mice with OCT were performed with a lower focus (D = 6.5 instead of D = 9.75), measures gained from those images might have been biased. To make further analysis sound, initial distances ($d_{initial}$) of focus-derived γ-cohort were compared with X-ray cohorts measured with the same focus as the γ-cohort 5.5 and 8.5 months after irradiation. Fortunately, potential distance measurement failures by significant differences between the cohort were not seen (Fig. 41). Therefore, every further correlation based on the initial distance measures was presumed to be sound.

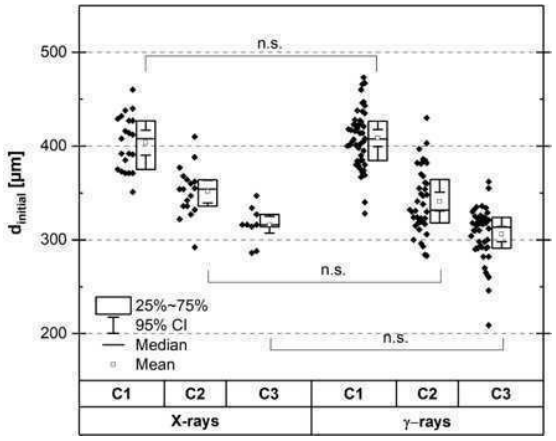

Figure 41.: Initial distances of lesion within X- and γ-irradiated neonatal mice at 2.5 months p.i. separated by lesion type. Significances determined with Mann-Withney test.

Positional shift

Cortical alterations in irradiated neonatal mice changed their position within the lens, either because of lens growth or compaction of the fibre cells, or both (Fig. 42, A-C). The distance of the lesion position was measured from the posterior pole to the inner scattering ring (especially important for consistency with occurring diastasis). As visible for the given example of a male WT after exposure to 2 Gy, the lesion started with a distance of 300 µm 2.5 months p.i., but was 436 µm away from the posterior pole 6 months later. This might be partially an explanation why Scheimpflug imaging could detect the alteration beginning with 5.5 months p.i.

Shifts of alterations within the lens were linearly dependent on their initial position at 2.5 months (Fig. 42, D) with correlation coefficients of over 0.8. The slope of the fitted data 5.5 months p.i. (black) was steeper than later at 8.5 months p.i.

(green). We conclude that shift of lesion position was higher for lesions starting at a shallower position measured from the posterior end in this period than for those which started relatively deeper in the cortex.

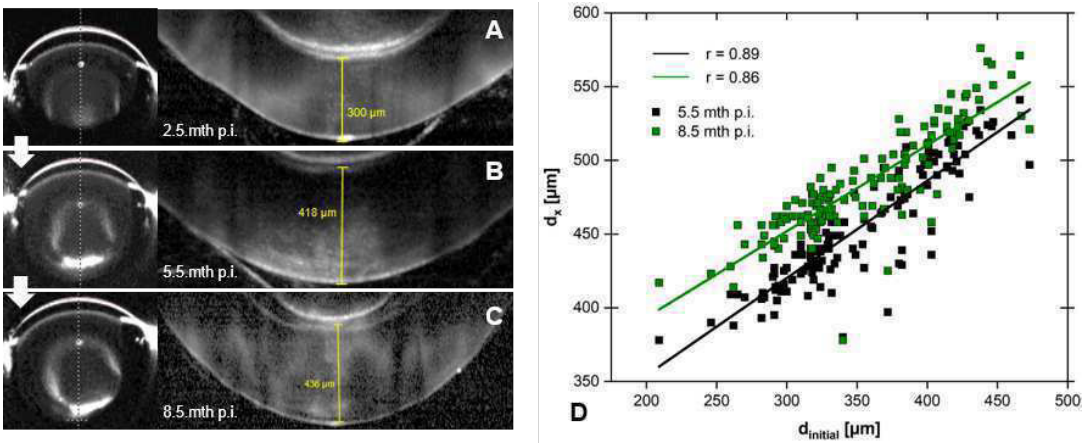

Figure 42.: Positional shift of a cortical lesion in time displayed in lenticular OCT and Scheimpflug for the same lens over time, 2.5 months p.i. **(A)**, 5.5 months p.i. **(B)** and 8.5 months p.i. **(C)**. Yellow bars indicate distances of cortical lesions to posterior pole. Position of every lenticular lesion at 5.5 months (black) and 8.5 months (green) vs. initial position at 2.5 months **(C)**.

When the entire shift within the observation time (Δd_{end}) was plotted against the initial position at 2.5 months p.i. ($d_{initial}$), this observation was supported by an fairly overall indirect correlation (Fig. 43, A). Furthermore, the labelling of every data point according to the lesion type classification (Fig. 36, B-D) revealed a substructure of the data set. Initial position and lesion shift within the observation time was dependent on the lesion type (Fig. 43, A). The former more than the later, because, although it was obvious that the more severe the lesion the closer it was to the posterior pole, it was also clear that the dependency with the lesion shift was only strong for the C2-type alterations (blue dots, R = -0.79). The weakest dependency of total lesion position shift with initial position displayed the C1-type lesions (black dots). Altogether, lesion shift within 6 months was around 100 µm for C1-types and around 180 µm for C3-types (Fig. 43, B). This analysis also strongly supported the decision to differ between C2- and C3-type lesions.

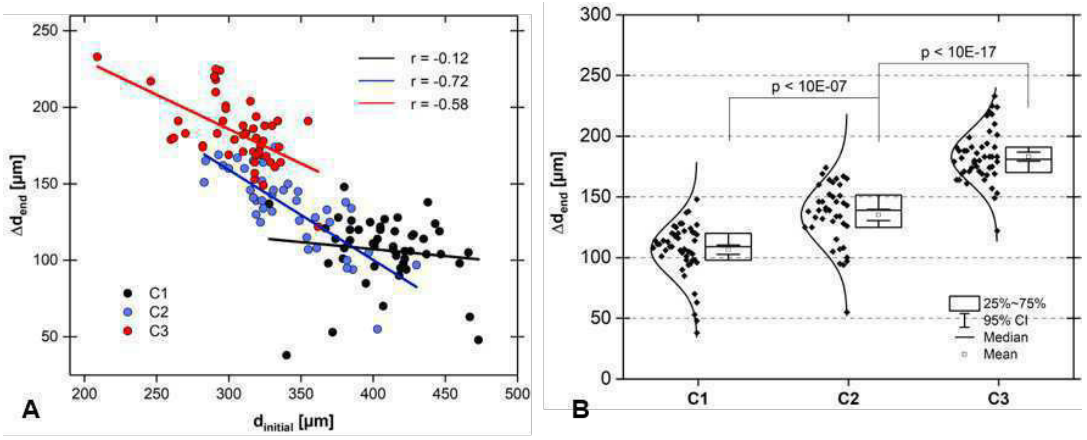

Figure 43.: Final position of cortical lesion at 8.5 months p.i. vs. initial posterior position at 2.5 months p.i. **(A)**. Average shift of every lesion sorted by lesion type **(B)**. Significances determined with Mann-Withney test.

5

OPHTHALMOLOGIC *IN-VIVO* CHARACTERISATION OF IRRADIATED NEONATAL MURINE RETINAE

Retinal thickness

With the first measurements 2.5 months after irradiation, clear differences between controls and irradiated mice were obvious (Fig. 44, A). Retinae of irradiated mice displayed a thickness reduced by at least 45 %. The effect was so strong that the data did not overlap at all. This reduction of mean retinal thickness continued with ageing in controls and within irradiated mice, until the thickness of irradiated retinae was reduced to maximal 42 % of the controls at the same age.

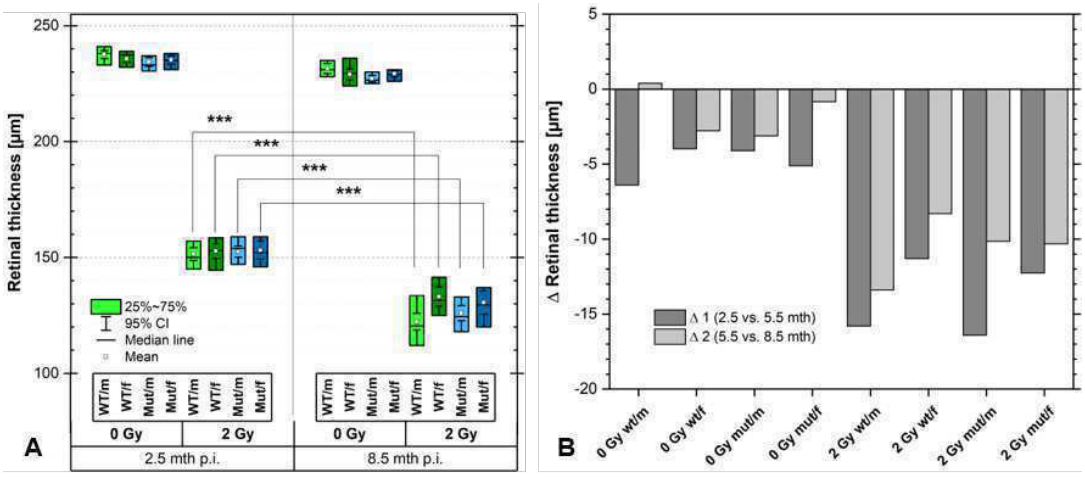

Figure 44.: OCT-based measurement of retinal thickness of irradiated neonatal mice (single retina analysis). Comparison of control and 2 Gy-irradiated cohort, 2.5 months p.i. vs. 8.5 months p.i. **(A)**. Differences of retinal thickness between every measurement taken **(B)**. Significances determined with paired t-test. Modified picture taken from [258].

This additional gap between control and irradiated murine retinae expressed in orientated differences (Fig. 44, B) was consistent for all groups and it could be forecasted that the thickness differences would have increased by progression in time, although the effect might slowed down as predictable by comparison of $\Delta 1$ and $\Delta 2$. Some controls stopped to shrink further in average (e.g. male WTs).

Atrophy variance

Retinal thickness in irradiated mice was not homogeneously reduced over the entire tissue. Some spots were much more affected (Fig. 45, compare B with C). In general, the reduction in thickness was obviously deducible from a thinner inner nuclear, outer nuclear and IS/OS-layer. Some spots of the retina were virtually indented (Fig. 45, C, red marked section). At these spots, the neuroretina seemed to be composed only of the ganglion cell layer, the inner plexiform and nuclear layer. In direct comparison with the control retina (Fig. 45, A) and a segment of the same irradiated retina (Fig. 45, B), a remarkable change was also discernible below the photoreceptor layer; the fine structure of the retinal pigment epithelium seemed to have collapsed (yellow arrowhead supposed to be Bruch's membrane).

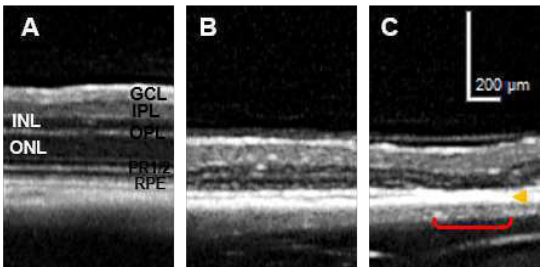

Figure 45: Close-up of retinae 8.5 months after sham **(A)** and 2 Gy-irradiation **(B+C)**. Red brace indicates indented spots of the irradiated retina. Yellow arrowhead indicates RPE collapse. Mind increased contrast and sharpness due to post-measurement editing.

Fundus analysis

The fundus of 8.5 months-old control mouse eyes were generally characterised by an almost regular grey value distribution with the typical better illuminated centre of the infrared picture (Fig. 46, A). Coming from the optic cup, several thick superficial vessels spread into the periphery of the retina (green arrowhead).

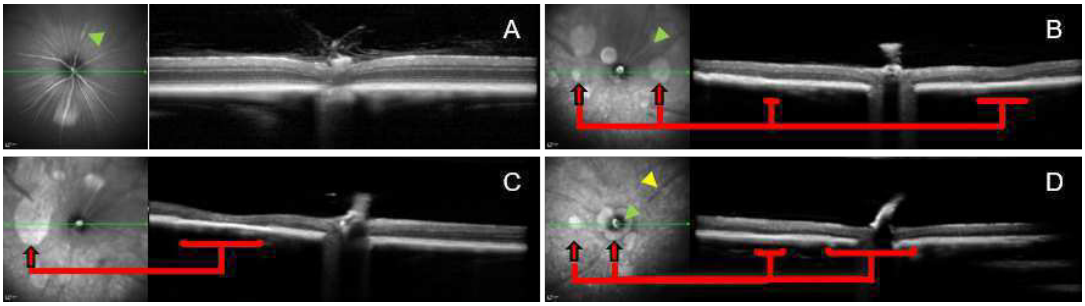

Figure 46.: Possible spots of retinal atrophy imaged with OCT (fundus pictures taken in infra-red modus). Control retina **(A)**. Spread spots of retinal atrophy **(B)**. Large spots of retinal atrophy **(C)**. Retinal atrophy around the optic coup **(D)**. Red arrows indicate highlighted spots in retinal sections. Modified picture taken from [258].

Fundus analysis of irradiated mice was very surprising (Fig. 46): The entire fundus of irradiated mice was patched with bright combs of increased infrared absorbance. Some spots stood out with a sharp-edged white patch appearance (Fig. 46, B-D, red arrows). Those patches revealed themselves as the retina indentations seen in Fig. 46, C. Basically, the spots were distributed over the entire fundus, but some were conspicuously regular and closely associated with the optic nerve (ON) (Fig. 46, D). The blood vessels displayed a variant occurrence. Sometimes they spread quite far (Fig. 46, B, green arrowhead), or vanished almost completely only with stumps very close to the ON ending (Fig. 46, D, green arrowhead). This was quite paradox, because one should expect no co-localisation of vessels and atrophied retinal segments. Lastly, the fundus was sometimes crossed by black furrows that could not be identified by educated advisers (Fig. 46, yellow arrowhead).

ONLA

ON-associated retinal atrophy was never seen in controls and was highly characteristic for the irradiated mice (Fig. 47, A). First indications of appearance were

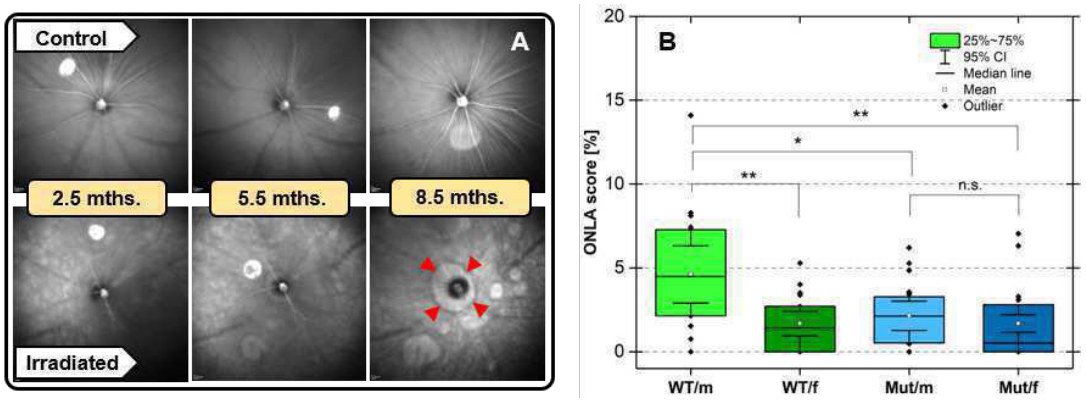

Figure 47.: Fundus analysis and optic nerve-associated lesion area. Fundus changes in controls (top) and 2 Gy-irradiated mice (bottom) **(A)**. ONLA (ON-surrounding retinal lesions area) score of each irradiated mouse) **(B)**. Significances determined with Mann-Withney test. Modified picture taken from [258].

recorded 5.5 months p.i.. This point of time marked also the first appearance of lesions on the rest of the fundus. ON-associated lesion could reach 3 months later remarkable areas of the fundus (Fig. 47, A, red arrowheads). Measurements at this time revealed that the mean size of those lesions ONLA (ON-surrounding retinal lesions area) took up to ~ 5 % of the fundus area in male WT (Fig. 47, B). This value was significantly higher than the ONLA across all the other irradiated groups. Males

were more prone to develop ON-associated lesions of any size 8.5 months p.i. (78 % in WT, 66 % in mutants). Females developed less frequently this retinal phenotype (51 % in WT, 46 % in mutants), which renders the difference between female WT and mutants as the highest.

6

VISUAL ACUITY OF INVESTIGATED COHORTS

6.1 METHODOLOGICAL REASSURANCE

Since a further set-up for automatic measurement of visual acuity was available (see methods chapter 2.4), opportunity was used to compare values determined with the manual approach by means of control mice (Fig. 48, VD2, 13 months p.i.). Automatically determined values fitted plausible into the framing data of manually examined mice (VD1). Mean spatial frequencies of mutants were slightly higher than of older manually examined mice, but the confidence intervals overlapped.

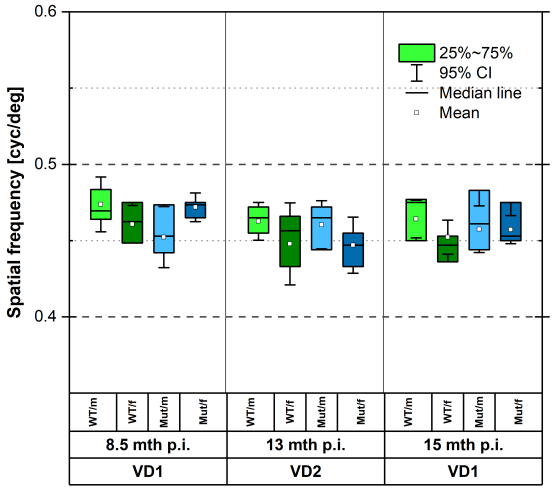

Figure 48: Virtual drum comparison with B6C3F1 control mice. Manual determination of control visual acuity with virtual drum 1 (VD1) at 8.5 and 15 months after sham-irradiation. Automatic determination of visual acuity with virtual drum 2 (VD2) 13 months after sham-irradiation.

6.2 VISUAL ACUITY OF IRRADIATED ADULTS

Factor dose

Applied doses of γ-radiation had a measurable effect on the visual acuity of mice determined by the spatial frequency of examined mice in the virtual drum (VD1). Already a dose of 0.5 Gy reduced the spatial frequency of mice irradiated as young adults significantly by relatively 10 % (Fig. 49, A). Between mice irradiated with 0.5 Gy and 1 Gy was no significant difference discernible, but again between the 1 Gy and 2 Gy cohort. The relative difference between mean spatial frequency of controls

and the 2 Gy cohort was 24 %.

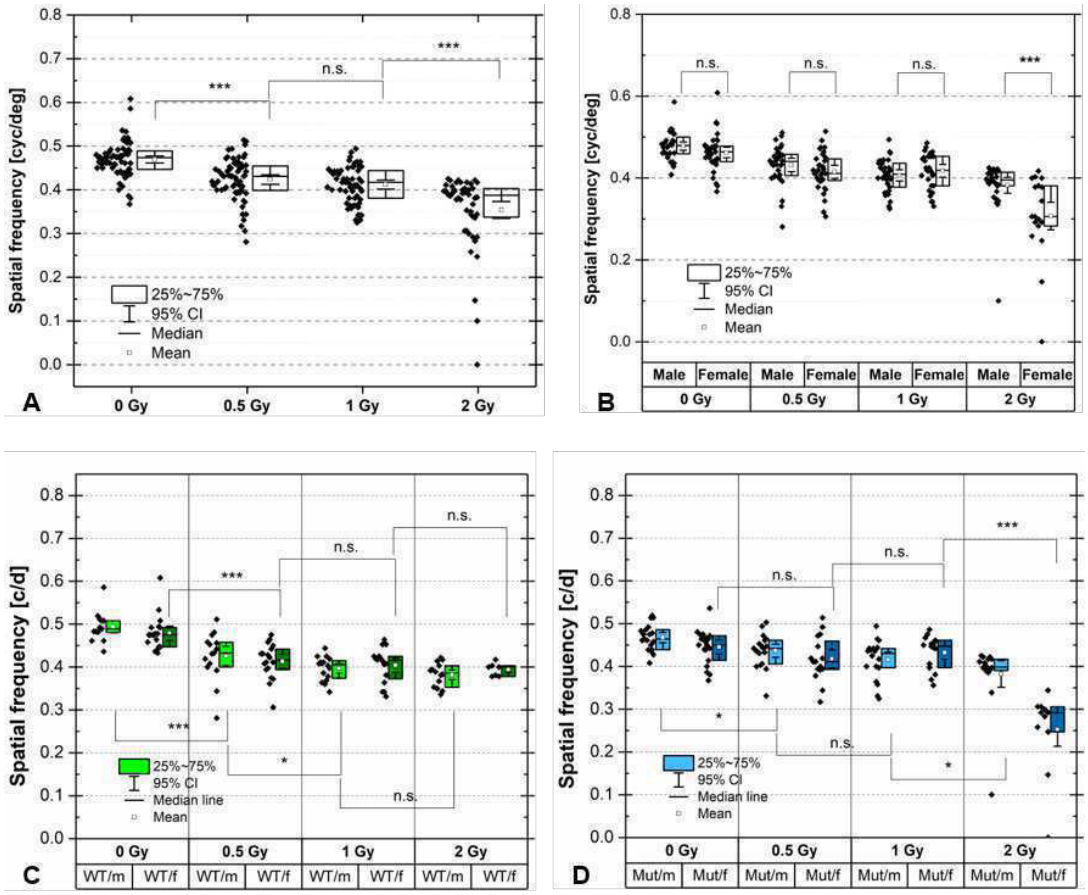

Figure 49.: Spatial frequency of irradiated P70 mice 20 months p.i., sorted by dose **(A)**, sorted by dose/sex **(B)**. Spatial frequency of every group of adult irradiated mice 20 months p.i.. wild-type mice **(C)** and mutant mice **(D)**. Significances determined with Mann-Withney test. Pictures C+D taken from [257].

Factor sex

Splitting of every cohort into sexes revealed that no significant differences existed within controls, the 0.5 Gy cohort and the 1 Gy cohort (Fig. 49, B). In the 2 Gy cohort, though, sex separation split the data in 2 statistically significant different bodies. Females of this cohort performed relatively 20 % worse than males. Missing differences in comparison of the 0.5 Gy and 1 Gy were only not observed for male WTs. On the other hand, group splitting revealed that the significant difference between the 1 Gy and 2 Gy cohort was mainly contributed by the significant differences of the mutants and not the WTs.

Further splitting of the cohorts considering the genotype (line WT and mutant), revealed that the visual acuity of the female 2 Gy-irradiated mice was not equally affected by IR (Fig. 49, C+D). Mean spatial frequency of female WTs was reduced by relatively 18 % compared to the controls, but by 43 % in female mutants. *Factor line*

Three-way ANOVA of spatial frequencies revealed that every population separation by the independent factors chosen (line, sex, dose) and every interaction of these factors, caused significant mean differences (Tab. 23). The overall p-value concerning analysis by the factor dose was asymptotically zero. Only between the 0.5 Gy cohort and the 1 Gy cohort no significant mean difference was identified. Levene's test assured that the variances within the populations were not significant different, which reinforced the statistical findings. *MANOVA*

Table 23.: Main effects for spatial frequencies in adult mice determined by three-way ANOVA and Tukey *post-hoc* test at the end of observation time (19-20 months p.i.).

Factor	Level	Mean	ΔMean	p-value
Line	WT	0.425	0.017	0.005
	Mut	0.414		
Sex	Male	0.425	0.02	$1.2*10^{-3}$
	Female	0.414		
Dose	0 Gy	0.469	0.048 **(0 vs. 0.5)** 0.059 **(0 vs. 1)** 0.118 **(0 vs. 2)**	$\rightarrow 0$
	0.5 Gy	0.423	0.011 (0.5 vs. 1) 0.07 **(0.5 vs. 2)**	
	1 Gy	0.411	0.059 **(1 vs. 2)**	
	2 Gy	0.354	-	
Line*Sex	-	-	-	$3.4*10^{-3}$
Line*Dose	-	-	-	$2.16*10^{-6}$
Sex*Dose	-	-	-	$2.6*10^{-3}$
Line*Sex*Dose	-	-	-	$2.9*10^{-4}$

Significant differences (Tukey test) are written in bold font. p-values refer to level-overarching significances. Model (DF = 15) $p \rightarrow 0$.

Main quantifiable eye changes that could be correlated to the determined re- *Correlations*

ductions in visual acuity were the lenticular signal-free areas as measures for a lens damage (though not necessarily, as speculated for the pure SF-type) and the corneal clouding. As shown for the group with the highest changes in spatial frequency, the female mutants (Fig. 50, A), correlation between the visual parameter spatial frequency and the lenticular damage observables (ΣPSFA/ASFA) was rather weak (r = -0.56).

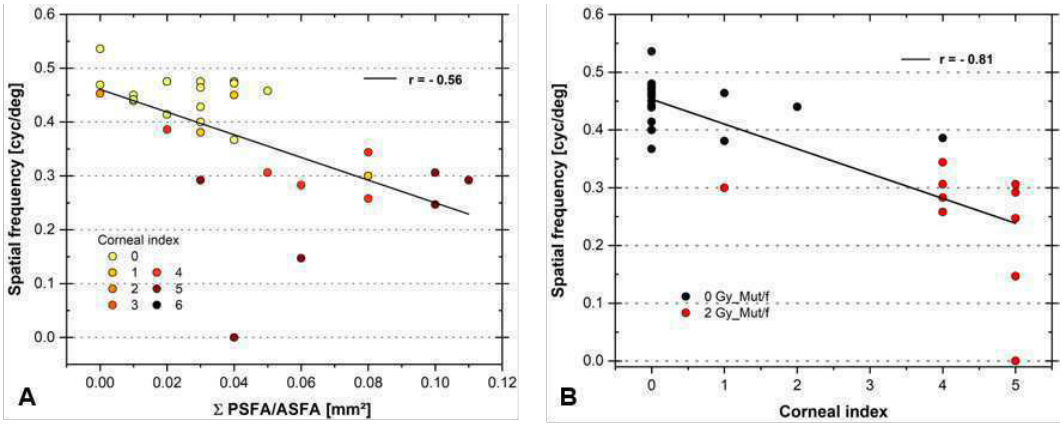

Figure 50.: Spatial frequency correlations in 2 Gy-irradiated P70 mice 20 months p.i. Spatial frequency vs. summed signal-free areas of every lens in an experimental mouse including controls **(A)**. Spatial frequency vs. corneal index **(B)**. Linear fits (black lines). Significances determined with Mann-Withney test. Modified pictures taken from [257].

Corneal index (see results chapter 3.2) of every mouse suggested that, although the lenticular variable did not completely fail, the clouding of the cornea might have had a more important impact on mice's vision. Indeed, plotting of spatial frequency against the discrete corneal index revealed a solid correlation for this group (r = -0.81, Fig. 50, B).

Correlation with posterior scattering score (SS_{post}) as the sum of posterior lenticular lesion types containing a scattering component (S- and SF/S-type, e.g. a mouse with two lesion of the SF/S-type has a SS_{post} of 2) revealed a statistically significant separation of the 2 Gy cohort and their controls (Fig. 51, A). The mean spatial frequency of mice carrying 2 lenticular lesions with scattering components (SS_{post} = 2) was ~ 15 % lower than in mice with only N- or SF-phenotypes (SS_{post} = 0). A scattering score including anterior and posterior scattering components of both lenses (SS_{AP}) was available for one third of the 2 Gy cohort (Fig. 51, B). The explanatory power was low due to few mice with an entire set of OCT data. However, increase of SS_{ges} beyond 2 resulted not in decreased mean spatial frequencies.

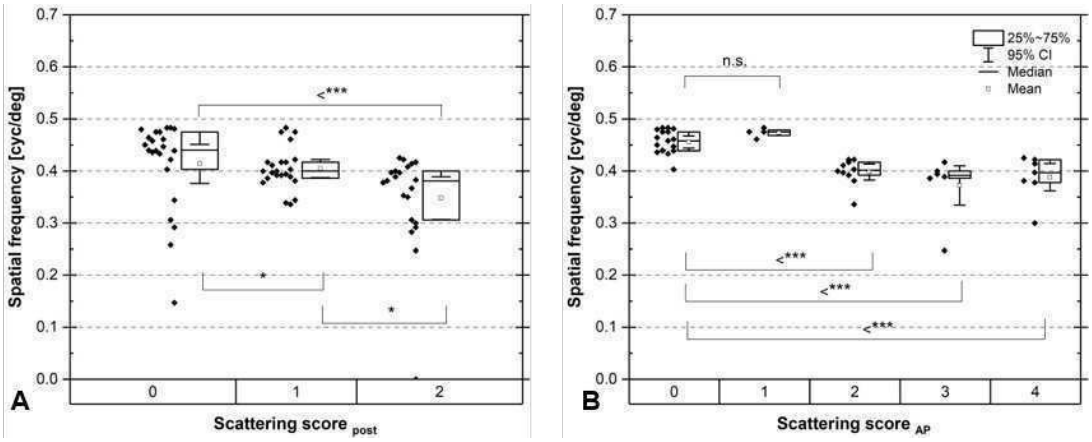

Figure 51.: Spatial frequency vs. SS_{post} **(A)** and spatial frequency vs. SS_{AP} **(B)** in adult 2 Gy-irradiated mice 20 months p.i. Significances determined with Mann-Withney test. Pictures taken from [257].

6.3 VISUAL ACUITY OF IRRADIATED NEONATALS

Early irradiation at P2 turned out to have more drastic effects on spatial frequencies than irradiation at P70. The mean spatial frequency was reduced between 45 % (female mutants) and 58 % (male WTs) (Fig. 52, A). It was quite obvious that dispersion of spatial frequency was much higher than in the P70 mice. Whereas the standard deviation for controls was around normal 5 % or less, the standard deviation for the irradiated groups added up to almost 50 %. Nonetheless, no distribution overlap between controls and the irradiation groups was observed. Applying an α-error of 5 %, Mann-Whitney test did not reveal solid mean differences between genotypes and sexes within the irradiated mice (Fig. 52, B).

Three-way ANOVA confirmed this finding with the information that, besides the factor dose ($p \rightarrow 0$), none of the other factors or the interaction of these created significant differences. Levene's test corroborated the data homogeneity.

Single damage scores

For correlation analysis several single damage scores were utilized:

CSn... Cataract score of neonatals (Cataract value left+right), [0; 10]

Ret... Retinal score (Retinal thickness left+right), [214; 487]

ON... Optic nerve-associated lesion area (ONLA, fraction of fundus left+right), [0 %; 14.09 %]

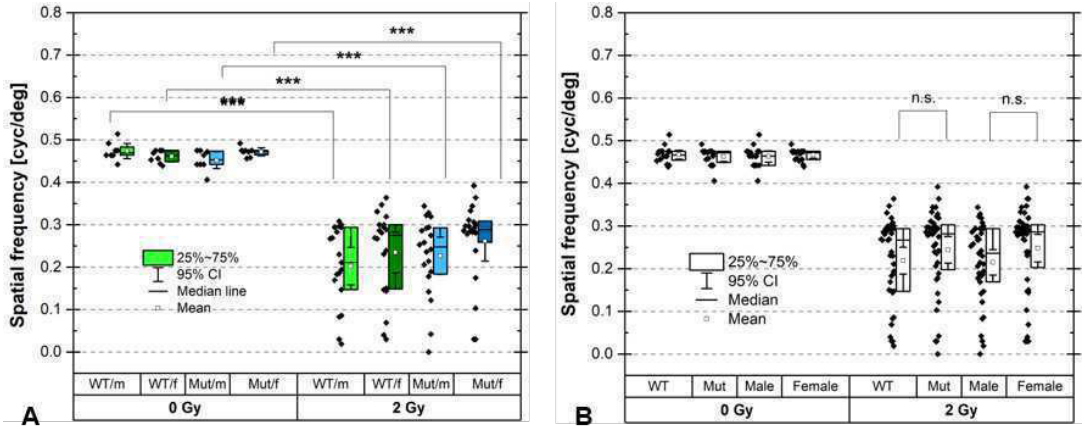

Figure 52.: Spatial frequency of neonatal irradiated mice 9 months p.i. Comparison of every group of each group **(A)**. Comparison of pooled WT, mutants, males and females **(B)**. Significances determined with Mann-Withney-test. Modified picture A taken from [258].

Apparently, severest damage, the retinal atrophy, plotted against the spatial frequency revealed a strong correlation (dashed line, r = 0.82) if controls are included (Fig. 53, A). Irradiated mice itself did not display this correlation satisfactorily

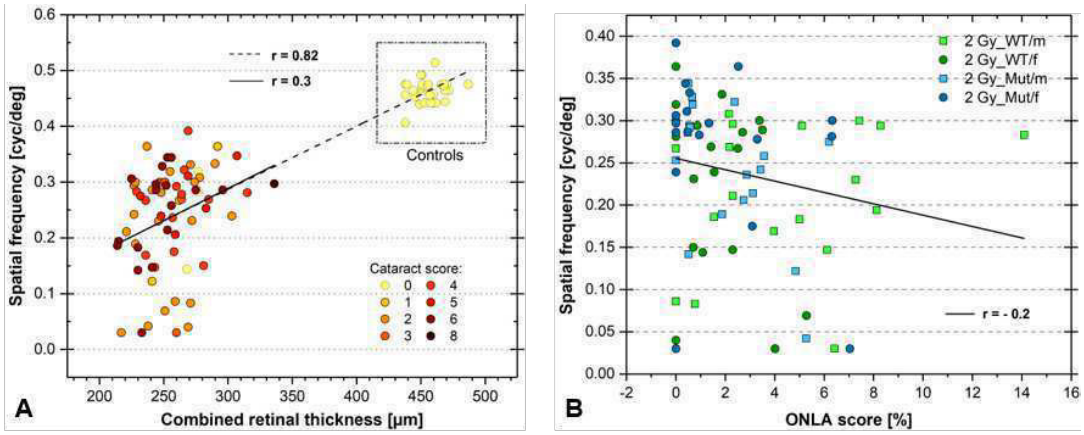

Figure 53.: Combined retinal thickness vs. spatial frequency of neonatal irradiated mice. Linear fit for all mice (black closed line). Linear fit only for the irradiated mice (black dashed line) **(A)**. ONLA score (see Fig. 47, B) vs. spatial frequency for every irradiated group. Linear fit for all mice (black line) **(B)**. Modified picture A taken from [258].

(closed line, r = 0.3). Additional information about the cataract score contributed to an even less conclusive result. Animals with severe lenticular damage (e.g. **CSn** of 6) were positioned above the fit line because they performed quite well in the visual

acuity test. On the other hand, several mice with minor lenticular damage (e.g. **CSn** of 2) were to be found below the fit, had comparable retinal atrophy as their cohort comrades, but performed worse. The cataracts score seemed therefore not suitable as a single correlation factor. In a second step, the other retinal variable, the ON was plotted against the spatial frequency and failed also to deliver a plausible correlation (r = -0.2, Fig. 53, B), which could be seen intuitively by the huge spread of the data cloud.

All three measures to describe observed damage in the eye were implemented into mathematical terms that could, at maximal degree, equal each other in hypothesised impact on the visual acuity. Here, **CSn** was independent on actual occurrence of cataracts (Equ. 5), while the **Ret** and **ON** were normalized on the median combined retinal thickness of controls in the first case and on the maximum ONLA in the second one (Equ. 6, 7).

$$\mathbf{A} = \mathbf{CSn} * 10 \tag{5}$$

$$\mathbf{B} = (456 - \mathbf{Ret}) * 0.4115\ [1/\mu m] \tag{6}$$

$$\mathbf{C} = \mathbf{ON} * 7.09\ [1/\%] \tag{7}$$

Impairments score

Those terms were used to define an impairment score (**IS**) dependent on the inherent initial variables **CSn**, **Ret** and **ON** (Equ. 8). The **IS** was calculated according reasonable cases defined by the biological importance of lenticular or retinal damage to incident light hampering.

$$\mathbf{IS\ (CSn;\ Ret;\ ON)} = \begin{cases} w_{11}\mathbf{A} + w_{12}\mathbf{B} + w_{13}\mathbf{C} & \text{for } \mathbf{CSn} \geqslant 6 \\ w_{21}\mathbf{A} + w_{22}\mathbf{B} + w_{23}\mathbf{C} & \text{for } 4 \leqslant \mathbf{CSn} < 6 \\ w_{31}\mathbf{A} + w_{32}\mathbf{B} + w_{33}\mathbf{C} & \text{else} \end{cases} \tag{8}$$

It was decided that the more upstream the damage the more influence it might have had on the spatial frequency measured. Therefore, lenticular damage was weighted higher, if it was high, and retinal damages were weighted higher, if the lens was less affected. This notion was implemented by a certain set of weighing factors:

$$W_{\text{neo}} = \begin{Bmatrix} w_{11} & w_{12} & w_{13} \\ w_{21} & w_{22} & w_{23} \\ w_{31} & w_{32} & w_{33} \end{Bmatrix} \stackrel{!}{=} \begin{Bmatrix} 0.8 & 0.1 & 0.1 \\ 0.3 & 0.4 & 0.3 \\ 0.05 & 0.5 & 0.45 \end{Bmatrix} \tag{9}$$

Since the measured optic nerve-associated lesion was not the only area of severely affected retinae, the **ON** was not equally integrated as the retinal thickness as a more global parameter. **IS** could be maximal 100 and minimal slightly negative, since the lower boundary is defined as the median of the control retinal thickness.
The **IS** as a comprehensive damage measure plotted against spatial frequency resulted in a more favourable data distribution (Fig. 54, A). Again, correlation between impairment score and spatial frequency was strong if controls and irradiated mice were included in the fit (r = -0.79), but was weak if the cohorts stood alone for themselves (r = -0.2 and r = -0.3 respectively, Fig. 54, B).

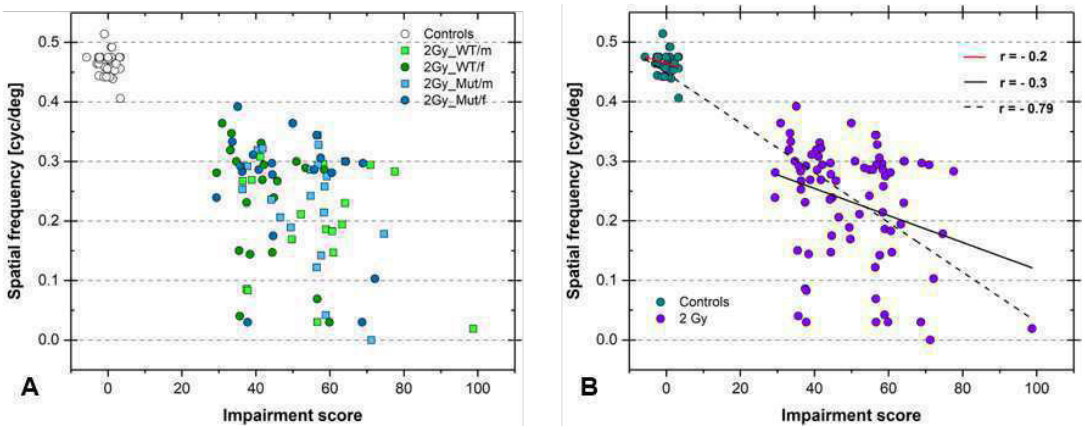

Figure 54.: Impairments score vs. spatial frequency of neonatal irradiated mice. Separated by controls and irradiated groups **(A)**. Separated by dose. Linear fit for controls (red line), irradiated mice (black line) and both together (black dashed line) **(B)**.

The group separation implied that the median **IS** was higher for males than for females (Tab. 24). This was modified by putting ΔSF in relation to the median **IS** (Tab.

Table 24.: Impact of impairment on spatial frequency for every irradiated group.

Group	ΔSF [cyc/deg]	Median IS	RIIS [cyc/deg]
WT ♂	0.27	58.6	$4.55*10^{-3}$
WT ♀	0.187	39.94	$4.69*10^{-3}$
Mut ♂	0.203	56.5	$3.58*10^{-3}$
Mut ♀	0.184	44.4	$4.15*10^{-3}$

Relative impairment impact score (RIIS) impact as quotient of spatial frequency (SF) differences ($SF_{controls}$ - $SF_{irradiated\ groups}$) and median impairment score (IS).

24, Relative impairment impact score (RIIS)). RISS showed that impact of IR on visual acuity was not sex-dependent.

7

LENS ALTERATIONS OF IRRADIATED ADULT MICE ANALYSED BY INTERMEDIATE HISTOLOGY

7.1 LENTICULAR ALTERATIONS IN IRRADIATED ADULT B6C3F1 MICE

Basic changes

Sighting of histological sections of irradiated adult B6C3F1 mice revealed almost exclusively 2 mayor alteration spots: the posterior subcapsular and the anterior subcapsular at the suture of the outer cortex. Maximal alterations at those sutures were identified as subcapsular cataracts or generally cataracts. Those lesions were composed of several cellular changes of different quality (Fig. 55, A+B).

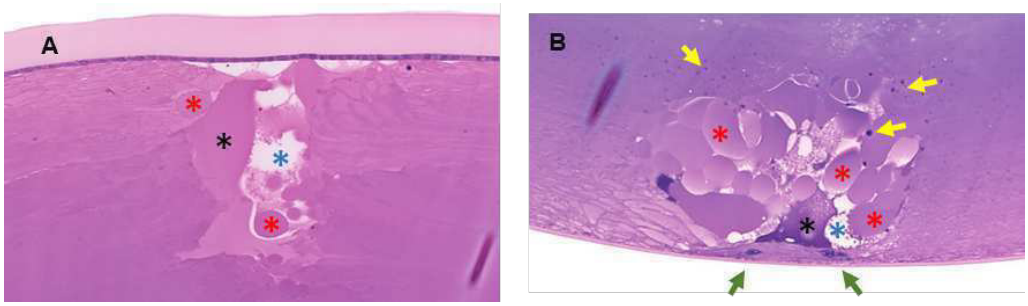

Figure 55.: Histological fine structure of representative subcapsular lesions in B6C3F1 mice. Anterior subcapsular cataract **(A)**. Posterior subcapsular cataract **(B)**. Enlarged fibre cells (red stars). Proteinaceous reservoirs (black stars). Intercellular spaces (blue stars). Pseudoepithelial cells (green arrows). Possible cellular/nuclei degradation products (yellow arrows). Modified picture taken from [257].

Most abundantly, fibre cells normally aligning at the suture with their basal ends, appeared to be swollen (Fig. 55, red stars). This fibre cell enlargement represents the first stage of lesion formation. Other structures could not be clearly identified as enlarged fibre cells and were recognisable as very large compounds with nor substructure (Fig. 55, black stars). Either those structures were very large fibre cells, which is unlikely, or they were large reservoirs of liquefied proteins or other biomacromolecules. For the sake of histological impartiality, we consider them both as one phenomenon. The fibre cell alterations were accompanied by the emergence of fibre cells that carried a nucleus (Fig. 55, green arrows). We designate those cells

hereinafter pseudoepithelial cells. As third characteristic, due to the fragmentation in the lesion area, intercellular areas appeared (Fig. 55, blue stars). Furthermore, in many posterior lesions possible spots of cellular debris were presumed and were every once in a while stained by methylene blue, which suggested nuclei degradation was resting (Fig. 55, yellow arrows).

Categorisation

In the here applied definition, a lesion at the suture that was composed by at least 2 of the possible characteristics (swollen fibre cells/reservoirs, pseudoepithelial cells, intercellular spaces) was designated posterior or anterior cataract and subcapsular in nature if placed directly beneath the capsule. For histological analysis, a regular lens was defined 'no finding' indicating the absence of those characteristics (Fig. 56, A+D). As intermediate category, we defined the appearance of one feature or two as 'Irregularity' (Fig. 56, B+E).

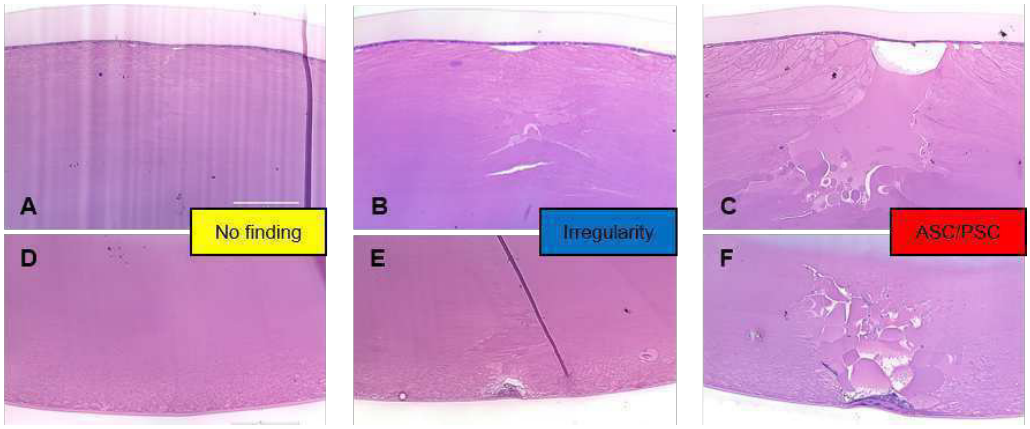

Figure 56.: Representative pictures of lenticular phenotypes in B6C3F1 histology. Normal suture **(A+D)**. First alterations with first slightly enlarged fibre at the suture and some pseudoepithelial cells **(B+E)**. Full developed subcapsular cataracts with 2 of 3 critical components (enlarged fibre cells, pseudoepithelial cells and intercellular spaces)**(C+F)**. Modified picture taken from [257].

PSC frequencies

According this rough classification of lenticular changes and by omitting the knowledge gathered from *in-vivo* examinations, the observation were gathered and pooled for every cohort (Fig. 57, A+B). 4 months after irradiation, no PSC was identified in any cohort, but 2 irregularities in the 2 Gy cohort (Fig. 57, A). 8 months later, the first PCSs were observed across all cohorts, while a high level of irregularities was established too, but not in the controls. Compared to controls,

only the odds ratio for PSCs from the 2 Gy cohort was significantly increased (Tab. 25, OR = 14.44), not for the lower doses. These findings changed 20 months after irradiation. Now, the occurrence of PSCs seemed to follow a linear dependency on dose (R = 0.99, corrected R^2 = 0.96 against R = 0.96 and corrected R^2 = 0.74 at 12 months p.i.). In fact, the calculated odds ratio for the 1 Gy cohort was significantly increased (OR = 6.46), also the one for the 2 Gy cohort (OR = 26.6), but not for the 0.5 Gy cohort! It is save to say that 2 Gy of γ-rays induced in almost every animal at least posterior subcapsular irregularities or worse. Lenticular alterations in controls (PSCs + irregularities) did not overstep one fifth of the samples and not one tenth of the samples at the approximative biological half-life of the mice.

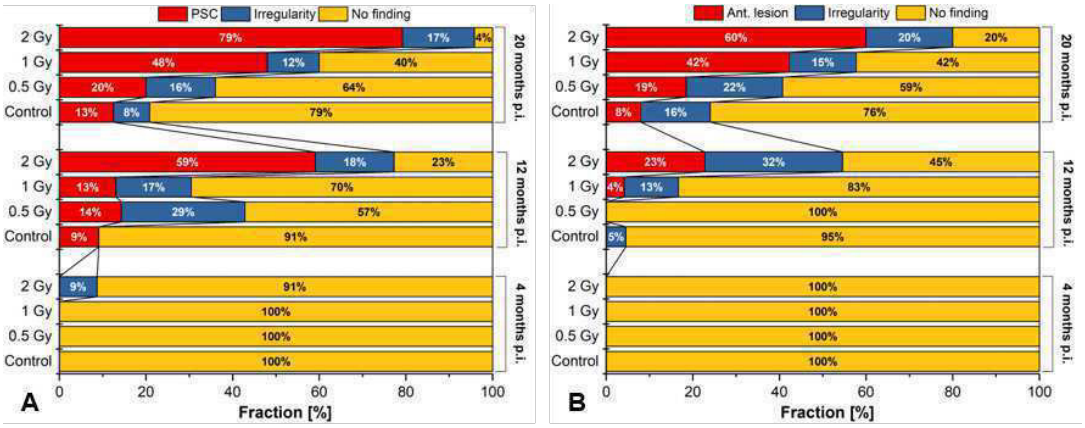

Figure 57.: Overview over histological findings in B6C3F1 mice as fractions of the pooled irradiated cohorts 4, 12 and 20 months following irradiation. Posterior findings **(A)**. Anterior findings **(B)**. Picture taken from [257].

Table 25.: Odds ratios for posterior subcapsular cataracts observed in histology of P70 B6C3F1 mice.

Time p.i.	Comparison	Odds ratio	95 % CI	p-value
12 months	0.5 Gy vs. 0 Gy	1.57	0.23 - 10.51	0.63
	1 Gy vs. 0 Gy	1.5	0.22 - 9.96	0.67
	2 Gy vs. 0 Gy	**14.44**	2.68 - 77.79	0.002
20 months	0.5 Gy vs. 0 Gy	1.75	0.36 - 8.3	0.48
	1 Gy vs. 0 Gy	**6.46**	1.52 - 27.32	0.011
	2 Gy vs. 0 Gy	**26.6**	5.58 - 126.59	< 0.001

Odds ratios of posterior subcapsular cataracts. Significantly increased ratios were written in bold font. No PSCs at 4 months p.i. observed. Table taken from [257].

Following the slit lamp-based classification from Merriam Jr and Focht [215], all lenses were assessed whether they fulfilled the criteria for stage 1+ (early changes at posterior pole) or stage 2+ cataracts (posterior opacification and first opacifications anterior). Here, irregularities and PSCs/ACs according the classification in this thesis were generally taken as an opacification. With these conditions the histological data was transformed to a Merriam&Focht-compatible data set (Tab. 26).

Table 26.: Stages in P70 mice according system of Merriam&Focht ([215]) 20 months p.i. after data transformation.

Dose	Stage 0	Stage 1+	Stage 2+	n_{tot}
0 Gy	15	3	6	24
0.5 Gy	8	8	11	27
1 Gy	4	7	15	26
2 Gy	1	4	20	25

Stage 0 as complemented equivalent to 'no findings'. Observed anterior irregularities/cataracts were taken as hint for certain posterior changes even these were not documented in histology and hence counted as stage 2+ cataract of the entire lens. Mind that stage 3+ cataracts were not ascertainable since the lenticular nucleus is not fixable with Davidson, and OCT data proved that no nuclear opacities occurred in P70 mice.

Based on this transformation, 25 % of the controls developed stage 2+ cataracts 20 months following irradiation and 80 % of P70 mice irradiated with 2 Gy.

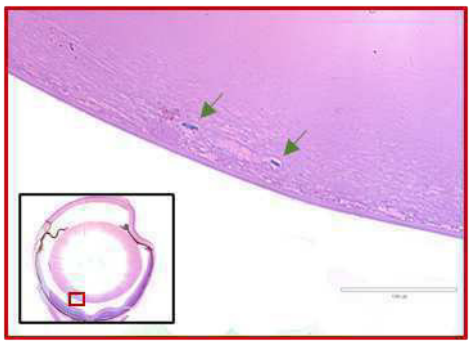

Figure 58.: Representative example of migrating nuclei (green arrows) in a 1 Gy-irradiated male mutant lens 12 months p.i. 20x-magnified close-up (red frame) of 4x-magnified record (black frame).

Lesion formation at the posterior suture was proceeded by migration of nuclei close to the capsule. This migrations was never observed to be directly beneath the capsule. The concerning cells escaped most likely from the differentiation process at the lensbow and eventually accumulated directly subcapsular at the suture. It became obvious that the cell bodies carrying the nuclei differed from the appearance of the pseudoepithelial cells at the pole (compare Fig. 58 with Fig. 56, F). In the migratory phase, the

respective aberrant fibre cells were akin to the bulk of surrounding fibre cells or slightly larger.

Ant. lesion frequencies

Anterior lesions were not exclusively observed as phenomena placed directly beneath the capsule. Therefore, anterior lesions/cataracts were grasped in a broader sense than posterior lesions in this study. The first remarkable observation in comparison with posterior alterations was the different latency of anterior changes (Fig. 57, B). No alterations whatsoever were sighted in samples taken 4 months after irradiation. First changes appeared 12 months following irradiation. But only across the 1 Gy and the 2 Gy cohort those changes were actual full classifiable cataracts. The controls exhibited first anterior cataracts 20 months after sham-irradiation. In contrast to the posterior findings, anterior lesions in the 2 Gy cohort were not significantly more frequent 12 months after irradiation (Tab. 27). A similar distribution of occurrences emerged 20 months after irradiation with an apparently linear dose response of the anterior lens. Here, the odds ratios for anterior lesions in the 1 Gy and 2 Gy cohort were significantly increased too (OR = 8.43 and OR = 17.25). The odds ratio for the 2 Gy failed to reach the same level as for the PSCs (exceeding odds ratio of 9.35).

Table 27.: Odds ratios for anterior cataracts observed in histology of B6C3F1 mice.

Time p.i.	Comparison	Odds ratio	95 % CI	p-value
12 months	1 Gy vs. 0 Gy	2.87	0.11 - 74.26	0.52
	2 Gy vs. 0 Gy	14.14	0.73 - 273.4	0.07
20 months	0.5 Gy vs. 0 Gy	2.61	0.45 - 14.9	0.27
	1 Gy vs. 0 Gy	**8.43**	1.63 - 43.52	0.01
	2 Gy vs. 0 Gy	**17.25**	3.3 - 89.97	$< 10^{-4}$

Odds ratios of anterior cataracts. Significantly increased ratios were written in bold font. No PSCs at 4 months p.i. observed. Table taken from [257].

Severe changes

Besides the highly characteristic changes at the sutures that could also appear caused by ageing, some features of these phenotype were exclusively radiation-related. The most distinctive feature was the abundant accumulation of pseudoepithelial cells. They could appear as a bulk at the anterior epithelium (Fig. 59, A, red arrowhead) or as a wide-stretching layer at the posterior lens rim (Fig. 59, B, red arrowheads). Furthermore, 2 lenses were analysed that displayed ruptures in the cortex unlike fixation/cutting artefacts (Fig. 59, C, yellow arrowhead) and massively arising intra-

or intercellular vacuoles (Fig. 59, C, green arrowheads) between the lensbows and the anterior segment (Fig. 59, C).

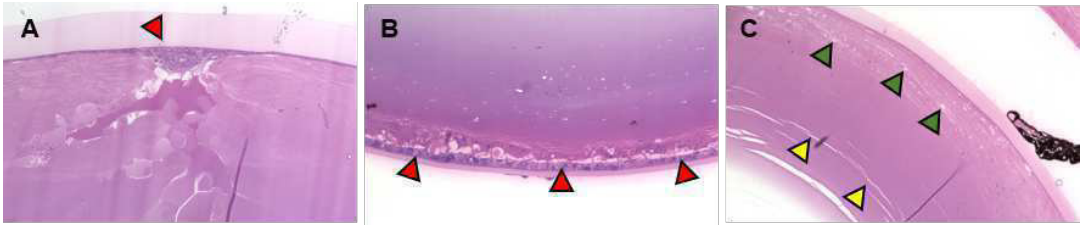

Figure 59.: Not-representative images of severe lenticular changes in adult B6C3F1 mice exposed to 1 Gy. Accumulation of pseudoepithelial cells (red arrowheads) beneath the anterior capsule directly at the suture (40x) **(A)**. Pseudoepithelial cells covering the entire posterior rim of the lens (40x) **(B)**. Vacuoles (green arrowheads) between the lensbow and the anterior segment of the lens and ruptures (yellow arrowheads) in the outer cortex (20x) **(C)**. Picture taken from [257].

Severest lesion

From a mechanistic point of view, it was very intriguing to study the most affected lens of all irradiated cohorts 20 months after exposure of a male WT of the 2 Gy cohort (Fig. 60). This lens was outstanding because of its disordered fibre cell organisation. Fibre cells of the inner and outer cortex differed drastically. While outer fibre cells were swollen (Fig. 60, B, black stars) and faintly stained, inner cortical fibre cells set themselves apart by more intense staining and unsuspicious organisation behind a distinct border including possible nuclei debris (Fig. 60, B+C, yellow arrowheads) that were very similar to the debris observable normally in the more inner lesion area of PSCs. Actually, many fibre cells with migratory nuclei were seen beyond the transitional zone (Fig. 60, C, red arrowheads). An anterior lesion and a PSC (Fig. 60, D) were also present.

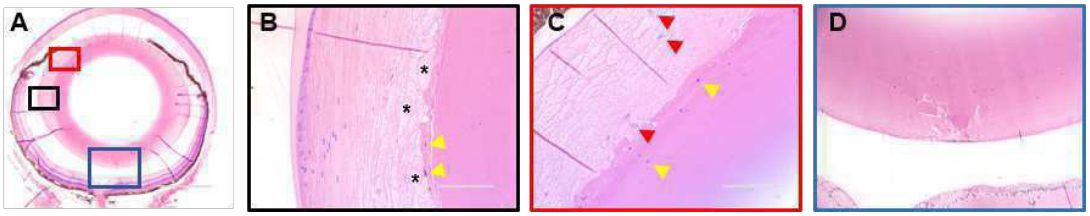

Figure 60.: Not-representative images of the severest lenticular changes in adult male B6C3F1 mouse exposed to 2 Gy. Overview over the entire eye (4x) **(A)**. Lens bow (40x) **(B)**. Anterior lens close to the iris (40x) **(C)**. Posterior lens part (20x) **(D)**.

With this comprehensive insights into the biological foundations of lesion structures, it was possible to match posterior *in-vivo* phenotypes observed with OCT (Fig. 61).

OCT phenotype matching

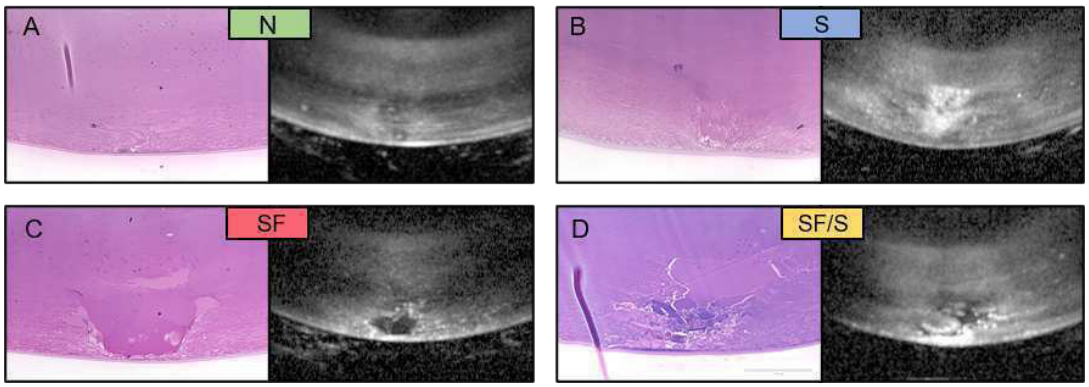

Figure 61.: Identification of biological structures underlying certain posterior phenotypes observed with OCT (Fig. 21) 20 months p.i.. N-type **(A)**. S-type **(B)**. SF-type **(C)**. SF/S-type **(D)**. Picture taken from [257].

The N-phenotype in OCT proved to depict a regular posterior outer cortex with a normally aligned suture (Fig. 61, A). The white-ish appearance of the cortex can be considered as background signal of a naturally scattering-prone tissue. In any case, no fibre cell abnormalities were recognised. The S-type in OCT was hard to identify in histological sections (Fig. 61, B): Scattering *in vivo* seemed to be caused by small irregularly aligned and posteriorly bent fibre cells. This orientation of cellular shape out of the parallelised layers might have been a mayor cause for scattering. In analysis of the histology gained by investigating lenses with the SF-type, it became clear that the huge signal-free area represents something designated either as big swollen fibre cell or, more likely, reservoirs of liquefied proteins with few membranes separating these (Fig. 61, C). Transition to the surrounding bulk of fibre cells was smooth and relatively sharp which means with few irregular shaped fibre cells separating the reservoirs from the rest of the lens. That might have contributed to the low scattering appearance *in vivo*. In the SF/S-type all those descriptions characterising the S- and the SF-type came together. Additionally, the massive scattering below the signal-free area could be identified as a mixture as pseudoepithelial cells and cellular debris (Fig. 61, D).

Inbred female C57BL/6J mice (BL6) investigated 18 months after irradiation were analysed with regard to possible dose rate effects. Independent of which cohort they came from, BL6 lenses appeared to be quite similar to B6C3F1 lenses; the inner and outer cortices were as sharply distinguishable as in the hybrids (Fig. 62, green arrows). Controls displayed at the first glance also the same phenotype variation as in old hybrids. Sutures were mostly regular, but irregularities seemed to be immanent (Fig. 62, yellow arrowhead).

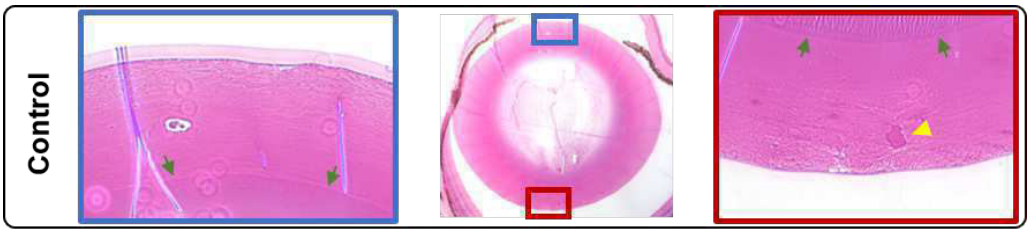

Figure 62.: Histology of the C57BL/6J control eye 18 month following sham-irradiation. Overview (middle, 4x), anterior segment (left, 40x), posterior segment (right, 40x). Boundary of inner and outer cortex (green arrows). Swollen fibre cell (yellow arrowhead).

It turned out that BL6 mice displayed at this high age the same linear dose response dependency as in the B6C3F1 hybrids 20 months after irradiation. Cataracts were seen in all irradiation cohorts (Fig. 63). No increased odds ratios for posterior or anterior cataracts in irradiated mice were expected, since the number of lenses investigated was only 5 per group. Nonetheless, odds ratio for PSCs in the 2 Gy cohorts of both applied dose rates were increased. For both groups the odds ratio was 33 (95 % CI: 1.06 - 1023; p = 0.04). It was surprising that in every irradiation cohort the number of PSCs was the same irrespective of dose rate (Tab. 28).
While in the posterior lens no posterior subcapsular cataract was observed, one anterior lesion was seen in the anterior lens of a control (Tab. 29). The general tendency seemed to be that anterior lesions were a bit more often present in lenses of animals exposed via a dose rate of 0.063 Gy/min than in animals exposed to γ-radiation with a higher dose rate of 0.3 Gy/min. Again, low numbers of mice hampered a statistical statement. Even in the 2 Gy cohorts, a statistical comparison with controls regarding the occurrence of anterior lesions was negative.
Close-ups of anterior and posterior cataracts were as insightful as in hybrids. Again,

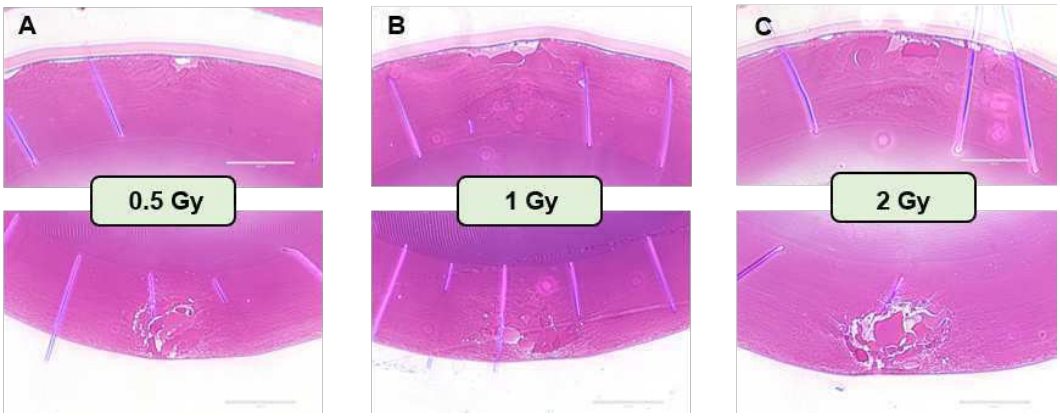

Figure 63.: Dose-dependent lenticular damage in histology of C57BL/6J mice, 18 months p.i. 0.5 Gy **(A)**. 1 Gy **(B)**. 2 Gy **(C)**. Chosen samples without regard to dose rate.

Table 28.: Posterior alteration occurrences in C57BL/6J mice 18 months p.i.

Dose [Gy]	Dose rate [Gy/min]	PSC	Irreg.	No findings
0	-	0	2	3
0.5	0.063	1	1	3
0.5	0.3	1	2	2
1	0.063	2	2	1
1	0.3	2	1	2
2	0.063	4	0	1
2	0.3	4	0	1

Occurrences of posterior subcapsular cataracts (PSCs), irregularities (Irreg.) and no findings.

Table 29.: Anterior alteration occurrences in C57BL/6J mice 18 months p.i.

Dose [Gy]	Dose rate [Gy/min]	Ant. lesions	Irreg.	No findings
0	-	1	0	4
0.5	0.063	2	0	3
0.5	0.3	1	1	3
1	0.063	3	0	2
1	0.3	1	2	2
2	0.063	3	1	1
2	0.3	2	2	1

Occurrences of anterior lesions, irregularities (Irreg.) and no findings.

anterior lesions were not necessarily subcapsular (Fig. 64, B) or not only subcapsular (Fig. 64, A). Generally, they were more complex. For instance, 2 structurally not

connected reservoirs in the anterior suture were observed (Fig. 64, A, black star vs. red star), separated by a zone of increased fragmentation (Fig. 64, A+B, green encircled area) and a second layer of less impaired fibre cells (Fig. 64, A). One could hypothesise that the green-marked zone was an area of increased cell lysis which 'feeds' the reservoir below with liquefied proteins. It became also clear that this feeding zone was enriched with fibre cells carrying nuclei (Fig. 64, B, yellow arrowheads). Zones of increased fragmentation, phenomenologically spoken, could of course also be a downstream feature replacing reservoirs (see PSFA dynamics in B6C3F1 mice). Posterior cataracts were of the same constitution as in the hybrids. One reservoir relatively close to the capsule and deformed fibre cells around (Fig. 64, C).

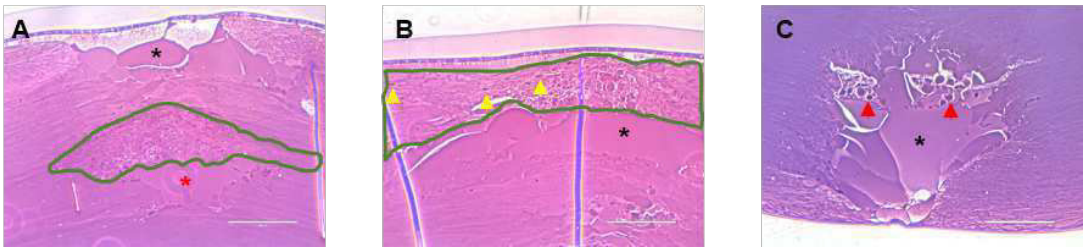

Figure 64.: Histological close-ups of irradiated 18 months old C57BL/6J mice. Anterior lesion **(A+B)**. Posterior lesion **(C)**. More subcapsular protein reservoirs (black stars), roundly shaped fibre cells (red arrowheads), cells with nuclei (yellow arrowheads), area of increased fragmentation and degradation (green encircled area).

7.3 LENTICULAR ALTERATIONS IN IRRADIATED ADULT 129S2/SVHSD MICE

The direct comparison with B6C3F1 at the same time point (12 months p.i.) revealed a higher frequency of PSCs in 129S2/SvHsd (129 mice) controls already. Whilst only 9 % of the pooled B6C3F1 controls formed a PSC, 33 % of the 129 controls displayed such a pathological finding (Tab. 30 vs. Tab. 25). General disorganised posterior cortices were not pathological but the common feature of 129 murine lenses as comparison of controls and irradiated samples proved (Fig. 65, A vs. B+C). Irradiated mice, irrespective of dose rate applied, showed frequencies of PSCs comparable to B6C3F1 mice (~ 60 %; please mind low numbers of 129 samples). No anterior lesions or irregularities were found in controls and also in the irradiated mice the fraction of anterior lesions in the 0.063 and 0.3 Gy/min cohort was less or lower than one fourth (Tab. 31).

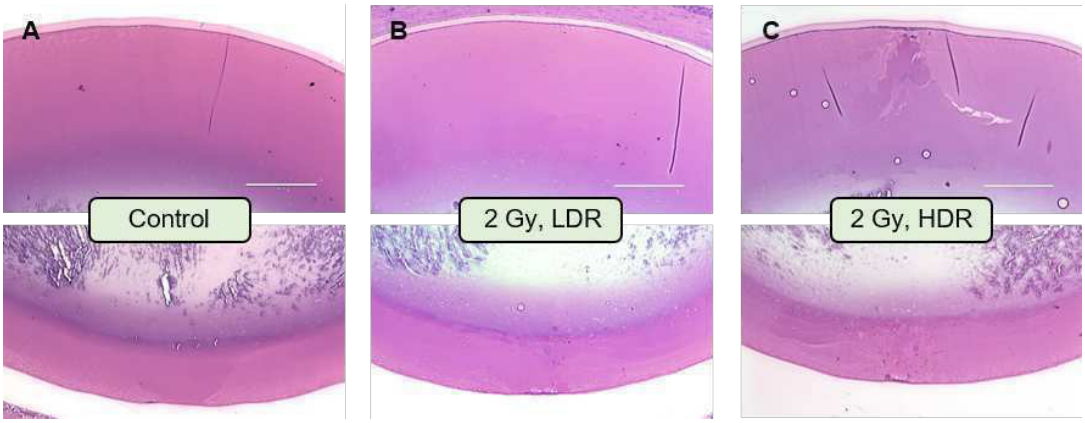

Figure 65.: Anterior and posterior lenticular histology of 129S2/SvHsd mice 12 months p.i., 20x-magnified. Control **(A)**. Lens exposed to 2 Gy, low dose rate (LDR) of 0.063 Gy/min **(B)**. Lens exposed to 2 Gy, high dose rate (HDR) of 0.3 Gy/min **(C)**.

Table 30.: Posterior alteration occurrences in 129S2/SvHsd mice.

Dose [Gy]	Dose rate [Gy/min]	PSC	Irreg.	No findings
0	-	2	0	4
2	0.063	5	1	2
2	0.3	3	1	1

Frequencies of posterior subcapsular cataracts (PSCs), posterior irregularities (Irreg.) and no findings 12 months p.i.

Table 31.: Anterior alteration occurrences in 129S2/SvHsd mice.

Dose [Gy]	Dose rate [Gy/min]	Ant lesion	Irreg.	No findings
0	-	0	0	6
2	0.063	2	2	4
2	0.3	1	2	2

Frequencies of anterior lesions, posterior irregularities (Irreg.) and no findings 12 months p.i.

The lenticular histology of 129S2/SvHsd mice differed drastically from B6C6F1 and C57BL/6J mice. Obviously, the lens nucleus of 129 mice was posteriorly relapsed, in controls and irradiated mice (Fig. 66, A+B). In B6C3F1 mice of the same age, posterior and anterior cortices were almost similarly thick (Fig. 66, C). In 129 mice the proportions were different. The organisation of the posterior cortex,

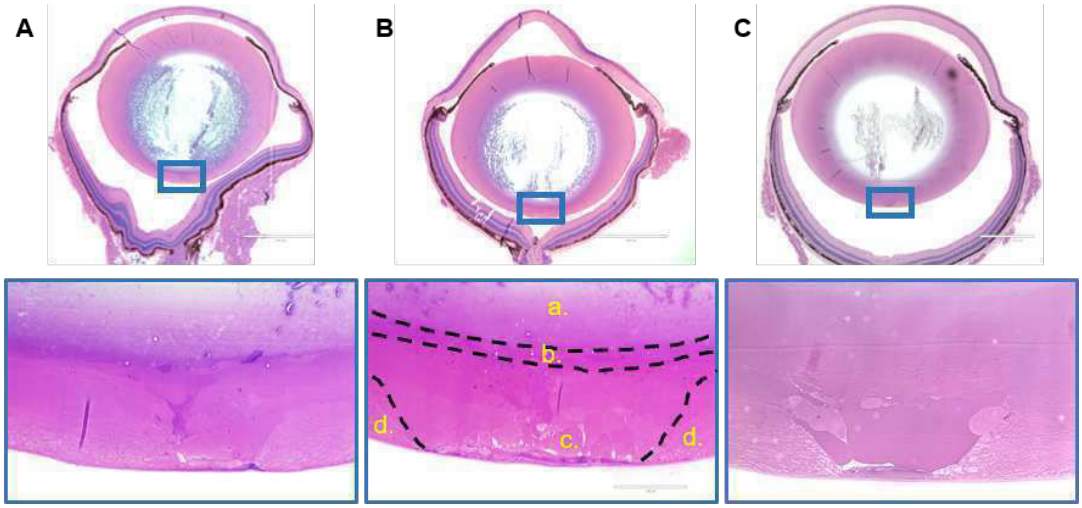

Figure 66.: Histological specifics of 129S2/SvHsd mice lenses in comparison to B6C3F1 lenses 12 months p.i. Control 129 mouse with 40x close-up of posterior cortex **(A)**. 2 Gy-irradiated 129 mouse lens with 40x close-up of the posterior cortex. Zones marked by dashed line explained in text **(B)**. B6C3F1 mouse exposed to 1 Gy with 40x close-up of posterior cortex **(C)**.

which was the thinner one of both cortical sides, was extremely irregular. A belt of increased staining containing more often dark blue-stained dots, approximately 200 µm below the posterior capsule, was observed genotype-overarching (Fig. 66, B, zone b, more predominant in 129 mice). Above this belt in the more inner cortex the fibre cells were untypically round in 129 mice, almost squamous and not tightly packed at all (Fig. 66, B, zone a.). The formation of a suture was completely missed in 129 mice. Lenses of 129 and B6C3F1 mice had actually only the lateral zones of the suture-located lesion in common (Fig. 66, B, zone d.). Here fibre cell organisation seemed to be regular the closer to the lensbow. The lesion (Fig. 66, B, zone c.) itself seemed to be more fragmented at this time point than in B6C3F1 mice (compare Fig. 66, A+B vs. C). Because there were no OCT records to prove it on the basis of scattering properties, one could only speculate that these lenticular features were light scattering.

8

LENTICULAR HISTOLOGY OF IRRADIATED NEONATAL B6C3F1 MICE

8.1 NEONATAL MICE IRRADIATED WITH X-RAYS

10 weeks old B6C3F1 mice irradiated at P2 with X-rays were just about suitable to show the biological fundaments of *in-vivo* cortical phenotypes measured with OCT (Fig. 67).

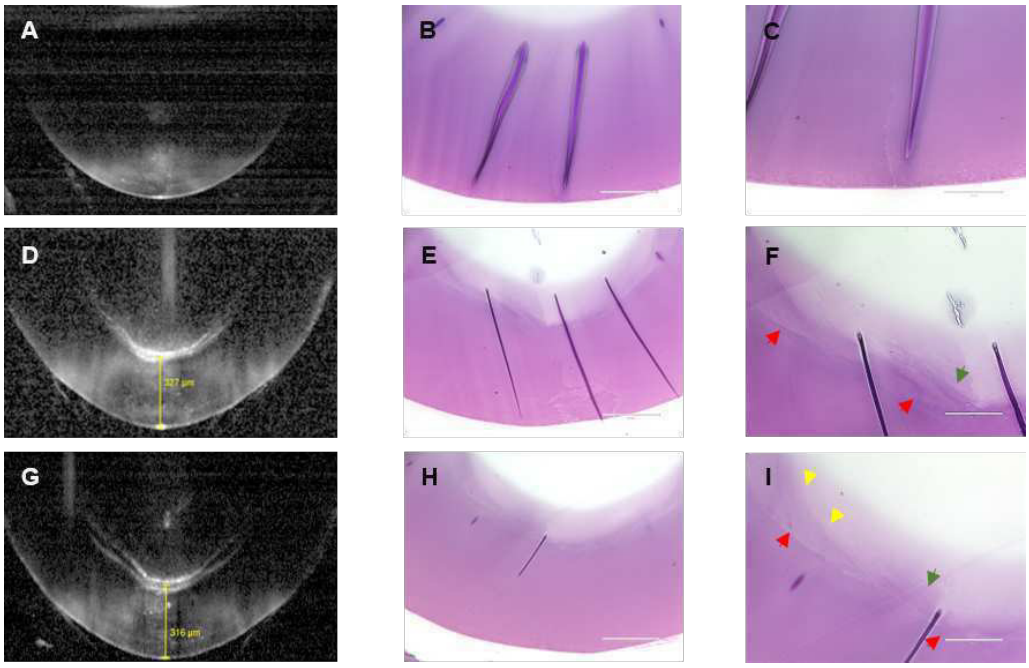

Figure 67.: Histological analysis of neonatal irradiated mice 10 weeks p.i. in comparison with OCT images of the same mice. Control mouse with normal lens **(A)** and two 2 Gy-irradiated murine lenses (X-rays) in OCT **(D+G)**. Histology of these lenses, 20x-magnified **(B+E+H)**. Lesion spots, 40x-magnified **(C+F+I)**. Cell debris or degenerated nuclei (red arrowheads). Slightly swollen, stretched fibre cell (green arrowheads). Areas with no recognisable cellular organisation (yellow arrowheads).

As shown in result section 4.7, severest lesions of C3 type were to find closer

to the posterior rim than less severe types, why visible alterations in histology were more likely to find in such specimens. Mice with such lesion as recorded *in vivo* (Fig. 67, D+G) displayed also alterations in histology, which could not be observed in controls of the same age (Fig. 67, compare with E+H with B). In the same distance as detected *in vivo*, alterations of the fibre cell bulk was observed in histology of the perinuclear zone. These alterations matched the shape of *in-vivo* lesions with their characteristic lateral indentations.
Closer examination revealed a fibre cell organisation not remotely reminding of the lesion features of irradiated P70 mice. No reservoir-like structures were to be found in the stained area, but possible cellular debris or degraded nuclei in the frontal zone of the lesions (Fig. 67, F+I, red arrowheads). Either way, these zones represented most likely the posterior scattering edge of the sickle-shaped lesion in OCT. The zone behind was more difficult to decipher. OCT records suggested an area of regularly organised cells or poorly scattering vacuoles. In fact, many densely packed fibre cells were recognised that were definitely swollen, but not round in shape and still aligning in parallel (Fig. 67, F+I, green arrowheads). Besides, there were areas that seemed void and without structure and could have contributed to the scattering-free appearance in OCT (Fig. 67, I, yellow arrowheads). The inner scattering edge in OCT could not be matched to any histological structure due to the poor fixation of the lens so close to the nucleus.

8.2 NEONATAL MICE IRRADIATED WITH γ-RAYS

It was much harder to find a γ-irradiated mouse lens sample 9 months p.i. in which the lesion was not almost entirely in the poorly fixed lens area. Only a sectioned lens with a C2-type lesion in OCT with visible diastasis (Fig. 68, D) actually displayed alteration at the presumed spot of the posterior lens in 20x-magnified images (Fig. 68, E, red arrowheads).

Here, the typical protruding rim of the C2-type was discernible. As in 10 weeks old mice irradiated with X-rays, the lesion was composed of a more posterior edge of possible cellular and nuclear debris (Fig. 67, F, red arrowheads) followed by a more anterior zone of long slightly swollen fibre cells (green arrowheads). A control, on the other hand, was completely unsuspicious concerning alterations in the inner cortex and was also in OCT scattering-free (Fig. 67, A-C).

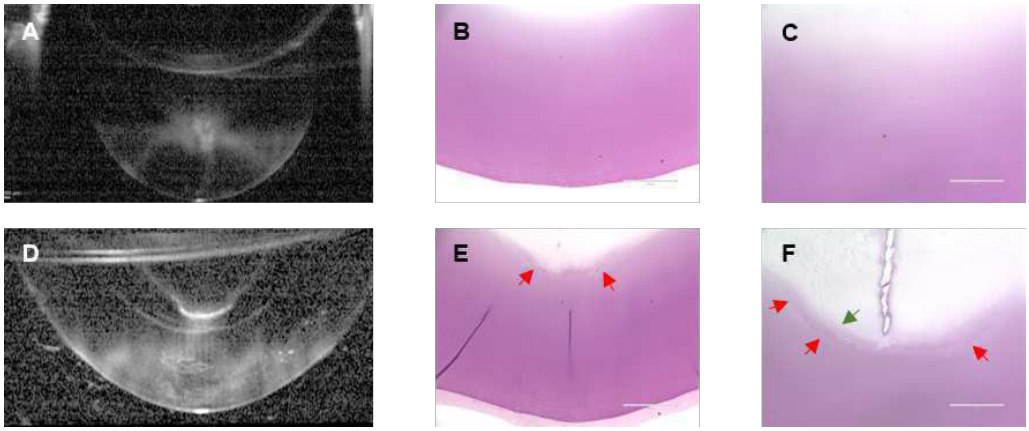

Figure 68.: Histological analysis of neonatal irradiated mice (γ-rays) 8.5 months p.i. in comparison with OCT images of the same mouse. OCT images of a control and an 2 Gy-irradiated mouse lens **(A+D)**. 20x-magnification of lesion site **(B+E)**. 40x-magnification of perinuclear zone **(C+F)**. Cell debris or degenerated nuclei (red arrowheads). Slightly swollen, stretched fibre cell (green arrowheads).

No histological basis for diastasis could be found in the irradiated lens with the C2-type lesion, although this area was generally better fixed by the Davidson solution.

The more severe alteration of the neonatal lenses, the lens extrusion phenotype was perfect to analyse (Fig. 69, A).

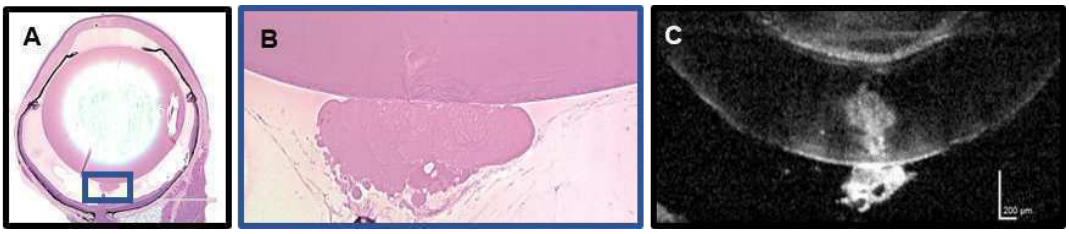

Figure 69.: Lens extrusion example in a 2 Gy-irradiated (γ-rays) neonatal mouse in OCT (8.5 months p.i.) and histology (9 months p.i.). 4x-magnified overview of entire eye **(A)**. 40x-magnified close-up of frame in A **(B)**. OCT record of selfsame lens **(C)**. Modified pictures B+C taken from [258].

As suspected by examination of the phenotype *in vivo* by volume scans (Fig. 69, C, single mid-tomography), lens material was pushed through the small leakages of the capsule into the vitreous. In fact, fine structure of the material in the vitreous proved that fibre cells were bend outside and mostly still intact (Fig. 69, B). Additional

material in the surrounding might be cellular material from burst fibre cells. Because no methylene blue staining was detected in these extrusions, we conclude that no nuclei were present in the extrusion bulge.

8.3 IHC OF THE LENS CAPSULE OF P2 MICE

The extrusion of lens material in 8.75 % of all the γ-irradiated P2 mice brought the lens capsule, especially the posterior lens capsule into the focus. The analysis of several capsules of irradiated P2 mice revealed no differences in comparison to controls (Fig. 70). Neither was the posterior capsule in average thicker or thinner than the capsule of controls (Fig. 70, F vs. H), nor were other parts suspicious or irregular, e.g. the anterior capsule (Fig. 70, B vs. D), or the capsule on top of the lensbow (Fig. 70, A vs. C and E vs. G).

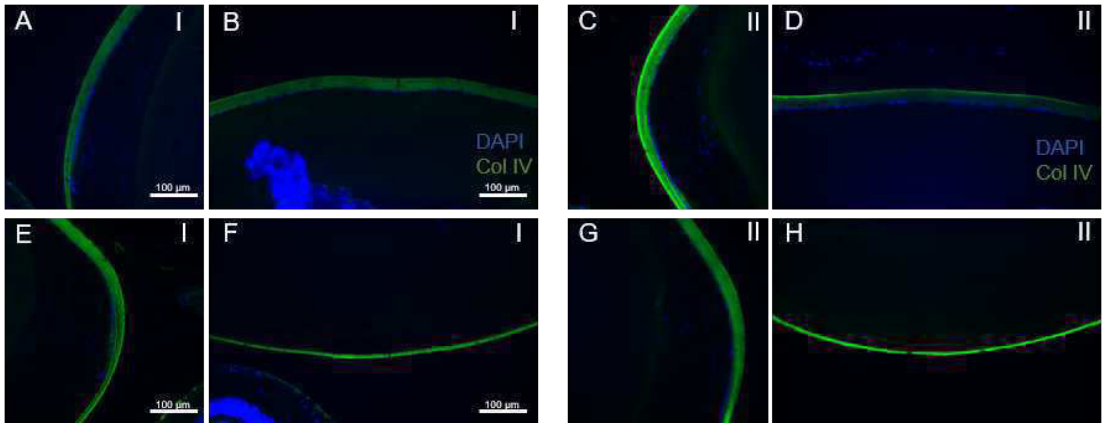

Figure 70.: Col IV distribution in a female control B6C3F1 mouse **(I)** and a female 2 Gy-irradiated (γ-rays) B6RCF1 mouse **(II)** 8.5 months p.i.. Left lensbow **(A+C)**. Anterior capsule **(B+D)**. Right lensbow **(E+G)**. Posterior capsule **(F+H)**. 20x-magnified. DAPI (blue). Col IV (green).

This analysis showed that lenses without lens extrusion had no weakened or impaired capsule, but it could not ruled out that samples with extrusions had irregularly grown capsules in the first place.

9

IMMUNOHISTOCHEMICAL CHARACTERISATION OF POSTERIOR LESIONS IN P70 MICE

Pseudoepithelial cells

To confirm the migration of nuclei in prolonged fibre cells to the posterior pole and the establishment of undifferentiated small pseudoepithelial cells respectively, DAPI-staining was applied to elucidate whether methylene blue-stained particles in histology were actually nuclei (see results section 7.1). As hinted by OCT, a thick posterior lenticular scattering in an irradiated mouse lens could be caused by additional scattering centre (Fig. 71, C, red arrowhead). The whole lens stained with DAPI displayed nuclei-containing cells at the anterior surface (epithelial monolayer) and in the lensbow/transitional zone (Fig. 71, A, yellow arrowheads), but also at the posterior pole appeared some regularly shaped nuclei and some ragged in appearance (Fig. 71, B). Nuclei-containing cells in the area between lensbow and the posterior pole were not identified as in histology (see Fig.58).

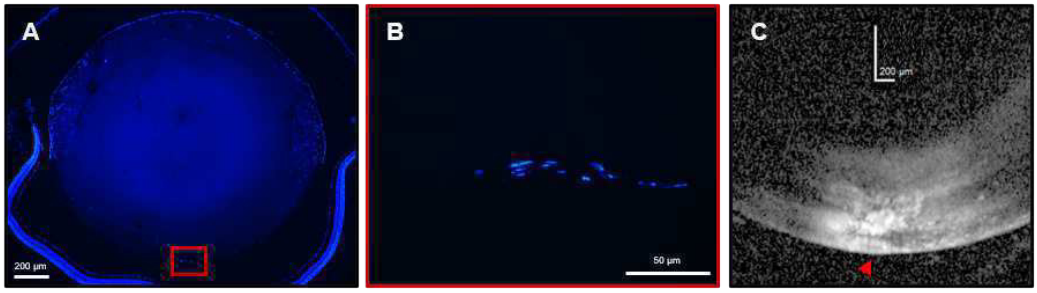

Figure 71.: Example of a DAPI-stained P70 mouse lens 20 months p.i. in comparison with OCT image. 4x-magnified DAPI-stained whole eye, enhanced exposure time for better visibility **(A)**. 40x-magnified close-up of marked red rectangle in A **(B)**. OCT image of the posterior 20 months p.i. **(C)**. Epithelial cells and differentiating fibre cells (yellow arrowheads). Dens scattering at the posterior pole (red arrowhead).

α-cry distribution

Apart from the accumulation of pseudoepithelial cells in the posterior lens, the presence of swollen fibre cells and bodies of liquefied proteins in histology was demonstrated before. Crystallin stainings of posterior lesions illuminated distribution differences for this crucial chaperone protein in the signal-free areas recordable

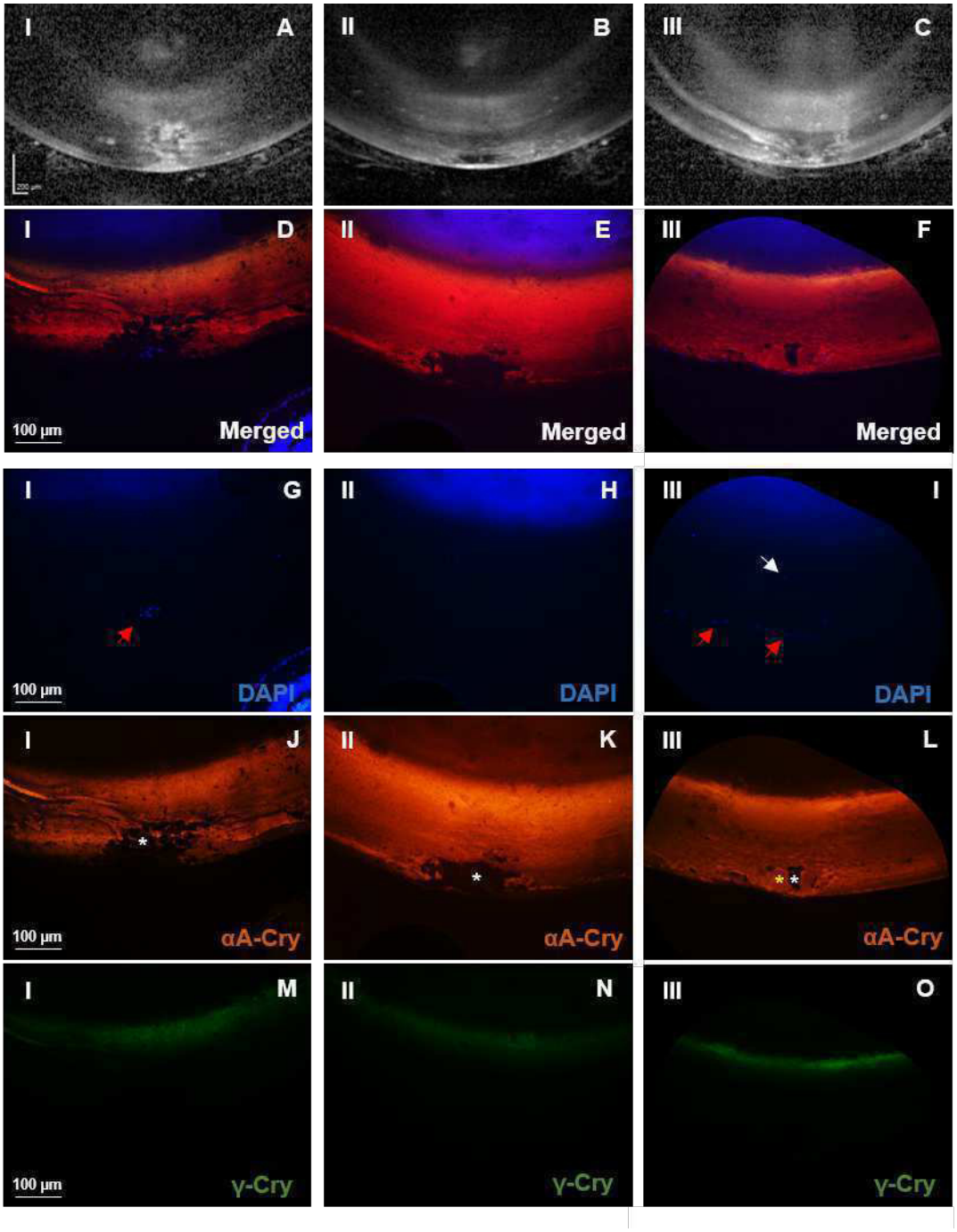

Figure 72.: Lenticular crystallin distribution in posterior lesions of a 2 Gy-irradiated male mutant **(I.)**, 0.5 Gy-irradiated female mutant **(II.)** and 2 Gy-irradiated female WT **(III.)** 20 months p.i.. OCT image **(A-C)**. Merged IHC image **(D-F)**. DAPI **(IG-I)**. αA-cry **(J-L)**. γ-cry **(M-O)**. Pictures D-O 20x-magnified. Red arrows indicate misplaced nuclei. White stars indicate correlates of SF-areas. Yellow star indicates swollen fibre cell. Picture taken from [257].

by OCT (Fig. 72). All three examples displayed posterior lenticular lesions of the SF/S-type (Fig. 72, I+III) or the SF-type (Fig. 72, II). Overall, αA-cry was present in the entire fixed cortex (Fig. 72, J-L), while γ-Cry appeared only as weak signal in the more inner cortex (Fig. 72, M-O). The lesion spots differed drastically. Remarkably, the signal-free areas in OCT correlated with areas devoid of crystallins (Fig. 72, J-L, white stars). As expected by the appearance in the OCT images, the signal-free areas in the SF/S-type lesions were rather fragmented and in the SF-type lesions a whole body. Swollen fibre cells in the lesion (Fig. 72, L, yellow star) emitted αA-cry signal like the surrounding more regular cells in distance to the lesion.

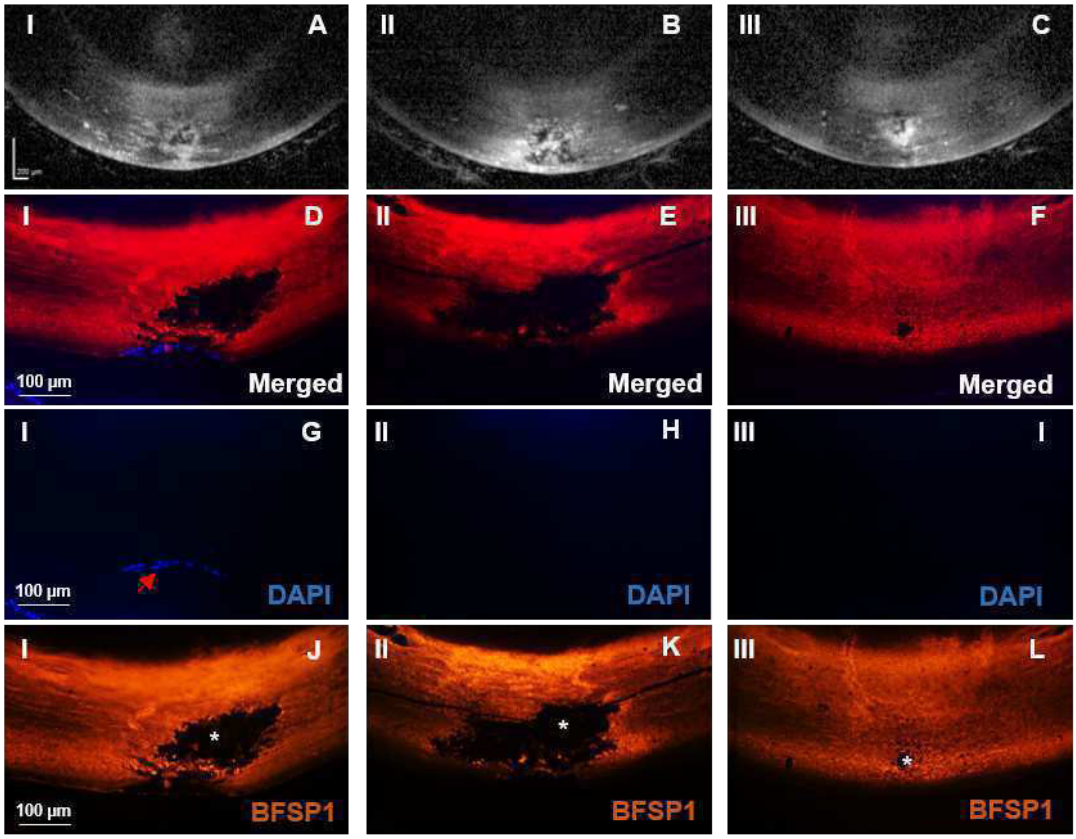

Figure 73.: Lenticular BFSP1-distribution in posterior lesions of a 2 Gy-irradiated female WT **(I.)** and two 2 Gy-irradiated male mutants **(II+III.)** 20 months p.i.. OCT image **(A-C)**. Merged IHC image **(D-F)**. DAPI **(G-I)**. BFSP1 **(J-L)**. Pictures D-L 20x-magnified. Red arrows indicate misplaced nuclei. White stars indicate correlates of SF-areas. Picture taken from [257].

Last but not least, nuclei-containing cells accumulated directly beneath the capsule (Fig. 72, G+I, red arrows) and very few nuclei were spotted within the cortex above

the lesion (Fig. 72, I, white arrow). Cells in the anterior epithelium including the lensbow contained crystallin, but the pseudoepithelial cells carrying nuclei in the PSC did not (Fig. 72, D)! The SF-type lesion was nuclei-free and (Fig. 72, H) and cells adjacent to the signal-free area were less swollen and the suture more normal in appearance (Fig. 72, K).

BFSP1 distribution

Very similar to the α- and γ-crystallin distribution, BFSP1, one of the main intermediate filament proteins of lenticular fibre cells, was neither present in the reservoirs, nor in the pseudoepithelial cells (Fig. 73, J-L). Unlike α-crystallin, BFSP1 was most likely also not present in large swollen fibre cells (contours imaginable in Fig. 73, J+K).

Investigations with another non selective cry-antibody (unsp.) confirmed the crystallin presence in swollen fibre cells (Fig. 74, A, D). Yet, some pseudoepithelial cells were still positive for crystallin (Fig. 74, A, white arrows), although others did not contain crystallin at all (Fig. 74, A, yellow arrows).

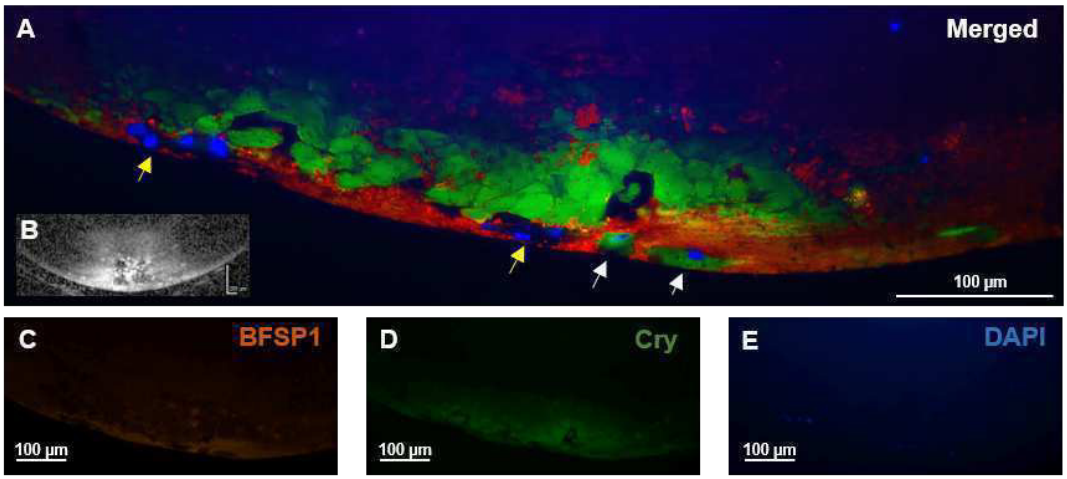

Figure 74.: Lenticular crystallin/BFSP1-distribution in a posterior lesions of a 1 Gy-irradiated B6C3F1 mouse 20 months p.i.. Merged IHC image **(A)**. OCT image **(B)**. BFSP1 **(C)**. Cry (unsp.) **(D)**. DAPI **(E)**. Pictures C-E 20x-magnified. White arrows indicate crystallin-containing pseudoepithelial cells. Yellow arrows crystallin-depleted pseudoepithelial cells.

10

PROTEIN SYNTHESIS ANALYSIS OF ENTIRE LENSES

The highest fold change of expressed proteins relevant for structural and functional integrity of the entire lens were generally expected in lenses irradiated with 2 Gy. Whole-lens lysates of 20 month old mice were tested on dose-dependent expressions of the more inner cortex-associated Cx50 (Fig. 75) and the more outer cortex-associated Cx46 (Fig. 76).

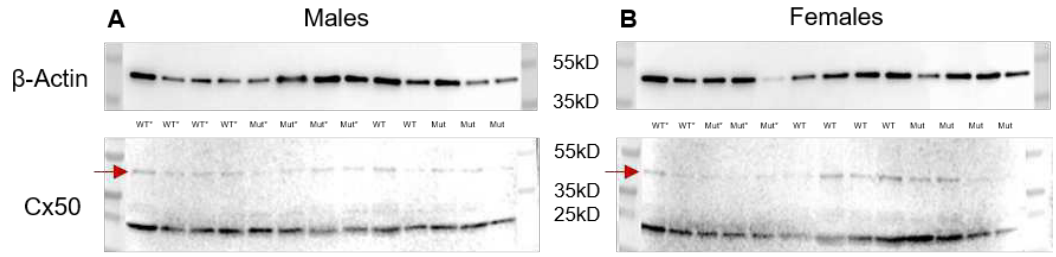

Figure 75.: Western blot with anti-β-actin (top) and anti-Cx50 antibody (bottom) of control and irradiatedlenses 20 months after sham- or 2 Gy irradiation. Males **(A)**. Females **(B)**.

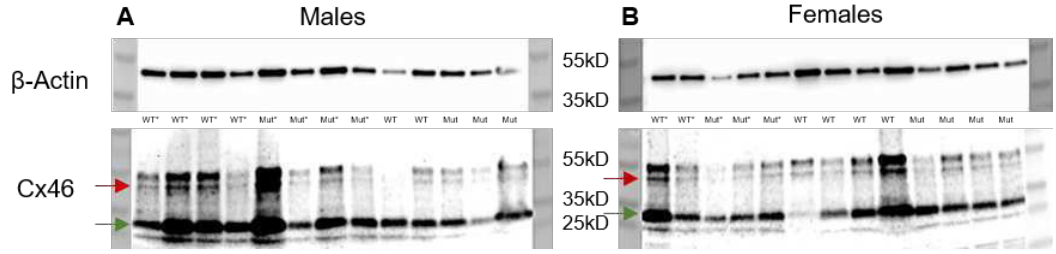

Figure 76.: Western blot with anti-β-actin (top) and anti-Cx46 antibody (bottom) of control and irradiated P70 lenses 20 months after sham- or 2 Gy irradiation. Males **(A)**. Females **(B)**. Stars at the samples indicate irradiation with 2 Gy *in vivo*. Heavy chain at 50 kDa (red arrow) and light chain at 25 kDa (green arrow).

The expression of both connexins was not significantly different in P70 mice exposed to 2 Gy (Fig. 77). There were also no differences along the factors sex and genotype. Data dispersion inconsistency was characteristic for the data set.

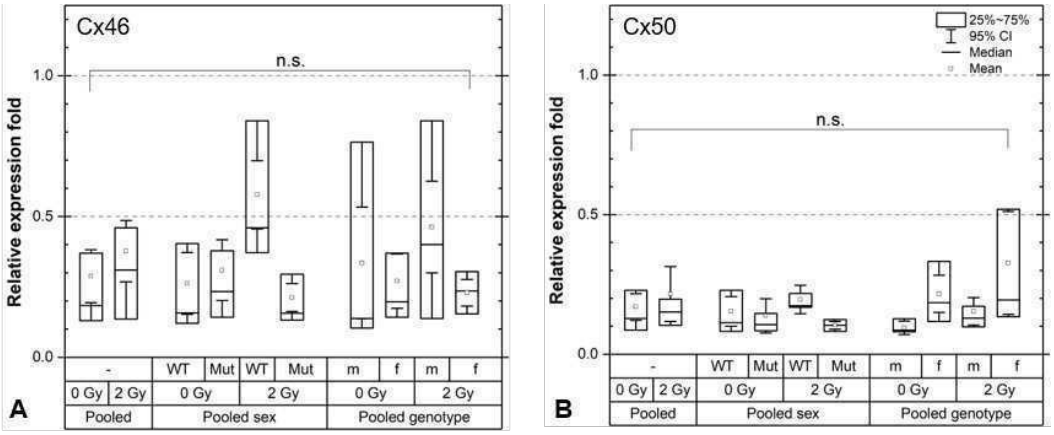

Figure 77.: Western blot statistics regarding Cx46 and Cx50 in 2Gy-irradiated P70 mice. Relative expression of Cx46 **(A)**. Relative expression of Cx50 **(B)**.

The collected samples were also tested on representatives of the direct (SOD1) and indirect (αA-cry) ROS protection system (Fig. 78)+79.

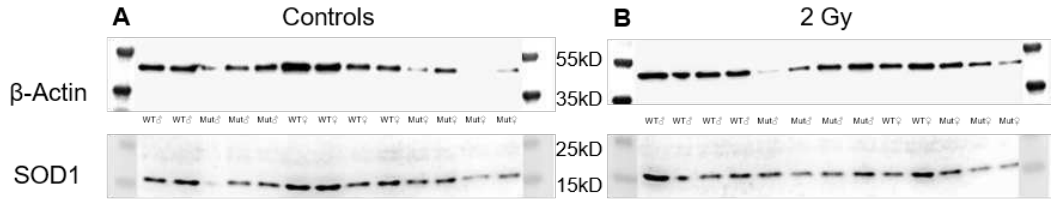

Figure 78.: Western blot with anti-β-actin (top) and anti-SOD1 antibody (bottom) of control and irradiated lenses 20 months after sham- or 2 Gy irradiation. Controls **(A)**. 2Gy-irradiated mice **(B)**.

Neither the expression of SOD1 nor αA-cry was significantly changed based on Western blot band intensities (Fig. 80).

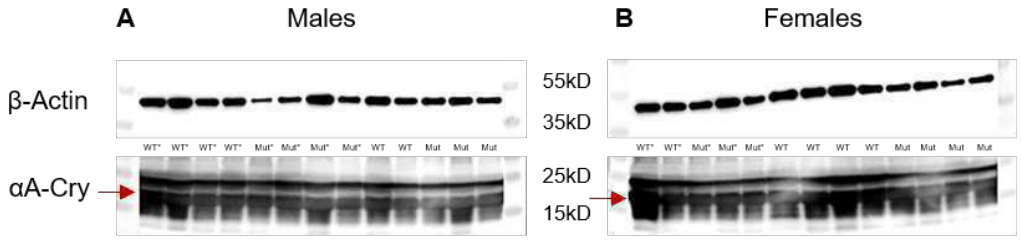

Figure 79.: Western blot with anti-β-actin (top) and anti-αA-cry antibody (bottom) of control and irradiated lenses 20 months after sham- or 2 Gy irradiation. Controls **(A)**. 2 Gy-irradiated mice **(B)**.

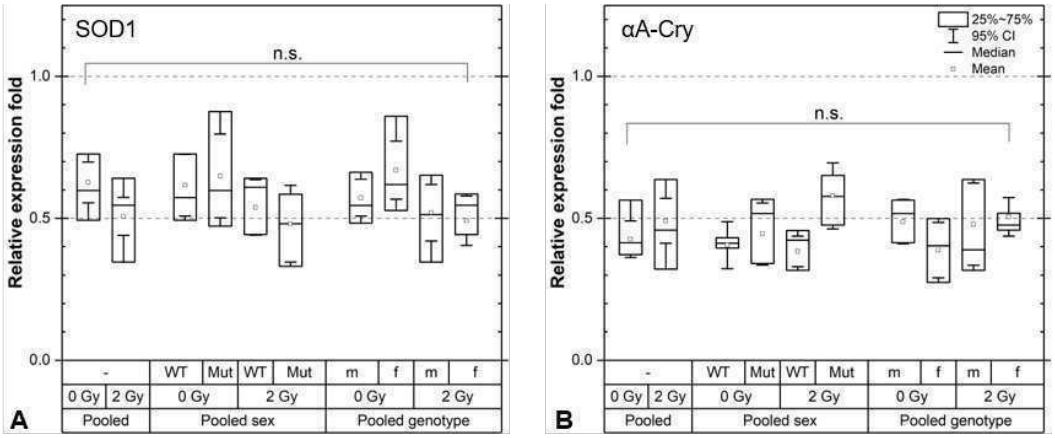

Figure 80.: Western blot statistics regarding SOD1 and αA-cry in adult mice irradiated with 2 Gy. Relative expression of SOD1 **(A)**. Relative expression of αA-cry **(B)**.

11

COMPARING HISTOLOGY AND IHC OF THE RETINA

11.1 HISTOLOGICAL ANALYSIS OF ADULT IRRADIATED MICE

Retinae of P70 mice 20 months p.i. were completely unsuspicious in comparison with controls which was in accordance with OCT measurements (Fig. 81).

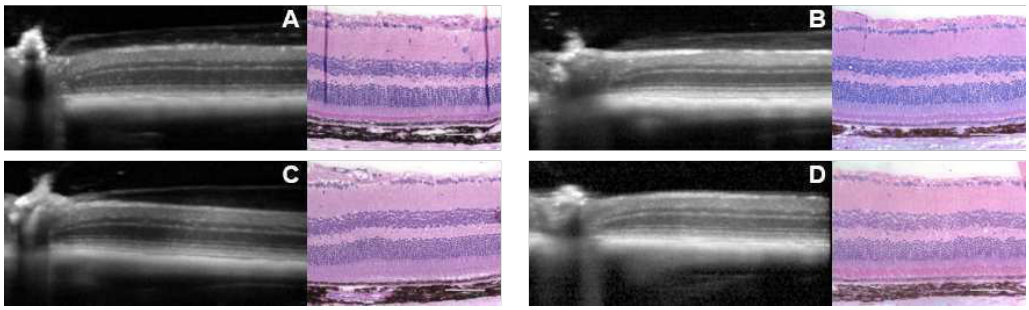

Figure 81.: Representative retinal histology examples of adult sham- and IR-irradiated male WT B6C3F1 mice 20 months after irradiation. Control **(A)**. 0.5 Gy **(B)**. 1 Gy **(C)**. 2 Gy **(D)**. Picture taken from [257].

In some mice, dramatic foldings of the retinae were seen. Single layers formed lopes in the section plain or bifurcated into several different layers (Fig. 82, B+C). Overall, outer nuclear layers could appear wavy and extremely disorganised, while the inner nuclear layer was less in disarray. Inner plexiform layer could swell 3-4 times over their usual thickness. But *in vivo* such retinae appeared to be perfectly normal (Fig. 82, A).

Figure 82.: Retinal foldings in histology in comparison with OCT records. OC tomography of a female mutant irradiated to 0.5 Gy. **(A)**. 10x-magnified retina around the ON **(B)**. 20x-magnified retina close to the ON **(C)**.

ON quantification

In-vivo imaging of neonatal irradiated mice demonstrated already the severe alterations of the retina including patches of complete photoreceptor cell depletion (see result chapter 5). Based on OCT measurements, reduced retinal thickness was hypothesised to be caused by reduced thickness of the neuroretina except the ganglion cell and inner plexiform layer. In histology this hypothesis could be substantiated by comparison of controls and samples of irradiated mice (Fig. 83).

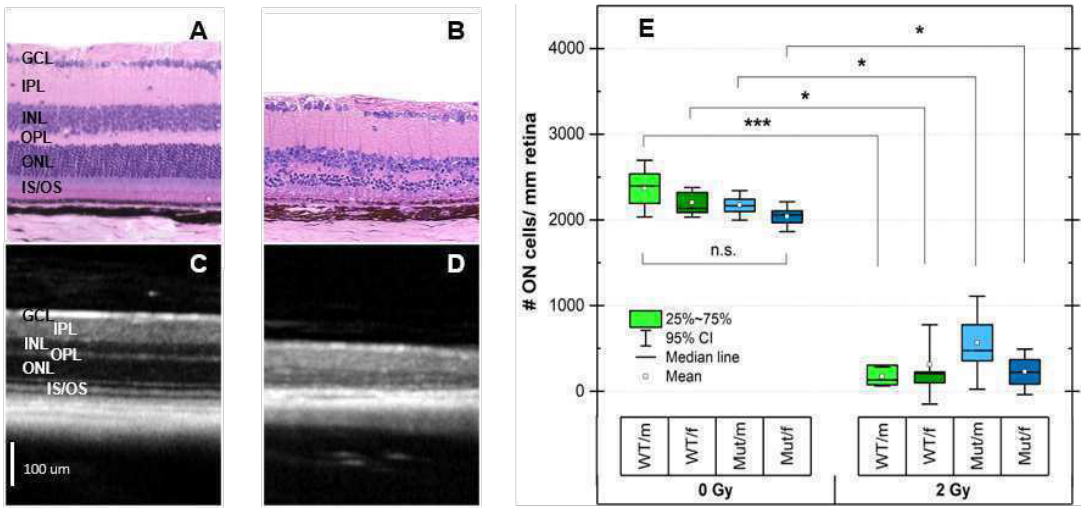

Figure 83.: Number of outer nuclear layer cells in histology of neonatal irradiated mice 9 months p.i. Histological example of a control mouse retina and her *in-vivo* OCT record **(A+C)**. Histological example of a 2 Gy-irradiated mouse retina and her *in-vivo* OCT record **(B+D)**. Number of outer nuclear cells of every group **(E)**. Ganglion cell layer (GCL), inner plexiform layer (IPL), inner nuclear layer (INL), outer plexiform layer (OPL), outer nuclear layer (ONL), inner/outer segments of photoreceptor cells (IS/OS). Significances were determined by Mann-Whitney test. Modified picture taken from [258].

In controls the nuclear layers were structured in aligned columns, the outer layer more than the inner one (Fig. 83, A). In irradiated retina, though, both layers appeared most irregular (Fig. 83, B). Here, no clear column organisation was recognisable and single outer nuclear cells intermingled with the outer plexiform layer or the inner nuclear layer. Number of outer nuclei (photoreceptor cells) was determined by counting in a 500 µm retina section 100 µm distant from the optic nerve. Mean differences were drastic, but statistically not overwhelming (Fig. 83, E). The highest reduction in wake of irradiation was ascertained in male WTs (relatively

94 %). Lowest reduction was found in male mutants (78 %). Female WTs, male and female mutants were only significantly different within an accepted α-error of 5 %.

Retinae of irradiated neonatal mice were remarkable dishevelled in layer organisation and perhaps tended to restructure their blood supply. In course of this process, several disorganised sites of possible neovascularisation were observed in histology (Fig. 84). Very typical for this was the breakthrough of the retinal pigment epithelium below at the spot, connecting the choroidea and the ganglion cell layer. *Structural loss*

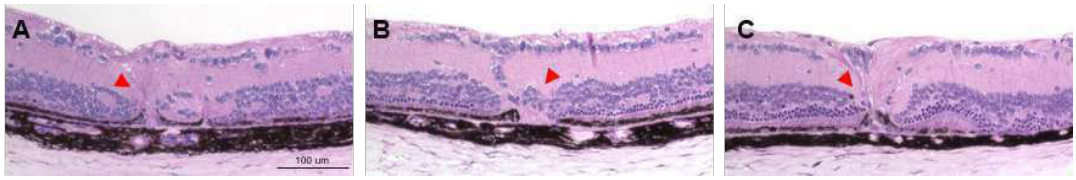

Figure 84.: Disordered retinal sites within histology of neonatal irradiated mice as possible spots of neovascularisation.

11.3 IMMUNOHISTOCHEMICAL DETECTIONS IN THE RETINA

Spots that matched the appearance of Fig. 84 in immunohistochemical experiments assessed by the composition of DAPI-positive cells in irradiated P2 mice were investigated on the vascular-associated marker α smooth muscle actin (αSMA). Actually, the example did not provide hints that vessels grew through the retina coming from the choroidea. αSMA was only detected in the choroidea (Fig. 85, white arrow).

Figure 85.: αSMA staining in the 2 Gy-irradiated P2 retina 9 months p.i. Staining with DAPI (blue) and αSMA (green). Modified pictures taken from [258].

Calretinin staining allowed to get insights into the neuronal condition of the severely impaired retinae of irradiated P2 mice. Controls at 9 months after sham-irradiation

displayed few amacrine cells in the top section of the inner nuclear layer, ganglion cells in the ganglion cell layer and regularly ordered synaptic connections in three distinguishable bands in the inner plexiform layer (Fig. 86, A+C). As demonstrated in histological sections, inner and outer nuclear layer of the 2 Gy-irradiated P2 retina were partially fused. Therefore, it appeared that in irradiated samples retinal amacrine cells were also in the upper outer nuclear layer and, more importantly, slightly enhanced in numbers (Fig. 86, E+G, blue arrow).

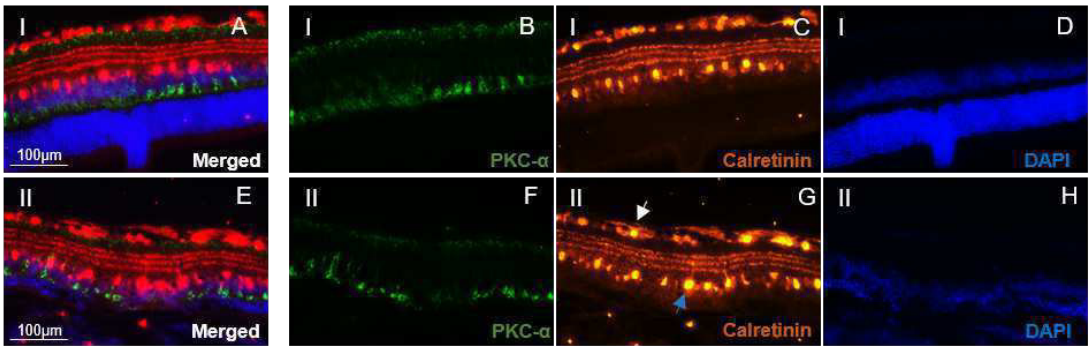

Figure 86.: Calretinin distribution in the P2 retina of a control **(I)** and a 2 Gy-irradiated (γ-rays) mouse **(II)** 9 months p.i. Merged **(A+E)**. PKC-α **(B+F)**. Calretinin **(C+G)**. DAPI **(D+H)**. 20x-magnified. Ganglion cell (white arrow). Amacrine cell (blue arrow). Pictures taken from [258].

Apart from that, the characteristic three strata in the inner plexiform layer were in disarray at some spots. Hence, a disruption of signal transduction in some retinal sections was plausible to assume. But, as displayed in Fig. 86 G, the layer composition could also be quite normal.

Bipolar cells recognisable by their characteristic high PKCα expression in the axons and dendrites in the upper inner and entire outer plexiform layer were in sham- and 2 Gy-irradiated P70 mice 20 months p.i. similarly distributed (Fig. 87, A+B). Irradiated retinae seemed to express more PKCα, but that might have been due to possible irregularities with the Sudan black blocking (Fig. 87, D+E). PKCα was also expressed in the 2 Gy-irradiated P2 retina 9 months p.i., nonetheless, distribution was not regular any more (Fig. 87, F and 86, F). Some sections in the retina were deleted of PKCα-signals. That could mean that despite a relatively less affected inner nuclear layer (which contains the nuclei of bipolar cells) either less bipolar cells were present in after exposure to IR (maybe only a population

of the two bipolar cells) or simply less connections were detected because missing innervation by photoreceptor cells.

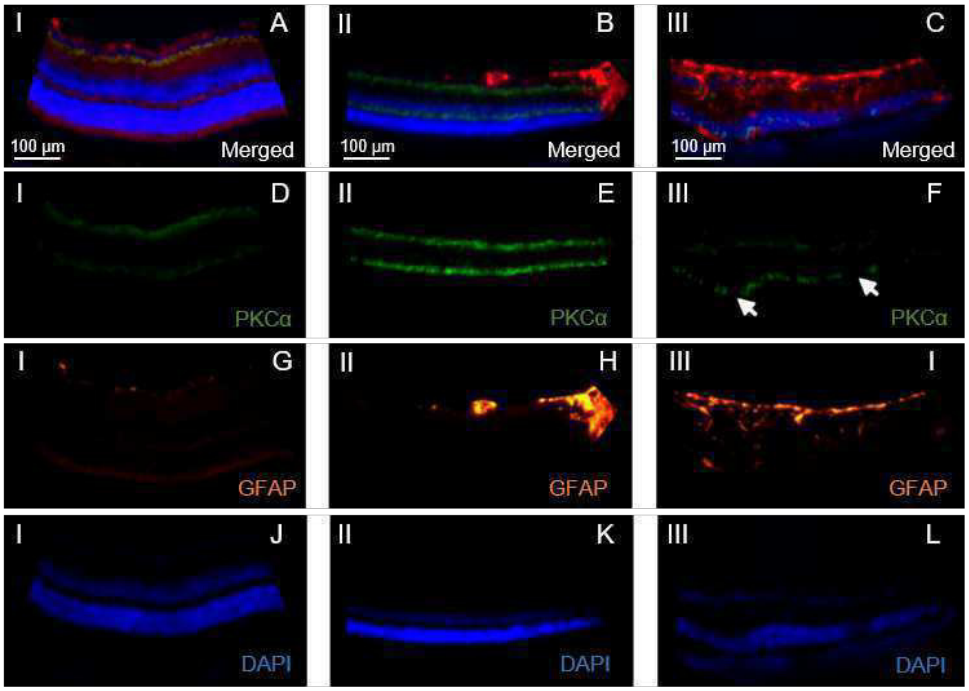

Figure 87.: PKCα and GFAP distribution in irradiated P2 and P70 retinae. P70 control **(I)**, 2 Gy-irradiated (γ-rays) retina 20 months p.i. **(II)** and 2 Gy-irradiated (γ-rays) P2 retina **(III)**. Merged **(A-C)**. PKCα **(D-F)**. GFAP **(G-I)**. DAPI **(J-L)**. 20x-magnified.

The intermediate filament GFAP produced by neuroglial cells in the retina was scarcely expressed in the ganglion cell layer of controls 20 months after irradiation (and 9 months after sham-irradiation, not shown) (Fig. 87, A+G). In 2 Gy-irradiated P70 mice, the expression was not significantly increased (Fig. 87, B+H, optic cup on the right side displayed also in controls always enhanced GFAP signal). Irradiated P2 mice, on the other hand, stood out with a remarkable higher GFAP expression in the ganglion cell layer and by bolt-like lines pervading the entire retina (Fig. 87, C+I).

These spikes were not only fine vertical lines predominately seen in the inner plexiform layer. As demonstrated in a younger sample irradiated with X-rays at P2,

Figure 88.: GFAP distribution in a X-irradiated P2 retinae 10 weeks p.i. GFAP (red). DAPI (blue). 40x-magnified.

GFAP could accumulate thickly in the nuclear layers too (Fig. 88).

The photoreceptor depletion in irradiated P2 retinae, hinted by DAPI-staining, was evaluated with rhodopsin staining. As assumed, rhodopsin, as visual pigment of these cells, was reduced in irradiated samples (89, F compared with B). General lower expression was accompanied by section with no rhodopsin signal at all (red bracket in F).

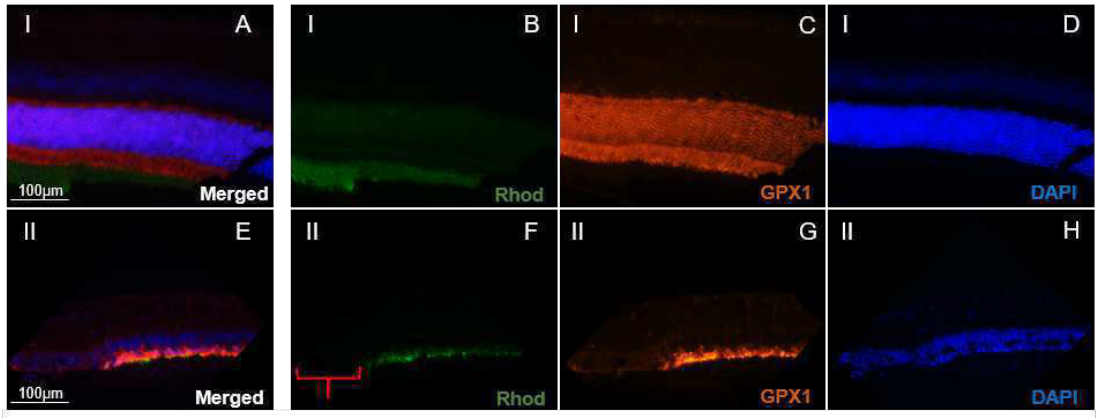

Figure 89.: Rhodopsin and GPX1 distribution in P2 retinae. Control **(I)** and 2 Gy-irradiated (γ-rays) P2 retina **(II)** 9 months p.i. Merged **(A+E)**. Rhodopsin **(B+F)**. GPX1 **(C+G)**. DAPI **(D+H)**. 20x-magnified. Red bracket indicates depleted photoreceptor sections. Pictures taken from [258].

The expression of glutathione peroxidase 1 (GPX1), an antioxidant enzyme to prevent ROS damage, was also altered. In controls, GPX1 was present in the entire outer nuclear layer and in the inner and outer segments (89, C). But in irradiated samples the enzyme appeared to be not present in the cell body any more (89, G). In the remaining inner and outer segments, though, GPX1 appeared to be overexpressed in comparison to the control.

12

COMPARING HISTOLOGY OF THE CORNEA

Samples displaying milky corneae in OCT and Scheimpflug measurements (Fig. 90, C+F) were only observed in P70 mice, never within the 9 months of the P2 mice lifetime. P70 samples were sectioned 20 months after irradiation to understand the reasons for late occurring corneal opacification of the aged concerning mice (Fig. 90, A+D).

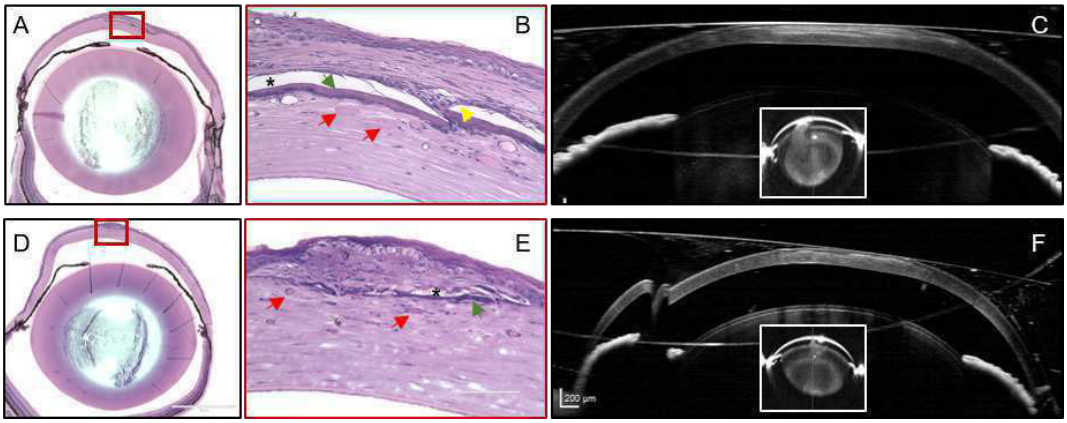

Figure 90.: Comparing histology of the cornea from both eyes of a 0.5 Gy-irradiated mouse 20 months p.i. 4x magnification of the entire eye **(A+D)**. 40x-magnified areas of corneal lesions **(B+E)**. OCT image of the belonging eye with inserted small Scheimpflug picture **(C+F)**. Vessels with erythrocytes (red arrows). Bifurcations of the basal lamina (green arrows). Misplaced epithelial cells (yellow arrow). Intercellular free space (black star). Modified pictures A-C taken from [257].

In-vivo records hinted that the lesion site was directly in the centre of the cornea opposite to the pupil (red frames). Apparently, additionally to the regular epithelium including the basal lamina, large layers of lamina-like structures grew into the stroma, quite beneath the epithelium (Fig. 90, B+E). Those layers were far thicker than the lamina under the columnar basal epithelial cells (Fig. 90, B, green arrow). Mainly over this pseudo-lamina, several epithelial cells of rather polyhedral shape gathered (Fig. 90, B, yellow arrow). The stromal/pseudoepithelial compound seemed to lack tight connections, because empty caverns appeared often (Fig. 90, E, black stars). In the altogether unaffected stroma below, several vessels could be detected by means

of erythrocytes (Fig. 90, B+E, red arrows) and more empty vacuoles were discernible than in controls (white spaces in the stroma).

13

BIOMETRICS, MOUSE CONDITIONS AND SURVIVAL ANALYSIS OF P70 COHORTS

13.1 WEIGHTS

The weight of investigated murine cohorts followed an almost regressive course. After a relatively linear increase of weight until 7-8 months after irradiation, weights either stagnated 4-8 months for males and dropped afterwards, or increased slightly 8 months further for females and stagnated afterwards (Fig. 91, A+B).

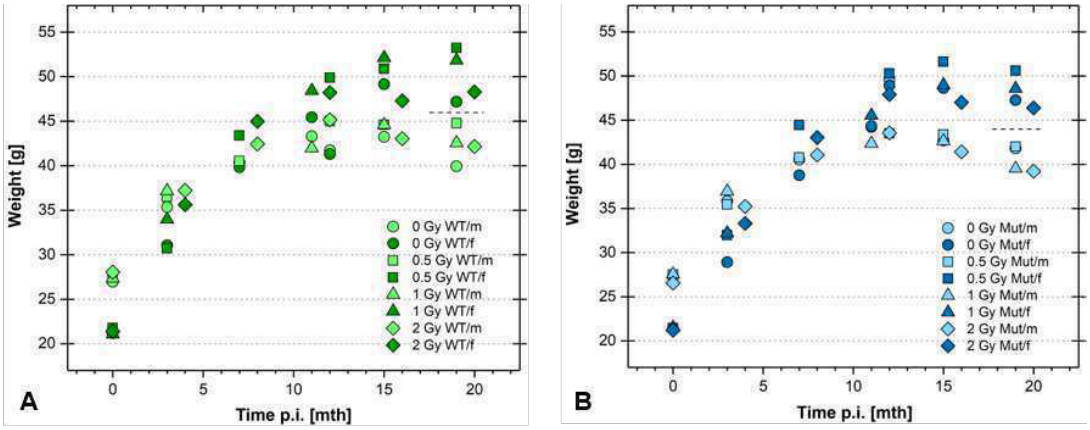

Figure 91.: Mean weight monitoring of control and irradiation cohorts at several time points. Weights of WTs **(A)**. Weights of mutants **(B)**. Sex separation (dashed line). No dispersion measure for clarities sake.

Three-way ANOVA was performed and analysed *post hoc* with Tukey correction (Tab. 32), in which cohorts of 19 and 20 months p.i. were pooled. All three independent main factors, genotype, sex and dose were significantly responsible for mean differences of population weights (dependent variable) sorted by these factors. The most discriminating factor was sex of the animals (Δmean = 7.64 g). The relatively lower weight of males (15.5 %) was highly significant ($p \rightarrow 0$). Dose-related discrepancies of mean weight were unravelled with *post hoc* testing: only in the 0

Gy/0.5 Gy and in the 0.5 Gy/2 Gy comparison mean differences were significant and defined the overall p-value for the factor dose (0.0002). Two-factor or three-factor interactions were not found.

Table 32.: Main effects for murine mean weights of long-term cohorts determined by three-way ANOVA and Tukey *post-hoc* test at the end of observation time (19-20 months p.i.).

Factor	Level	Mean	ΔMean	p-value
Line	WT	46.39	1.79	$5*10^{-3}$
	Mut	44.36		
Sex	Male	41.52	7.64	$\rightarrow 0$
	Female	49.32		
Dose	0 Gy	44.36	-3.47 **(0 vs. 0.5)**	$2*10^{-4}$
			-1.43 (0 vs. 1)	
			0.03 (0 vs. 2)	
	0.5 Gy	47.72	2.04 (0.5 vs. 1)	
			3.51 **(0.5 vs. 2)**	
	1 Gy	45.52	1.46 (1 vs. 2)	
	2 Gy	43.1	-	

Significant differences (Tukey test) were written in bold font. p-values referred to level-overarching significances. Model (DF = 5) $p \rightarrow 0$.

13.2 LENS SIZE OF CHOSEN EXPERIMENTAL GROUPS

Lens thickness was determined by LASER interference biometry (LIB), 20 months after irradiation, but did not reveal any thickness differences between controls, animals of the 0.5 Gy cohort or males of the 1 Gy cohort (Fig. 92, A). Even pooled mean lenticular thicknesses revealed no relevant differences (Fig. 92, B).

13.3 MOUSE CONDITIONS AND BARBERING

The barbering of P70 mice was punctual noticed for 2/3 of the controls and the 1 Gy and 2 Gy cohort approximately 4 months after irradiation (Tab. 33, 0.5 Gy mice conditions were not recorded). Noticed were barbers (separated) and animals with removed body hair (mostly in the face) and plucked whiskers. Since the compilation represented just the point prevalence of behaviour (barbers) and grooming phenotypes (hair and whiskers loss), higher prevalences of barbers and recipients 20

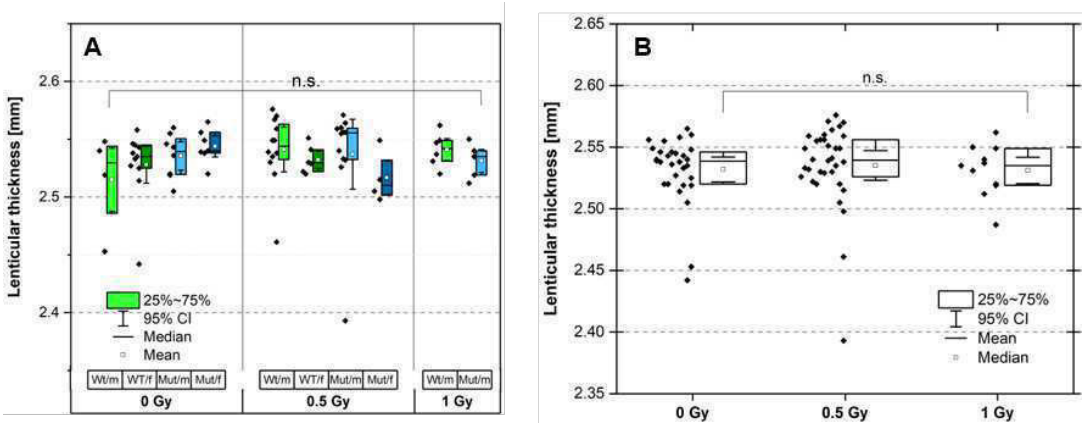

Figure 92.: Lenticular thickness measured with LIB. Groups of all sham- and γ-irradiated adults 20 months p.i. **(A)**. Lenticular thickness pooled by dose; only males in the 1 Gy cohort **(B)**. Significances determined by Mann-Whitney test.

months after irradiation have to be considered. Altogether, data was biased because male mice (sham- and γ-irradiated) of the 0.5 Gy and 1 Gy cohort were held with houses in the their cages, whereas the 2 Gy cohort males were held without houses in their second half of life.

Table 33.: Barbers and recipients of barbering.

Dose	Group	#Barbers	#Hair	#Whiskers	#Hair&Whiskers
0 Gy	WT ♂	2/14	0/14	0/14	0/14
	WT ♀	1/14	2/14	0/14	0/14
	Mut ♂	0/14	0/14	0/14	0/14
	Mut ♀	0/14	0/14	0/14	0/14
1 Gy	WT ♂	2/20	0/20	3/20	3/20
	WT ♀	3/20	0/20	1/20	8/20
	Mut ♂	0/20	0/20	0/20	0/20
	Mut ♀	2/20	0/20	3/20	3/20
2 Gy	WT ♂	0/20	0/20	0/20	0/20
	WT ♀	1/20	2/20	0/20	3/20
	Mut ♂	1/20	0/20	3/20	3/20
	Mut ♀	1/20	0/20	0/20	5/20

Number of barbers in a group (#Barbers). Number of animals with partially removed hair (#Hair). Number of animals with removed whiskers (#Whiskers). Number of animals with partially partially removed hair and whiskers (#Hair&Whiskers).

Pooled cohorts

The Kaplan-Meier plots of controls, the 0.5 Gy and the 1 Gy cohorts were within their respective 95 % confidence interval (Fig. 93). Only the survival probability of the 2 Gy cohort began to differ ~ 600 days after birth. Overall log-rank test, though, revealed significant differences between the overall survival probabilities of all cohorts ($p = 2.6*10^{-4}$). This analysis was based on the definition of an event that included eye swelling, visible tumour growth and subsequently killing (in accordance with animal welfare), severe worsening of general condition and animals found dead. Death following anaesthesia and killings after skin abscesses, broken limbs or penis prolapses were not count as events.

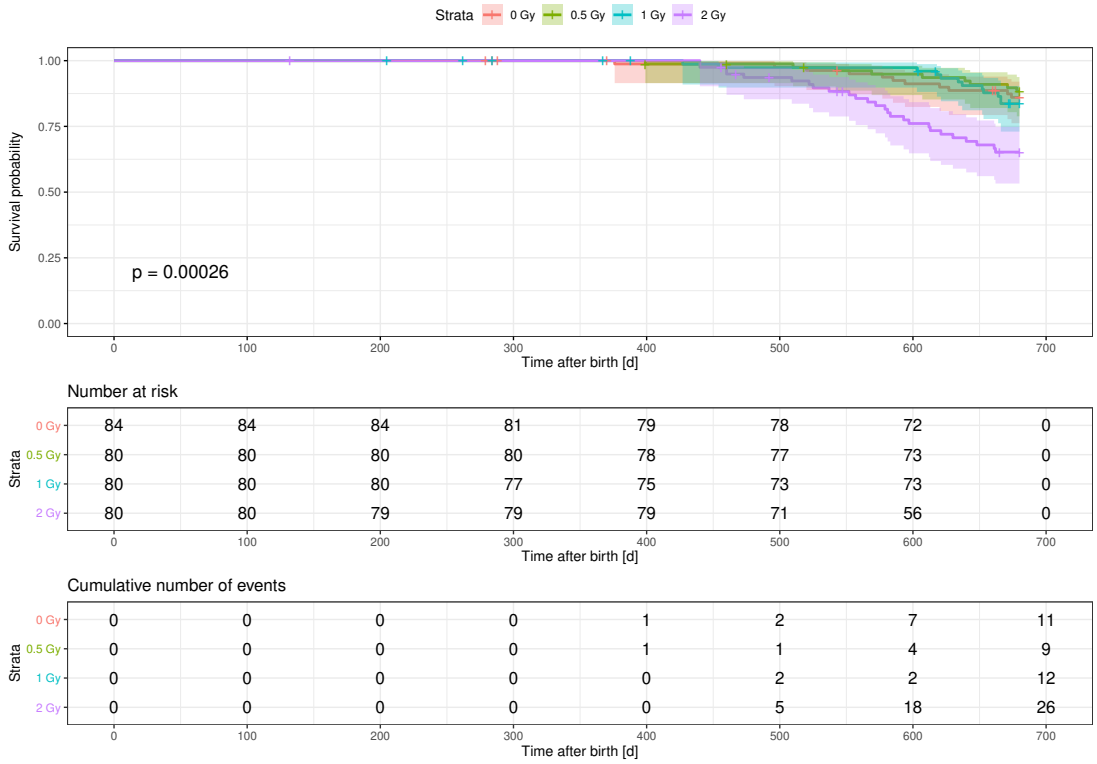

Figure 93.: Survival probabilities of long-term cohorts (Kaplan-Meier plot) beginning at birth (Irradiation at P70). 95 % confidence interval as coloured coat of every stratum. Event-free deceased animals marked with little perpendicular bars. Note that numbers at risk were also reduced by non-eventual dead. Picture taken with permission from the supplement of [248].

Hazard ratios

By using Cox regression model to estimate the impact of independent variables for survival until an event occurred, hazard ratios were determined (Fig. 94). Survival hazard for animals irradiated with 2 Gy was 3.06 higher than for controls ($p = 0.002$), whilst exposure to 0.5 Gy and 1 Gy had no influence on the survival hazard [248]. Surprisingly, the heterozygous *Ercc2* mutation was almost protective for the animals, halving the hazard to 0.64 ($p = 0.09$). No sex differences were recognised in the survival analysis.

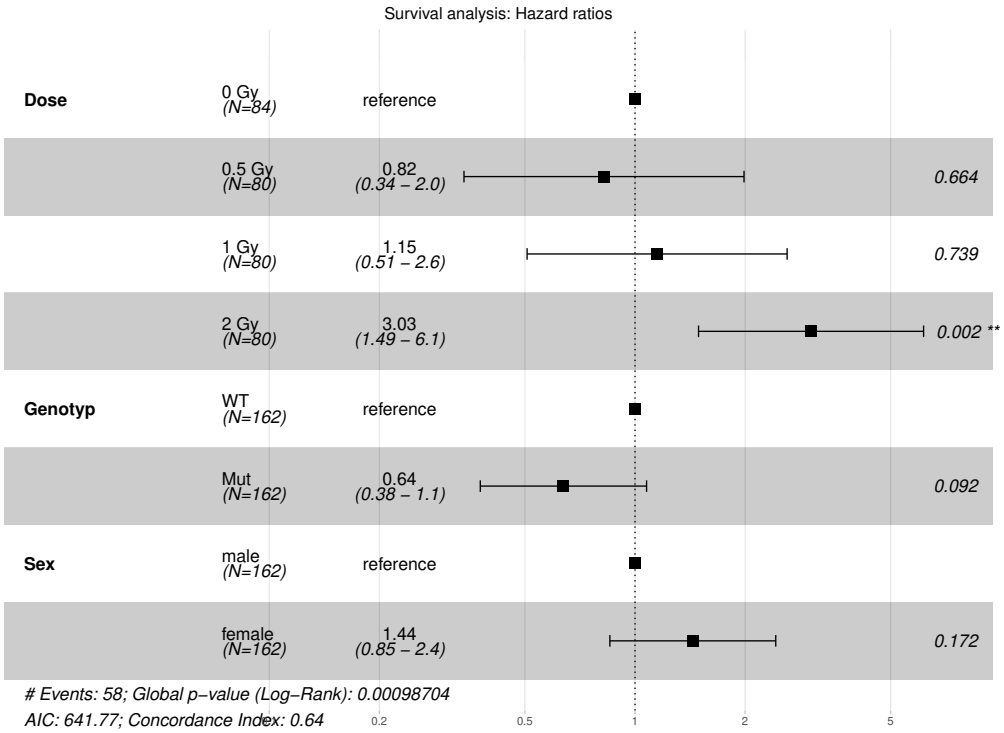

Figure 94.: Survival hazard ratios with regard to main factors for long-term P70 cohorts.

2 Gy-irradiated females

Of all groups the female WT group exposed to 2 Gy of IR was the most prone for early death (Fig. 95, violet line). In fact, 65 % died an event-related natural or forced death within the observation time, but only ~ 9 % of the controls. One fifth of the cohort had to be killed because of eye swelling. Hazard for this irradiated group to suffer an early death due to the dose of 2 Gy was 13 times higher than in controls ($p < 0.001$, plot not shown). The second group highly affected was constituted by the irradiated female mutants (purple line). Females together were responsible for

20 of 26 events in the 2 Gy cohort until 680 days after irradiation. Of all criteria

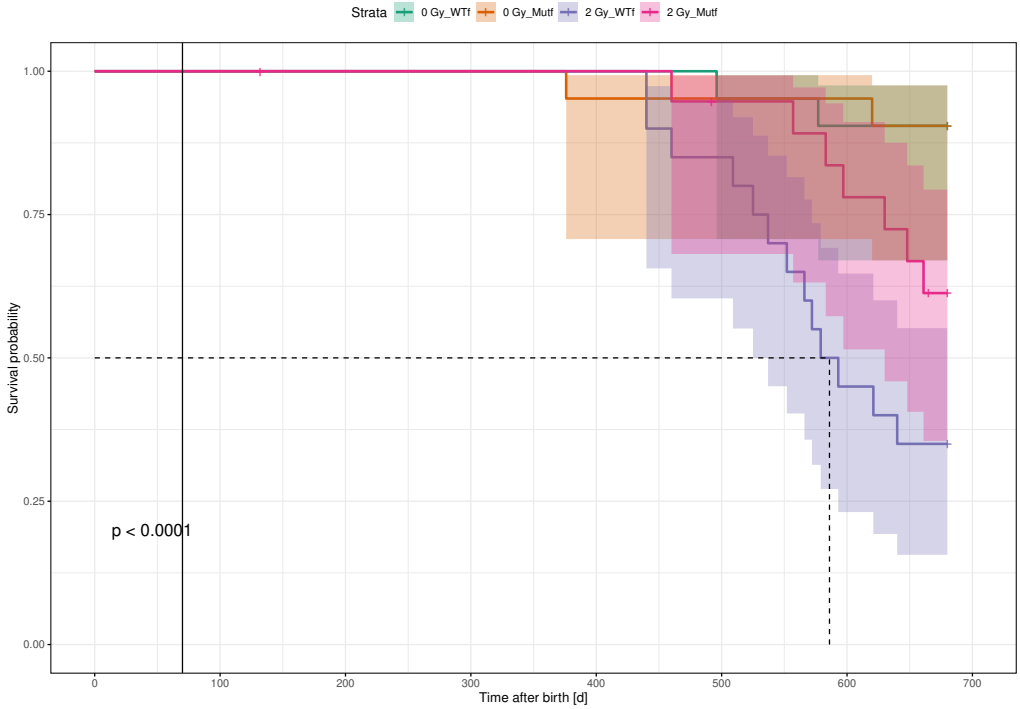

Figure 95.: Kaplan-Meier plot for sham- and 2 Gy-irradiated female WTs and mutants. Vertical line indicates irradiation. Dashed line indicates median survival time if reached. p-value of overall log-rank test. Coloured area around survival probability plots indicates 95 % CI.

Events

of events that sampled out an animal, besides it was found dead, eye swellings, tumours/belly swelling and a poor general condition comprised the better part of reasons (Tab. 34). 51 of 58 events were triggered by them. 7 mice were killed in the wake of anaesthesia, broken legs or penis prolapses and considered non-eventual.

Most affected organs in *post-mortem* pathological analysis in all cohorts were the murine genitals. Of course they were less often cause for experimental abortion, but were seen in the final pathological examination. A dose of already 0.5 Gy made it 10.03 times more likely that animals formed a genital neoplasia (Fig. 96, p = 0.027). Further increase of dose to 2 Gy almost doubled the hazard risk. The heterozygous *Ercc2* mutation had no effect, but sex had. Females developed 12.04 times more likely a genital neoplasia than males.

Table 34.: Event-defining causes before regular endpoint.

Cause	Dose	#events/#cohort	Median age [d]
Found death	0 Gy	2/84	557
	0.5 Gy	3/80	569
	1 Gy	6/80	651
	2 Gy	6/80	523
Tumour/Swelling	0 Gy	2/84	581
	0.5 Gy	1/80	542
	1 Gy	2/80	652
	2 Gy	7/80	593
Eye swelling	0 Gy	1/84	620
	0.5 Gy	2/80	454
	1 Gy	3/80	603
	2 Gy	9/80	583
Poor general condition	0 Gy	4/84	524
	0.5 Gy	2/80	657
	1 Gy	1/80	664
	2 Gy	4/80	576

Most abundant causes for premature losses of experimental animals before endpoint at 680 d. Found dead, irrespective of reason, swelling of the stomach or visible tumours at the body, eye swelling, poor general condition especially because of weight loss.

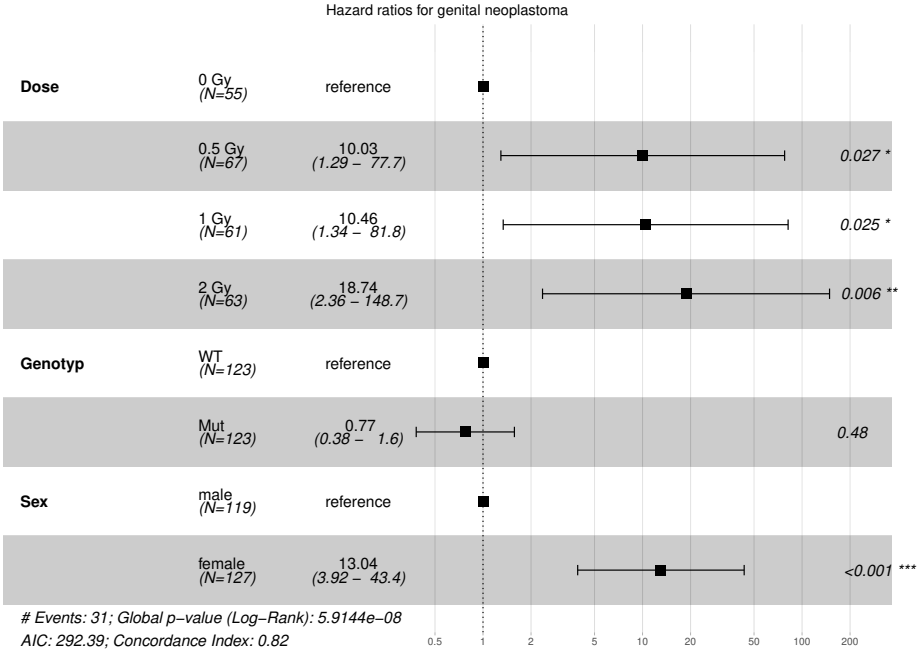

Figure 96.: Hazard ratios for genital neoplasm in all investigated cohorts.

Part IV.

Discussion and conclusions

1

METHOD ASSESSMENT

Every applied method had to be tested on the criteria validity, objectivity and reliability to fulfil scientific requirements. These criteria are intuitively accessible by the keywords 'explanatory power', 'subject independence' and 'reproducibility' [259, chapter 1].
In the following paragraphs, every method used in this thesis was critically assessed, whereas experimental certainty was combined with theoretical considerations (Tab. 35).

Table 35.: Overview over method quality ranking.

		Criteria		
		Validity	**Objectivity**	**Reliability**
Method	Histology	+	+	+
	Immunolocalisation	++	++	++
	LIB	+++	+++	+++
	OCT	++	+++	+++
	Scheimpflug*	+++	+	++
	Virtual drum	+	+	–

Combined potential and practical validation. Validity relates to nature of method, objectivity to final analysis and reliability to the process of method. Flawless (+++), satisfying (++), limited satisfying (+), doubtful (-). Scheimpflug measurement in one image mode (*).

Histology

A histological section of the eye can never be completely valid respective scientific questions concerning all parts of the eye. Especially the lens nucleus is not accessible for fixation solutions (paraformaldehyde as well as Davidson solution) as experience tells (Fig. 97, A+B, red encircled area). Questions about pathological alterations of the lens are therefore only partially possible to answer. Additionally, section interpretation is highly subjective (e.g. nuclei identification). Assessments are also dependent on the chosen section with occasionally very localized alterations which renders assessments upon it theoretical, but not practical 100 % reliable.

IHC

The perniciousness of the immunohistochemical *in-situ* method lies of course in the assignment of chosen target proteins and the corresponding biological pro-

cesses which the experimenter believes to read in it. If the experimenter hypothesises about the distribution of a certain molecule in a sample, then the method is to be consider content-valid. But should findings be connected with interpretations of biological processes, it is highly doubtful to expect something meaningful from immunohistochemical stainings. For instance, it is obvious to relate the phosphorylated histone γH2AX with radiation-induced double strain breaks and their repair. But this is not at all the only possibility for the occurrence of γH2AX foci. Besides, the validity is also reduced by the lacking specificity of primary antibodies for a certain epitope.

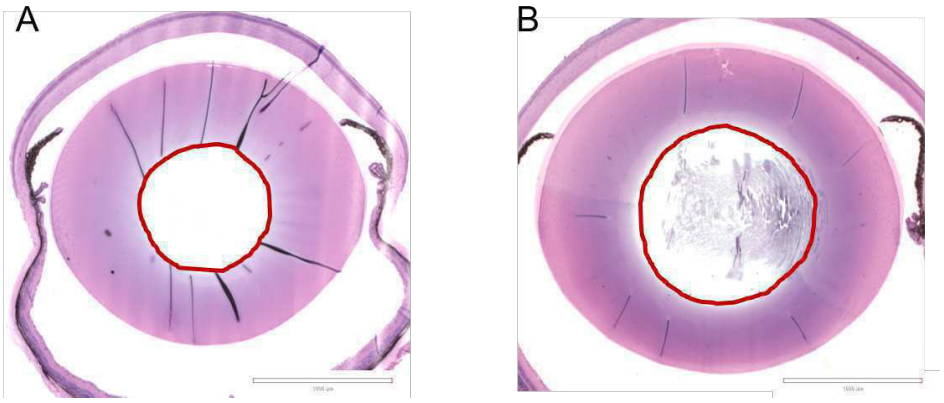

Figure 97.: Degree of fixation of Davidson-fixed and plastic-embedded eyes. Representative section of the mid-sagittal eye plane of a 10 weeks old female WT mouse irradiated with 2 Gy at P2 **(A)** and a 20 months old male mutant mouse irradiated with 1 Gy at the age of 10 weeks **(B)**. Red-marked areas sign lens tissue that missed fixation as recognisable by missing staining.

Immunohistochemistry is basically objective, if grey value-based tools are applied on equally recorded specimens. Actually, the antibody/antigen complex formation has a condition-dependent probability. A simple fluctuation of moisture whilst the incubation or insufficient blocking of antigens could lead to increased signal backgrounds [259, pp. 171-172]. This compromises the reliability.

LIB The LASER interference biometry is a flawless valid, objective and reliable method. Due to the property of interfaces to bring coherent light out of phase, it is possible to measure those interfaces along the optic axis, which renders this method valid. Provided the optimal signal to noise ratio and the recording of at least 5 measurements, variances between two operators are negligible and the results can

be perfectly reproduced.

Scheimpflug

Scheimpflug imaging is a valid method without restrictions. The method inquires the degree of opacification in the eye lens and exactly this parameter is delivered (please mind that there is no contradiction between the high validity of the method and the fallacies we introduced in the result section 2.5). Imaging data of the Scheimpflug camera is nonetheless not satisfying objective within the measuring and analysis process. The method is not objective (in the one image measurement mode) because anterior reflection events are assessed by operators differently. Therefore, reflections might be omitted in recording by purpose, though the might have a real cause in the lens (Fig. 98, Scheimpflug record represent a false negative without scattering apart from the corneal reflection point (A), but OCT revealed existence of a lesion (B)). This dilemma is reducible to the fact that enhanced anterior scattering is not surely recognisable as corneal reflection or as lenticular defect without a cross validation method (Fig. 98, OCT image (D) confirms lens-located scattering-causing lesion detected in true positive Scheimpflug imaging (C)). Lacking reliability evidently follows suit. Objectivity and reliability are not affected if the multi-image recording mode is used (several images with one measurement to cover the lens from different angle).

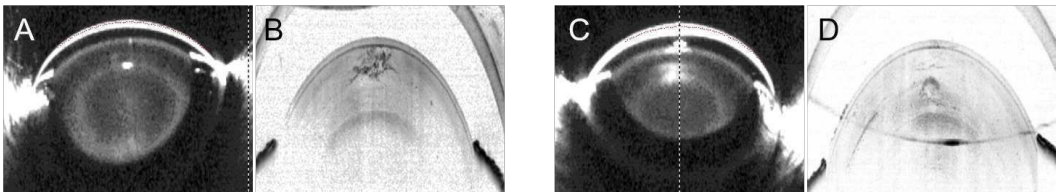

Figure 98.: Biases in Scheimpflug recording and analysis; Anterior Scheimpflug and OCT imaging of a 19 month old male WT. Scheimpflug image without recognisable lesion **(A**. OCT image of the same lens at the same point in time with considerable anterior lens damage **(B**. Scheimpflug image of an animal with scattering in the anterior lens **(C**. OCT image of the same lens at the same point in time with matching lesions in the anterior lens cortex **(D**.

OCT

In OCT, optical path differences of the interfering LASER light is depicted as increased grey values in the live image. Under certain circumstance, the unfavourable positioning of the device can cause increased scattering within the target tissue for imaging. Therefore, posterior cortices of control mice appear opaque, despite no existing lesion. On the other hand, actual lesions scatter naturally

detection light and any depicting of structures behind that lesions are invisible due to the signal overlay, e.g. a retina behind a damaged lens. This makes the OCT method not 100 % valid. If the analysing person has proper knowledge of the image gaining and their vicissitudes of overlaying structures resulting in imaging folding, no restrains can be enumerated for a reduced objectivity, either in recording, nor via image analysis (not the same situation as with Scheimpflug imaging because of the resolution power of the OCT and the subsequent clearly interpretation of scattering events). Nothing is conceivable that reduces reliability of OCT imaging if the experimenter scans through the eye before taking images.

Virtual drum

The virtual drum is a device to determine the visual acuity of mice - the ability of the animals to differ two nearby objects. The value of this test is debatable. Indeed, the experimental set-up is suitable to engage the scientific question, but the means of the experimenter to connect reactions of the animal with an initial incentive is restricted. Visible reactions of the animal are not necessarily due to the visual incentive and near the threshold of visual acuity not clearly assignable at all. Therefore, validity and objectivity is severely shortened for the same reasons.
Tightly connected with that is the evaluation of the reliability. Precisely because the experimenter has a huge space for interpretation, e.g. putative movement of the nose or even the eyes, the final threshold is rather a rough approximation then a sharp fact. Also the behaviour of the mice is strongly dependent on marginal conditions as daytime, adaption to the measurement environment and possible previous experiments. Altogether, the virtual drum is one of the least reproducible methods.

2

DISCUSSION

2.1 THE SURPRISING LESSONS FROM LENTICULAR QUANTITIES

In several sections it was already hinted to the shortcomings of the Scheimpflug method in high-throughput lens monitoring in the single image mode (see method section 2.2 and result section 2.5). Nonetheless, of both applied *in-vivo* lens imaging methods, Scheimpflug measurements deliver at least comparable quantities, the mean and maximum lenticular density.
Furthermore, it was shown via histology and OCT that exposure to γ-radiation, starting with a dose of 1 Gy, induces in average the formation of very defined and locally restricted lesions at the posterior and anterior suture (Tab. 25 and 27) in result section 7.1. As explained, neither of them were detected by Scheimpflug imaging. In the posterior case because the mouse lens geometry limits the possibility to record the posterior lens and in the anterior case because no parallel evaluation with continuous OCT data was available to differ between reflections and actual lesion-induced scattering. Therefore, the mean lens density data presented reflected only the global changes in the lens. In this context two working hypotheses were stated which could be actually 'verified' with the Scheimpflug measures at hand because they targeted on global lenticular alterations. They first was:

'Linear increase of mean and maximum lens density with dose in B6C3F1 mice.' — *1st hypothesis*

Mean lens density in P70 mice irradiated with 1 Gy was slightly higher, but the 2 Gy cohort oddly displayed no differences to the controls (see MANOVA, Tab. 13, mind significantly different variances). Mean lens density in P2 mice was significantly increased (see MANOVA, Tab. 21), yet, no other doses between 0 and 2 Gy were applied to infer a dose response function. Thus, no linear increase of mean lens density with dose could be supported for the P70 mice within observation time if anterior reflections were generally neglected. Since we could evaluate Scheimpflug images of the P2 and P70 cohorts exposed to 2 Gy with OCT images, corrected mean densities modified the conclusion (see Fig. 31, A+B and 40, C+D). These corrected values, including the proven radiation-induced anterior lesion in P70 mice

and posterior inner cortical lesions in P2 mice, were naturally higher (Fig. 99, A). Irradiated P70 murine lenses were clouded with a significant mean excess density of absolute 0.63 % compared to the not-corrected 2 Gy data. Corrected mean lens density of irradiated P2 mice 9 months after irradiation displayed even an absolute mean excess density of 1.2 %. Therefore, the initial hypothesis of a dose-dependent scattering increase was not refuted, but the threshold model was not corroborated either due to the lack of evaluative OCT images for lower doses (0.5 and 1 Gy).

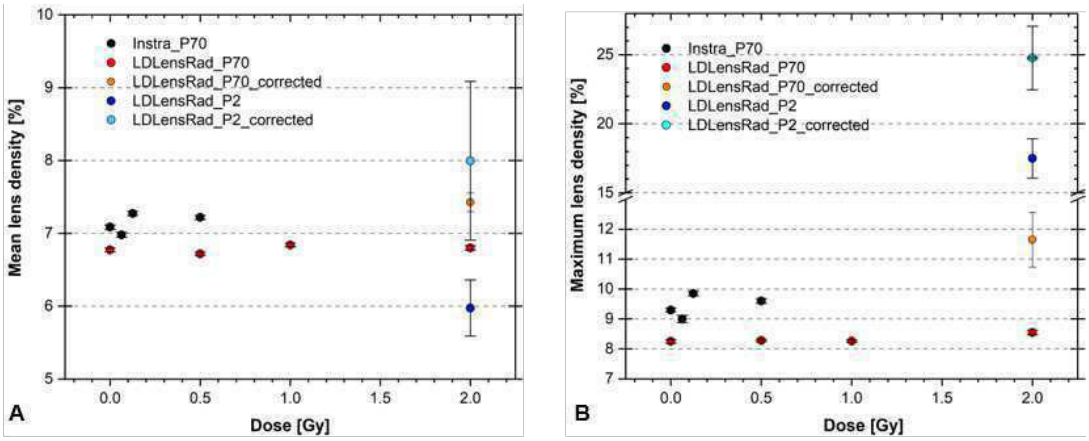

Figure 99.: Overview of lens densities of B6C3F1 mice of the INSTRA [237] and LDLensRad project (this thesis). P70 data (red dots) pooled for period of 18-20 months p.i., P2 data (blue and light blue) at 9. month p.i. and corrected P70 data (orange) 20 months p.i. Mean lens density **(A)** and maximum lens density **(B)**. Note truncated ordinate in B. Error bars indicate ± SEM.

The mean lens density did not show a large separation by the factor age at irradiation. However, real differences along this factor were obvious in analysis of the maximum density (Fig. 99, B). Here, the cortical damage in P2 mice included in average spots which were more clouded than the anterior lesions of the P70 mice.

A recent study by Dalke et al. [237] based on the INSTRA project concerning the lifetime monitoring of B6C3F1 mice after low dose exposure to 0.063 Gy, 0.125 Gy and 0.5 Gy at P70 came to slightly different results. Here, the mean lens densities were in general one decimal place higher (Fig. 99, A+B, black data points, pooled raw data of period 18-20 months (not published, with permission of Dr. Claudia Dalke). This was arguable: density measures from Scheimpflug images could be fallacious if the anterior rim of the lens was included. In the present study, the measuring bar was therefore always laid in a certain distance below the rim. This

avoided phantom signals in the maximum density data, since the anterior rim was the most scattering structure in an undamaged lens. The mean density, on the other hand, should not be strongly affected by this, why there may be an additional non-biological explanation for the differences displayed in Fig. 99, A. Especially for the mean density, the proportion of cortex and nucleus along the measuring bar was decisive. The higher the fraction of the cortex, the lower the mean density because of the natural age-dependent increase via beginning nuclear clouding (compare controls in Fig. 29, B+C). Of course, the proportions relied on the image quality which increases with measurement experience (higher image depth). Since this study (LDLensRad project) followed the INSTRA project, this could be a very plausible explanation for the generally higher values of the INSTRA project. Low dose effects were discarded because the differences incurred also in controls.

All mean lens density increases presented in this thesis, which were statistically sound, could be refuted being clinically relevant because, as we know from the human correlation between mean Scheimpflug values and LOCS III cataracts stages according to Pei et al. [217], all values below 9.7 % count as controls (Fig. 29, A, at least for nuclear cataracts). It is highly doubtful, though, whether a human lens density correlation with grades of nuclear cataracts according to the LOCS III system is very useful for an assessment. These deliberations were sufficient to correct the second hypothesis concerning nuclear scattering (see discussion section 2.3).

Other mice strains and lines have been also investigated by LDLensRad colleagues at PHE and ENEA via Scheimpflug imaging every month for 12 months in a row (129S2/SvHsd) and for 18 months following irradiation (males and females of WT C57BL/6J mice, *Ptch1*$^{+/-}$ C57BL/6J mice, as well as *Ptch1*$^{+/-}$ CD1 mice). McCarron et al. [248] stated that only the WT and *Ptch1*$^{+/-}$ CD1 mice had lens densities which reached the threshold of 14.1% for a score 2.0 LOCS III cataract according Pei et al. [217], although it is unclear whether the authors referred to the maximum or also to the relevant mean density. However, this comprehensive study demonstrated the high relevance of the genetic background (strain, line) for the impact of IR on lenticular opacification.

In context of this thesis, the ability of the Spectral domain OCT (SD-OCT) to monitor alterations of the entire murine lens was published [195]. Given the general understanding of the posterior subcapsular cataract as the hallmark for radiation-induced lenticular damage, this was helpful to complement Scheimpflug imaging.
Most importantly, we could prove with this approach that subcapsular (PSCs + ASCs) and suture-related (ACs) alterations were indeed the only form of cataract appearing in our investigated cohorts of irradiated P70 mice, and that these cataracts, although of the same location category (PSCs and anterior lesions including ASCs), could be divided in sub-types (Fig. 21+23). Especially the PSC was also correlated with ageing, but we demonstrated that the occurrence of all subtypes PSCs and ACs (including ASCs) clearly correlated with the exposure to a IR dose too (Tab. 11+12). These *in-vivo* subtypes of posterior and anterior lesions were introduced as something completely new. It was possible because the OCT allowed to identify scattering-based fine structures not recordable with other *in-vivo* techniques (Fig. 100).

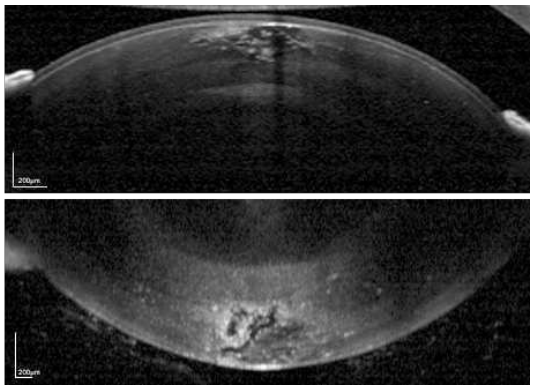

Figure 100.: Subcapsular cataracts as hallmark of radiation-induced damage in P70 mice. Both of SF/S-type.

As any unprecedented system, this new classification of suture-related mostly subcapsular lesions dependent on their scattering properties in SF-, SF/S, S- and N-type has to be critically discussed: the introduced quantitative classification was subjective by nature because features of one type could possibly be found in another type. This was in particular true for the differentiation between the SF- and SF/S-type. To decide on relatively scattering-free edges - defining partially the SF-type - was in some cases more strictly possible then in others (due to breathing movements of particular old mice). But this is a general problem of every qualitative classification. It can be stated, though, that the decision on the N- and on the S-type was unambiguous. Based on the (rather fuzzy) differentiation between the SF- and SF/S-type it was shown how statistically different radiation-induced and age-related subcapsular cataracts were. In histology they might seem both drastic in appearance, but only

the OCT reveals their different light scattering properties yielding the result that SF/S-type lesions caused more scattering (see SS_{post}).
Theoretically, the classification of cortical cataracts of neonatal mice in OCT images was more error-prone. Whilst C1-type lesions were without any doubt a sharply separated sub-population of all lenticular alteration in the 2 Gy-irradiated neonatals, the distinction between C2- and C3-type lesions appeared to more difficult. One result that supported the soundness of differentiation according the features cleft formation and prolongation to the more anterior perinuclear area, was the correlation between initial distance at 2.5 months p.i. and 8.5 months p.i. (result section 4.7). The sufficient linear regression for the C2-type subgroup in contrast to the C1- and C3-type groups could clearly contribute to the classification judgement proposed.
Of course, as an additional technical problem, the scattering background of a lens was dependent on the position of the OCT device at a defined focus. Nevertheless, the spots of increased scattering were always quite clear to identify, and, fundamentally spoken, large homogeneously light-scattering lens areas were not to assume to be real as verified via Scheimpflug measurements of the anterior segment. Either way, because of this adverse effect a theoretically more robust quantitative approach could not be applied.

With regard to high radiation experiments and observation on human patients, a distinctive hypothesis related to posterior subcapsular cataracts was articulated:

> *'Partial progression of posterior subcapsular cataracts to nuclear cataracts in B6C3F1 mice after exposure to a dose $\leqslant$ 2 Gy.'*

2^{nd} hypothesis

In fact, not a single lens of any cohort of the sham- or IR-radiated P70 mice exhibited alterations of the nucleus. Yet, we defined the process domagenesis based on scattering layers appearing above some posterior lesions (see result section 2.3). This scattering increase was always PSC-associated and restricted to the outer posterior cortex. Since the mice were almost at the end of their lifetime, a further deterioration or NC development was not to expect. Generally, P2 mice did not develop subcapsular alterations of any kind (1 lens out of 160 irradiated lenses displayed a PSC of the SF-type). Although few cases of nuclear/total cataracts were observed, observation of cortical cataracts in these mice hinted only to the potential development of nuclear cataracts in lenses affected by stage 3 lesions (see Fig. 39, D, enhanced contrast). Therefore, we precise:

> *'Radiation-induced posterior subcapsular cataracts do not proceed to nuclear*

Updated 2^{nd} hypothesis

cataracts within the lifetime of adult B6C3F1 mice following an exposure to a dose of $\leqslant$ 2 Gy.'

2.3 RELATABLE CATARACT PREVALENCES AND LATENCIES

2.3.1 *Perspective-dependent inferences concerning irradiated adult mice*

Our working hypothesis for cataracts based on the recommendations of the ICRP [219] and recent murine experiments [260] was the following:

3rd hypothesis

'Linear subcapsular cataract occurrence in B6C3F1 mice after exceeding an IR threshold of 0.5 Gy with a dose-dependent latency of a few months.'

Most interestingly, the histological data presented, in terms of significantly increased odds ratios for anterior or posterior cataracts, could not support a threshold of 0.5 Gy. The mice examined within the scope of this work were significantly more affected 20 months after irradiation with a dose of 1 Gy with a dose rate of 0.3 Gy/min (Fig. 101, A). If all findings *in vivo* were taken together measured 20 months p.i. (SF-, SF/S- and S-types), the odds ratio for a posterior lesion was indeed already increased with 0.5 Gy (Fig. 101, B). But, as explicated in result section 7.1, lesions recorded by OCT could be mere irregularities in histology, which would explain the high cataract point prevalence level for all doses including controls displayed for OCT data. Therefore, histological findings can not be neglected despite the mentioned shortcomings (see discussion chapter 1).

The only previous study that analysed cataract frequencies in irradiated adult B6C3F1 mice was done by Kunze et al. [260]. The authors found in mice of the same strain (sex and line also pooled) - irradiated with 0.5 Gy of γ-radiation at a lower dose rate of 0.063 Gy/min - an significantly increased occurrence of PSCs in histological sections (OR = 9.28). The findings of the here presented thesis contradict to this. That could be explained by several reasons. Letting the criteria for posterior cataracts aside, a lower dose rate could actually have caused the increased cataract formation. In fact, inverse dose rate effects in the lens epithelium of Bl6 mice were recently described by Barnard et al. [261]. That would mean that increased damage in the low dose-irradiated lens epithelium correlated directly with higher incidence of PSCs in those mice. That mice irradiated with 0.3 Gy did not display significantly

increased odds ratios after exposure to 0.5 Gy would then fit perfectly. On the other hand, mice in the study of Kunze et al. [260] were analysed 24 months p.i. and the mice in the study at hand 20 months after p.i., which could explain the differences (more irregularities would have proceeded to form fully grown PSCs). It is also

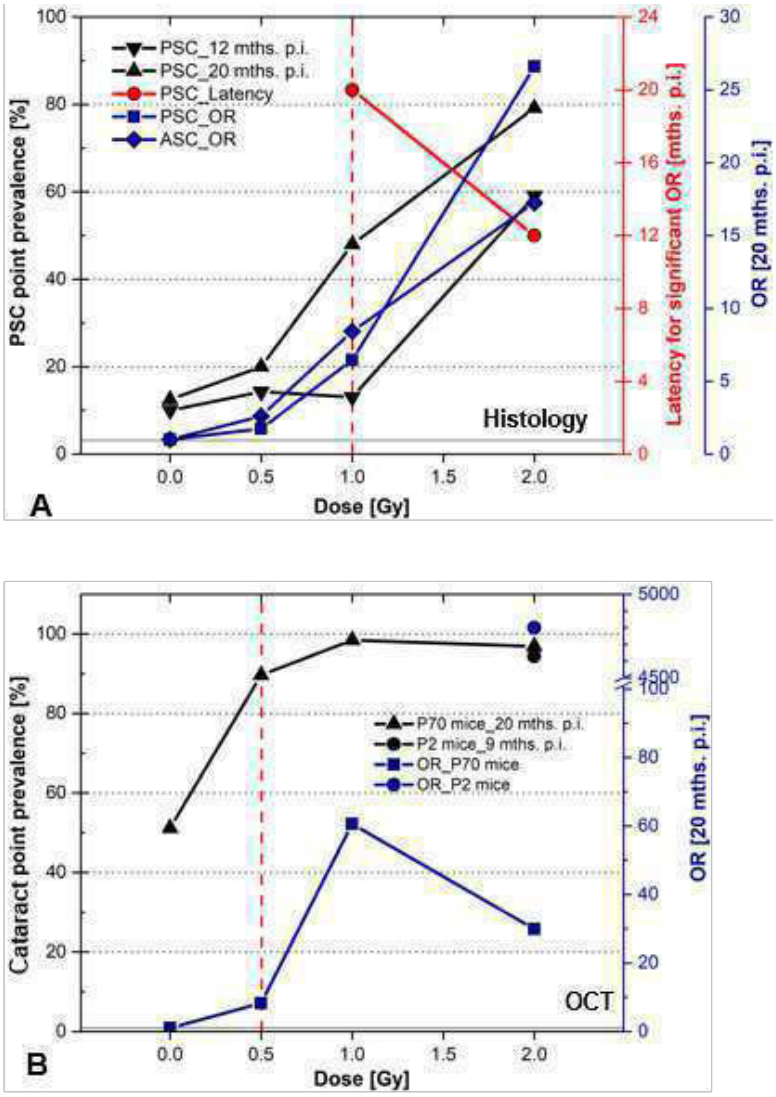

Figure 101.: Odds ratios, point prevalences and latencies for pooled PSC/Anterior cataract (AC) occurrences in histology (Tab. 25) of P70 B6C3F1 mice **(A)**. Latency for first significant OR of the 1 Gy and 2 Gy cohort (red ordinate). Odds ratios and point prevalences for cataract occurrences in OCT data (Fig. 24, Tab. 11 lower part and result section 4.2) of P2 and P70 B6C3F1 mice **(B)**. Red dashed line indicates beginning of significant increased odds ratios of lesion occurrence compared to controls (blue ordinates).

important to know that fewer lenses were examined in Kunze et al. [260] (maximum 10 against 20 in this study) and that the classification of PSCs was perhaps not perfectly congruent (though agreed on beforehand). In this thesis, every posterior lens morphology classifiable according to Merriam&Focht as cataract stage below 2 was strictly counted as irregularity (only few vacuoles and swollen fibre cells respectively [215]).
Anterior cataracts were in Kunze et al. [260] and this study not significantly increased for 0.5 Gy. Also in this context, the late revision 24 months p.i. could have resulted in a different outcome, but has not. Beyond comparison, this work supports that anterior cataracts follow suit the significant posterior cataract occurrence for 1 and 2 Gy (see Tab. 27 and Fig. 101, A).

The presented pooled findings in B6C3F1 and B6RCF1 mice could also be compared to other murine irradiation studies. Worgul et al. [262] investigated hybrids of 129SvEv and Black Swiss strain mice, irradiated at 4 weeks *post partum* (6 weeks after birth) with X-rays (0.5 Gy/min). They found only cataracts of stage 1 (according to the system by Merriam&Focht) in the 0.5 Gy cohort in barely 10 % of the mice within 33 weeks p.i. On the other hand, the prevalence of stage 2 cataracts in WT mice irradiated with 2 Gy was 100 % after only 47 weeks. The here investigated B6C3F1 mice (pooled sex and line) showed after 52 weeks p.i. (12 mths. p.i.) a posterior irregularity prevalence of 28 % (43 %, including PSCs), but not more than a 59 % PSC prevalence (77 %, including irregularities) after 52 weeks p.i. For comparison of the stage 1 cataracts, irregularities are suitable and PSCs for stage 2 cataracts according to Merriam&Focht. Following this scheme, B6C3F1 mice had a higher posterior alteration prevalence after exposure to 0.5 Gy and a lower one for 2 Gy in comparison with the mice examined in [262]. Especially the comparison of the 2 Gy cataract prevalences entices to consider B6C3F1 mice relatively less radiation-sensitive with regard to the lens.

The threshold component of the prevalent hypothesis was most certainly supported by the presented data, the linear increase of the significant odds ratios for anterior or posterior cataracts not coercively. This was due to the simple fact that only 2 data points of significantly increased odds ratios with overlapping 95 % confidence intervals existed (1+2 Gy, 20 months p.i.). That means also that a linear dose dependency could not definitely refuted either. The latency of anterior and posterior cataracts, on the other hand, was within the 'histological resolution' of

investigating eyes 4, 12 and 20 months after irradiation quite convincing indirectly linearly proportional to the applied dose (Fig. 101, A, red plot). We therefore precise the initial hypothesis based on histological findings:

'Linear posterior subcapsular cataract occurrence in adult B6C3F1 mice after exceeding an IR threshold (IR_{th}) of 0.5 Gy $< IR_{th} \leqslant$ 1 Gy (dose rate 0.3 Gy/min) with a dose-dependent latency of at least 20 months p.i.'

Updated 3rd hypothesis

That means, the exposure to a relatively high single dose is required (2 Gy), compared with the average annual exposure known for man, that a mouse cohort develops PSCs in a frequency above the control level within half lifetime. Lower doses (0.5 Gy or less) cause soonest in the last quartile of murine lifetime significantly more PSCs or never (compared to a male C57BL/6J median lifetime of 878 $\pm$ 10 days and 794 $\pm$ 7 days for females according to Kunstyr and Leuenberger [263]).

All these considerations favour the notion of cataracts as deterministic effect. But could a longer monitoring of bigger cohorts exposed to lower doses than 0.5 Gy reveal a rather stochastic correlation eventually? In fact, both perspectives are justified. Pivotal for understanding this superficial contrast is the term 'latency'. Yes, statistical relevant findings could have been found for lower doses, maybe so low that a threshold model falls apart. But which relevance would that have? The author of this thesis advocates the introduction of an 'effective threshold' expressing a dose that leads to increased cataract occurrence in a reasonable latency (for instance half life for irradiation in the first life quartile and necessarily on the type II cataract pathway). The effective threshold for a typical radiation-associated posterior subcapsular cataract would than be 2 Gy and more than 2 Gy for anterior cataracts.

2.3.2 *Contextualisation of findings in irradiated neonatal mice*

Our findings in P2 mice could only compared to two other studies of Gajewski et al. [212] and De Stefano et al. [213]. Gajewski et al. irradiated inbred strain A mice at several postnatal stages including P2 with 300 R (~ 2.88 Gy) of X-radiation. De Stefano et al. irradiated P2 mice of CD1 background with 3 Gy of X-radiation. Gajewski et al. assessed cataracts by slit lamp (see introduction section 3.3), whilst De Stefano et al. evaluated cataracts macroscopically with a stereo-microscope.

'Irradiated neonatal mice (P2) develop predominantly and exclusively type I

4th hypothesis

cataracts with a latency of a few months.'

B6C3F1 WTs, irradiated at P2, developed in 92.5 % of the lenses (males+females) cortical cataracts (in 55 % if mild C1-types were excluded). Gajewski et al. [212] found in 96.7 % of the lenses (males+females) a stage 1 cataract (type I+II) and in 76.6 % a stage 2 cataract (type I+II) within lifetime and De Stefano et al. [213] in only 9.4 % of the lenses (males + females) a cataract (despite higher dose). Median latency was below 100 days (stage 1) and below 200 days (stage 2) in the strain A case and 9.5 weeks in CD1 mice. The cortical cataracts in B6C3F1 mice irradiated either with γ or X-rays were identified with the first measurement 10 weeks after irradiation, but were most likely earlier present. Taken in account the quite late appearance of subcapsular cataracts in irradiated P70 mice (see result section 7.1), our hypothesis with regard to the factor age in combination with the predominant cataract type stood the test.

The prevalence was closer to the strain A inbred mice than the CD1 mice. This was not necessarily caused by strain differences of the investigated mice. It is more likely that the three different examination methods created the differences (slit lamp vs. OCT vs. stereo-microscope). Mild cortical cataracts of type C1 may have not even visible as opacification by visual examination.

In principle, the type I/type II ratio discrepancies to Gajewski et al. [212] were more grave. We formulated the following hypothesis:

5th hypothesis

'Irradiated neonatal mice (P2) are prone to develop earlier stage 1+ posterior subcapsular cataracts (type II cataracts) than young adult mice (P70).'

In Gajewski et al. [212] 40 % of the strain A mice lenses developed a type II cataract, but only 0.006 % in the B6C3F1 mice! The only reasonable cause for this may have been a strain-dependent latency spread of type I and type II cataracts (Gajewski et al. [212] did not analysed strain differences). Therefore, the initial hypothesis was premature and had to be corrected in the light of the new findings:

Updated 5th hypothesis

'Irradiated neonatal mice of B6C3F1 background (P2) are less prone to develop stage 1+ posterior subcapsular cataracts (type II cataracts) than P70 B6C3F1 mice and P2 mice of strain A background.'

2.3.3 *Strain-specifics in cataract formation*

Statistically profound statements based on histology were generally restricted by the number of samples. This limited the calculations to the 2 Gy-cohorts of BL6 mice. No statistics of value could be calculated for the 129 mice. But the proof of 2 posterior cataracts in 6 investigated control lenses was a solid hint that 129 mice are generally a bad mouse model for experimental investigations of radiation-induced cataracts.
Conditional on low lens numbers of BL6 mice, odds ratio for PSCs in 2 Gy-irradiated mice were higher for both dose rates in BL6 mice compared with B6C3F1 mice. Yet, confidence intervals were 1.06 - 2034 (BL6) against 5.58 - 126.59 (B6C3F1). This rendered the difference in ORs quite worthless. But, given the existing data, the related initial hypothesis was not refuted:

> *'Inbred C57BL/6J mice are more prone to form radiation-induced posterior lesions than B6C3F1 mice.'*

6^{th} hypothesis

BL6 mice were, within the extend of the analysed samples, not less prone to IR expressed by the formation of posterior subcapsular cataracts. Therefore, the restated working hypothesis is:

> *'Inbred C57BL/6J mice are equally susceptible to 2 Gy of IR as B6C3F1 mice in terms of PSC formation independent of dose rate.'*

Updated 6^{th} hypothesis

2.4 THE MULTIPATH VISION IMPAIRMENT BY IONISING RADIATION

As argued in discussion chapter 1, measurements with the virtual drum were the least valid and least reliable of all applied methods. Hence, visual acuity data of C57BL/6J mice for comparison was gainable, but not completely satisfying for a fruitful discussion of a possible radiation-induced vision impairment. For instance, mean spatial frequency for mixed sex C57BL/6J mice measured with the same device (VD1) were determined by Lehmann et al. [264] to be 0.34 $\pm$ 0.005 cyc/deg 23 months after birth, while a mean spatial frequency of 0.48 $\pm$ 0.03 cyc/deg was measured for mixed sex WT controls in the here presented study 22.5 months after birth. In another study, a median spatial frequency of $\sim$ 0.3 cyc/deg was determined for 16 month old male C57BL/6J mice and $\sim$ 0.29 cyc/deg for 25 months old mice [265]. Since both studies presented far lower spatial frequencies for control mice (even few months old mice exhibited lower frequencies than 0.4), a general high

Inter-study comparison

systematic absolute failure of roughly ~ 0.15 cyc/deg has to be considered realistic.

This clarified, it has to be stressed that visual impairment is the main criterium for the pathological quality of a cataract, but, unfortunately, not the only reason for it. We demonstrated in the result section 6.2 how corneal clouding could influence visual acuity in P70 mice and in section 6.3 how strong retinal atrophy could reduce visual acuity in P2 mice even without cataracts.

2.4.1 *Lenticular impact on visual acuity*

Led by data indicating the predominant formation of posterior subcapsular cataracts after exposure to IR, we conducted experiments in spirit of the following hypothesis:

7th hypothesis

> *'Possible radiation-induced posterior subcapsular cataracts cause vision impairment.'*

It turned out this assumption based on human observations was far too simplistic or plainly not transferable without adjustments to mice. Indeed, as shown, PSCs occurred statistically more often in the 1 Gy cohort of γ-irradiated P70 mice and visual acuity was also statistically lower than in controls (Tab. 23). But is the reduction of acuity by roughly 12 %/Gy vision-impairing (~ 0.055 $\pm$ 0.005 cyc/deg*Gy, based on linear regression, r = -0.58)? Unfortunately, we have no virtual drum to LogMAR test (logarithm to minimum angle of resolution) relation upon which we could assess the clinical relevance of the here presented reductions (Tab. 36). Actually, only the lens density gained by Scheimpflug imaging could answer the question indirectly and was already refuted to be critically changed including the data of highest dose of 2 Gy for both P2 and P70 mice.
With regard to Scheimpflug, visual acuity determined for P2 mice seemed to be inconsistent. Spatial frequencies of 2 Gy-irradiated mice were half of the controls. Yet, mean lenticular density was only ~ 8 % (see Fig. 99, A, P2_corrected) and thus far from a 2.0 score cataract according to LOCS III and a doubled visual angle respectively (doubling of visual angle in LogMAR test equals roughly the reduction of resolution by ~ 50 %, see [217]). Such inconsistencies were unavoidable simply because Pei et al. [217] established correlations based on nuclear cataracts, while subcapsular cataracts were found in irradiated P70 mice and inner cortical cataracts in P2 mice.

Table 36.: Summary of visual acuity results.

Mice	Dose	Mean spatial frequency [cyc/deg]
P2	Control	0.46 ± 0.02
	2 Gy	0.23 ± 0.09
P70	Control	0.46 ± 0.04
	0.5 Gy	0.42 ± 0.04
	1 Gy	0.41 ± 0.04
	2 Gy	0.35 ± 0.08

Mean spatial frequencies of every irradiated cohort (sex and line pooled) in comparison to controls. Errors indicate ± standard deviation.

Despite lacking possibilities to embed the gathered data into the existing scientific context, we could nonetheless extract correlations that connect lenticular damage and vision impairment by the aspect visual acuity. As shown in result section 6.2, by calculating simple posterior scattering scores (SS_{post}), it was on average influential, whether subcapsular cataracts in P70 mice were of SF-, S- or SF/S-type (Fig. 51). Of course, the scattering score could not convey information about the volume of scattering fibre cells in the lens. The more impressive that scattering was assessable dichotomously. The analysis revealed that mice with 2 SF-lesions saw better than with 2 SF/S-lesions in the 2 Gy cohort including at least 4 controls! Since the differences in visual acuity between the applied doses was low but existing, the here presented SS_{post} was strictly spoken a 2 Gy-SS_{post} and could not be compared with scores of lower doses. It is important to understand that the 2 Gy-SS_{post} delivered no dose-dependent information, but a differentiation of existing cataracts by their physical properties regardless corneal clouding (because no correlation exist between corneal clouding and lenticular phenotype).

The inclusion of anterior scattering by determination of the SS_{AP} was rather unsurprising. As stated in the introduction, a failure of the posterior subcapsular lens has the most hampering impact, because it is a region of light convergence. Therefore, anterior alterations should not have the same vision-impairing effect. The stagnation of the SS_{AP} beyond a value of 2 supported this theory. It made even more sense considering the fact that no lens developed a ASC before an PSC (*in vivo* not to prove otherwise), why no SS_{AP} lower or equal 2 represented more than 1 scattering anterior lesion.

Correlation between the only lenticular quantity in P70 mice, the posterior and anterior scattering-free area (PSFA/ASFA) yielded no statistically significant linear correlation with visual acuity (Fig. 50, A). Since these quantities represented a

lenticular volume less scattering than the bulk of fibre cells, this came not as a surprise. The indication of a linear correlation (r = 0.56) was still recognisable and easy to explain. As shown in Fig. 26, D, it was simply more likely that an irradiated mouse with a lenticular lesion of the SF- or SF/S-type formed larger imaginable areas (volumes in reality) free of scattering.

Inner cortical lesion in irradiated P2 mice were always scattering. A type score was determined (CSn) based on the severity of the lesion (see result section 6.3). Counting steps between C1-, C2- and C3-type lesions were equally 1. It could be argued that the scattering increase between of the steps C1/C2 are biologically more severe than between C2/C3. This may be right for the utmost posterior edge of the scattering fringe, but certainly not at the more equatorial scattering fringe sections. Anyway, as inherently displayed in Fig. 53, A, many mice with high scores saw perfectly well, while animals were examined which had a low CSn of 2 or less and were basically blind (with equally atrophied retinae). Thus, in contrast to P70 mice, no impact approximation for the single factor lens alteration could be extracted from the visual acuity data gathered. Considering this and the results from P70 mice, the initial hypothesis had to be changed:

Updated 7th hypothesis

*'Posterior subcapsular cataracts in P70 mice following exposure to γ-radiation contribute to an average reduction of visual acuity by 0.055 ± 0.005 cyc/deg*Gy.'*

2.4.2 *Corneal and retinal impact on visual acuity*

Valid correlations of visual acuity with corneal clouding (especially in the female mutants) was sufficiently demonstrated for P70 mice (Fig. 50, B, r = 0.81). Generally, the corneal index (CoI) could be considered as even more robust than the scattering score, due to the inclusion of clouding position and extent (see result section 3.2). However, the CoI is only a semi-quantitative measure with all the disadvantages going along with it.
Controls without corneal clouding displayed a mean visual acuity of 0.46 ± 0.01 cyc/deg, identical with the not-corrected data, but the mean visual acuity of the 2 Gy cohort increased to 0.39 ± 0.02 cyc/deg, if only cornea-clear P70 mice were included in the analysis. Accordingly, the average reduction of visual acuity per 1 Gy of IR decreased practically to 0.04 ± 0.02 cyc/deg.

Retinal degeneration was not observed in P70. A rather tiny, but significant increase of retinal thickness was observed for all irradiation cohorts (Fig. 32, E). This finding deviated from results in B6RCF1 mice 20 and 24 months after irradiation with 0.5 Gy (0.063 Gy/min) of the previous study by Dalke et al. [237].
In sharp contrast, retinae of P2 mice were the most irradiation-affected tissue judged by the punctual relative thickness in (Fig. 44, A). Additionally, the high irregularity of the malformed retina was apparent in fundus images (Fig. 47). Both retinal information sources were forged into scores that could be correlated with the measured visual acuity (Ret and ONLA). Neither the Ret score as sum of the both thickness in both retinae ($r = 0.3$), nor the ONLA as fraction of the lesion area around the optic nerve ($r = -0.2$) could deliver a statistically significant correlation with the spatial frequency of the experimental mice (Fig. 53). This came to no surprise because the vision impairment in irradiated P2 mice was obviously a multi-factorial phenomenon. However, missing correlation could have had also intrinsic reasons. For instance, the combined retinal thickness at a chosen spot in the retinae might have been a steady measure, but surely not a wholly representative measure given the variance of retinal thickness in irradiated P2 mice (see Fig. 46). The ONLA represented also only connected lesions around the optic nerve and neglected necessarily the rest of the fundus (section data of the entire fundus was not recorded, e.g. with a grid scan).

These considerations prompted the necessity of a composite score including all the data gathered of the lens, the retinal thickness and the retinal fundus in the surrounding of the optic nerve. The introduced impairment score (IS) was conceived to deliver on this purpose, but failed to reveal a combined correlation of the observed damage and the measured visual acuity (Fig. 54, B). Actually, the IS correlation coefficient was as bad as the correlation with the Ret score. This could have several reasons: formula imbalances based on wrong assumptions concerning the impact of singular damage and initial failure of the cataract priority in formula (Eq. 8), or an unrefined weighing factor matrix (Eq. 9). Either way, incomplete representation of damages in associated scores as well as missing crucial factors not recognised at all were more likely.
The brain is paradigmatically considered to be radiation-insensitive due its low mitotic rate [266]. Nonetheless, it has been shown that galactic cosmic rays (high LET radiation) are detrimental as well as some Grays of low LET radiation [267]. Neonatal rats (P1) irradiated with low doses of X-rays (20-40 R) displayed already a lag in

development and alterations of the cortical architecture even after a long period of follow-up time [268]. The exposure to 2 Gy of IR must have had detrimental effects in the brain of P2 mice which could possibly have included the visual system (but no brain histology to prove the claim).

2.5 CONTRIBUTIONS TO THE MECHANISTIC UNDERSTANDING OF LENTICULAR, RETINAL AND CORNEAL ALTERATIONS

2.5.1 *Mechanism of IR-induced cataracts*

The entire theory of posterior subcapsular cataracts bases on two columns: genomic damage in the epithelial cells with subsequent aberration of fibre cell differentiation [269] and biomacromolecular modifications in the entire lens according the refined concept of the cataractogenic load [119].
The here presented thesis contributed less to the elucidation of fibre cell differentiation failure or the reasons of locally relevant biomacromolecular modifications, than to the better understanding of the formation and dynamic of the phenomena of posterior subcapsular and of cortical cataracts.

With regard to PSCs in irradiated young adult mice, the first step is hypothesised to be a turbidity at the posterior suture caused by the accumulation of nuclei-containing cells and the appearance of swollen fibre cells. Accordingly, our hypothesis for these type II ([212]) cataracts was:

8th hypothesis

> *'Radiation-induced alterations in murine lenses start with the simultaneous appearance of vacuoles and nuclei-containing cells at the posterior pole.'*

Worgul et al. [243] investigated this appearance of first nuclei in the posterior lens of Columbia- Sherman albino rats exposed to X-rays 4 weeks following birth. They found no nuclei after irradiation with doses below 2 Gy within the observation time 90 weeks (~ 21 months p.i.). First irregularities in B6C3F1 mice of this study were observed 12 months p.i. with less than 2 Gy (but could have developed early between 4 and 12 months). Furthermore, Worgul et al. [243] found first nuclei approximatively after 66 weeks (~ 15 months p.i.) in rats exposed to 2 Gy. B6C3F1 mice, on the other hand, displayed this particular irregularity already 4 months p.i. (see Fig. 56, E) with a point prevalence of 8.7 % (see Fig. 57, A). Of course, the

organismic differences between mice and rats could explain such a difference in the latency period. Apart from that, the used slit lamp by Worgul et al. [243] might have been unable to identify just a couple of nuclei as opacification.
It is very important to state that the few endpoints for histological analysis might have been insufficient to finalise a statement about the hierarchy of lesion features. Accumulation of nuclei-containing cells and swelling of suture-related fibre cells could actually occur after the same period of time. Thus far, there is no data that falsifies the 8th hypothesis.
The refined cataractogenic load concepts by Uwineza et al. [119] apprehends the PSC as an ageing phenomenon accelerated by the exposure of the lens to IR. It could be shown that this is actual true. Not only by sheer lower prevalences in controls at every given observation point (see Fig. 57) but in a more detailed manner by the PSC *in-vivo* characterisation. In fact, 63 % of the observed lesions in P70 controls 20 months p.i. (pooled sex and line) were of the SF-type, whilst only 36 % of the irradiated P70 lenses (pooled sex, line, dose) remained at this stage (Fig. 24).
Histological sections substantiated the theory of migratory nuclei (Fig. 58) that accumulate eventually at the posterior suture (Fig. 102, A) and the formation of swollen fibre cells and reservoirs possibly without membrane enclosure (Fig. 102, B). Both features resemble the SF-type and have natural reasons.

Figure 102.: The PSC as accelerated ageing phenomenon. Early irregularity **(A)**. The SF-type correlate **(B)**. The SF/S-correlate **(C)**. 40x-magnified records.

Crystallin stainings contributed to the understanding that the reservoirs and swollen fibre cells are actually different entities. Swollen fibre cells contained explicitly α-Cry (irregularity in Fig. 72, F and 74, A), but the rest of the lesion, recognised as signal-free space in OCT and as reservoir in histology was most likely crystallin-free (PSCs in Fig. 72, I+K, white stars). Since the capsule was most likely intact in lesions of P70 mice (also pseudoepithelial cells were still present as to find true by DAPI-positive nuclei in the reservoir Fig. 72, D+G), the substrate in the reservoirs had to be of lenticular origin. Possible is the rupture of fibre cells at the suture

and subsequent enzymatic lysis of crystallins or the simple accumulation of water streaming along the microcirculation system direction [39], although the obvious fixation by PFA did not support the notion of a pure water reservoir.

How triggers ionising radiation the promotion of the SF/S-type correlate (Fig. 102, C)? The manifest answer would be by increasing the number of aberrative fibre cells due to higher genomic damage in the epithelial cells. The hypothesis would be that more pseudoepithelial cells would be metabolically active at one of the most critical spots for the physical properties of the lens. The higher occurrence of methylene blue-positive fragments around the lesion (Fig. 56, B, yellow arrows) would support this assumption of additionally disrupted nuclei-containing fibre cells. But how would the additional pseudoepithelial cells promote the relative increase of swollen fibre cells to the reservoir? And what would be the further mechanism behind the lesion dynamic in form of domagenesis (Fig. 25)? We demonstrated that this process occurred in 5.5 % of the irradiated samples and in 3.8 % of the controls. Domagenesis seemed to describe the possible precipitation of macrobiomolecules in fibre cells more anteriorly placed to the lesion spot. The concerning cells did not seem to be osmotically enlarged. The clouding may also have been occurred based on membrane rearrangements not yet understood. Since domagenesis is also an age-related process enhanced by IR, the standard theory has to be applied: interaction of the pseudoepithelial cells with their cellular neighbourhood and oxidation processes, although it seems unlikely that IR should affect cells that locally.

Strictly spoken, this study buttressed that not PSCs but anterior cataracts are the exclusive hallmark of lenses irradiated with moderate doses (based on *in-vivo* data). Their initial appearance, though, was highly connected with overstepping a threshold of 2 Gy 20 months p.i. in OCT (Fig. 24, B) and 1 Gy in histology until 12 months p.i.. After 20 months, they occurred also in histology in a more linear dose-dependent manner. In any case, ACs never appeared in controls before 12 months p.i. and are therefore true markers for an irradiation with relatively high doses of γ-radiation. This finding was quite in coherence with the cataract stage model according Merriam Jr and Focht [215] and applied by Worgul et al. [243], where anterior subcapsular involvements were connected with the 2+ stage, subordinated to the posterior changes.

Subcapsular lesions were revealed in P70 mice already known in nature but re-

fined in understanding by closer examination *in vio* and enhanced plastic embedding techniques applied in histology. In P2 mice we could investigate a phenotype that was different from the PSCs and ACs in P70 mice (Fig. 103, B vs. A). The inner cortical cataracts investigated did not match any lenticular cytopathology documented. Even the type I cataracts described by Gajewski et al. [212] did not fit the phenotypes in irradiated P2 mice (although also an *in-vivo* description).

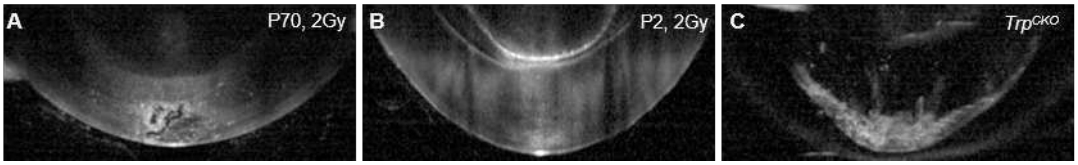

Figure 103.: Variety of posterior alterations in experimental mice. PSC in a 2 Gy-irradiated P70 mouse **(A)**. Inner cortical cataract in a 2 Gy-irradiated P2 mouse **(B)**. Massive posterior plaque in $Trp53^{CKO}$ mouse **(C)**.

It was demonstrated that these lesions can be roughly categorised in three types of severity (C1, C2, C3), that they behaved dynamically (diastasis, see result section 4.4) and that they were connected with severe phenotypes of lens extrusions (see result section 4.5). Because no samples were taken before 10 weeks p.i. we could nothing contribute to a possible mechanism beyond speculations. If aberrant differentiating fibre cells are to expect in neonatal mice too, they obviously followed another insertion into the bulk of fibre cells. It seemed likely that the still growing lens had something to do with it. Damaged fibre cells in course of irradiation simply formed a single layer, clearly discernible from the bulk of fibre cells by strong light scattering determined via OCT. Cells differentiated normally after radiation insult and added to the lens as regular secondary fibre cell layers. Histology could add few but helpful details (Fig. 67+68). Clearly, lateral connection between fibre cells in the concerning layer were disrupted. Also the alignment of basal ends of the closest fibre cells to form a suture failed, but obviously not posterior the lesion (formed by cells coming from the epithelium after irradiation). Capsular thickness of irradiated P2 mice (without extrusion) was not verifiable thinner than in controls of the same age at investigation (Fig. 70). Nonetheless, capsular breaks with extrusion of fibre cell material was observed in 8.75 % of all the investigated irradiated lenses. Extrusion was tightly connected with the inner cortical cataract as demonstrated with OCT (Fig. 38). One possible explanation would be outward oriented shear forces emanate from the lesion site in combination with irregular perforations of the capsule not

detected. Ruptures of the capsule were observed before in RLC mice as natural development without irradiation and were signalised by swollen posterior fibre cells and failing suture alignment [270]. None of those features were observed in the P2 mice irradiated with IR. Either way, more early investigations of the lens, preferably 1 week after irradiation, would be helpful for a better understanding of the lesion formation and the obvious less affected apical ends of fibre cells forming the lesion.

Did the *Trp53*^{CKO} mouse lens deliver a model for radiation-induced cataracts (Fig. 103, C)? Or reversely asked, could the reduced expression of TRP53 due to IR exposure be responsible for the phenotypes seen in irradiated P2 and P70 mice?

9th hypothesis

'The Trp53^{CKO} mouse lens is a structural model for radiation-induced posterior cataracts.'

Actually, both phenotypes were seen in the variety of *Trp53*^{CKO} lenses. In the representative phenotype published by Wiley et al. [204] massive posterior plaques of pseudoepithelial cells were seen as well as reservoirs like those observed in anterior as well in posterior lesion of P70 mice (see Fig. 15). Furthermore, pseudoepithelial cells in the posterior lens were also depleted of crystallins (Fig. 17, D). Strangely, also the P2 phenotype of a scattering fringe in the inner cortex plus lens extrusion was seen in two lenses (Fig. 17). But apart from these similarities, a lot was very different. For instance, the appearance of real Morgagnian cells (Fig. 15, F, red stars) was never witnessed in P70 lenses. Neither the massive failure of basal fibre cell end alignment at the posterior end (Fig. 15, H, red arrow) nor the apparent nucleus prolapse (Fig. 15, C). Also the crystallin distribution, with mixed populations of αA- and γ-cry-dominant cells, especially in the anterior lens was ever seen in P70 mice. Therefore, no, the *Trp53*^{CKO} mouse could hardly act as a model for radiation-induced-like posterior subcapsular cataracts (without radiation), although, it is baffling how such a completely different phenotype as the inner cortical scattering fringe could also be induced by the lack of *Trp53*.

Updated 9th hypothesis

'The Trp53^{CKO} mouse lens is not as sufficient structural model for radiation-induced posterior cataracts.'

2.5.2 *Insights in IR-induced retinal atrophy*

While the lenses of both, P2 and P70 mice, were altered verifiable, the impact on the retina was drastically dependent on age at irradiation. In P70 mice, layers of retinae were cytological not differentiable. This was in coherence with experiments performed on C57BL/6 adult mice [221] and contradictory to low dose findings in the retina by Overbey et al. [222] and Mao et al. [223]. The contrast might support the concept of strong influence of microgravity on the murine organism in space. One has also to keep in mind that organism on space flights are potentially exposed to different qualities of IR like high LET radiation which is far more damaging than low LET (higher radiation weighting factors for calculation of equivalent doses).

P2 mice displayed unique retinal phenotypes. The outer nuclear layer and the IS/OS-layer was partially depleted of photoreceptor cells, and also the outer plexiform layer was shrunken (Fig. 83, B). Actually, this thesis presents the first time such grave damage in P2 mice after irradiation with 2 Gy. All other studies exposed organism to at least the doubled dose either before birth [226] or at later postnatal stages [225]. Based on the histology of not yet differentiated P2 retinae (Fig. 3) it is safe to claim that affected retinal layers did not develop properly instead of degenerated. The finding was corroborated by the thinner layers of rhodopsin-positive cells in P2 mice (Fig. 89, E), a feature control or irradiated P70 mice did not share (not shown).

Besides the evident lack of full stacks of photoreceptor cells in P2 mice, the retinae were also characterised by further effects in the downstream elements in the machinery of visual information processing.
Calcium-binding proteins are commonly expressed by neurons and therefore by ganglion, amacrine and horizontal cells. Several cell bodies stained by calretinin matching the site of ganglion cells (Fig. 86, D, white arrow) and amacrine/horizontal cells (Fig. 86, D, yellow arrow) were found in controls at 9 and 20 months as well as in 2 Gy-irradiated P2 and P70 mice 9 and 20 months p.i. It might be that slightly more amacrine/horizontal cells were observed in irradiated P2 mice. But, more importantly, synaptic staining in the IPL typically discernible by 3 layers of calretinin-positive layers was regular in the controls and not any more in the irradiated P2 mice (Fig. 86, B). Connections seemed to be in disarray. If the finding of more amacrine/horizontal cells and less regular connections at the same time

would be correct, contrast regulation in murine vision of irradiated P2 mice could have been reduced (but not substantiated by measurements).
The ragged appearance of the irradiated P2 retinae was matched by the irregular distribution of bipolar cells revealed by staining with PKCα antibody. In the upper IPL part, they did not form a uniform layer as in controls (compare Fig. 87, D with F). Same was true for the OPL where over short distances no horizontal bipolar cells at all were present (Fig. 87, F white arrow).

Most striking was the difference in GFAP labelling. As introduced in introduction section 4.1, macroglial cells react with a higher expression of the intermediate filament if photoreceptor cells experience stress. In fact, GFAP expression was visibly enhanced in irradiated P2 mice, but not convincingly in 2 Gy-irradiated P70 mice or any controls (Fig. 87, H+I). Thus, a dose of 2 Gy γ-rays reproduced findings after irradiation with visible light by Eisenfeld et al. [229] in Sprague-Dawley rats and the phenotype of C3H mice lacking naturally photoreceptor cells as shown by Pieroth [271]. Highly characteristic was not only the stronger signal were astrocytes were supposed to be (GC), but also along the retina, indicating an enhanced expression by Müller cells (Fig. 88, white arrows), although this is just a fraction of about 15 % of the actual present Müller cells according Wang et al. [272]. Since the photoreceptors were not damaged but hampered in differentiation, this reaction of the macroglia was rather surprising. This long-lasting stress signal after insult by irradiation suggested a reactive gliosis as known from other experiments on not-regenerating retinal tissue [273].

The retinal vessels of P2 mice, as identifiable with OCT seemed to stop completely their development since irradiation. As demonstrated by Fruttiger [274] with col IV staining, vessels grown until P2 do principally not spread far from the optic nerve, which changes between P4 and P8. Therefore, it appeared, vessel growth was partially completely stopped in P2 B6C3F1 mice in consequence of irradiation. Why the photoreceptor depletion was especially high in the optic nerve-associated region, despite the fact that this was the only region covered by short-reaching vessels, seemed to be counter-intuitive. But the ONLA was nonetheless a distinctive feature of the irradiated P2 mice (Fig. 47+46). Anyway, short-reaching vessels within the ON-related lesion area were a strong hint that other processes like ROS-induced impairment were responsible for the photoreceptor depletion and not the blood supply.

Characterisation of retinae concerning neovascularisation in P2 mice was purely done based on comparisons with other rodent models. Phenotypes as the ones depicted in Fig. 84 were labelled as neovascularisation events because they match suspiciously the observations in rats with experimental autoimmune uveitis (EAU) published by Diedrichs-Möhring et al. [275, p. 10, Fig. 6, 458 A+D] and in Norrie disease mutant mice published by Ohlmann et al. [276, p. 6, Fig. 4D]. Still, these sites of disarray could not definitely assigned as neovascularisation events because SMAα staining was negative.

2.5.3 *Causes of IR-induced corneal injuries*

Corneal clouding observed in sham- and IR-irradiated P70 mice solely was most puzzling. The opacification appeared in a phase between 15 and 18 months p.i. which does not favour a radiation-related reaction. Also the fact that female mice were always more affected, assessed by the mean corneal index (CoI, see Tab. 15) based on Scheimpflug images independent of dose (female WTs irradiated with 2 Gy are an exception and suffer from bias due to higher mortality), was striking.
Despite this, it could not be ignored that female mutants irradiated with 2 Gy stood out with a frequency of corneal clouding of 100 % and a median CoI of 5. A plausible explanation might be that grooming (including licking of the eye) was a promoted behaviour in irradiated mice due to possible neuronal alterations. Hence, the observed corneal damages resulted probably from mechanical insults. The (incomplete) data concerning barbering did not support such a correlation of dose and barbering (more barbers and recipients respectively). In fact, in some groups of the 1 Gy cohort were more barbers and recipients identified than in the 2 Gy cohort. Nonetheless, median CoI was in no group of the 1 Gy cohort higher or equal 1. Therefore, no final conclusion concerning the cause of corneal opacification can be drawn.

2.5.4 *Influence of the heterozygous Ercc2 mutation*

Assuming the single nucleotide damage in course of irradiation to be rather of minor relevance, partial repair mechanism deficiency investigated by examination of heterozygous *Ercc2* mutants was gauged with the following hypothesis:

'No influence of the heterozygous Ercc2 mutation on lenticular and retinal phe- 10^{th} *hypothesis*

notypes in B6RCF1 mice within the observation time of max. 20 months p.i.'

Overall, the influence of the *Ercc2* mutation on several determined lenticular, retinal and corneal parameters was negligible. For several measures the mutation had no significant influence at all, e.g. for the ASFA, the PSFA, lens size, domagenesis or corrected 2 Gy mean plus maximum lenticular density in P70 mice and for lenticular extrusions as well as diastasis in P2 mice (though almost at the α-failure threshold of 5 %, Mann-Whitney test). More importantly, for both P2 and P70 mice, the lenticular OCT-type occurrences and the mean plus maximum lenticular densities were not significantly different along the factor line. Accordingly, the hypothesis was not refuted.

Of the retinal parameters neither the retinal thickness in P2 or P70 mice, nor the ONLA in P2 mice was significantly different. The corneae of mutants irradiated with 2 Gy were the only ocular tissue displaying a significantly increased parameter (mean CoI, $p < 0.001$, Mann-Whitney test) compared to irradiated wild-type mice. This was not the case for the lower doses of 0.5 or 1 Gy.

Although single measures of ocular parts did not support convincingly a mutational impact, vision of P70 mice was. MANOVA revealed that the independent factor line separated mean visual acuity of WTs and mutants significantly and all other interactions with the other factors sex and dose (Tab. 23). But, as mentioned above, visual acuity was a composite measure and corneal clouding could have had the highest impact (especially mediated by the female mutants irradiated with 2 Gy).

It appeared that the nucleotide excision repair in heterozygous mutants was either not strongly enough reduced to differ from WTs, or that fewer copies of the *Ercc2* gene product were simply not relevant because few events in form of pyrimidine dimers or radical nucleotides occurred. Maybe they did but had no deciding influence on the genetic programme for fibre cell differentiation.

Finally, survival was analysed in light of different factors. Most surprisingly, female WTs were more prone to die early after exposure to IR than female mutants (Fig. 95). This effect was seen in the 2 Gy cohort. Hazard ratios in the global survival analysis, though, were not significantly decreased for mutants in comparison to WTs (Fig. 93, Genotype, $p = 0.092$). The difference to a significant lower hazard

ratio was equal to 2 mice theoretically flipping censored status. Since censoring is a debatable matter, the analysis could hint prematurely to a possible reduced hazard for heterozygous mutation bearer to suffer a radiation-associated event (leading to death or killing because of murine welfare).
In combination with the factor female sex, the lower occurrence of defined events was undeniable. In general, a compensation theory is conceivable in relation to such phenomena: a lower concentration of repair enzymes in mutants (maybe even lower in females) might enhance the expression of other repair mechanism. This explanation, though, is highly speculative in nature. However, such a conceivable compensative mechanism has to be involved in cancer suppression (tumours in the belly, swelling of the eye conjunctiva) and metabolic stabilisation (general condition failure).

2.5.5 *Relative radiation sensitivity*

The contemporary common understanding of the ophthalmic radiation sensitivity acknowledges the lens as the most sensitive ocular tissue [233] [244]. Led by this assumption our hypothesis for experimental mice was:

'The lens is the most radiation-sensitive ocular tissue in B6C3F1 mice.' *11^{th} hypothesis*

Results of this thesis indicated that this general statement could not be supported. In fact, radiation-sensitivity was highly dependent on the factor age at irradiation. Yes, lenses of 2 Gy-irradiated neonatal mice were partially heavily damaged in comparison to controls and P70 mice irradiated to any dose up to 2 Gy and any observation time point after exposure (see result section 4.1 and 4.2).
Quantitatively, those impairments were nothing against the total developmental disorder in retinae of P2 mice. 2 Gy of IR in form of γ- and X-radiation respectively induced a developmental pathway at which end retinae were half as thick as controls at the same time (Fig. 44+47) and in some experimental groups populated by less than 10 % of photoreceptor cells observed in controls (male WTs, Fig. 83, E). But also distributional retinal changes in irradiated P2 mice were vast. Maximum lenticular thickness in a irradiated P2 mouse was 171 µm, whilst the minimal lenticular thickness in a control was 215 µm. In at least 25 % of the irradiated P2 mice however, only mild C1 or no pathological changes were observed.
Justified considerations were presented to discard radiation-induced corneal alterations too. These seemed to occur indirectly by modified grooming behaviour and

therefore neuronal changes or coincidence. Altogether, it is justified to adjust the initial hypothesis:

Adjusted 11th hypothesis

'The lens is the most radiation-sensible ocular tissue in mice irradiated as young adults independent of latency, but the retina in neonatal B6C3F1 mice.'

3

CONCLUSIONS

In many ways the murine eye lens is not the obvious choice for a cataractogenesis model organism. The murine lens possesses a different geometry than the human lens and differs in GRIN and physiology (see introduction section 1.1). Nonetheless, we have chosen this vertebrate to acquire comparable and broad data and succeeded in this regard.
The here presented thesis substantiated the risks for relative vision impairment after exposure to IR in mice, but revealed also that not only lenticular alterations had to be taken into account to understand the effects on vision. Retinal alterations, corneal opacification and possible neuronal changes too were involved and have to be embedded in a multifactorial assessment for a vision-based radiation protection agenda for humans. General guidelines focusing on the putative most sensible ocular lens as determinant for possible LET radiation-induced vision impairment are insufficient. The P70 mice results of this thesis corroborate the necessity for guidelines established for adults working in an environment of above average radiation level that focus on the lens (provided the transferability). For several reasons this thesis could not answer, whether 0.5 Gy are a reasonable threshold for human adults to expect a vision impairment rate of 1 % of the irradiated individuals.

Measurements of the visual acuity were the centre piece of this thesis to assess the impact of low LET on mice. P70 mice suffered an acuity loss of roughly 10 %/Gy (determined in the 4. quartile of murine life) and P2 mice an approximative loss of 20 %/Gy (determined in the 2. quartile). The underlying pathological alterations of the lens in form of cataractogenesis, retinal developmental disorders and corneal injuries were specific for a certain set of biological and radiological factors: genetic background, sex, dose, and age at irradiation and their combinations. For example, the same relatively high moderate dose of 2 Gy did not affect the retina of P70 at all, while the same dose vastly hampered the development of retinaea in P2 mice. The gathered data allowed also comparisons to older data sets. The mice with the triadic properties [B6C3F1 * P2 * 2 Gy] (genotype * age at irradiation * dose) developed completely different lenticular phenotypes than inbred mice with

the parameters [strain A * P2 * 2 Gy]. In the former case, the type II cataracts were practically not existent, while in the later case, 40 % developed a type II cataract. The sum of possible radiation-induced alterations is a multidimensional matrix still dominated by voids. The data of this thesis has helped to fill some.

Apart from the bigger picture, this thesis was successful to describe several changes in course of cataractogenesis in a highly detailed manner, and could contribute some phenomenological details that were not described before. Cataracts are literally an antediluvian topic. Yet, the methodological dedication was always improvable. In the here presented thesis, the imaging device OCT was diverted from its intended use to monitor retinal alterations. By doing so, the type I cataract was revealed as an inner cortical cataract with a canonical development, and a posterior lens extrusion was found to be a hallmark of irradiated neonatal mice. It was also possible to establish a fine classification of subcapsular cataracts within the posterior and anterior outer cortex, and it was possible to reveal the connection of scattering-structures and applied doses. Furthermore, immunohistochemical analysis showed that signal-free areas were actually areas of degraded crystallins and intermediate filaments.

But more is needed to grasp all aspects of radiation-induced cataractogenesis. What are the biomacromolecular correlates of the scattering areas in the observed lesions? What are the reasons for some epithelial cells not to undergo differentiation? Why do non-degraded nuclei migrate mainly to the posterior pole and accumulate there first? Are swollen fibre cells part of a failure sequence initiated by pseudoepithelial cells? Further studies should include techniques that help to extract the very spots causing scattering increase and should also apply mass spectrometry or micro Raman spectroscopy to identify biochemical shifts. Last but not least, electroretinograms would be pertinent to complement the quite unreliable visual acuity data with a method more independent on eye movements.

If all fundamental aspects concerning cataractogenesis are understood, cataracts could get finally targeted by pharmaceutical approaches for the benefit of all patients independent of their cataract aetiology.

[1] Ulrich Nierste. Wie nützlich ist grundlagenforschung? *Grundlagenforschung? Recherche fondamentale?*, page 16.

[2] Martin Heidegger. *Die Technik und Die Kehre*. Klett-Cotta, 2012.

[3] Ernst Bloch. *Das Prinzip Hoffnung*, volume 3. Suhrkamp Frankfurt am Main, 1959.

[4] Jochen Graw. Genetics of crystallins: cataract and beyond. *Experimental eye research*, 88(2):173–189, 2009. doi: 10.1016/j.exer.2008.10.011.

[5] Leonard A Levin, Siv FE Nilsson, James Ver Hoeve, Samuel Wu, Paul L Kaufman, and Albert Alm. *Adler's Physiology of the Eye E-Book: Expert Consult-Online and Print*. Elsevier Health Sciences, 2011.

[6] Steven Bassnett and M Joseph Costello. The cause and consequence of fiber cell compaction in the vertebrate lens. *Experimental eye research*, 156:50–57, 2017. doi: 10.1016/j.exer.2016.03.009.

[7] Harry Maisel. *The Ocular lens: structure, function, and pathology*. Marcel Dekker Incorporated, 1985.

[8] Matthias Ott. Visual accommodation in vertebrates: mechanisms, physiological response and stimuli. *Journal of Comparative Physiology A*, 192(2):97, 2006. doi: 10.1007/s00359-005-0049-6.

[9] Josh Wallman and Jonathan Winawer. Homeostasis of eye growth and the question of myopia. *Neuron*, 43(4):447–468, 2004. doi: 10.1016/j.neuron.2004.08.008.

[10] David P Crewther. The role of photoreceptors in the control of refractive state. *Progress in retinal and eye research*, 19(4):421–457, 2000. doi: 10.1016/S1350-9462(00)00004-5.

[11] Qi Yan, John I Clark, Thomas N Wight, and E Helene Sage. Alterations in the lens capsule contribute to cataractogenesis in SPARC-null mice. *Journal of cell science*, 115(13):2747–2756, 2002.

[12] Fred T Bosman, Jack Cleutjens, Cor Beek, and Michael Havenith. Basement membrane heterogeneity. *The Histochemical Journal*, 21(11):629–633, 1989.

[13] Nicholas A Kefalides, Robert Alper, and Charles C Clark. Biochemistry and metabolism of basement membranes. In *International review of cytology*, volume 61, pages 167–228. Elsevier, 1979. doi: 10.1016/S0074-7696(08)61998-1.

[14] FJ Lovicu and JW McAvoy. Growth factor regulation of lens development. *Developmental biology*, 280(1):1–14, 2005. doi: 10.1016/j.ydbio.2005.01.020.

[15] M Joseph Costello, Lisa A Brennan, Subhasree Basu, Daniel Chauss, Ashik Mohamed, Kurt O Gilliland, Sönke Johnsen, A Sue Menko, and Marc Kantorow. Autophagy and mitophagy participate in ocular lens organelle degradation. *Experimental eye research*, 116:141–150, 2013. doi: 10.1016/j.exer.2013.08.017.

[16] Gijs FJM Vrensen, Jochen Graw, and Anneke De Wolf. Nuclear breakdown during terminal differentiation of primary lens fibres in mice: a transmission electron microscopic study. *Experimental eye research*, 52(6):647–659, 1991. doi: 10.1016/0014-4835(91)90017-9.

[17] John P Sundberg, Richard S Smith, and Simon WM John. Selection of controls. In *Systematic Evaluation of the Mouse Eye*, pages 93–96. CRC Press, 2001.

[18] Steven Bassnett. On the mechanism of organelle degradation in the vertebrate lens. *Experimental eye research*, 88(2):133–139, 2009. doi: 10.1016/j.exer.2008.08.017.

[19] Andrew I Jobling and Robert C Augusteyn. What causes steroid cataracts? A review of steroid-induced posterior subcapsular cataracts. *Clinical and experimental optometry*, 85(2):61–75, 2002. doi: 10.1111/j.1444-0938.2002.tb03011.x.

[20] Shuhua Song, Andrew Landsbury, Ralf Dahm, Yizhi Liu, Qingjiong Zhang, and Roy A Quinlan. Functions of the intermediate filament cytoskeleton in the eye lens. *The Journal of clinical investigation*, 119(7):1837–1848, 2009. doi: 10.1172/JCI38277.

[21] Werner W Franke, HP Kapprell, and P Cowin. Plakoglobin is a component of the filamentous subplasmalemmal coat of lens cells. *European journal of cell biology*, 43(3):301–315, 1987.

[22] Beate K Straub, Judit Boda, Caecilia Kuhn, Martina Schnoelzer, Ulrike Korf, Tore Kempf, Herbert Spring, Mechthild Hatzfeld, and Werner W Franke. A novel cell-cell junction system: the cortex adhaerens mosaic of lens fiber cells. *Journal of cell science*, 116(24):4985–4995, 2003. doi: 10.1242/jcs.00815.

[23] Kyoung-hye Yoon and Paul G FitzGerald. Periplakin interactions with lens intermediate and beaded filaments. *Investigative ophthalmology & visual science*, 50(3):1283–1289, 2009. doi: 10.1167/iovs.08-2894.

[24] Woo-Kuen Lo, Andrew P Shaw, and Xiao-Jun Wen. Actin filament bundles in cortical fiber cells of the rat lens. *Experimental eye research*, 65(5):691–701, 1997. doi: 10.1006/exer.1997.0375.

[25] Elaine Fuchs and Don W Cleveland. A structural scaffolding of intermediate filaments in health and disease. *Science*, 279(5350):514–519, 1998. doi: 10.1126/science.279.5350.514.

[26] A Millar, A Hooper, L Copeland, F Cummings, and A Prescott. Reorganisation of the microtubule cytoskeleton and centrosomal loss during lens fibre cell differentiation. *Nova Acta Leopoldiana*, 299: 169–83, 1997.

[27] Morten Ø Jensen, Ron O Dror, Huafeng Xu, David W Borhani, Isaiah T Arkin, Michael P Eastwood, and David E Shaw. Dynamic control of slow water transport by aquaporin 0: implications for hydration and junction stability in the eye lens. *Proceedings of the National Academy of Sciences*, 105(38):14430–14435, 2008. doi: 10.1073/pnas.0802401105.

[28] S Sindhu Kumari, Neha Gupta, Alan Shiels, Paul G FitzGerald, Anil G Menon, Richard T Mathias, and Kulandaiappan Varadaraj. Role of aquaporin 0 in lens biomechanics. *Biochemical and biophysical research communications*, 462(4):339–345, 2015. doi: 10.1016/j.bbrc.2015.04.138.

[29] Kristie M Lindsey Rose, Robert G Gourdie, Alan R Prescott, Roy A Quinlan, Rosalie K Crouch, and Kevin L Schey. The C terminus of lens aquaporin 0 interacts with the cytoskeletal proteins filensin and CP49. *Investigative ophthalmology & visual science*, 47(4):1562–1570, 2006. doi: 10.1167/iovs.05-1313.

[30] Surya Prakash G Ponnam, Kekunnaya Ramesha, Sushma Tejwani, Jyoti Matalia, and Chitra Kannabiran. A missense mutation in LIM2 causes autosomal recessive congenital cataract. *Molecular vision*, 14:1204, 2008.

[31] Steven Bassnett, Yanrong Shi, and Gijs FJM Vrensen. Biological glass: structural determinants of eye lens transparency. *Philosophical Transactions of the Royal Society B: Biological Sciences*, 366(1568): 1250–1264, 2011. doi: 10.1098/rstb.2010.0302.

[32] Alan S Fanning and James M Anderson. Zonula occludens-1 and-2 are cytosolic scaffolds that regulate the assembly of cellular junctions. *Annals of the New York Academy of Sciences*, 1165:113, 2009. doi: 10.1111/j.1749-6632.2009.04440.x.

[33] EL Benedetti and NM Kumar. Lens connexins alpha3Cx46 and alpha8Cx50 interact with zonula occludens protein-1 (ZO-1). *Mol Biol Cell*, 14(6):24702481OConnell, 2003.

[34] Hans Bloemendal, Wilfried de Jong, Rainer Jaenicke, Nicolette H Lubsen, Christine Slingsby, and Annette Tardieu. Ageing and vision: structure, stability and function of lens crystallins. *Progress in biophysics and molecular biology*, 86(3):407–485, 2004. doi: 10.1016/j.pbiomolbio.2003.11.012.

[35] Joseph Horwitz. Alpha-crystallin. *Experimental eye research*, 76(2):145–153, 2003. doi: 10.1016/S0014-4835(02)00278-6.

[36] Roland J Siezen, Elaine Wu, Elizabeth D Kaplan, John A Thomson, and George B Benedek. Rat lens γ-crystallins: characterization of the six gene products and their spatial and temporal distribution resulting from differential synthesis. *Journal of molecular biology*, 199(3):475–490, 1988. doi: 10.1016/0022-2836(88)90619-5.

[37] Mireille Delaye and Annette Tardieu. Short-range order of crystallin proteins accounts for eye lens transparency. *Nature*, 302(5907):415, 1983. doi: 10.1038/302415a0.

[38] Kenneth R Robinson and John W Patterson. Localization of steady currents in the lens. *Current eye research*, 2(12):843–847, 1982. doi: 10.3109/02713688209020020.

[39] Richard T Mathias, Joerg Kistler, and Paul Donaldson. The lens circulation. *Journal of Membrane Biology*, 216(1):1–16, 2007. doi: 10.1007/s00232-007-9019-y.

[40] Lisa Ebihara, Yegor Korzyukov, Sorabh Kothari, and Jun-Jie Tong. Cx46 hemichannels contribute to the sodium leak conductance in lens fiber cells. *American Journal of Physiology-Cell Physiology*, 306(5):C506–C513, 2013. doi: 10.1152/ajpcell.00353.2013.

[41] Ralf Dahm, Jan van Marle, Roy A Quinlan, Alan R Prescott, and Gijs FJM Vrensen. Homeostasis in the vertebrate lens: mechanisms of solute exchange. *Philosophical Transactions of the Royal Society B: Biological Sciences*, 366(1568):1265–1277, 2011. doi: 10.1098/rstb.2010.0299.

[42] Valery I Shestopalov and Steven Bassnett. Development of a macromolecular diffusion pathway in the lens. *Journal of cell science*, 116(20):4191–4199, 2003. doi: 10.1242/jcs.00738.

[43] Yanrong Shi, Kelly Barton, Alicia De Maria, J Mark Petrash, Alan Shiels, and Steven Bassnett. The stratified syncytium of the vertebrate lens. *Journal of cell science*, 122(10):1607–1615, 2009. doi: 10.1242/jcs.045203.

[44] Junyuan Gao, Xiurong Sun, Leon C Moore, Thomas W White, Peter R Brink, and Richard T Mathias. Lens intracellular hydrostatic pressure is generated by the circulation of sodium and modulated by gap junction coupling. *The Journal of general physiology*, 137(6):507–520, 2011. doi: 10.1085/jgp.201010538.

[45] Junyuan Gao, Xiurong Sun, Leon C Moore, Peter R Brink, Thomas W White, and Richard T Mathias. The effect of size and species on lens intracellular hydrostatic pressure. *Investigative ophthalmology & visual science*, 54(1):183–192, 2013. doi: 10.1167/iovs.12-10217.

[46] Junyuan Gao, Xiurong Sun, Thomas W White, Nicholas A Delamere, and Richard T Mathias. Feedback regulation of intracellular hydrostatic pressure in surface cells of the lens. *Biophysical journal*, 109(9):1830–1839, 2015. doi: 10.1016/j.bpj.2015.09.018.

[47] Françoise Vérétout, Mireille Delaye, and Annette Tardieu. Molecular basis of eye lens transparency: osmotic pressure and x-ray analysis of α-crystallin solutions. *Journal of molecular biology*, 205(4):713–728, 1989. doi: 10.1016/0022-2836(89)90316-1.

[48] Rachelle Merriman-Smith, Paul Donaldson, and Joerg Kistler. Differential expression of facilitative glucose transporters GLUT1 and GLUT3 in the lens. *Investigative ophthalmology & visual science*, 40(13):3224–3230, 1999.

[49] B Rachelle Merriman-Smith, Anatoly Krushinsky, Joerg Kistler, and Paul J Donaldson. Expression patterns for glucose transporters GLUT1 and GLUT3 in the normal rat lens and in models of diabetic cataract. *Investigative ophthalmology & visual science*, 44(8):3458–3466, 2003. doi: 10.1167/iovs.02-1235.

[50] Elena Ganea and John J Harding. Glutathione-related enzymes and the eye. *Current eye research*, 31(1):1–11, 2006. doi: 10.1080/02713680500477347.

[51] Franz Grehn. Augenheilkunde (30. überarbeitete und aktualisierte Auflage). *Kapitel*, 18:316, 2008.

[52] Frank Schaeffel, Leslie Farkas, and Howard C Howland. Infrared photoretinoscope. *Applied Optics*, 26(8):1505–1509, 1987. doi: 10.1364/AO.26.001505.

[53] Christine Schmucker and Frank Schaeffel. A paraxial schematic eye model for the growing C57BL/6 mouse. *Vision research*, 44(16):1857–1867, 2004. doi: 10.1016/j.visres.2004.03.011.

[54] Xiangtian Zhou, Meixiao Shen, Jing Xie, Jianhua Wang, Liqin Jiang, Miaozhen Pan, Jia Qu, and Fan Lu. The development of the refractive status and ocular growth in C57BL/6 mice. *Investigative ophthalmology & visual science*, 49(12):5208–5214, 2008. doi: 10.1167/iovs.07-1545.

[55] A Hughes. A schematic eye for the rat. *Vision research*, 19(5):569–588, 1979. doi: 10.1016/0042-6989(79)90143-3.

[56] S Remtulla and PE Hallett. A schematic eye for the mouse, and comparisons with the rat. *Vision research*, 25(1):21–31, 1985. doi: 10.1016/0042-6989(85)90076-8.

[57] Hussein Baradia, Negin Nikahd, and Adrian Glasser. Mouse lens stiffness measurements. *Experimental eye research*, 91(2):300–307, 2010. doi: 10.1016/j.exer.2010.06.003.

[58] Hermann von Helmholtz. Ueber die Accommodation des Auges. *Graefe's Archive for Clinical and Experimental Ophthalmology*, 1(2):1–74, 1855.

[59] Gordon Lynn Walls. *The vertebrate eye*. 1942.

[60] H Kolb, E Fernández, and R Nelson. Webvision-the organization of the retina and visual system (salt lake city (ut): University of utah health sciences center). 1995.

[61] Andrew D Huberman and Cristopher M Niell. What can mice tell us about how vision works? *Trends in neurosciences*, 34(9):464–473, 2011. doi: 10.1016/j.tins.2011.07.002.

[62] Chang-Jin Jeon, Enrica Strettoi, and Richard H Masland. The major cell populations of the mouse retina. *Journal of Neuroscience*, 18(21):8936–8946, 1998. doi: 10.1523/JNEUROSCI.18-21-08936.1998.

[63] John C Saari. Biochemistry of visual pigment regeneration the Friedenwald lecture. *Investigative ophthalmology & visual science*, 41(2):337–348, 2000.

[64] Richard W Young. Cell differentiation in the retina of the mouse. *The Anatomical Record*, 212(2):199–205, 1985. doi: 10.1002/ar.1092120215.

[65] Elena Vecino, F David Rodriguez, Noelia Ruzafa, Xandra Pereiro, and Sansar C Sharma. Glia–neuron interactions in the mammalian retina. *Progress in retinal and eye research*, 51:1–40, 2016. doi: 10.1016/j.preteyeres.2015.06.003.

[66] Akane Morita, Hiroko Ushikubo, Asami Mori, Shiho Arima, Kenji Sakamoto, Tohru Nagamitsu, Kunio Ishii, and Tsutomu Nakahara. A delay in vascularization induces abnormal astrocyte proliferation and migration in the mouse retina. *Developmental Dynamics*, 246(3):186–200, 2017. doi: 10.1002/dvdy.24484.

[67] Elena Vecino and Arantxa Acera. Development and programed cell death in the mammalian eye. *International Journal of Developmental Biology*, 59(1-2-3):63–71, 2015. doi: 10.1387/ijdb.150070ev.

[68] Andreas Bringmann, Thomas Pannicke, Jens Grosche, Mike Francke, Peter Wiedemann, Serguei N Skatchkov, Neville N Osborne, and Andreas Reichenbach. Müller cells in the healthy and diseased retina. *Progress in retinal and eye research*, 25(4):397–424, 2006. doi: 10.1016/j.preteyeres.2006.05.003.

[69] Silke Agte, Stephan Junek, Sabrina Matthias, Elke Ulbricht, Ines Erdmann, Antje Wurm, Detlev Schild, Josef A Käs, and Andreas Reichenbach. Müller glial cell-provided cellular light guidance through the vital guinea-pig retina. *Biophysical journal*, 101(11):2611–2619, 2011. doi: 10.1016/j.bpj.2011.09.062.

[70] Elmar Willbold and PG Layer. Muller glia cells and their possible roles during retina differentiation *in vivo* and *in vitro*. *Histology and histopathology*, 13(2):531–552, 1998.

[71] Andreas Bringmann, Ianors Iandiev, Thomas Pannicke, Antje Wurm, Margrit Hollborn, Peter Wiedemann, Neville N Osborne, and Andreas Reichenbach. Cellular signaling and factors involved in Müller cell gliosis: neuroprotective and detrimental effects. *Progress in retinal and eye research*, 28(6):423–451, 2009. doi: 10.1016/j.preteyeres.2009.07.001.

[72] Teri L Belecky-Adams, Ellen C Chernoff, Jonathan M Wilson, and Subramanian Dharmarajan. Reactive Müller glia as potential retinal progenitors. *Neural Stem Cells New Perspect*, 75, 2013. doi: 10.5772/55150.

[73] Michael J Tolentino, D Scott Mcleod, Makoto Taomoto, Tsuyoshi Otsuji, Anthony P Adamis, and Gerard A Lutty. Pathologic features of vascular endothelial growth factor-induced retinopathy in the nonhuman primate. *American journal of ophthalmology*, 133(3):373–385, 2002. doi: 10.1016/S0002-9394(01)01381-2.

[74] Luis E Politi, Mohamed Lehar, and Ruben Adler. Development of neonatal mouse retinal neurons and photoreceptors in low density cell culture. *Investigative ophthalmology & visual science*, 29(4): 534–543, 1988.

[75] Johanna Tukler Henriksson, Alison M McDermott, and Jan PG Bergmanson. Dimensions and morphology of the cornea in three strains of mice. *Investigative ophthalmology & visual science*, 50 (8):3648–3654, 2009. doi: 10.1167/iovs.08-2941.

[76] Elizabeth D Hay. Development of the vertebrate cornea. In *International review of cytology*, volume 63, pages 263–322. 10.1016/S0074-7696(08)61760-X, 1980.

[77] Mitchell Vincent Gossman. Systematic evaluation of the mouse eye: anatomy, pathology, and biomethods. *Journal of Neuro-Ophthalmology*, 24(1):84–85, 2004.

[78] John P Sundberg, Simon WM John, Patsy M Nishina, and Richard S Smith. *Systematic evaluation of the mouse eye: anatomy, pathology, and biomethods*. CRC press, 2001.

[79] C Rehbinder. Fine structure of the mouse cornea. *Zeitschrift für Versuchstierkunde*, 1978.

[80] AP Cullen, BR Chou, M Gm Hall, and SE Jany. Ultraviolet-B damages corneal endothelium. *American journal of optometry and physiological optics*, 61(7):473–478, 1984.

[81] Scheffer CG Tseng. Concept and application of limbal stem cells. *Eye*, 3(2):141–157, 1989. doi: 10.1038/eye.1989.22.

[82] J Haustein. On the ultrastructure of the developing and adult mouse corneal stroma. *Anatomy and embryology*, 168(2):291–305, 1983.

[83] Jessica H Mathew, Jan PG Bergmanson, and Michael J Doughty. Fine structure of the interface between the anterior limiting lamina and the anterior stromal fibrils of the human cornea. *Investigative ophthalmology & visual science*, 49(9):3914–3918, 2008. doi: 10.1167/iovs.07-0707.

[84] Kai Siegbahn. *Alpha-, beta-and gamma-ray spectroscopy*. Elsevier, 2012.

[85] Gregory Choppin, Jan-Olov Liljenzin, and Jan Rydberg. *Radiochemistry and nuclear chemistry*. Butterworth-Heinemann, 2002.

[86] George V Buxton. An overview of the radiation chemistry of liquids. *Radiation Chemistry from Basics to Applications in Material and Life Sciences*, 2008.

[87] WS Osburn. Primordial radionuclides: their distribution, movement, and possible effect within terrestrial ecosystems. *Health Physics*, 11(12):1275–1295, 1965.

[88] Jürg Beer, Ken McCracken, and Rudolf Steiger. *Cosmogenic radionuclides: theory and applications in the terrestrial and space environments*. Springer Science & Business Media, 2012.

[89] John Peter Oyardo Manrique and Alessandro Martins da Costa. Reconstruction of x-rays spectra of clinical linear accelerators from transmission data with generalized simulated annealing. *Radiation Physics and Chemistry*, 155:4–8, 2019. doi: 10.1016/j.radphyschem.2018.08.018.

[90] Claudia Spix, Bernd Grosche, Martin Bleher, Peter Kaatsch, Peter Scholz-Kreisel, and Maria Blettner. Background gamma radiation and childhood cancer in Germany: an ecological study. *Radiation and environmental biophysics*, 56(2):127–138, 2017. doi: 10.1007/s00411-017-0689-2.

[91] Rebecca Smith-Bindman, Diana L Miglioretti, Eric Johnson, Choonsik Lee, Heather Spencer Feigelson, Michael Flynn, Robert T Greenlee, Randell L Kruger, Mark C Hornbrook, Douglas Roblin, et al. Use of diagnostic imaging studies and associated radiation exposure for patients enrolled in large integrated health care systems, 1996-2010. *Jama*, 307(22):2400–2409, 2012. doi: 10.1001/jama.2012.5960.

[92] Sujeenthar Tharmalingam, Shayenthiran Sreetharan, Adomas V Kulesza, Douglas R Boreham, and TC Tai. Low-dose ionizing radiation exposure, oxidative stress and epigenetic programing of health and disease. *Radiation research*, 188(4.2):525–538, 2017. doi: 10.1667/RR14587.1.

[93] Lawrence T Dauer, Elizabeth A Ainsbury, Joseph Dynlacht, David Hoel, Barbara EK Klein, Donald Mayer, Christina R Prescott, Raymond H Thornton, Eliseo Vano, Gayle E Woloschak, et al. Guidance on radiation dose limits for the lens of the eye: overview of the recommendations in NCRP commentary No. 26. *International journal of radiation biology*, 93(10):1015–1023, 2017. doi: 10.1080/09553002.2017.1304669.

[94] Jonas Fontenot, Phillip Taddei, Yuanshui Zheng, Dragan Mirkovic, Thomas Jordan, and Wayne Newhauser. Equivalent dose and effective dose from stray radiation during passively scattered proton radiotherapy for prostate cancer. *Physics in Medicine & Biology*, 53(6):1677, 2008.

[95] RM Sánchez, E Vañó, JM Fernández, S Rosati, and L Lopez-Ibor. Radiation doses in patient eye lenses during interventional neuroradiology procedures. *American Journal of Neuroradiology*, 37(3): 402–407, 2016. doi: 10.3174/ajnr.A4549.

[96] T Moritake, Y Matsumaru, T Takigawa, K Nishizawa, A Matsumura, and K Tsuboi. Dose measurement on both patients and operators during neurointerventional procedures using photoluminescence glass dosimeters. *American journal of neuroradiology*, 29(10):1910–1917, 2008. doi: 10.3174/ajnr.A1235.

[97] Michael Sandborg, Sandro Rossitti, and Håkan Pettersson. Local skin and eye lens equivalent doses in interventional neuroradiology. *European radiology*, 20(3):725–733, 2010. doi: 10.1007/s00330-009-1598-9.

[98] EP Efstathopoulos, I Pantos, M Andreou, A Gkatzis, E Carinou, C Koukorava, NL Kelekis, and E Brountzos. Occupational radiation doses to the extremities and the eyes in interventional radiology and cardiology procedures. *The British journal of radiology*, 84(997):70–77, 2011. doi: 10.1259/bjr/83222759.

[99] Alice J Sigurdson and Elaine Ron. Cosmic radiation exposure and cancer risk among flight crew. *Cancer Investigation*, 22(5):743–761, 2004. doi: 10.1081/CNV-200032767.

[100] Donald M Hassler, Cary Zeitlin, Robert F Wimmer-Schweingruber, Bent Ehresmann, Scot Rafkin, Jennifer L Eigenbrode, David E Brinza, Gerald Weigle, Stephan Böttcher, Eckart Böhm, et al. Mars' surface radiation environment measured with the Mars science laboratory's curiosity rover. *science*, 343(6169):1244797, 2014. doi: 10.1126/science.1244797.

[101] Brandi L Mahaney, Katheryn Meek, and Susan P Lees-Miller. Repair of ionizing radiation-induced DNA double-strand breaks by non-homologous end-joining. *Biochemical Journal*, 417(3):639–650, 2009. doi: 10.1042/BJ20080413.

[102] Detlef Blöcher. DNA double-strand break repair determines the rbe of α-particles. *International journal of radiation biology*, 54(5):761–771, 1988. doi: 10.1080/09553008814552201.

[103] Grigory L Dianov, Peter O'Neill, and Dudley T Goodhead. Securing genome stability by orchestrating DNA repair: removal of radiation-induced clustered lesions in DNA. *Bioessays*, 23(8):745–749, 2001. doi: 10.1002/bies.1104.

[104] Lawrence F Povirk. Biochemical mechanisms of chromosomal translocations resulting from DNA double-strand breaks. *DNA repair*, 5(9-10):1199–1212, 2006. doi: 10.1016/j.dnarep.2006.05.016.

[105] Thomas Helleday, Justin Lo, Dik C van Gent, and Bevin P Engelward. DNA double-strand break repair: from mechanistic understanding to cancer treatment. *DNA repair*, 6(7):923–935, 2007. doi: 10.1016/j.dnarep.2007.02.006.

[106] A Gräslund, A Ehrenberg, A Rupprecht, and G Ström. Ionic base radicals in γ-irradiated DNA. *Biochimica et Biophysica Acta (BBA)-Nucleic Acids and Protein Synthesis*, 254(2):172–186, 1971. doi: 10.1016/0005-2787(71)90826-4.

[107] Stacey D Wetmore, Russell J Boyd, and Leif A Eriksson. Electron affinities and ionization potentials of nucleotide bases. *Chemical Physics Letters*, 322(1-2):129–135, 2000. doi: 10.1016/S0009-2614(00)00391-2.

[108] Tzu-chien V Wang and Kendric C Smith. Enzymatic photoreactivation of escherichia coli after ionizing irradiation: chemical evidence for the production of pyrimidine dimers. *Radiation research*, 76(3):540–548, 1978. doi: 10.2307/3574803.

[109] PV Hariharan and PA Cerutti. Repair of γ-ray-induced thymine damage in Micrococcus radiodurans. *Nature New Biology*, 229(8):247–249, 1971. doi: 10.1038/newbio229247a0.

[110] RF Fisher and Barbara E Pettet. Presbyopia and the water content of the human crystalline lens. *The Journal of physiology*, 234(2):443–447, 1973. doi: 10.1113/jphysiol.1973.sp010353.

[111] Itte Siebinga, Gijs FJM Vrensen, Frits FM De Mul, and Jan Greve. Age-related changes in local water and protein content of human eye lenses measured by Raman microspectroscopy. *Experimental eye research*, 53(2):233–239, 1991. doi: 10.1016/0014-4835(91)90079-T.

[112] PA Riley. Free radicals in biology: oxidative stress and the effects of ionizing radiation. *International journal of radiation biology*, 65(1):27–33, 1994. doi: 10.1080/09553009414550041.

[113] GV Buxton. Radiation chemistry of the liquid state. In *Radiation chemistry*. VCH Publishers Inc, 1987.

[114] George V Buxton, Clive L Greenstock, W Phillips Helman, and Alberta B Ross. Critical review of rate constants for reactions of hydrated electrons, hydrogen atoms and hydroxyl radicals in aqueous solution. *Journal of physical and chemical reference data*, 17(2):513–886, 1988.

[115] Jay A LaVerne. Oh radicals and oxidizing products in the gamma radiolysis of water. *Radiation research*, 153(2):196–200, 2000. doi: 10.1667/0033-7587(2000)153[0196:ORAOPI]2.0.CO;2.

[116] JF Ward. DNA damage as the cause of ionizing radiation-induced gene activation. *Radiation research*, 138(1s):S85–S88, 1994. doi: 10.2307/3578769.

[117] Britton Chance, Helmut Sies, and Alberto Boveris. Hydroperoxide metabolism in mammalian organs. *Physiological reviews*, 59(3):527–605, 1979.

[118] Julie A Reisz, Nidhi Bansal, Jiang Qian, Weiling Zhao, and Cristina M Furdui. Effects of ionizing radiation on biological molecules: mechanisms of damage and emerging methods of detection. *Antioxidants & redox signaling*, 21(2):260–292, 2014. doi: 10.1089/ars.2013.5489.

[119] Alice Uwineza, Alexia A Kalligeraki, Nobuyuki Hamada, Miguel Jarrin, and Roy A Quinlan. Cataractogenic load – a concept to study the contribution of ionizing radiation to accelerated aging in the eye lens. *Mutation Research/Reviews in Mutation Research*, 2019. doi: 10.1016/j.mrrev.2019.02.004.

[120] Jean Cadet and J Richard Wagner. Oxidatively generated base damage to cellular DNA by hydroxyl radical and one-electron oxidants: similarities and differences. *Archives of biochemistry and biophysics*, 557:47–54, 2014. doi: 10.1016/j.abb.2014.05.001.

[121] Phillip Achey and Hollis Duryea. Production of DNA strand breaks by the hydroxyl radical. *International Journal of Radiation Biology and Related Studies in Physics, Chemistry and Medicine*, 25(6):595–601, 1974. doi: 10.1080/09553007414550791.

[122] Mark K Shigenaga, Carlos J Gimeno, and Bruce N Ames. Urinary 8-hydroxy-2'-deoxyguanosine as a biological marker of *in vivo* oxidative DNA damage. *Proceedings of the National Academy of Sciences*, 86(24):9697–9701, 1989. doi: 10.1073/pnas.86.24.9697.

[123] Ja-Eun Kim, Seongwon Choi, Ju-Ah Yoo, and Myung-Hee Chung. 8-oxoguanine induces intramolecular DNA damage but free 8-oxoguanine protects intermolecular DNA from oxidative stress. *FEBS letters*, 556(1-3):104–110, 2004. doi: 10.1016/S0014-5793(03)01385-1.

[124] Steen Steenken and Slobodan V Jovanovic. How easily oxidizable is DNA? One-electron reduction potentials of adenosine and guanosine radicals in aqueous solution. *Journal of the american chemical society*, 119(3):617–618, 1997. doi: 10.1021/ja962255b.

[125] Barry Halliwell and Susanna Chirico. Lipid peroxidation: its mechanism, measurement, and significance. *The American journal of clinical nutrition*, 57(5):715S–725S, 1993. doi: 10.1093/ajcn/57.5.715S.

[126] Giuseppina Barrera, Stefania Pizzimenti, and Mario Umberto Dianzani. Lipid peroxidation: control of cell proliferation, cell differentiation and cell death. *Molecular aspects of medicine*, 29(1-2):1–8, 2008. doi: 10.1016/j.mam.2007.09.012.

[127] Lawrence J Marnett. Lipid peroxidation – DNA damage by malondialdehyde. *Mutation Research/Fundamental and Molecular Mechanisms of Mutagenesis*, 424(1-2):83–95, 1999. doi: 10.1016/S0027-5107(99)00010-X.

[128] Nicola Traverso, Stefano Menini, Elena Pesce Maineri, Stefania Patriarca, Patrizio Odetti, Damiano Cottalasso, Umberto M Marinari, and M Adelaide Pronzato. Malondialdehyde, a lipoperoxidation-derived aldehyde, can bring about secondary oxidative damage to proteins. *The Journals of Gerontology Series A: Biological Sciences and Medical Sciences*, 59(9):B890–B895, 2004. doi: 10.1093/gerona/59.9.B890.

[129] Alicja Winczura, Daria Zdżalik, and Barbara Tudek. Damage of DNA and proteins by major lipid peroxidation products in genome stability. *Free radical research*, 46(4):442–459, 2012. doi: 10.3109/10715762.2012.658516.

[130] Elena M Oborina and M Cecilia Yappert. Effect of sphingomyelin versus dipalmitoylphosphatidylcholine on the extent of lipid oxidation. *Chemistry and physics of lipids*, 123(2):223–232, 2003. doi: 10.1016/S0009-3084(03)00003-3.

[131] Isabelle Corre, Colin Niaudet, and Francois Paris. Plasma membrane signaling induced by ionizing radiation. *Mutation Research/Reviews in Mutation Research*, 704(1-3):61–67, 2010. doi: 10.1016/j.mrrev.2010.01.014.

[132] Jirasak Wong-Ekkabut, Zhitao Xu, Wannapong Triampo, I-Ming Tang, D Peter Tieleman, and Luca Monticelli. Effect of lipid peroxidation on the properties of lipid bilayers: a molecular dynamics study. *Biophysical journal*, 93(12):4225–4236, 2007. doi: 10.1529/biophysj.107.112565.

[133] John J Harding. The lens: development, proteins, metabolism and cataract. *The eye*, 1:207–492, 1984.

[134] Allen Taylor and Kelvin JA Davies. Protein oxidation and loss of protease activity may lead to cataract formation in the aged lens. *Free Radical Biology and Medicine*, 3(6):371–377, 1987. doi: 10.1016/0891-5849(87)90015-3.

[135] Ashraf G Madian and Fred E Regnier. Proteomic identification of carbonylated proteins and their oxidation sites. *Journal of proteome research*, 9(8):3766–3780, 2010. doi: 10.1021/pr1002609.

[136] Fu Shang, Minyi Lu, Edward Dudek, John Reddan, and Allen Taylor. Vitamin C and vitamin E restore the resistance of GSH-depleted lens cells to H2O2. *Free Radical Biology and Medicine*, 34(5): 521–530, 2003. doi: 10.1016/S0891-5849(02)01304-7.

[137] Raphael Ceccaldi, Beatrice Rondinelli, and Alan D D Andrea. Repair pathway choices and consequences at the double-strand break. *Trends in cell biology*, 26(1):52–64, 2016. doi: 10.1016/j.tcb.2015.07.009.

[138] Lorraine S Symington and Jean Gautier. Double-strand break end resection and repair pathway choice. *Annual review of genetics*, 45:247–271, 2011. doi: 10.1146/annurev-genet-110410-132435.

[139] Wil L Santivasi and Fen Xia. Ionizing radiation-induced DNA damage, response, and repair. *Antioxidants & redox signaling*, 21(2):251–259, 2014. doi: 10.1089/ars.2013.5668.

[140] Jan de Boer, Ingrid Donker, Jan de Wit, Jan HJ Hoeijmakers, and Geert Weeda. Disruption of the mouse xeroderma pigmentosum group d DNA repair/basal transcription gene results in preimplantation lethality. *Cancer research*, 58(1):89–94, 1998.

[141] Nukhet Aykin-Burns, Benjamin G Slane, Annie TY Liu, Kjerstin M Owens, Malinda S O'Malley, Brian J Smith, Frederick E Domann, and Douglas R Spitz. Sensitivity to low-dose/low-let ionizing radiation in mammalian cells harboring mutations in succinate dehydrogenase subunit c is governed by mitochondria-derived reactive oxygen species. *Radiation research*, 175(2):150–158, 2010. doi: 10.1667/RR2220.1.

[142] Tohru Yamamori, Hironobu Yasui, Masayuki Yamazumi, Yusuke Wada, Yoshinari Nakamura, Hideo Nakamura, and Osamu Inanami. Ionizing radiation induces mitochondrial reactive oxygen species production accompanied by upregulation of mitochondrial electron transport chain function and mitochondrial content under control of the cell cycle checkpoint. *Free Radical Biology and Medicine*, 53(2):260–270, 2012. doi: 10.1016/j.freeradbiomed.2012.04.033.

[143] Alton Meister and Mary E Anderson. Glutathione. *Annual review of biochemistry*, 52(1):711–760, 1983.

[144] VN Reddy. Metabolism of glutathione in the lens. *Experimental eye research*, 11(3):310–328, 1971. doi: 10.1016/S0014-4835(71)80043-X.

[145] Frank J Giblin. Glutathione: a vital lens antioxidant. *Journal of Ocular Pharmacology and Therapeutics*, 16(2):121–135, 2000. doi: 10.1089/jop.2000.16.121.

[146] Paul J Donaldson, Angus C Grey, Bianca Maceo Heilman, Julie C Lim, and Ehsan Vaghefi. The physiological optics of the lens. *Progress in retinal and eye research*, 56:e1–e24, 2017. doi: 10.1016/j.preteyeres.2016.09.002.

[147] Thomas D Ingolia and Elizabeth A Craig. Four small drosophila heat shock proteins are related to each other and to mammalian alpha-crystallin. *Proceedings of the National Academy of Sciences*, 79(7):2360–2364, 1982. doi: 10.1073/pnas.79.7.2360.

[148] Charistina M Sax and Joram Piatigorsky. Expression of the α-crystallin/small heat-shock protein/molecular chaperone genes in the lens and other tissues. *Advances in enzymology and related areas of molecular biology*, 69:155–201, 1994. doi: 10.1002/9780470123157.

[149] Joseph Horwitz. Alpha-crystallin can function as a molecular chaperone. *Proceedings of the National Academy of Sciences*, 89(21):10449–10453, 1992. doi: 10.1073/pnas.89.21.10449.

[150] Ram Kannan, Bin Ouyang, Eric Wawrousek, Neil Kaplowitz, and Usha P Andley. Regulation of GSH in αA-expressing human lens epithelial cell lines and in αA knockout mouse lenses. *Investigative ophthalmology & visual science*, 42(2):409–416, 2001.

[151] Jean-Marie Bruey, Cécile Ducasse, Philippe Bonniaud, Luigi Ravagnan, Santos A Susin, Chantal Diaz-Latoud, Sandeep Gurbuxani, André-Patrick Arrigo, Guido Kroemer, Eric Solary, et al. Hsp27 negatively regulates cell death by interacting with cytochrome c. *Nature cell biology*, 2(9):645, 2000. doi: 10.1038/35023595.

[152] Yu-Chi Liu, Mark Wilkins, Terry Kim, Boris Malyugin, and Jodhbir S Mehta. Cataracts. *The Lancet*, 390(10094):600–612, 2017. doi: 10.1016/S0140-6736(17)30544-5.

[153] Rita Hiller, Robert D Sperduto, and Fred Ederer. Epidemiologic associations with nuclear, cortical, and posterior subcapsular cataracts. *American journal of epidemiology*, 124(6):916–925, 1986. doi: 10.1093/oxfordjournals.aje.a114481.

[154] Roger JW Truscott and Robert C Augusteyn. Oxidative changes in human lens proteins during senile nuclear cataract formation. *Biochimica et Biophysica Acta (BBA)-Protein Structure*, 492(1): 43–52, 1977. doi: 10.1016/0005-2795(77)90212-4.

[155] JS Zigler, Igal Gery, David Kessler, and Jin H Kinoshita. Macrophage mediated damage to rat lenses in culture: a possible model for uveitis-associated cataract. *Investigative ophthalmology & visual science*, 24(5):651–654, 1983.

[156] EA Ainsbury, SD Bouffler, W Dörr, J Graw, CR Muirhead, AA Edwards, and J Cooper. Radiation cataractogenesis: a review of recent studies. *Radiation research*, 172(1):1–9, 2009. doi: 10.1667/RR1688.1.

[157] David Whitaker, Richard Steen, and David B Elliott. Light scatter in the normal young, elderly, and cataractous eye demonstrates little wavelength dependency. *Optometry and Vision Science*, 70 (11):963–968, 1993. doi: 10.1097/00006324-199311000-00014.

[158] M Joseph Costello, Sönke Johnsen, Kurt O Gilliland, Christopher D Freel, and W Craig Fowler. Predicted light scattering from particles observed in human age-related nuclear cataracts using mie scattering theory. *Investigative ophthalmology & visual science*, 48(1):303–312, 2007. doi: 10.1167/iovs.06-0480.

[159] William B Rathbun, Ann M Holleschau, Debra L Murray, Anita Buchanan, Shoichi Sawaguchi, and Robert V Tao. Glutathione synthesis and glutathione redox pathways in naphthalene cataract of the rat. *Current eye research*, 9(1):45–53, 1990. doi: 10.3109/02713689009000054.

[160] Matthew HJ Sweeney and Roger JW Truscott. An impediment to glutathione diffusion in older normal human lenses: a possible precondition for nuclear cataract. *Experimental eye research*, 67 (5):587–595, 1998. doi: 10.1006/exer.1998.0549.

[161] Roger JW Truscott. Age-related nuclear cataract – oxidation is the key. *Experimental eye research*, 80(5):709–725, 2005. doi: 10.1016/j.exer.2004.12.007.

[162] M Joseph Costello, Sönke Johnsen, Sangeetha Metlapally, Kurt O Gilliland, Lesley Frame, and Dorairajan Balasubramanian. Multilamellar spherical particles as potential sources of excessive light scattering in human age-related nuclear cataracts. *Experimental eye research*, 91(6):881–889, 2010. doi: 10.1016/j.exer.2010.09.013.

[163] Toyoichi Tanaka, Coe Ishimoto, and Leo T Chylack. Phase separation of a protein-water mixture in cold cataract in the young rat lens. *Science*, 197(4307):1010–1012, 1977. doi: 10.1126/science.887936.

[164] Max Bücklers. Histologische Untersuchungen über die Schädigungen des Auges durch kurzwellige ultrarote Strahlen. *Albrecht von Graefes Archiv für Ophthalmologie*, 117(1):1–32, 1926.

[165] Russell L Carpenter. Ocular effects of microwave radiation. *Bulletin of the New York Academy of Medicine*, 55(11):1048, 1979.

[166] Piró Kramár, Carrol Harris, and Arthur W Guy. Thermal cataract formation in rabbits. *Bioelectromagnetics: Journal of the Bioelectromagnetics Society, The Society for Physical Regulation in Biology and Medicine, The European Bioelectromagnetics Association*, 8(4):397–406, 1987. doi: 10.1002/bem.2250080408.

[167] Kazuyuki Sasaki, Hiroshi Sasaki, Masami Kojima, Ying Bo Shui, Otto Hockwin, Fridbert Jonasson, Hong Ming Cheng, Masaji Ono, and Nobuyo Katoh. Epidemiological studies on UV-related cataract in climatically different countries. *Journal of epidemiology*, 9(6sup):33–38, 1999. doi: 10.2188/jea.9.6sup_33.

[168] Jule Griebrok Jose. Posterior cataract induction by UV-B radiation in albino mice. *Experimental eye research*, 42(1):11–20, 1986. doi: 10.1016/0014-4835(86)90013-8.

[169] Toshiyasu Imaizumi, Daijiro Kurosaka, Umi Tanaka, Daisuke Sakai, Kazuhiro Fukuda, and Atsushi Sanbe. Topical administration of a ROCK inhibitor prevents anterior subcapsular cataract induced by UV-B irradiation. *Experimental eye research*, 181:145–149, 2019. doi: 10.1016/j.exer.2019.01.016.

[170] Linda M Meyer, Per Söderberg, Xiuqin Dong, and Alfred Wegener. UVR-B induced cataract development in C57 mice. *Experimental eye research*, 81(4):389–394, 2005. doi: 10.1016/j.exer.2005.02.009.

[171] Linda M Meyer, Stefan Löfgren, Frank G Holz, Alfred Wegener, and Per Söderberg. Bilateral cataract induced by unilateral UVR-B exposure–evidence for an inflammatory response. *Acta ophthalmologica*, 91(3):236–242, 2013. doi: 10.1111/j.1755-3768.2012.02384.x.

[172] Kenneth R Hightower. The role of the lens epithelium in development of UV cataract. *Current eye research*, 14(1):71–78, 1995. doi: 10.3109/02713689508999916.

[173] Hassan Hashemi, Mahmood Jabbarvand, and Mehrdad Mohammadpour. Bilateral electric cataracts: clinicopathologic report. *Journal of Cataract & Refractive Surgery*, 34(8):1409–1412, 2008. doi: 10.1016/j.jcrs.2008.03.044.

[174] Dilraj Singh Grewal, Rajeev Jain, Gagandeep Singh Brar, and Satinder Pal Singh Grewal. Unilateral electric cataract: Scheimpflug imaging and review of the literature. *Journal of Cataract & Refractive Surgery*, 33(6):1116–1119, 2007. doi: 10.1016/j.jcrs.2007.01.041.

[175] E Flockerzi, M El-Husseiny, U Löw, L Daas, and B Seitz. Cataract development after electrical injury. *Der Ophthalmologe: Zeitschrift der Deutschen Ophthalmologischen Gesellschaft*, 113(11):950–951, 2016. doi: 10.1007/s00347-016-0245-5.

[176] A Verma. Electric cataract: a case report. *MOJ Biol Med*, 3(5):201–202, 2018.

[177] Jeffrey R Saffle, Alan Crandall, and Glenn D Warden. Cataracts: a long-term complication of electrical injury. *The Journal of trauma*, 25(1):17–21, 1985.

[178] Deepali Singhal, Ruchita Falera, and Manpreet Kaur. *Traumatic Cataract*. JP Medical Ltd, 2017.

[179] Robert C Urban Jr and Edward Cotlier. Corticosteroid-induced cataracts. *Survey of ophthalmology*, 31(2):102–110, 1986. doi: 10.1016/0039-6257(86)90077-9.

[180] Mark C Gillies, Maciek Kuzniarz, Jamie Craig, Matthew Ball, Wei Luo, and Judy M Simpson. Intravitreal triamcinolone-induced elevated intraocular pressure is associated with the development of posterior subcapsular cataract. *Ophthalmology*, 112(1):139–143, 2005. doi: 10.1016/j.ophtha.2004.07.017.

[181] Andreas Pollreisz and Ursula Schmidt-Erfurth. Diabetic cataract – pathogenesis, epidemiology and treatment. *Journal of ophthalmology*, 2010, 2010. doi: 10.1155/2010/608751.

[182] SD Varma and JH Kinoshita. The absence of cataracts in mice with congenital hyperglycemia. *Experimental eye research*, 19(6):577–582, 1974. doi: 10.1016/0014-4835(74)90095-5.

[183] Jin H Kinoshita. Mechanisms initiating cataract formation proctor lecture. *Investigative Ophthalmology & Visual Science*, 13(10):713–724, 1974.

[184] Sadaf Saba, Maryam Ghahramani, and Reza Yousefi. A comparative study of the impact of calcium ion on structure, aggregation and chaperone function of human αA-crystallin and its cataract-causing R12C mutant. *Protein and peptide letters*, 24(11):1048–1058, 2017. doi: 10.2174/0929866524666170807125658.

[185] Suman Biswas, Frederick Harris, Sarah Dennison, Jaipaul Singh, and David A Phoenix. Calpains: targets of cataract prevention? *Trends in molecular medicine*, 10(2):78–84, 2004. doi: 10.1016/j.molmed.2003.12.007.

[186] Shin-ichiro Hino, Shinichi Kondo, Hiroshi Sekiya, Atsushi Saito, Soshi Kanemoto, Tomohiko Murakami, Kazuyasu Chihara, Yuri Aoki, Masayuki Nakamori, Masanori P Takahashi, et al. Molecular mechanisms responsible for aberrant splicing of SERCA1 in myotonic dystrophy type 1. *Human molecular genetics*, 16(23):2834–2843, 2007. doi: 10.1093/hmg/ddm239.

[187] Jarig Junge. Ocular changes in dystrophia myotonica, paramyotonia and myotonia congenita. *Documenta Ophthalmologica*, 21(1):1–115, 1966.

[188] Stephen Barnes and Roy A Quinlan. Small molecules, both dietary and endogenous, influence the onset of lens cataracts. *Experimental eye research*, 156:87–94, 2017. doi: 10.1016/j.exer.2016.03.024.

[189] Jochen Graw, Jana Löster, Dian Soewarto, Helmut Fuchs, André Reis, Eckhard Wolf, Rudi Balling, and Martin Hrabě de Angelis. *Aey2*, a new mutation in the βB2-crystallin–encoding gene of the mouse. *Invest Ophthalmol Vis Sci.*, 42(7):1574–1580, 2001.

[190] Jochen Graw, Jana Löster, Dian Soewarto, Helmut Fuchs, André Reis, Eckhard Wolf, Rudi Balling, and Martin Hrabě de Angelis. V76D mutation in a conserved γD-crystallin region leads to dominant cataracts in mice. *Mamm Genome.*, 13(8):452–455, 2002. doi: 10.1007/s00335-002-3021-6.

[191] Jochen Graw, Jana Löster, Dian Soewarto, Helmut Fuchs, Birgit Meyer, André Reis, Eckhard Wolf, Rudi Balling, and Martin Hrabě de Angelis. Characterization of a new, dominant V124E mutation in the mouse αA-crystallin–encoding gene. *Invest Ophthalmol Vis Sci.*, 42(12):2909–2915, 2001.

[192] Koustav Ganguly, Jack Favor, Angelika Neuhäuser-Klaus, Rodica Sandulache, Oliver Puk, Johannes Beckers, Marion Horsch, Sandra Schädler, Daniela Vogt-Weisenhorn, Wolfgang Wurst, et al. Novel allele of *Crybb2* in the mouse and its expression in the brain. *Invest Ophthalmol Vis Sci.*, 49(4):1533–1541, 2008. doi: 10.1167/iovs.07-0788.

[193] Peter F Kador, Henry N Fukui, Suguru Fukushi, Howard M Jernigan Jr, and Jin H Kinoshita. Philly mouse: a new model of hereditary cataract. *Exp Eye Res.*, 30(1):59–68, 1980. doi: 10.1016/0014-4835(80)90124-4.

[194] Oliver Puk, Nafees Ahmad, Sibylle Wagner, Martin Hrabě de Angelis, and Jochen Graw. First mutation in the βA2-crystallin encoding gene is associated with small lenses and age-related cataracts. *Invest Ophthalmol Vis Sci.*, 52(5):2571–2576, 2011. doi: 10.1167/iovs.10-6443.

[195] Daniel Pawliczek, Claudia Dalke, Helmut Fuchs, Valerie Gailus-Durner, Martin Hrabě de Angelis, Jochen Graw, and Oana Veronica Amarie. Spectral domain-optical coherence tomography (SD-OCT) as a monitoring tool for alterations in mouse lenses. *Experimental Eye Research*, 190:107871, 2019. doi: 10.1016/j.exer.2019.107871.

[196] S Sindhu Kumari, Subramaniam Eswaramoorthy, Richard T Mathias, and Kulandaiappan Varadaraj. Unique and analogous functions of aquaporin 0 for fiber cell architecture and ocular lens transparency. *Biochimica et Biophysica Acta (BBA)-Molecular Basis of Disease*, 1812(9):1089–1097, 2011. doi: 10.1016/j.bbadis.2011.04.001.

[197] Alan Shiels, Steven Bassnett, Kulandaiappa Varadaraj, Richard Mathias, Kristin Al-Ghoul, Jer Kuszak, Dorit Donoviel, Stan Lilleberg, Glenn Friedrich, and Brian Zambrowicz. Optical dysfunction of the crystalline lens in aquaporin-0-deficient mice. *Physiological genomics*, 7(2):179–186, 2001. doi: 10.1152/physiolgenomics.00078.2001.

[198] Ana B Chepelinsky. Structural function of MIP/aquaporin 0 in the eye lens; genetic defects lead to congenital inherited cataracts. In *Aquaporins*, pages 265–297. 2009. doi: 10.1007/978-3-540-79885-9_14.

[199] Aileen Sandilands, Alan R Prescott, Alfred Wegener, Rebecca K Zoltoski, Aileen M Hutcheson, Shigeo Masaki, Jer R Kuszak, and Roy A Quinlan. Knockout of the intermediate filament protein CP49 destabilises the lens fibre cell cytoskeleton and decreases lens optical quality, but does not induce cataract. *Experimental eye research*, 76(3):385–391, 2003. doi: 10.1016/S0014-4835(02)00330-5.

[200] Yanrong Shi, Alicia De Maria, Thomas Bennett, Alan Shiels, and Steven Bassnett. A role for epha2 in cell migration and refractive organization of the ocular lens. *Investigative ophthalmology & visual science*, 53(2):551–559, 2012. doi: 10.1167/iovs.11-8568.

[201] Sarah Kunze, Claudia Dalke, Helmut Fuchs, Matthias Klaften, Ute Rössler, Sabine Hornhardt, Maria Gomolka, Oliver Puk, Sibylle Sabrautzki, Ulrike Kulka, et al. New mutation in the mouse *Xpd/Ercc2* gene leads to recessive cataracts. *PLoS One.*, 10(5):e0125304, 2015. doi: 10.1371/journal.pone.0125304.

[202] Jill O Fuss and John A Tainer. XPB and XPD helicases in TFIIH orchestrate DNA duplex opening and damage verification to coordinate repair with transcription and cell cycle via CAK kinase. *DNA repair*, 10(7):697–713, 2011. doi: 10.1016/j.dnarep.2011.04.028.

[203] Michael Reed, Birgit Woelker, Pin Wang, Yun Wang, Mary E Anderson, and Peter Tegtmeyer. The C-terminal domain of p53 recognizes DNA damaged by ionizing radiation. *Proceedings of the National Academy of Sciences*, 92(21):9455–9459, 1995. doi: 10.1073/pnas.92.21.9455.

[204] Luke A Wiley, Ramya Rajagopal, Lisa K Dattilo, and David C Beebe. The tumor suppressor gene *Trp53* protects the mouse lens against posterior subcapsular cataracts and the BMP receptor Acvr1 acts as a tumor suppressor in the lens. *Disease models & mechanisms*, 4(4):484–495, 2011. doi: 10.1242/dmm.006593.

[205] BV Worgul, Yu I Kundiyev, NM Sergiyenko, VV Chumak, PM Vitte, C Medvedovsky, EV Bakhanova, AK Junk, OY Kyrychenko, NV Musijachenko, et al. Cataracts among Chernobyl clean-up workers: implications regarding permissible eye exposures. *Radiation research*, 167(2):233–243, 2007. doi: 10.1667/RR0298.1.

[206] Tamara V Azizova, Evgeny V Bragin, Nobuyuki Hamada, and Maria V Bannikova. Risk of cataract incidence in a cohort of mayak pa workers following chronic occupational radiation exposure. *PloS one*, 11(10):e0164357, 2016.

[207] Barbara W Streeten and Joseph Eshaghian. Human posterior subcapsular cataract: a gross and flat preparation study. *Archives of ophthalmology*, 96(9):1653–1658, 1978. doi: 10.1001/archopht.1978.03910060279020.

[208] Joseph Eshaghian and Barbara W Streeten. Human posterior subcapsular cataract: an ultrastructural study of the posteriorly migrating cells. *Archives of Ophthalmology*, 98(1):134–143, 1980. doi: 10.1001/archopht.1980.01020030136016.

[209] C Wedl. Atlas der pathologischen Histologie des Auges, with the collaboration of C. Stellwag von Carion, 1860.

[210] Joah F Aliancy and Nick Mamalis. Crystalline lens and cataract. In *Webvision: The Organization of the Retina and Visual System [Internet]*. University of Utah Health Sciences Center, 2017.

[211] GR Merriam Jr and A Szechter. The relative radiosensitivity of rat lenses as a function of age. *Radiation research*, 62(3):488–497, 1975. doi: 10.2307/3574142.

[212] AK Gajewski, K Majewska, MG Słowikowska, K Chomiczewski, and A Kulig. Types and rate of cataract development in mice irradiated at different ages. *Radiation research*, 71(2):471–480, 1977.

[213] Ilaria De Stefano, Barbara Tanno, Paola Giardullo, Simona Leonardi, Emanuela Pasquali, Francesca Antonelli, Mirella Tanori, Arianna Casciati, Simonetta Pazzaglia, Anna Saran, et al. The patched 1 tumor-suppressor gene protects the mouse lens from spontaneous and radiation-induced cataract. *The American journal of pathology*, 185(1):85–95, 2015. doi: 10.1016/j.ajpath.2014.09.019.

[214] Joseph R Dynlacht, Shailaja Valluri, Jennifer Lopez, Falon Greer, Colleen DesRosiers, Andrea Caperell-Grant, Marc S Mendonca, and Robert M Bigsby. Estrogen protects against radiation-induced cataractogenesis. *Radiation research*, 170(6):758–764, 2008. doi: 10.1667/RR1416.1.

[215] George R Merriam Jr and Elizabeth F Focht. A clinical and experimental study of the effect of single and divided doses of radiation on cataract production. *Transactions of the American Ophthalmological Society*, 60:35, 1962.

[216] Leo T Chylack, John K Wolfe, David M Singer, M Cristina Leske, Mark A Bullimore, Ian L Bailey, Judith Friend, Daniel McCarthy, and Suh-Yuh Wu. The lens opacities classification system III. *Archives of ophthalmology*, 111(6):831–836, 1993. doi: 10.1001/archopht.1993.01090060119035.

[217] X Pei, Y Bao, Y Chen, and X Li. Correlation of lens density measured using the Pentacam Scheimpflug system with the lens opacities classification system III grading score and visual acuity in age-related nuclear cataract. *British journal of ophthalmology*, 92(11):1471–1475, 2008. doi: 10.1136/bjo.2007.136978.

[218] JM Sparrow, AJ Bron, NAP Brown, W Ayliffe, and AR Hill. The Oxford clinical cataract classification and grading system. *International ophthalmology*, 9(4):207–225, 1986. doi: 10.1007/BF00137534.

[219] FA Stewart, AV Akleyev, M Hauer-Jensen, JH Hendry, NJ Kleiman, TJ Macvittie, BM Aleman, AB Edgar, K Mabuchi, CR Muirhead, et al. ICRP publication 118: ICRP statement on tissue reactions and early and late effects of radiation in normal tissues and organs–threshold doses for tissue reactions in a radiation protection context. *Annals of the ICRP*, 41(1-2):1–322, 2012. doi: 10.1016/j.icrp.2012.02.001.

[220] Nobuyuki Hamada, Tamara V Azizova, and Mark P Little. An update on effects of ionizing radiation exposure on the eye. *The British journal of radiology*, 93:20190829, 2020. doi: 10.1259/bjr.20190829.

[221] Theo GMF Gorgels, Ingrid van der Pluijm, Renata MC Brandt, George A Garinis, Harry van Steeg, Gerard van den Aardweg, Gerard H Jansen, Jan M Ruijter, Arthur AB Bergen, Dirk van Norren, et al. Retinal degeneration and ionizing radiation hypersensitivity in a mouse model for Cockayne syndrome. *Molecular and cellular biology*, 27(4):1433–1441, 2007. doi: 10.1128/MCB.01037-06.

[222] Eliah G Overbey, Willian Abraham da Silveira, Seta Stanbouly, Nina C Nishiyama, Gina D Roque-Torres, Michael J Pecaut, David Carl Zawieja, Charles Wang, Jeffrey S Willey, Michael D Delp, et al. Spaceflight influences gene expression, photoreceptor integrity, and oxidative stress-related damage in the murine retina. *Scientific reports*, 9(1):1–12, 2019. doi: 0.1038/s41598-019-49453-x.

[223] Xiao Mao, Stephanie Byrum, Nina Nishiyama, Michael Pecaut, Vijayalakshmi Sridharan, Marjan Boerma, Alan Tackett, Dai Shiba, Masaki Shirakawa, Satoru Takahashi, et al. Impact of spaceflight and artificial gravity on the mouse retina: Biochemical and proteomic analysis. *International journal of molecular sciences*, 19(9):2546, 2018. doi: 10.3390/ijms19092546.

[224] XW Mao, M Boerma, D Rodriguez, M Campbell-Beachler, T Jones, S Stanbouly, V Sridharan, A Wroe, and GA Nelson. Acute effect of low-dose space radiation on mouse retina and retinal endothelial cells. *Radiation research*, 190(1):45–52, 2018. doi: 10.1667/RR14977.1.

[225] DR Lucas. The effect of x-radiation on the mouse retina at different stages of development. *International Journal of Radiation Biology and Related Studies in Physics, Chemistry and Medicine*, 3(2):105–124, 1961. doi: 10.1080/09553006114550131.

[226] Sergio L Schmidt, Renan WF Vitral, and Rafael Linden. Effects of prenatal ionizing irradiation on the development of the ganglion cell layer of the mouse retina. *International Journal of Developmental Neuroscience*, 19(4):469–473, 2001. doi: 10.1016/S0736-5748(00)00068-X.

[227] Doris Dahl. The radial glia of Müller in the rat retina and their response to injury. an immunofluorescence study with antibodies to the glial fibrillary acidic (GFA) protein. *Experimental eye research*, 28(1):63–69, 1979. doi: 10.1016/0014-4835(79)90106-4.

[228] Jens Grosche, Wolfgang Härtig, and Andreas Reichenbach. Expression of glial fibrillary acidic protein (GFAP), glutamine synthetase (GS), and Bcl-2 protooncogene protein by Müller (glial) cells in retinal light damage of rats. *Neuroscience letters*, 185(2):119–122, 1995. doi: 10.1016/0304-3940(94)11239-F.

[229] Amy J Eisenfeld, AH Bunt-Milam, and P Vijay Sarthy. Müller cell expression of glial fibrillary acidic protein after genetic and experimental photoreceptor degeneration in the rat retina. *Investigative ophthalmology & visual science*, 25(11):1321–1328, 1984.

[230] Frederick C Blodi. The late effects of x-radiation on the cornea. *Transactions of the American Ophthalmological Society*, 56:413, 1958.

[231] Hiroshi Fujishima, Jun Shimazaki, and Kazuo Tsubota. Temporary corneal stem cell dysfunction after radiation therapy. *British journal of ophthalmology*, 80(10):911–914, 1996. doi: 10.1136/bjo.80.10.911.

[232] DC Lloyd, RJ Purrott, GW Dolphin, Dawn Bolton, AA Edwards, and MJ Corp. The relationship between chromosome aberrations and low LET radiation dose to human lymphocytes. *International Journal of Radiation Biology and Related Studies in Physics, Chemistry and Medicine*, 28(1):75–90, 1975. doi: 10.1080/09553007514550781.

[233] Elizabeth A Ainsbury, Stephen Barnard, Scott Bright, Claudia Dalke, Miguel Jarrin, Sarah Kunze, Rick Tanner, Joseph R Dynlacht, Roy A Quinlan, Jochen Graw, et al. Ionizing radiation induced cataracts: recent biological and mechanistic developments and perspectives for future research. *Mutation Research/Reviews in Mutation Research*, 770:238–261, 2016. doi: 10.1016/j.mrrev.2016.07.010.

[234] John B Storer, TJ Mitchell, and RJM Fry. Extrapolation of the relative risk of radiogenic neoplasms across mouse strains and to man. *Radiation research*, 114(2):331–353, 1988. doi: 10.2307/3577229.

[235] Ewa M Nowosielska, Aneta Cheda, Jolanta Wrembel-Wargocka, and Marek K Janiak. Effect of low doses of low-LET radiation on the innate anti-tumor reactions in radioresistant and radiosensitive mice. *Dose-Response*, 10(4):dose–response, 2012. doi: 10.2203/dose-response.12-018.Nowosielska.

[236] Douglas Grahn. Acute radiation response of mice from a cross between radiosensitive and radioresistant strains. *Genetics*, 43(5):835, 1958.

[237] Claudia Dalke, Frauke Neff, Savneet Kaur Bains, Scott Bright, Deborah Lord, Jochen Graw, Peter Reitmeir, Ute Rößler, Daniel Samaga, Kristian Unger, Herbert Braselmann, et al. Lifetime study in mice after acute low-dose ionizing radiation: a multifactorial study with special focus on cataract risk. *Radiat Environ Biophys.*, 57(2):99–113, 2018. doi: 10.1007/s00411-017-0728-z.

[238] Xiaoping Ao, Lujun Zhao, Mary A Davis, David M Lubman, Theodore S Lawrence, and Feng-Ming Kong. Radiation produces differential changes in cytokine profiles in radiation lung fibrosis sensitive and resistant mice. *Journal of hematology & oncology*, 2(1):6, 2009. doi: 10.1186/1756-8722-2-6.

[239] Christine L Dileto and Elizabeth L Travis. Fibroblast radiosensitivity *in vitro* and lung fibrosis *in vivo*: comparison between a fibrosis-prone and fibrosis-resistant mouse strain. *Radiation research*, 146(1):61–67, 1996. doi: 10.2307/3579396.

[240] FA Bettelheim and LT Chylack Jr. Light scattering of whole excised human cataractous lenses. relationships between different light scattering parameters. *Experimental eye research*, 41(1):19–30, 1985.

[241] Nicholas A Phelps Brown. The morphology of cataract and visual performance. *Eye*, 7(1):63–67, 1993.

[242] MS Lasa, Marvin J Podgor, MB Datiles, Rafael C Caruso, and Benjamin V Magno. Glare sensitivity in early cataracts. *British journal of ophthalmology*, 77(8):489–491, 1993. doi: 10.1136/bjo.77.8.489.

[243] Basil V Worgul, GR Merriam, and Cecily Medvedovsky. Accelerated heavy particles and the lens II. cytopathological changes. *Investigative ophthalmology & visual science*, 27(1):108–114, 1986.

[244] Erik Poppe. Experimental investigations on cataract formation following whole-body Roentgen irradiation. *Acta radiologica*, (2):138–148, 1957.

[245] Jos Jonkers, Ralph Meuwissen, Hanneke van der Gulden, Hans Peterse, Martin van der Valk, and Anton Berns. Synergistic tumor suppressor activity of BRCA2 and p53 in a conditional mouse model for breast cancer. *Nature genetics*, 29(4):418–425, 2001. doi: 10.1038/ng747.

[246] Ruth Ashery-Padan, Till Marquardt, Xunlei Zhou, and Peter Gruss. Pax6 activity in the lens primordium is required for lens formation and for correct placement of a single retina in the eye. *Genes & development*, 14(21):2701–2711, 2000. doi: 10.1101/gad.184000.

[247] Elizabeth F Focht, George R Merriam JR, Melvin S Schwartz, and R Wayne Prsons. The relative biologic effectiveness of cobalt 60 gamma and 200 kv. x radiation for cataract induction. *American Journal of Roentgenology*, 102(1):71–80, 1968.

[248] R.A. McCarron, S.G.R. Barnard, G. Babini, C. Dalke, J. Graw, S. Leonardi, M. Mancuso, J.E. Moquet, D. Pawliczek, S. Pazzaglia, I. De Stefano, and E.A. Ainsbury. Radiation induced lens opacity and cataractogenesis? A lifetime study using mice of varying genetic backgrounds. *Radiation research*, 2021.

[249] Oliver Puk, Martin Hrabě de Angelis, and Jochen Graw. Longitudinal fundus and retinal studies with SD-OCT: a comparison of five mouse inbred strains. *Mamm Genome.*, 24(5-6):198–205, 2013. doi: 10.1007/s00335-013-9457-z.

[250] H Mayer. Theodor Scheimpflug. *Ophthalmic Research*, 26(Suppl. 1):3–9, 1994. doi: 10.1159/000267508.

[251] Alfred Wegener and Heike Laser-Junga. Photography of the anterior eye segment according to Scheimpflug's principle: options and limitations – a review. *Clinical & experimental ophthalmology*, 37(1):144–154, 2009. doi: 10.1111/j.1442-9071.2009.02018.x.

[252] Oliver Puk, Claudia Dalke, Jack Favor, Martin Hrabe de Angelis, and Jochen Graw. Variations of eye size parameters among different strains of mice. *Mammalian genome*, 17(8):851–857, 2006. doi: 10.1007/s00335-006-0019-5.

[253] Glen T Prusky, Nazia M Alam, Steven Beekman, and Robert M Douglas. Rapid quantification of adult and developing mouse spatial vision using a virtual optomotor system. *Investigative ophthalmology & visual science*, 45(12):4611–4616, 2004. doi: 10.1167/iovs.04-0541.

[254] Qing Xie, Rebecca McGreal, Raven Harris, Chun Y Gao, Wei Liu, Lixing W Reneker, Linda S Musil, and Ales Cvekl. Regulation of c-Maf and αA-crystallin in ocular lens by fibroblast growth factor signaling. *Journal of Biological Chemistry*, 291(8):3947–3958, 2016. doi: 10.1074/jbc.M115.705103.

[255] Douglas G Altman. *Practical statistics for medical research*. CRC press, 1990.

[256] Marcello Pagano and Kimberlee Gauvreau. *Principles of biostatistics*. CRC Press, 2018.

[257] Daniel Pawliczek, Helmut Fuchs, Valerie Gailus-Durner, Martin Hrabě de Angelis, Roy Quinlan, Jochen Graw, and Claudia Dalke. On the nature of murine radiation-induced subcapsular cataracts: optical coherence tomography-based fine classification, *in-vivo* dynamics and impact on visual acuity (accepted for publication). *Radiation Research*, 2021.

[258] Daniel Pawliczek, Helmut Fuchs, Valerie Gailus-Durner, Martin Hrabě de Angelis, Jochen Graw, and Claudia Dalke. Ionising radiation causes vision impairment in neonatal B6C3F1 mice. *Experimental Eye Research*, 204:108432, 2021. doi: 10.1016/j.exer.2020.108432.

[259] W Köhler, GA Schachtel, and P Voleske. Biostatistik, 4, aktualisierte und erw. Aufl., 2007.

[260] Sarah Kunze, Alexander Cecil, Cornelia Prehn, Gabriele Möller, Andreas Ohlmann, Gerhild Wildner, Stephan Thurau, Kristian Unger, Ute Rößler, Sabine M Hölter, et al. Posterior subcapsular cataracts are a late effect after acute exposure to 0.5 Gy ionizing radiation in mice. *International Journal of Radiation Biology*, 0(ja):1–38, 2021. doi: 10.1080/09553002.2021.1876951.

[261] Stephen GR Barnard, Roisin McCarron, Jayne Moquet, Roy Quinlan, and Elizabeth Ainsbury. Inverse dose-rate effect of ionising radiation on residual 53BP1 foci in the eye lens. *Scientific reports*, 9(1):1–8, 2019. doi: 10.1038/s41598-019-46893-3.

[262] Basil V Worgul, Lubomir Smilenov, David J Brenner, Anna Junk, Wei Zhou, and Eric J Hall. Atm heterozygous mice are more sensitive to radiation-induced cataracts than are their wild-type counterparts. *Proceedings of the National Academy of Sciences*, 99(15):9836–9839, 2002. doi: 10.1073/pnas.162349699.

[263] Ivo Kunstyr and Hans-georg W Leuenberger. Gerontological data of C57BL/6J mice. i. Sex differences in survival curves. *Journal of gerontology*, 30(2):157–162, 1975.

[264] Konrad Lehmann, Karl-Friedrich Schmidt, and Siegrid Löwel. Vision and visual plasticity in ageing mice. *Restorative neurology and neuroscience*, 30(2):161–178, 2012. doi: 10.3233/RNN-2012-110192.

[265] Frauke Neff, Diana Flores-Dominguez, Devon P Ryan, Marion Horsch, Susanne Schröder, Thure Adler, Luciana Caminha Afonso, Juan Antonio Aguilar-Pimentel, Lore Becker, Lillian Garrett, et al. Rapamycin extends murine lifespan but has limited effects on aging. *The Journal of clinical investigation*, 123(8):3272–3291, 2013. doi: 10.1172/JCI67674.

[266] Eugenio Picano, Eliseo Vano, Luciano Domenici, Matteo Bottai, and Isabelle Thierry-Chef. Cancer and non-cancer brain and eye effects of chronic low-dose ionizing radiation exposure. *BMC cancer*, 12(1):157, 2012. doi: 10.1186/1471-2407-12-157.

[267] Francis A Cucinotta, Murat Alp, Frank M Sulzman, and Minli Wang. Space radiation risks to the central nervous system. *Life Sciences in Space Research*, 2:54–69, 2014. doi: 10.1016/j.lssr.2014.06.003.

[268] Samuel P Hicks and Constance J D'Amato. Low dose radiation of the developing brain. *Science*, 141(3584):903–905, 1963.

[269] BV Worgul, Jr GR Merriam, and C Medvedovsky. Cortical cataract development–an expression of primary damage to the lens epithelium. *Lens and eye toxicity research*, 6(4):559–571, 1989.

[270] Yuri Teramoto, Shigekazu Uga, Yoshibumi Matsushima, Kimiya Shimizu, Tetsuya Morita, and Shinji Shirakawa. Morphological study on rupture of posterior capsule in RLC mouse lens. *Graefe's archive for clinical and experimental ophthalmology*, 238(12):970–978, 2000. doi: 10.1007/s004170000190.

[271] Judith Pieroth. Charakterisierung der Mausmutanten *Fun6* und *Fun22*. 2011.

[272] Jingjing Wang, Matthew L O'Sullivan, Dibyendu Mukherjee, Vanessa M Puñal, Sina Farsiu, and Jeremy N Kay. Anatomy and spatial organization of müller glia in mouse retina. *Journal of Comparative Neurology*, 525(8):1759–1777, 2017. doi: 10.1002/cne.24153.

[273] Michael A Dyer and Constance L Cepko. Control of müller glial cell proliferation and activation following retinal injury. *Nature neuroscience*, 3(9):873–880, 2000. doi: 10.1038/78774.

[274] Marcus Fruttiger. Development of the mouse retinal vasculature: angiogenesis versus vasculogenesis. *Investigative ophthalmology & visual science*, 43(2):522–527, 2002. doi: TheAssociationforResearchinVisionandOphthalmology.

[275] Maria Diedrichs-Möhring, Johann Leban, Stefan Strobl, Franz Obermayr, and Gerhild Wildner. A new small molecule for treating inflammation and chorioretinal neovascularization in relapsing-remitting and chronic experimental autoimmune uveitis. *Investigative ophthalmology & visual science*, 56(2):1147–1157, 2015. doi: 10.1167/iovs.14-15518.

[276] Andreas Ohlmann, Michael Scholz, Andreas Goldwich, Bharesh K Chauhan, Kristiane Hudl, Anne V Ohlmann, Eberhart Zrenner, Wolfgang Berger, Aleš Cvekl, Mathias W Seeliger, et al. Ectopic norrin induces growth of ocular capillaries and restores normal retinal angiogenesis in norrie disease mutant mice. *Journal of Neuroscience*, 25(7):1701–1710, 2005. doi: 10.1523/JNEUROSCI.4756-04.2005.

Publications in context of this thesis

Journal publications

Pawliczek D, Dalke C, Fuchs H, Gailus-Durner V, Hrabě de Angelis M, Graw J & Amarie OV (2020). Spectral domain-Optical coherence tomography (SD-OCT) as a monitoring tool for alterations in mouse lenses. *Exp Eye Res*, 190, 107871.

Pawliczek D, Fuchs H, Gailus-Durner V, Hrabě de Angelis M, Graw J & Dalke C (2021). Ionizing radiation causes vision impairment in neonatal B6C3F1 mice. *Exp Eye Res*, 204, 108432.

Pawliczek D, Fuchs H, Gailus-Durner V, Hrabě de Angelis M, Quinlan R, Graw J & Dalke C (2021). On the nature of murine radiation-induced subcapsular cataracts: OCT-based fine classification, *in-vivo* dynamics and impact on visual acuity. Accepted for publication 01/21 by *Radiat Res*

McCarron RA, Barnar, SGR, Babini G, Dalke C, Graw J, Leonardi S, Mancuso M, Moquet JE, Pawliczek D, Pazzaglia S, De Stefano I & Ainsbury EA (2021). Radiation induced lens opacity and cataractogenesis? A lifetime study using mice of varying genetic backgrounds. Accepted with minor revisions 01/21 by *Radiat Res*

Talks to the scientific community

05/2019	'Cataract type and magnitude in mice are highly dependent on dose and age at irradiation', **CONRAD**, Munich, Germany
07/2019	'Retinal dysplasia and cortical cataracts in neonatal mice exposed to ionizing radiation reduce visual acuity', ZEISS poster price talk, **Young Researchers Vision Camp**, Leibertingen, Germany

08/2019 'Radiation-induced posterior lesions in mouse eye lenses: Size and possible effects on visual acuity' and poster,
ICRR, Manchester, UK

10/2019 'Cataract type in mice exposed to moderate doses of ionizing radiation depends on mouse age at irradiation',
EVER, Nice, France

Poster presentations

03/2018 'Early observations on mouse lenses after irradiation with low and moderate doses of ionizing radiation',
Interact, Munich, Germany

09/2018 'Minor changes in irradiated mouse eye lenses challenge cataract danger of ionizing radiation',
GBS, Frankfurt, Germany

Acknowledgements

A doctoral thesis is only partially the effort of the candidate. The right circumstances, a decent portion of luck at the right time, and especially the constructive help and guidance of several associated people is needed too. I profited from all these factors together.

First of all, I have to thank Dr. Claudia Dalke for the direct supervision over the entire time in the group 'Eye Disease' of the Helmholtz-Center Munich. Her calm and steadfast support was a huge contribution to the final completion of this work and the published papers. I thank also Prof. Dr. Jochen Graw for accepting me as doctoral candidate for this quite delicate project in the first place. My contradictory demeanour must have been quite annoying. All the more I am grateful to have experienced free space for my own strategies and decisions. I am also extremely grateful that PD Dr. Sabine Hölter-Koch took over my supervision without further ado and helped me via her lucid understanding for priorities. I thank also the entire thesis committee, including Prof. Dr. Angelika Schnieke, PD Dr. Anna Friedl and Prof. Dr. Gabrielle Multhoff for their advice and commitment.

For all the help in the German Mouse Clinic I want to thank Dr. Oana Amarie; mainly for the introducing of the virtual drum and the lenticular options of the OCT which proofed the be pivotal for the outcome of this thesis.

Our experienced technicians, Erika Bürkle and Monika Stadler, were the highly efficient backbone of the lab and the mouse facilities. Without their hard work, especially in mouse breeding, genotyping and Scheimpflug experiments, the entire project would have been impossible.

What I lacked in veterinary competence to assess pathological alterations in the long-term cohorts was overcompensated by Dr. Manuel Miller and Carolin Becher, who had always time to perform an autopsy on a deceased mouse and giving educated assessments. In course of this project, they gauged over 200 animals and thus contributed valuable information which nobody in our group could have delivered.

The LDLensRad consortium, which consisted of partners from Public Health England, University of Durham, ENEA and Oxford Brooks University, turned out to be a perfect learning environment. I enjoyed our fruitful discussions in the retreats (Oxford, Munich, Rome) and the conferences we attended (CONRAD Munich, ICRR Manchester, EVER Nice). I dedicate a special thank to Dr. Liz Ainsbury for the professional project lead, manuscripts proofreading and the possibility to visit PHE for project-related work.

Finally, I want to thank the European Union for their generous funding of the radiation-related eye research under the umbrella of the joint CONCERT program. Under the provided conditions, unimpeded research was possible to a degree almost impossible to imagine for so many destitute PhD students.

Ebersberg, 4th of June, 2020

Funding

This study was financed by the LDLensRad project that received funding from the Euratom research and training programme 2014-2018 under grant agreement No 662287. This publication reflects only the authors view. Responsibility for the information and views expressed therein lies entirely with the authors. The European Commission is not responsible for any use that may be made of the information it contains.

The German Mouse Clinic received funding by the German Federal Ministry of Education and Research (Infrafrontier grant 01KX1012 to MHdA).